

Dissertation
submitted to the
Combined Faculties for the Natural Sciences and for Mathematics
of the Ruperto-Carola University of Heidelberg, Germany
for the degree of
Doctor of Natural Sciences

presented by
Arne Schoch, Master of Science
born in: Reutlingen, Germany
Oral examination: July 12th, 2019

Quantitative Analysis of Information Transfer in Signal Transduction

Referees: PROF. DR. URSULA KUMMER
DR. JÜRGEN PAHLE

Abstract

Biological signal transduction pathways evolved to reliably transmit information from input signals inducing appropriate cellular responses in the process. Along signaling pathways, information is often successively relayed to several types of transmitter molecules. In some cases, particular transmitter molecules do not only receive one kind of information, but several. To this end, information can for instance refer to the identity or quantity of first messengers. By encoding particular bits of information into specific characteristics of such shared transmitters, the information can be decoded downstream. Here, transmitter characteristics may refer to the absolute level of transmitter molecules, the duration of transmitter activation or, in case of activation pulses, the pulse frequency. In this thesis, I analyzed encoding and decoding in two prime examples of signal transduction: calcium signaling in non-excitable cells and *Escherichia coli* chemotaxis. For this purpose, I present several methods allowing for a quantitative analysis of information transfer, whereas methods are partly based on measures from the field of information theory.

With regards to calcium signaling, I focused on the frequency-decoding of calcium oscillations by dependent proteins. Particularly, variations in the quantity of input signals can account for modulations of the calcium oscillation frequency. Several proteins like NFAT, NF- κ B, CaMKII and calpain were found to be sensitive to such frequency-modulations. To this end, most frequency-decoding proteins exhibit increased activities for fast calcium oscillations and decreased activities for slow oscillations. I refer to this form of frequency-decoding as high-pass activation. In contrast, the transcription factor NFAT was reported to exhibit an optimal frequency for its activation, while slower or faster frequencies only result in a reduced protein activity. In turn, I refer to this form of frequency-decoding as band-pass activation. On the basis of kinetic models, I identified requirements for high-pass and band-pass activation. In more detail, I employed optimization algorithms aiming at a maximization of the high-pass or band-pass activation distinctness. Among other things, I found that antagonistic, oscillator-dependent regulation of the decoder was essential for band-pass activation, whereas regulator species had to be differently responsive to upstream calcium oscillations. Further, I defined favorable parameter margins and confirmed reports on the importance of cooperative protein activation for distinct frequency-decoding. Additionally, I employed channel capacity estimates to quantify the discriminability of particular calcium oscillation frequencies in the presence of realistic stochastic fluctuations. For the application of channel capacity estimations and the interpretation of the resultant estimates, I discuss several possible pitfalls.

With regards to *Escherichia coli* chemotaxis, I focused on the encoding of attractant levels into receptor methylation levels using an established kinetic model. On the basis of results by a collaborateur, encoding was investigated by inferring expected attractant levels from present receptor methylation levels. In addition, I used delayed mutual information estimates to quantify the dynamic processes of memory formation and memory loss. Here, memory formation and memory loss were characterized by targeted transient changes in receptor methylation levels in response to changes in ambient attractant levels. In *Escherichia coli* chemotaxis, single receptors can be methylated multiple times. By means of the aforementioned methods, I found that, for extreme attractant levels, chemotactic behavior failed due to limitations in the encoding of ambient attractant levels into receptor methylation levels, whereas a reduction

of the maximal number of methylations per receptor resulted in severer limitations in the encoding, thus, greater impairments in *Escherichia coli* chemotaxis.

For both examples of signal transduction, I examined information transmission through molecular communication channels. To this end, the input was the variable to be encoded or decoded and the output was the encoding or decoding variable. Changes in model characteristics, such as the model parameterization or network structure, greatly impacted the number of input signals that could be reliably encoded or decoded. Both example systems distinguished themselves by a pronounced ultrasensitivity of the output variable to changes in the input variable. I found that this ultrasensitivity helped in increasing the discriminability between input signals.

Zusammenfassung

Biologische Signaltransduktionswege entstanden, um die Information eines Eingangssignal zuverlässig zu übertragen und eine passende Zellantwort auszulösen. Oftmals wird die Eingangsinformation entlang des Signalwegs nacheinander an verschiedene Arten von Transmittermolekülen weitergegeben. In einigen Fällen nehmen bestimmte Transmittermoleküle nicht nur eine bestimmte Information entgegen, sondern mehrere, die etwa Aufschluss über die Identität oder Dosis des Eingangssignals geben. Da diese Informationen in modulierbare Eigenschaften des Transmitters enkodiert werden, können sie im Anschluss wieder dekodiert werden. Solche Eigenschaften können sich zum Beispiel auf die absolute Menge an Transmittermolekülen, die Dauer der Transmitteraktivierung oder, im Falle von Aktivierungspulsen, die Pulsfrequenz beziehen. In dieser Arbeit untersuchte ich Enkodierung und Dekodierung in zwei bekannten Beispielen der Signaltransduktion: in der Calciumsignalkaskade in nichterregbaren Zellen und in dem Chemotaxisignalweg von *Escherichia coli*. Hierzu wendete ich mehrere Methoden an, die quantitative Analysen des Informationstransfers ermöglichten und teilweise auf informationstheoretischen Größen beruhten.

Bei meiner Untersuchung der Calciumsignalkaskade konzentrierte ich mich auf die Frequenzdekodierung von Calciumoszillationen durch abhängige Proteine. Hierbei wird die Oszillationsfrequenz von Calcium durch die Dosis eines Eingangssignals moduliert. Es wurde berichtet, mehrere Proteine, darunter NFAT, NF- κ B, CaMKII und Calpain, seien sensitiv gegenüber solchen Frequenzmodulationen. Genauer gesagt ist die Aktivität der meisten frequenzdekodierenden Proteinen bei schnellen Calciumoszillationen erhöht und bei langsamen Oszillationen erniedrigt. Diese Form der Frequenzdekodierung nenne ich Hochpassaktivierung. Dagegen wurde berichtet, NFAT weise eine maximale Aktivität bei einer bestimmten Frequenz auf und eine erniedrigte Aktivität bei langsameren oder schnelleren Frequenzen. Diese Form der Frequenzdekodierung nenne ich wiederum Bandpassaktivierung. Mittels kinetischer Modelle identifizierte ich Voraussetzungen für Hochpass- und Bandpassaktivierung. Hierzu verwendete ich Optimierungsalgorithmen, die auf eine Maximierung der Ausgeprägtheit der Hochpass- oder Bandpassaktivierung abzielten. Unter anderem fand ich heraus, dass eine antagonistische, oszillatorabhängige Regulation des Dekodierers essentiell für die Erzeugung einer Bandpassaktivierung war, wobei die Regulatoren des Dekodierers unterschiedlich reaktionsschnell sein mussten. Außerdem konnte ich besonders günstige Parametrisierungsbereiche für eine ausgeprägte Frequenzdekodierung bestimmen und bestätigte Berichte über eine positive Korrelation zwischen der Ausgeprägtheit der Frequenzdekodierung und der Stärke der kooperativen Proteinaktivierung. Des Weiteren setzte ich Kanalkapazitätsschätzungen ein, um die Unterscheidbarkeit verschiedener Calciumoszillationsfrequenzen unter realistischen stochastischen Bedingungen zu quantifizieren. Bezüglich des Einsatzes und der Interpretation von Kanalkapazitätsschätzungen weise ich in dieser Arbeit auf mögliche Stolpersteine hin.

Bei meiner Untersuchung des Chemotaxisignalwegs von *Escherichia coli* konzentrierte ich mich auf die Enkodierung der Lockstoffkonzentration in die Methylierungsstufen der Rezeptorproteine. Hierzu verwendete ich ein etabliertes kinetisches Model. In Zusammenarbeit mit einem Kooperationspartner untersuchte ich die Enkodierung, indem ich anhand von vorhandenen Methylierungsstufen auf eine erwartete Lockstoffkonzentration zurückschloss. Außerdem nutzte ich zeitversetzte Transinformationsschätzungen, um die dynamischen Prozesse der

Gedächtnisbildung und des Gedächtnisverlusts zu vermessen. Dabei waren beide Prozesse durch gezielte, transiente Veränderungen der Rezeptormethylierungsstufen in Folge einer Änderung der Lockstoffkonzentration gekennzeichnet. In dem Chemotaxisignalweg von *Escherichia coli* können einzelne Rezeptorproteine mehrfach methyliert werden. Mittels der beschriebenen Methoden fand ich heraus, dass in Gegenwart von extremen Lockstoffkonzentrationen eine chemotaktische Reaktion scheiterte, weil bereits die Enkodierung der Lockstoffkonzentration in die Rezeptormethylierungsstufen fehlschlug. Eine Verminderung der maximal möglichen Zahl an Methylierungen pro Rezeptor führte hierbei zu stärkeren Einschränkungen bei der Enkodierung und somit im chemotaktischen Verhalten des Bakteriums.

In beiden Fallbeispielen untersuchte ich Informationstransfer durch molekulare Kommunikationskanäle, wobei der Kanalinput die zu enkodierende oder dekodierende Variable und der Kanaloutput die enkodierende oder dekodierende Variable darstellte. Änderungen der Modelleigenschaften, wie zum Beispiel der Modelparametrisierung oder der Netzwerkstruktur, beeinflussten maßgeblich die Anzahl an Inputsignalen, die eindeutig enkodiert oder dekodiert werden konnten. Die beiden untersuchten Systeme zeichneten sich durch eine ausgeprägte Ultrasensitivität der Outputvariable in Bezug auf Änderungen der Inputvariable aus. Meine Ergebnisse zeigen, dass diese Ultrasensitivität maßgeblich die Unterscheidbarkeit einzelner Inputsignale förderte.

Acknowledgments

First, I would like to thank my supervisors Ursula Kummer and Jürgen Pahle. I came in contact with the field of systems biology in a practical in Ursula's group during my bachelor's studies. She also convinced me to join the systems biology major in Heidelberg. I joined Jürgen's work group at the end of my master's studies. Both, Ursula and Jürgen, consulted me many times and for that I am grateful. I would also like to thank the other two members of the examination commission, Frederik Graw and Thomas Holstein, for their effort and time.

Further, I could always count on my colleagues for lending me more than just one helping hand. From Michael Gabel, Jonas Förster and Peter Kumberger I learned a lot about mathematics and programming, Irina Surovtsova and Aarón Vásquez Jiménez helped me in getting a better understanding of information theory and, finally, Martin Zauser provided answers to almost all of my questions with incomparable patience and care. I seriously believe that I have never met a friendlier and more good-hearted person than Martin in my life.

It is not a secret that PhD studies can get exhausting and tiresome. Without frequent coffee breaks, work-out beers, dinners, wine festivals, trips to the lake, athletic challenges and a lot of ice cream, I am not entirely sure whether I could have preserved my sanity¹. For this reason, I would like to thank Lilija Aprupe, Sirac Baz, Nils Bundgaard, Sophia Eijkman, Juan Estupiñán Mendéz, Jana Fehr, Jonas Förster, Michael Gabel, Jan Jongmanns, Oskar, Priyata Kalra, Sarah Kaspar, Verena Koerber, Vineet Kumar, Peter Kumberger, Anika Liu, Babak Loghmani, Ramin Safarpour, Astrid Stubbusch, Neha Thakre, Niklas Vockert, Samuel Wilks and Martin Zauser for plenty of opportunities to refresh my mind. In particular, I would like to highlight the following people: Michael Gabel for being the ringleader, for adjusting his pace when jogging with me, for posing as Miguel, for cooling my twisted ankle after I fell down the stair case and for providing dry humor. Priyata Kalra for sharing words of wisdom, for being overly generous² and for keeping our circle of friends together. Samuel Wilks for being a muppet, for traumatizing me in the sauna, for pouring a drink in my face, which was totally uncalled for, for correcting my balancing issues and for making me laugh a lot. And finally, Ramin Safarpour for being a really good friend, for lending me an ear or two, for having those dance moves that I could not copy and for going on a hiking trip to Scotland with me despite my warnings that I might have to eat him in case we get lost. Without you life at and outside of work would not have been as colorful.

Lastly, I would like to thank the people who brought me up, my family and hometown friends. In particular, I would like to mention my parents who provided financial and emotional support during my studies and inherited me the necessary stubbornness and resilience to withstand also the greatest of my academic challenges. My siblings Nono and Jojo who often acted as role models. And my grandparents that always believed in me succeeding in this PhD program and that I shall remember fondly.

¹ Some of the people mentioned in the following might argue that I actually lost my sanity or never had any to begin with, but who would trust people that associate themselves with an insane person.

² I am certain I still owe you money and I will pay you back and you will not be able to stop me.

Contents

Abstract	v
Zusammenfassung	vii
Acknowledgments	ix
I Main introduction	1
1 Main introduction	3
1.1 Biological communication	3
1.1.1 Signal transduction	3
1.1.2 Signal encoding and decoding	4
1.2 Calcium signaling	6
1.2.1 Calcium as a second messenger	6
1.2.2 On the encoding of first messenger signals into calcium oscillations . .	7
1.2.3 On the decoding of calcium oscillations	9
1.3 <i>Escherichia coli</i> chemotaxis	13
1.3.1 The chemotaxis signaling pathway	13
1.3.2 Memory in <i>Escherichia coli</i> chemotaxis	16
1.4 Information theory in the biosciences	18
1.4.1 On the advancement of information theory in the biosciences	18
1.4.2 On mutual information	18
1.4.3 On channel capacity	19
1.5 Outline of the thesis	22
II Materials and methods	25
2 Materials and methods	27
2.1 Used hardware	27
2.2 Deterministic simulations	27
2.3 Stochastic simulations	27
2.4 Optimizations	28
2.5 Estimations of mutual information	28
2.6 Estimations of channel capacity	29
2.7 Data presentation	31
III Results	33
3 Method development and investigation	35
3.1 The <i>OscillatorGenerator</i> package for R	35

3.2	A theoretical analysis of channel capacity estimates	40
3.2.1	A measure for quantifying the discriminability of input signals in the presence of fluctuations	40
3.2.2	Channel capacity is limited by the number of input signals considered	41
3.2.3	Input recurrence in channel capacity estimates	43
3.2.4	Reducing overlaps between output distributions increases channel capacity estimates	45
4	Analyzing the frequency-decoding of calcium oscillations	47
4.1	Chapter introduction	47
4.1.1	About this chapter	47
4.1.2	Outside assistance	49
4.2	The high-pass activation model	51
4.3	The band-pass activation model	54
4.4	A framework for maximizing frequency-decoding efficiencies	57
4.5	Testing for basic frequency-decoding functionalities	59
4.6	Band-pass activation of the transcription factor NFAT	60
4.6.1	The NFAT model	60
4.6.2	Definition of an objective function for an optimization of the NFAT model	62
4.6.3	Antagonistic, oscillator-dependent regulation enables band-pass activation of NFAT	63
4.6.4	Effect of variations in T_{slow} on optimization results	64
4.7	The importance of being cooperative in frequency-decoding	66
4.8	Detecting conserved parameter margins for efficient frequency-decoding	68
4.8.1	Isolating the best parameter sets for particular optimization problems	68
4.8.2	Single parameter analysis	69
4.8.3	Analysis of parameter couples	72
4.9	Constraint optimizations reveal consequences of unfavorable parameterization margins	75
4.10	Dependence of the binding constant parameterization on the calcium oscillation amplitude	79
4.11	Precision versus efficiency in frequency-decoding	81
4.12	Recreating high-pass activation under stochastic conditions	83
4.13	Impact of model responsiveness on frequency-decoding under stochastic conditions	85
4.14	Effect of cooperativity strength on frequency-decoding under stochastic conditions	90
4.14.1	Increases in the cooperativity strength lead to increases in the frequency-decoding distinctness under stochastic conditions	90
4.14.2	Increases in cooperativity coefficients foster the robustness against noise	91
4.15	Chapter discussion	94
4.15.1	Summary and conclusions	94
4.15.2	Pitfalls for the application of channel capacity	98
4.15.3	Simplifications in the applied communication channel	98
4.15.4	Simplifications in the NFAT model	99
4.15.5	On the efficiency of the applied optimization workflow	100
5	Analyzing the encoding of attractant levels in the chemotaxis of <i>E. coli</i>	101
5.1	Chapter introduction	101

5.1.1	About this chapter	101
5.1.2	Outside assistance	102
5.2	The employed model for <i>Escherichia coli</i> chemotaxis	103
5.3	Defining the chemotaxis model's dynamic range	106
5.4	Inferring attractant levels from receptor methylation levels	110
5.4.1	Inferring attractant levels in continuous environments	110
5.4.2	Inferring attractant levels in changing environments	111
5.5	Analyzing the methylation-based memory by means of mutual information . .	114
5.6	Consequences of reducing the maximal number of receptor methylations . .	119
5.6.1	Loss in the dimensions of the dynamic range	119
5.6.2	Loss in the dimensions of the encoding range	122
5.6.3	Shifts in the optimal attractant baseline level for memory formation . .	123
5.7	Chapter discussion	126
5.7.1	Summary and conclusions	126
IV	Main discussion	131
6	Main discussion	133
6.1	Contributions to the analysis of information transfer in signal transduction . .	133
6.2	Outlook	136
	List of Abbreviations	139
	List of Figures	141
	List of Tables	145
V	Appendix	147
A	Additional material to Chapter 4: Analyzing the frequency-decoding of calcium oscillations	149
A.1	The high-pass and band-pass activation models	149
A.1.1	List of optimized parameter sets	149
A.1.2	Additional analysis results of parameter couples	159
A.1.3	Dependence of the optimal parameterization of binding constants on the calcium oscillation amplitude - additional parameter distributions .	165
A.1.4	Applied parameterizations of the stochastic high-pass model	166
A.2	The NFAT model	168
A.2.1	Parameterization of square-wave inputs in the NFAT model	168
A.2.2	Optimized parameter sets of the NFAT model	168
B	Additional material to Chapter 5: Analyzing the encoding of attractant levels in the chemotaxis of <i>E. coli</i>	173
B.1	Additional estimates of mutual information showing memory formation in the original model	173
B.2	Additional estimates of mutual information showing memory loss in the original model	179

B.3 Time scales for memory formation and memory loss in model versions differing in the maximal number of receptor methylations	184
Bibliography	187

Part I

Main introduction

Main introduction

1.1 Biological communication

1.1.1 Signal transduction

Similar to technological communication channels, biological signal transduction pathways receive information from input signals and transmit this information to an output element. At the end piece of a signal transduction pathway, an appropriate cellular response is initiated. This could, for instance, refer to the expression of a particular set of genes. Since signaling pathways developed under evolutionary pressure to be highly reliable, information transmission in cells is often characterized by a striking robustness against biochemical fluctuations [1, 2, 3]. The importance of reliable information transmission becomes evident in cells that exhibit spurious signal transduction due to mutations. Such mutations are often linked to severe malfunctions and diseases like cancer [4, 5].

With respect to a ligand-mediated stimulation, signal transduction is initiated upon the binding of first messenger molecules to receptor proteins. In multicellular organisms, first messengers often originate from other cells of the same organism. To this end, the transportation of first messenger molecules between cells is facilitated by connecting architecture. Plant cells, for instance, exhibit plasmodesmata, i.e., channel-like structures that link the cytosols of neighboring cells and serve as passageways for small molecules [6], while, in animal cells, gap junctions and tunneling nanotubes fulfill a similar purpose [7, 8]. In endocrine signaling, first messengers travel over long distances to reach their target cells. Here, first messengers are transmitted via the vascular system of an organism, i.e., the xylem and phloem in plants or the blood and lymph in animals [9, 10]. Furthermore, external ligands may also act as first messengers. For example, microorganisms that perform quorum sensing react to autoinducer molecules that are secreted by other microorganisms [11].

Upon ligand binding, receptor molecules undergo conformational changes allowing them to interact with downstream molecules [12]. Subsequently, a first messenger's information is often not just relayed to one type of transmitter molecule, but passed on to several discriminable types of transmitter molecules in a sequential fashion. In such signaling cascades, the involvement of mobile transmitter molecules enables the signal to spread within the cell, whereas signal propagation is not left to chances. Forgacs *et al.* found that known transmitter molecules and proteins that act as building blocks of the cytoskeleton share a particularly strong connection. Thus, it was concluded that the cytoskeleton serves as tracks supporting mobile transmitter molecules in reaching their destination in a reliable manner [13]. Also localization sequences, i.e., amino acid motifs recognized by import facilitators to particular cell compartments, grant spatial specificity in signal transduction [14].

The relaying of information in signal transduction may also benefit signal amplification. In case the binding of a first messenger to a receptor leads to a change in the receptor's conformation enabling it to interact with downstream molecules, dependent on the persistence of the conformational change and the availability of downstream interaction partners, a single receptor may activate a much larger number of downstream transmitter molecules (see for instance signal amplification via cGMP after photoreceptor excitation [15]). In theory, every activated transmitter molecule can account for additional signal amplification by interacting with a larger number of transmitter molecules next in line in the cascade [16]. In reality, however, such a signal amplification mechanism is likely confined by the energetic costs for the production of large amounts of transmitter molecules.

1.1.2 Signal encoding and decoding

In this study, I investigated signal transduction in two prominent example cases: calcium signaling in non-excitabile cells and *Escherichia coli* chemotaxis. In particular, I analyzed the frequency-decoding of calcium oscillations by dependent proteins and the encoding of attractant levels into methylation levels of chemoreceptors. For a detailed introduction to calcium signaling, please refer to Section 1.2. For a detailed introduction to *Escherichia coli* chemotaxis, please refer to Section 1.3. In the following, I provide a definition of encoding and decoding in signal transduction.

Claude E. Shannon defined a universal model of communication that can also be applied to describe biological signal transduction [17]. In the model, an input signal is encoded and transmitted through a communication channel to a receiver. In turn, the receiver infers the input signal by decoding the encoded message. In general terms, encoding relates to the conversion of a message into a different form of code. Encoding might be necessary to compress a signal, to allow for its transmission through a particular channel, to make it readable for a receiving element or to make it unreadable for other elements. In contrast, decoding relates to the process of interpreting an encoded message.

With respect to signal transduction pathways, often the "identity and quantity of a stimulus" is encoded [18]. For example, the identities of epidermal growth factor (EGF) and nerve growth factor (NGF) are encoded into the dynamics of extracellular signal-regulated kinases (ERK), with EGF being associated with a transient activation and NGF being associated with a sustained activation of ERK [19, 20, 21]. Similarly, tumor suppressor p53 exhibits different patterns upon activation by γ -radiation and activation by UV-radiation; while γ -radiation leads to transient pulses of p53, UV-radiation leads to a single, sustained pulse of p53. Moreover, dynamics of p53 are also modulated by the radiation dose [22, 23] (examples taken from a review by Purvis *et al.* [18]).

In both cases, information from different input signals is encoded into the dynamics of a single transmitter. By choosing a single, versatile transmitter over multiple, less versatile transmitters, biological systems can save energy that would be required for the production of additional types of molecules. Further, the sharing of transmitter molecules may also allow for crosstalk, as frequently observed in signal transduction. For instance, in a proteomics study, Geva-Zatorsky *et al.* found that the combined administration of specific drugs was associated

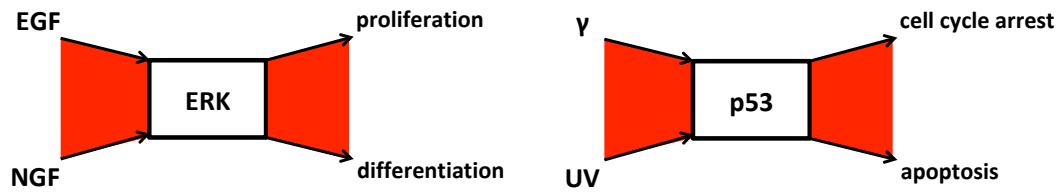


Fig. 1.1. Schematic: Encoding and decoding of biological signals. In some signal transduction networks, information from different input signals is encoded into properties of a single transmitter, whereas the encoded message is decoded by downstream pathway elements to induce input-specific cellular responses. In the presented examples, different dynamics of ERK arise after cell stimulation with different hormones. For p53, different dynamics arise upon cell stimulation with different types of radiation. To this end, input-specific transmitter dynamics distinctly modulate the activities of downstream pathway elements giving rise to particular cellular responses.

with distinct dynamical patterns of protein activation compared to single drug administrations in human cells [24]. While crosstalk between signaling pathways is sometimes labeled as noise impairing unambiguous information transmission, in recent studies, its upside was attested in directing complex cellular responses involving multiple pathways [25, 26].

The encoding of input signals makes only sense in the light of downstream pathway elements being able to interpret, i.e., decode, the encoded message. In response to EGF, ERK is transiently activated. This leads to the initiation of proliferation in neuronal precursor cells. In contrast, sustained ERK activation in response to NGF stimulation leads to the initiation of differentiation [27]. Similarly, γ -radiation leads to p53 pulses that result in cell cycle arrest, while UV-radiation leads to sustained p53 activity that results in apoptosis [28]. In conclusion, decoding elements downstream of the shared transmitter molecules must be able to discriminate between different transmitter dynamics. In particular, the activities of decoding elements must be differently modulated in response to distinct patterns of a transmitter in order to give rise to distinct cellular responses [18, 29, 30, 31]. The described signaling pathways can be simplified as bow-tie structures. Bow-tie structures are recurring motifs in biological pathways (Figure 1.1) [32].

1.2 Calcium signaling

1.2.1 Calcium as a second messenger

Calcium is a ubiquitous second messenger controlling a plethora of diverse, sometimes even opposing, cellular functions such as the fertilization of mammalian eggs, the regulation of muscle contractions, cell differentiation, proliferation, but also apoptosis. More information on calcium-controlled cellular functions can be found in [33] and [34].

In calcium signaling, calcium levels, either within an entire cellular compartment (e.g., the ER, the cytosol or mitochondria) or in microdomains within compartments, are modulated in response to an upstream stimulation. For instance, calcium signaling can be initiated upon the binding of external ligands to G protein-coupled receptors (GPCRs) or tyrosine-kinase-coupled receptors (RTKs). The binding of ligands to both types of receptors leads to the activation of phospholipase C (PLC), albeit different isoforms; PLC- β with respect to GPCRs and PLC- γ with respect to RTKs [35]. Subsequently, active PLC catalyzes the hydrolysis of the membrane lipid phosphatidylinositol 4,5-bisphosphate (PIP₂) to membrane-bound diacylglycerol (DAG) and diffusible inositol 1,4,5-trisphosphate (IP₃).

Both hydrolysis products impact calcium signaling. DAG activates protein kinase C (PKC) isoforms that are assumed to provide a negative feedback to calcium signaling by means of receptor phosphorylations. Corresponding findings were reported for GPCR-type cholecystokinin 1 receptors (CCK1Rs) [36]. More prominently, IP₃ binds to IP₃-receptor calcium channels (IP₃R) at the ER. In consequence, IP₃R's sensitivity to cytosolic calcium is altered. In the absence of IP₃, IP₃R is inhibited by low levels of cytosolic calcium. For elevated levels of IP₃, much higher levels of cytosolic calcium are required to cause an inhibition, while lower levels actually activate the calcium channels [35, 37]. Once activated, calcium passes into the cytosol powered by a steep concentration gradient. In addition, phosphorylations of IP₃R, partly due to the action of calcium-dependent proteins like conventional PKC isoforms or Ca²⁺/calmodulin-dependent protein kinase II (CaMKII), regulate the channeling activity of IP₃R [38].

A different type of channel, the ryanodine receptor (RyR), also mediates the release of calcium out of the ER. Similar to IP₃R, its channeling activity is sensitive to the abundance of cytosolic calcium, with low levels of cytosolic calcium causing enhanced channel activity and high levels of cytosolic calcium having an inhibitory effect on the calcium channel. As for IP₃R, calcium interacts with RyR either directly or by means of calcium-dependent proteins [35, 39].

The described signaling cascade exemplifies how cytosolic calcium levels rise in response to an upstream stimulation of a cell. However, in response to some agonists in non-excitable cells, cytosolic calcium signals oscillate and are generally transient. Thus, calcium is actively removed to prevent its accumulation in the cytosol. To this end, it is exported back into storage compartments, for example by means of sarco/endoplasmic reticulum Ca²⁺-ATPases (SERCA) into the ER or mitochondrial uniporters into mitochondria, or even outside of the cell, for example by means of plasma membrane Ca²⁺ ATPases (PMCA) or sodium-calcium exchangers (NCX) [35].

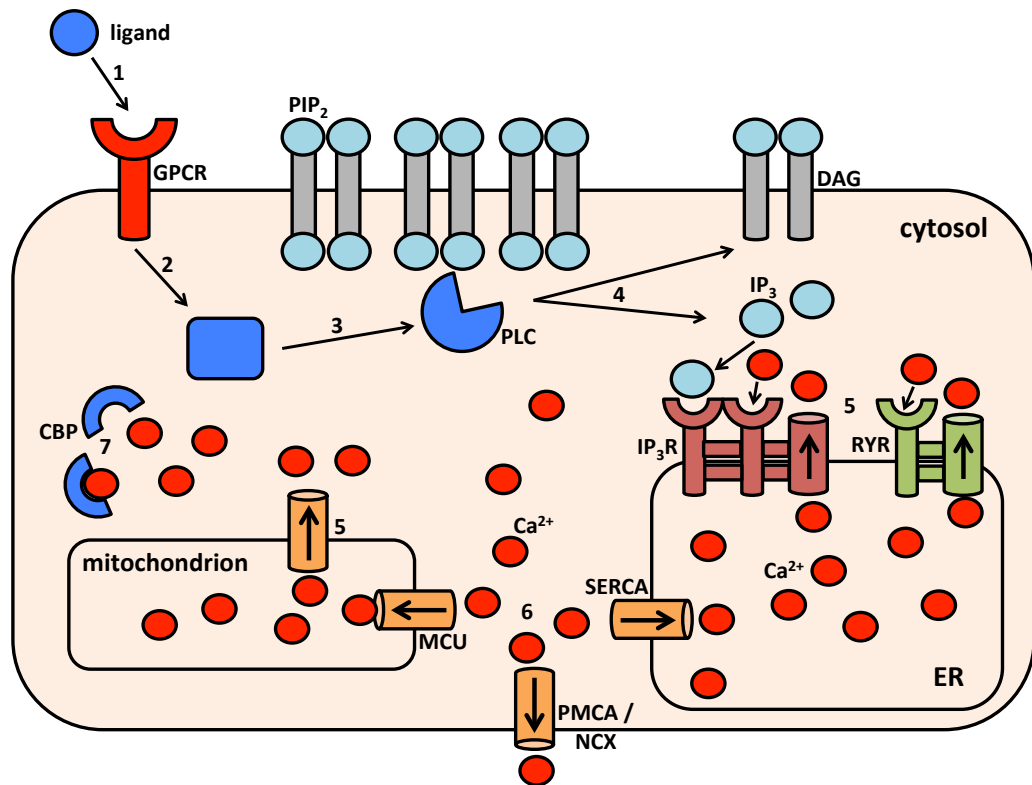


Fig. 1.2. Schematic: Emergence of a calcium signal after a GPCR stimulation. (1) External agonist binds to a GPCR-type receptor. (2) Conformational changes in the receptor lead to the activation of downstream proteins (G proteins). (3) Activated PLC catalyzes the hydrolysis of the membrane lipid PIP₂. (4) Hydrolysis of PIP₂ results in DAG and IP₃. (5) ER-resident calcium ions enter the cytosol through IP₃R and RYR channels driven by IP₃ and low levels of cytosolic Ca²⁺ or through mitochondrial channels. (6) Ca²⁺ is transported from the cytosol into the ER, into mitochondria or is removed from the cell. (7) Other Ca²⁺ ions are bound by calcium-binding proteins (CBPs) that either act as buffers or mediate cellular responses. Due to the restoration of low levels of freely available cytosolic Ca²⁺, ER channels can be activated once again.

The removal of calcium along with its fine-tuned release from storage compartments and the action of buffer proteins tightly regulate its availability in the cytosol. The importance of these measures becomes apparent upon a disruption of the calcium regulation. Sustained, high levels of calcium are linked to a wide array of ailments including heart disease [40], neuronal diseases like Alzheimer's disease [41] and cancer [42].

1.2.2 On the encoding of first messenger signals into calcium oscillations

Calcium's versatility in transmitting signals from various first messengers is accounted for by the multitude of spatial and dynamic variations its own signal can exhibit after a stimulation [43]. Thus, particular signals from first messengers are encoded into particular types of calcium signals. In turn, calcium signals are decoded by specific downstream proteins in order to initiate appropriate cellular responses.

An especially high degree of diversity is recognizable in calcium signals that manifest as oscillations over time. Dependent on the first messenger signal, oscillation dynamics vary significantly. Oscillation frequency, duration, amplitude as well as the general oscillation shape (for instance spiking oscillations exhibiting only one major peak in an oscillation cycle versus bursting oscillations exhibiting a major primary peak succeeded by a variable number of minor secondary peaks) can all be modulated by an upstream stimulation.

In several instances, it was reported that the quantity of a first messenger is encoded into the calcium oscillation frequency, with increases in the quantity resulting in higher oscillation frequencies [44]. This was found in salivary glands of the blowfly *Calliphora erythrocephala* upon stimulation with the hormone serotonin [45] and in isolated rat hepatocytes upon stimulation with the hormone vasopressin [46].

In contrast, in fish, in particular in hepatocytes of the rainbow trout *Oncorhynchus mykiss* and in the fish cell line RTL-W1, the quantity of several first messenger molecules was found to be encoded into the calcium oscillation amplitude, with larger first messenger levels leading to larger amplitudes. These findings were reported after stimulation with phenylephrine, several toxicants and the nucleotide ATP [47]. It is believed that, in poikilothermal animals like fish, amplitude-encoding is preferred over frequency-encoding, since it is more robust to variations in the temperature [48]. Further, modulations of the calcium oscillation amplitude were also observed in B lymphocytes, whereas naïve cells generate calcium oscillations with larger amplitudes compared to self-tolerant cells upon stimulation with the same amount of identical antigen [44]. A coincidence of amplitude- and frequency-encoding was shown in guard cells of wild-type *Arabidopsis thaliana*. To this end, the external administration of calcium induced cytosolic calcium oscillations that varied in amplitude and frequency dependent on the administration dosage [49].

Additionally, different calcium oscillation shapes were observed upon stimulating rat hepatocytes with different types of agonists. The hormone vasopressin resulted in spiking oscillations [46], while ATP led to bursting oscillations [50].

It seems reasonable to assume that a modulation of the calcium oscillation frequency or amplitude by the quantity of a first messenger is connected to the occupation of a larger number of receptors for a longer duration of time. As a result, more calcium channels and pumps could be activated leading to faster and/or larger oscillations in the cytosol. For entirely different oscillation shapes relating to different types of first messenger molecules, as observed in rat hepatocytes stimulated by either vasopressin or ATP, the recruitment of different receptor types might be crucial. Receptors could directly determine specific oscillation shapes due to their own kinetic properties or indirectly by interacting with different isoforms of pathway proteins. For instance, various isoforms of G proteins or PLCs can play a role in calcium signaling. For a summary of relevant molecular players involved in calcium signaling, please refer to the "calcium-signaling toolkit" as described by Michael J. Berridge in [35].

The encoding of information from first messenger signals into parameters of calcium oscillations was also investigated *in silico*. To this end, calcium oscillator models were proposed that can roughly be classified into two categories. Calcium oscillator models in which oscillations arise due to oscillations of IP_3 (see [51, 52, 53, 54]), and oscillator models in which oscillations

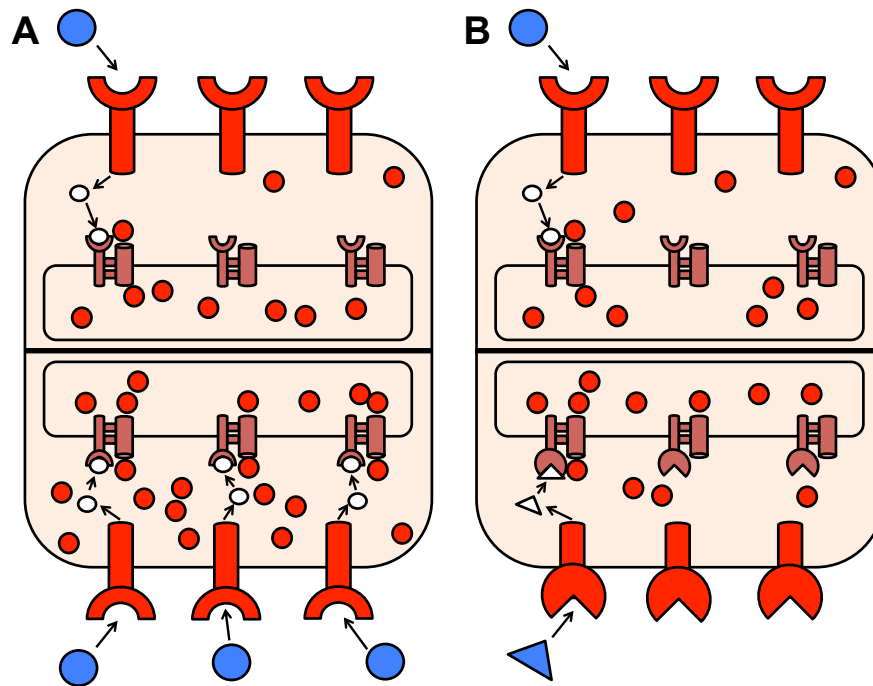


Fig. 1.3. Schematic: Encoding of first messenger characteristics into calcium oscillation parameters. (A) The abundance of first messengers is often encoded into the amplitude and/or frequency of calcium oscillations. For larger first messenger quantities resulting in a larger number of bound receptors, more of a downstream signaling protein could be activated leading to a stronger and more spread out activation of calcium channels. As a result, more calcium is released from the ER. In case calcium removal out of the cytosol and release from storage compartments into the cytosol are able to follow through on small time scales, the oscillation frequency might rise. (B) Different stimulus types can lead to different oscillation shapes, like spiking and bursting oscillations. This could be achieved by the recruitment of different receptor species leading to distinguishable oscillation shapes by means of their receptor-specific kinetic properties. Also, different receptors could interact with different isoforms of signaling proteins or, more generally, entirely different signaling proteins. Blue shapes: first messengers; white shapes: pathway proteins activated by stimulated receptors (in red); red spheres: calcium.

are independent of IP_3 oscillations and instead based on calcium-induced calcium release (see [55, 56]). In many calcium oscillator models, frequency-encoding could be reproduced by changes in model parameters (for instance [55, 56, 53, 54, 57, 58]). In the calcium model by Kummer *et al.*, changes in a model parameter could also account for the experimentally observed diversity in calcium oscillation shapes in response to different agonists (for instance spiking versus bursting oscillations) [53]. For reviews on calcium oscillator models, please refer to [59, 60, 61].

1.2.3 On the decoding of calcium oscillations

As characteristics of first messengers are encoded into parameters of calcium oscillations, downstream pathway elements decode the calcium signal in order to mediate appropriate cellular responses. Since a multitude of proteins are regulated by calcium controlling a wide array of diverse cellular functions, calcium signals have to target dependent proteins in a highly selective and reliable manner.

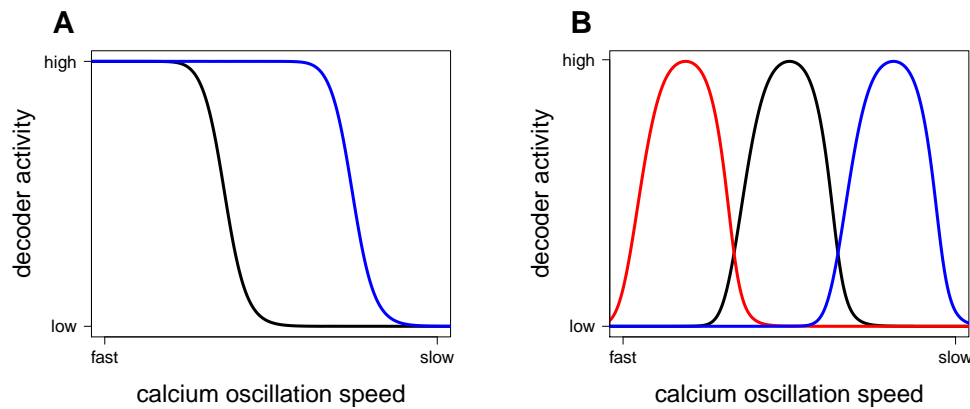


Fig. 1.4. Selective activation of frequency-decoding proteins exhibiting high-pass or band-pass activation. (A) The activities of two proteins are modulated by the calcium oscillation frequency, whereas both proteins exhibit high-pass activation. For fast oscillations, both proteins are active, for slow oscillations, only the blue protein is active. A similar phenomenon was observed for NFAT and NF- κ B in [63]. (B) Further experiments in which a broader range of calcium oscillation frequencies was applied resulted in the conclusion that NFAT exhibits maximal transcriptional activity for a particular optimal frequency [62, 64]. It is imaginable that more proteins exhibit a corresponding decoding mechanism allowing for a highly selective, isolatory activation dependent on the calcium oscillation frequency. Note that, opposed to in (A), every single protein can be selectively activated.

Most prominently, the calcium oscillation frequency was identified as a parameter decoded by multiple dependent proteins [62]. With respect to frequency-decoding, changes in the calcium oscillation frequency go hand in hand with changes in a dependent protein's activity. A pronounced sensitivity to modulations of the calcium oscillation frequency was for instance attested for the pro-inflammatory transcription factors NFAT, NF- κ B and Oct/OAP in Jurkat T cells. All transcription factors indicated high gene expression activities for fast calcium oscillations and low activities for slower oscillations. However, while the activities of NFAT and Oct/OAP declined entirely in response to particularly slow calcium oscillations (oscillation period larger than 500 s), NF- κ B still exhibited a clearly measurable transcriptional activity. In conclusion, it is believed that different genetic programs are run in case only NF- κ B is active in response to slow calcium oscillations or in case all three transcription factors are active in response to fast calcium oscillations [63]. In the following, I call frequency-decoding that is characterized by a high protein activity for fast calcium oscillations and a low protein activity for slow oscillations high-pass activation. In Figure 1.4 A, I show how two co-existing high-pass activation proteins can be selectively activated dependent on the calcium oscillation frequency.

Further experiments in RBL-2H3 cells in which the range of the applied calcium oscillation frequencies was extended led to the conclusion that NFAT exhibits a maximal activity for a particular oscillation frequency. Frequencies slower or faster than this optimal frequency only resulted in a decreased transcriptional activity [64]. I call this form of frequency-decoding band-pass activation. Opposed to high-pass activation, band-pass activation offers considerable advantages in the selective activation of single proteins in a mix of multiple frequency-decoding proteins (Figure 1.4 B).

Another prominent decoder of the calcium oscillation frequency is the serine/threonine-specific kinase CaMKII. For CaMKII, in an *in vitro* study as well as in a study in mouse neurons, it was revealed that increases in the frequency of calcium oscillation spikes resulted in an increase in the autonomous kinase activity [65, 66]. To gain autonomous activity, two neighboring sub-units of the about twelve, circular-arranged sub-units of the holoenzyme have to be bound to $\text{CaM}/\text{Ca}^{2+}$. Subsequent phosphorylations between bound sub-units grant autonomous activity that persists even after the dissociation of $\text{CaM}/\text{Ca}^{2+}$. Since particularly neighboring sub-units have to be bound to $\text{CaM}/\text{Ca}^{2+}$, infrequent spikes only have a small chance of boosting the autonomous kinase activity. This explains the experimentally observed reduced autonomous activity for slower calcium oscillations [67]. In addition, it was found that different splice variants of β -CaMKII show distinguishable frequency-decoding patterns. Differences were traced back to variations in the initial rate of autophosphorylation and the CaM activation constant that are presumably connected to differences in sub-unit positioning [68]. Later, in *in silico* studies, Dupont *et al.* also identified an optimal frequency for the maximization of autonomous CaMKII activity [69], while Li *et al.* concluded that the frequency of calcium spikes could act as a switch determining whether CaMKII or its adversary, the calcium-dependent phosphatase calcineurin, is dominant.

Other frequency-decoders of calcium oscillations, that were experimentally identified as such, include PKC- γ [70], μ -calpain [71] as well as Ras and the connected MAPK pathway [72]. In plants, also the stomatal movement of guard cells appears to be sensitive to modulations of the cytosolic calcium oscillation frequency [73]. For a review on proteins able to perform frequency-decoding of calcium oscillations, please refer to Smedler and Uhlén [62].

As pointed out in Section 1.2.2, first messenger signals cannot only modulate the calcium oscillation frequency, but also the amplitude, duration and general shape of calcium oscillations. In conclusion, it is likely that some calcium-dependent proteins can also decode other parameters of calcium oscillations. For instance, in an experimental study in B lymphocytes, it was found that the differential calcium-dependent activation of the transcription factors NFAT, NF- κ B and JNK is not only accomplished by modulations of the calcium oscillation frequency [63], but also by modulations of the calcium oscillation amplitude and duration [74].

While some computational studies focused on the decoding of calcium oscillations by particular proteins (for example [69, 75]), in others, analyses were centered around generic protein models. In many generic models of calcium-dependent protein activation, researchers described the decoding of information encoded in the frequency of calcium oscillation spikes [56, 76, 77]. In contrast, Larsen and Kummer as well as Larsen *et al.* and Rozi and Jia also investigated the decoding of bursting oscillations [78, 79, 80]. To this end, Larsen and Kummer and Larsen *et al.* reported that a generic protein model was able to discriminate between calcium oscillation shapes, like spiking or bursting oscillations, based on its average activity [79]. In addition, Schuster *et al.* and Knoke *et al.* found that bursting oscillations can also regulate different proteins simultaneously [81, 82]. Further, Marhl *et al.* added yet another layer of complexity to the analysis of frequency-decoding. In a generic protein model, they showed that time-limited spiking oscillations can induce clear frequency-decoding, even band-pass activation, opposed to much longer oscillations [83]. Since short calcium oscillations are a common sight in cells [84, 85], Marhl *et al.* reasoned that short oscillations could be prevalent not only due to energetic constraints but also due to advantages in information transmission.

Lastly, Salazar *et al.* employed a generic protein model to identify requirements for frequency-decoding as well as demonstrated the advantages of calcium oscillations compared to constant calcium signals in the activation of target proteins [86, 87].

1.3 *Escherichia coli* chemotaxis

1.3.1 The chemotaxis signaling pathway

In *Escherichia coli* chemotaxis, cell locomotion is directed by the perception of gradients in the abundance of a chemical, whereas chemicals may act as attractants or repellents. Chemotaxis was already described in the late 1800s in pioneering studies by Engelmann and Pfeffer [88, 89, 90].

While larger eukaryotic cells use temporal and spatial gradients for chemotaxis, it is believed that, in most cases, smaller prokaryotic cells cannot extract meaningful information from the concentration difference of a chemical between opposing cell ends [91]. An exception to this rule was reported for marine bacteria that can utilize spatial information from unusually steep oxygen gradients [92]. More commonly, bacterial chemotaxis was found to be based on temporal gradients, as chemotactic behavior was detected after the administration of rapid changes in the abundance level of attractants or repellents in well-mixed media [93, 94].

To this end, chemotactic behavior is often detected by measuring a change in the cell's tumbling frequency. While unguided bacterial locomotion resembles a random walk in which straight runs are frequently interrupted by tumbles, chemotactic cues bias cell locomotion. For positive attractant gradients or negative repellent gradients, the tumbling frequency decreases and, in consequence, the duration of runs increases. In contrast, for positive repellent gradients or negative attractant gradients, the tumbling frequency increases and the duration of runs decreases [91].

A signaling pathway is responsible for the perception of changes in attractant or repellent levels and the transmission of this information to downstream effector elements directing cell locomotion. At the beginning of this pathway, methyl-accepting chemotaxis proteins (MCPs) act as chemoreceptors for attractants or repellents. As the name suggests, several glutamate residues of an MCP protein can be methylated by the constitutively active methyl-transferase CheR [95]. Ambient attractant or repellent levels along with the number of receptor methylations modulate the receptor activity with respect to the phosphorylation of the histidine kinase CheA [96]. In response to a decline in ambient attractant levels, the receptor activity temporarily increases. As a result, CheAp levels rise. To this end, CheAp mediates the phosphorylation of the protein CheY forming CheYp. The diffusible CheY protein was identified as a key player in chemotaxis signaling. In particular, CheYp is able to bind to flagellar motors increasing the chances for a clockwise rotation of bound flagella which in turn increases the cell's tumbling frequency [97, 98, 99, 100, 101, 102]. Further, CheAp also mediates the phosphorylation of the methylesterase CheB providing a negative feedback to its own activation. To this end, the phosphorylation of CheB is slower than the phosphorylation of CheY. In consequence, while, in response to a decline in ambient attractant levels, receptor activity increases, initially, it eventually returns to a default due to the action of the methylesterase CheBp [103, 104]. Thus, CheAp and CheYp levels as well as the cell's tumbling frequency return to pre-stimulation default values, too. Conversely, if ambient attractant levels rise, the receptor activity declines, initially. In consequence, CheAp and CheYp levels decrease along with the cell's tumbling frequency. Only with time, the receptor activity is

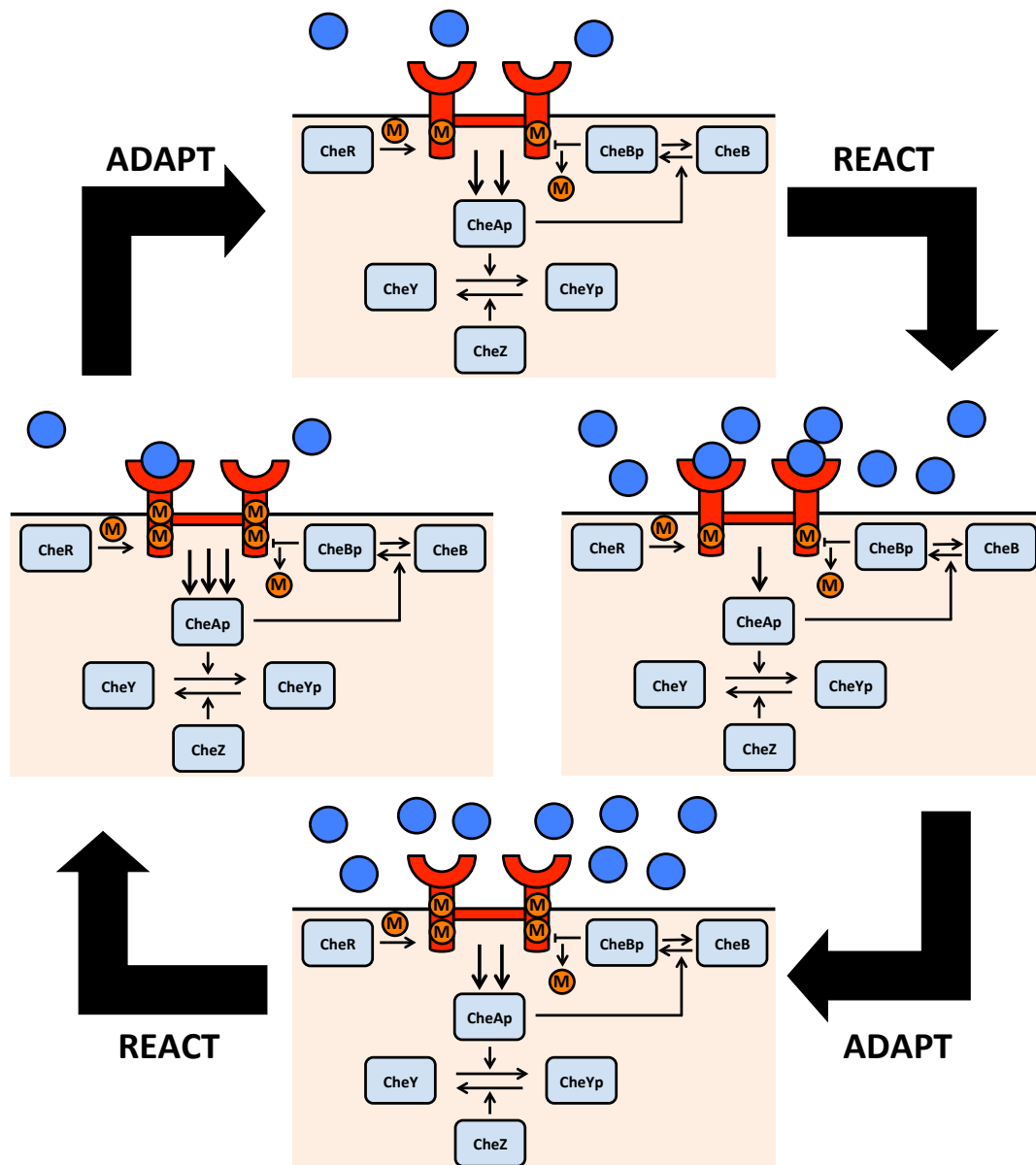


Fig. 1.5. Schematic: The chemotaxis pathway of *Escherichia coli*. Top to right: A rise in ambient attractant levels results in a decrease in receptor activity, thus, a decreased activation of CheA. Bottom to left: A decline in ambient attractant levels results in an increase in receptor activity, thus, an increased activation of CheA. Active, i.e., phosphorylated, CheAp is able to phosphorylate the motor regulator CheY. CheYp modulates the rotation direction of flagellar motors increasing the tumbling frequency. CheAp also initiates a negative feedback by activating the methylesterase CheB. CheBp demethylates receptors, whereas receptors with a lesser number of methylations exhibit a decreased activity. A constitutively active methyltransferase CheR counters CheBp-mediated demethylations. Within the dynamic range of the system, after a change in attractant or repellent levels, CheAp and CheYp levels, thus, also the cell's tumbling frequency, return to pre-stimulation standard values (right to bottom and left to top). This effect is controlled by the activities of CheR and CheBp as well as receptor desensitization. In order to infer gradients of a chemical, information about ambient attractant or repellent levels is stored in receptor methylation levels. In consequence, in response to changes in ambient attractant or repellent levels, receptor methylation levels change as well. As long as receptor methylation levels are adjusting to a new abundance level, a downstream pathway response is taking place. Soon after receptor methylation levels have adjusted, effector proteins, such as CheAp and CheYp, complete adaptation.

restored due to the action of the constitutively active methyltransferase CheR and a decrease in active methylesterase CheBp. Once again, CheAp and CheYp levels as well as the cell's tumbling frequency return to default values. The described sensory adaptation mechanism is crucial for the cell to maintain a sensitivity to new changes in attractant or repellent levels. In case adaptation fails, chemotactic behavior is severely impaired and cells exhibit excessive tumbling or running (Figure 1.5) [105, 106, 107].

Escherichia coli chemotaxis is not only characterized by precise sensory adaptation, but also by a striking sensitivity to changes in attractant or repellent levels. In detail, changes as small as 3.2 nM of the attractant L-aspartate were reported to elicit a measurable chemotactic response [108]. In order to transmit such minor changes in attractant levels, the incoming signal is amplified by means of cooperative interactions among receptors and cooperative binding of CheYp to flagellar motors [97, 109, 110]. Additionally, due to the methylation-based receptor desensitization and sensory adaptation, chemotaxis can exhibit a dynamic range of up to five orders of magnitude for certain amino acid attractants [111, 112]. Receptor desensitization is also linked to a decreased sensitivity for large attractant levels allowing for the detection of relative gradients rather than absolute gradients [112].

Moreover, due to its pathway structure, *Escherichia coli* chemotaxis is particularly robust against concerted variations in chemotaxis proteins. To this end, the negative feedback via CheBp and the action of the phosphatase CheZ that dephosphorylates CheYp were shown to be crucial. In contrast, chemotaxis is much more sensitive to uncorrelated variations in chemotaxis proteins with regards to protein steady-state behavior and adaptation time. The precision in adaptation, however, was found to be protected also against uncorrelated variations in chemotaxis proteins [3, 113]. In order to maintain the ratio of chemotaxis proteins, corresponding genes are comprised in the *mocha* and *meche* operons, both parts of a single regulon [114].

Already in the early 1970s, first mathematical models were published describing the migration of chemotactic cells in response to changes in attractant or repellent levels [115]. In particular, the models by Keller and Segel paved the way for future studies in this direction [116, 117]. In my analysis, I focused on the transmission of information through the molecular chemotaxis pathway in a single cell excluding a detailed description on cell movement and population dynamics. In this regard, in the 1980s, first models of the adaptation process in bacterial chemotaxis considered interactions between pathway proteins, i.e., methylations and demethylations of receptor proteins by enzyme entities [118, 119, 120, 121]. In the following decade, chemotaxis models were published that comprised receptor dynamics as well as parts of the phosphorylation cascade [1, 122, 123, 124, 125, 126, 127].

In this thesis, I employed a chemotaxis pathway model by Kollmann *et al.* that includes a two-state model of receptor dynamics and a description of the phosphorylation cascade culminating in the phosphorylation of CheY [3]. In detail, receptor proteins can be existent in an inactive and an active conformation in the model, whereas the chances of a receptor to be active depend on the number of methylations it exhibits and the ambient attractant level. The kinetics of the model by Kollmann *et al.* are based on another model by Rao *et al.* [128]. Further pathway models with a similar or even broader scope include Vladimirow *et al.* and Clausznitzer *et al.* [129, 130]. In more detail, the *RapidCell* model by Vladimirow

et al. comprises a Monod-Wyman-Changeux (MWC) model of receptor coupling, a model of the phosphorylation cascade as well as a model of cell tumbling, while Clausznitz *et al.* linked a MWC model to a cascade model, too, claiming that their model grants a more realistic representation of adaptation dynamics. For a review on single-cell chemotaxis models, please refer to [131].

1.3.2 Memory in *Escherichia coli* chemotaxis

In chemotaxis, memory can relate to different system properties. For one, after a cell experiences a significant change in ligand levels, CheA levels temporarily increase or decrease before returning to standard values. The time span between system stimulation and the end of CheA recovery is sometimes referred to as the memory length [104]. It is in this time span that a cell initiates directed changes in its locomotion. In experimental studies, it was found that the memory length is variable, with stronger stimuli leading to longer memory lengths. Further, the memory length is additive. When a cell experiences a large increase from an attractant baseline level to a step level, the corresponding memory length is equal to the sum of the memory lengths associated with incremental increases over the same range of attractant levels [132, 133].

It is believed that the memory length was optimized in the course of evolution. If the memory length was too long, cells were unable to react to a new stimulation in time overshooting the target. If the memory length was too short, a cell's chemotactic response accuracy was severely affected [93, 104]. In extreme cases, a bacterium exhibiting a very short memory length would have been non-chemotactic, since it would have been too slow to translate temporal gradients of attractant levels into directed changes in its locomotion. In conclusion, interspecies variations in the chemotaxis memory length are assumed to originate from different living environments [104].

Secondly, memory can relate to receptor methylation levels storing information about ambient attractant or repellent levels. Within seconds to minutes, increases in ambient attractant levels result in a larger number of receptor methylations and vice versa. If there is no change in ambient attractant or repellent levels, also receptor methylation levels do not vary significantly [134]. In particular, in response to an increase in ambient attractant levels, *Escherichia coli* responds by decreasing the tumbling frequency and increasing the duration of runs. If there are no further changes in attractant levels, the cell exhibits sensory adaptation, thus, CheAp and CheYp levels as well as the tumbling frequency return to standard values. Like the effector proteins CheA and CheY, also receptor methylation levels respond to the rise in attractant levels, but unlike them receptor methylation levels do not return to pre-stimulation standard values. If cells, adapted to the same attractant level, are separated with different cell aliquots being stimulated by differently large increases in attractant levels, the magnitude of the chemotactic response is dependent on the step size in ambient attractant levels [93, 132, 133]. Upon blocking methylations and demethylations of receptor proteins, this effect is disrupted [134] and abnormal chemotaxis is taking place [135, 136]. Thus, information about previous and new attractant levels is encoded in receptor methylation levels and used to infer gradients modulating the chemotactic response.

Similarities between the sensory reception in bacterial cells and neurons were briefly discussed in [104, 137]. In particular, while, in bacterial cells, levels of specific chemoreceptor ligands are encoded into receptor methylation levels, in neurons, levels of neuronal stimulants are encoded into the level of adenylyl cyclase enzyme [138].

1.4 Information theory in the biosciences

1.4.1 On the advancement of information theory in the biosciences

The person most commonly linked to information theory is Claude Elwood Shannon. As author of the seminal study "A Mathematical Theory of Communication" [17], he is widely considered as the field's founding father. In his work, Shannon defined measures to quantify the information content in messages and presented ways for efficient message encoding in noiseless as well as noisy communication channels. Today, information-theoretic principles are indispensable for efficient communication systems. But, due to the universality of Shannon's research, his ideas are also in use in other fields, such as linguistics [140, 141], psychology [142, 143] and of course molecular biology [144, 145], to characterize various forms of communication. Throughout this thesis, I applied measures from the field of information theory to quantify the flow of information in signaling pathways. To this end, I regarded signaling pathways as biological communication channels.

In Figure 1.6, I present the per-year numbers of biomedical and life science publications that contained relevant information-theoretic keywords. Evidently, information theory gained popularity over the course of the last decades in the biosciences.

1.4.2 On mutual information

Mutual information is described as a measure of dependence between variables [146]. With respect to an application of mutual information to molecular biology, variables could, for instance, refer to time series data of different proteins. While, in this study, I only estimated the mutual information between two variables, estimations between more than two variables are possible, as for example shown in [147]. For the two-variable case at hand, mutual

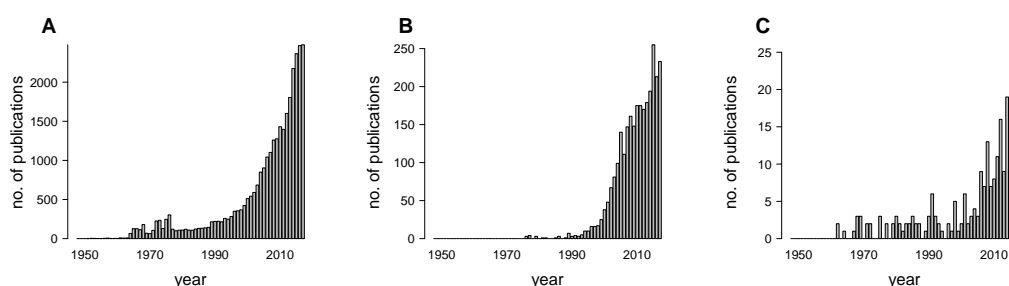


Fig. 1.6. Number of publications in the NCBI database PubMed that contain information-theoretic keywords. The NCBI (National Center for Biotechnology Information) database PubMed encompasses more than 28 million citations for biomedical and life science literature (as of October 2018) [139]. Here, I searched for citations containing particular keywords linked to the field of information theory: (A) "information theory", (B) "mutual information" and (C) "channel capacity". For all keywords, a clear rise in the number of publications per year was recognizable. I searched for "mutual information" and "channel capacity", since I applied both information-theoretic measures in this thesis.

information is defined as the reduction in uncertainty of one variable given knowledge of the other variable. This is equivalent to the gain in information about one variable by knowledge of the other [146]. The mutual information between the variables X and Y , $I(X;Y)$, is computed based on the variables' marginal and joint probabilities. In the discrete case, $I(X;Y)$ is formulated as:

$$I(X;Y) = \sum_{y \in Y} \sum_{x \in X} p(x,y) \cdot \log_2 \left(\frac{p(x,y)}{p(x) \cdot p(y)} \right) \quad (1.1)$$

With respect to related information-theoretic measures, mutual information can be described as the uncertainty in one variable, defined by its Shannon entropy $H(X)$, minus the remaining uncertainty in the same variable given the second variable defined by the conditional entropy $H(X|Y)$ [17]. Importantly, mutual information is symmetric, thus:

$$I(X;Y) = H(X) - H(X|Y) = H(Y) - H(Y|X), \quad (1.2)$$

with X 's Shannon entropy equal to

$$H(X) = - \sum_{x \in X} p(x) \cdot \log_2 (p(x)) \quad (1.3)$$

and X 's conditional entropy given Y equal to

$$H(X|Y) = - \sum_{y \in Y} \sum_{x \in X} p(x,y) \cdot \log_2 \left(\frac{p(x,y)}{p(y)} \right) \quad (1.4)$$

1.4.3 On channel capacity

Channel capacity C is defined as the "maximum amount of information that can possibly be transmitted through a [memoryless communication] channel" [148]. It is the supremum of the mutual information I between a channel input X and an output Y , whereas C is maximized by optimizing the input distribution $p(x)$ [17]:

$$C(X;Y) = \sup_{p(x)} I(X;Y) \quad (1.5)$$

Originally designed for technological communication channels, channel capacity can also be applied to assess maximal information transmission in biological signaling. In 2010, Nakano and Liu applied the measure to characterize molecular communication via second messengers in reference to calcium [149], in 2011, Cheong *et al.* analyzed information transmission in tumor necrosis factor signaling by means of channel capacity [147], in 2013, Hormoz quantified the channel capacity between transcription factor and gene expression levels [150] and, only recently in 2018, Keshelava *et al.* estimated the channel capacity in GPCR signaling [151].

In the following example case, I consider a signaling pathway in which two agonists induce distinct cellular responses by causing a differently strong activation of the transcription

factor TF. The agonist kind can be defined as the input of a communication channel and the abundance of active transcription factor $[TF^*]$ as the same channel's output (Figure 1.7). Since biological processes are affected by stochastic effects, not a single abundance level of active transcription factor is linked to a particular agonist but rather a distribution of transcription factor levels. Thus, upon repeating the stimulation with agonist an x_i , an x_i -specific output distribution $p(y|x_i)$ is received, where $y \in Y$. By means of the output distribution data $p(y|x_1)$ and $p(y|x_2)$, the channel capacity of the biological communication channel can be quantified by optimizing the input distribution $p(x)$ (see Section 2.6 for details).

Because only two kinds of inputs signals are considered in the example case, channel capacity is limited to 1 bit. This can be inferred from Equation 1.2 in which mutual information is defined as the Shannon entropy $H(X)$ minus the corresponding conditional entropy $H(X|Y)$. For two possible input signals, $H(X)$ is equal to its maximum of 1 bit given a uniform input distribution $p(x)$ ($x_1 = 0.5$; $x_2 = 0.5$), while $H(X|Y)$ equals to 0 bits if there is absolutely no uncertainty regarding the identity of an input signal x_i given an output y_j . In this case, the logarithm in Equation 1.4 is equal to 0 bits. However, in Figure 1.7, input-specific output distributions partially overlap. Therefore, channel capacity has to be smaller than 1 bit in this example. In conclusion, channel capacity informs on the discriminability of input signals. The

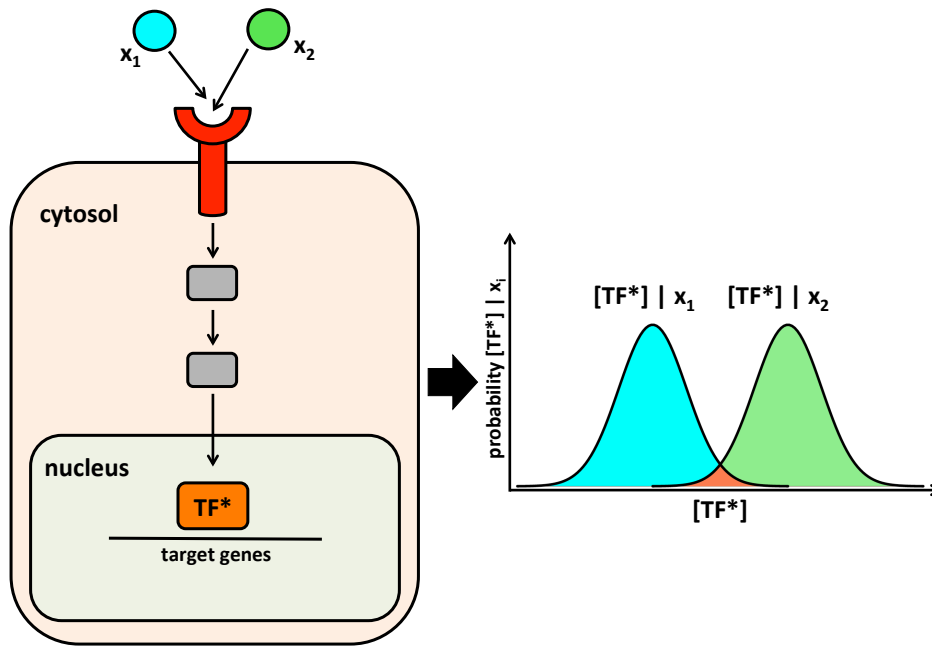


Fig. 1.7. Example case: discrimination of agonist types based on the abundance of active transcription factor. In this theoretical example case, two agonists, x_1 and x_2 , induce a differently strong activation of the transcription factor TF in order to trigger distinct cellular responses. Due to stochastic effects, the repeated administration of a particular agonist x_i is linked to multiple possible abundance levels of active transcription factor $[TF^*]$. Hence, an input-signal-specific output distribution $p([TF^*]|x_i)$ can be inferred. To this end, input-specific output distributions may partially overlap. For $[TF^*]$ levels within the overlap, the applied agonist type cannot be clearly determined. Input-signal-specific output distributions can also be used to estimate the channel capacity providing valuable information about the discriminability of input signals.

smaller the overlap between the input-specific output distributions is, the closer the channel capacity is to 1 bit.

While, in the presented example case considering only two input signals, a conclusion about the discriminability of input signals can be readily drawn from the input-specific output distribution data, the same becomes increasingly more difficult upon considering more input signals. It is here the measure of channel capacity truly starts to show its merits providing valuable information otherwise not recognizable. For a better understanding of channel capacity, please refer to Section 3.2. There, I present a theoretical analysis to exemplify the measure's informative value as well as to point out pitfalls for its application.

1.5 Outline of the thesis

In this thesis, I analyzed encoding and decoding in two prime examples of signal transduction: calcium signaling in non-excitable cells and *Escherichia coli* chemotaxis. For my analyses, I employed kinetic models and introduced methods allowing for a quantitative analysis of information transfer. To this end, methods were partly based on measures from the field of information theory.

The thesis structure is as follows.

2 Materials and methods.

With respect to deterministic simulations, I frequently ran optimizations to assess a model's potential to fulfill certain objectives given set conditions. Information about the employed deterministic simulation and optimization algorithms can be found in this chapter.

For my analyses of stochastic simulation data, I applied information-theoretic measures, in particular mutual information and channel capacity. Information about the applied estimators for both measures and about the stochastic simulation algorithm can be found in this chapter as well.

3 Method development and investigation.

In this chapter, I showcase the *OscillatorGenerator*, a self-designed package for the R language. The package enables the user to generate discrete time series of oscillations. In particular, the user can select distinct basic shapes, for example, sinusoids, square-waves, spiking oscillations or bursting oscillations, and customize the selected shapes by defining oscillation parameters, for example, the oscillation period, duty cycle, baseline or peak levels. In the context of this thesis, I used the *OscillatorGenerator* to mimic calcium oscillations applying the generated time series as inputs to kinetic models of calcium-dependent protein activation. The *OscillatorGenerator* package was published on the Comprehensive R Archive Network (CRAN) and is available at <https://cran.r-project.org/package=OscillatorGenerator>.

Secondly, I present a theoretical analysis of the information-theoretic measure of channel capacity using simple example cases. Since the application of channel capacity is fairly new to the analysis of biological signal transduction, I aimed at shedding light on the meaning of the measure and point out possible pitfalls.

4 Analyzing the frequency-decoding of calcium oscillations.

In my first case study, I analyzed the frequency-decoding of calcium oscillations by dependent proteins. Most proteins were found to perform high-pass activation, a behavior characterized by high protein activity for fast calcium oscillations and low protein activity for slow calcium oscillations. In contrast, the transcription factor nuclear factor of activated T cells (NFAT) was reported to perform band-pass activation exhibiting a maximal activity in response to an optimal calcium oscillation frequency with slower or faster frequencies only leading to a reduced protein activity [62, 64].

In this chapter, I present minimal kinetic protein models able to recreate high-pass and band-pass activation as well as a more specific model showing the calcium-dependent activation of NFAT. By means of an optimization-based workflow, I identified requirements for distinct frequency-decoding with regards to model parameterization and model network structure.

Further, I employed estimations of channel capacity to quantify a protein's ability to discriminate between calcium frequencies in the presence of stochastic fluctuations. Again, I identified model requirements for the clear discrimination of given frequencies.

Parts of this chapter were published in our publication "Requirements for band-pass activation of Ca^{2+} -sensitive proteins such as NFAT" [152].

5 Analyzing the encoding of attractant levels in the chemotaxis of *E. coli*.

In my second case study, I analyzed the encoding of ambient attractant levels into receptor methylation levels in *Escherichia coli* chemotaxis. To this end, I employed an established chemotaxis model by Kollmann *et al.* [3]. The process of receptor methylation governs the adaptation of downstream chemotaxis proteins controlling cell locomotion and is essential for the detection of temporal attractant or repellent gradients.

I performed a quantitative analysis of encoding by inferring expected attractant levels from present receptor methylation levels comparing the expected attractant level to the true attractant level. Further, I employed delayed mutual information estimations to monitor the formation and loss of the methylation-based memory.

In *Escherichia coli* chemotaxis, chemoreceptors can be methylated multiple times. In my analysis, I set a particular focus on analyzing the consequences of a reduction in the maximal number of receptor methylations on the system's encoding capabilities.

Part II

Materials and methods

Materials and methods

2.1 Used hardware

I ran computations on a Linux (CentOS 6.4 x86 64-bit Kernel 2.6.32) compute cluster with Sun Fire AMD Opteron and IBM Quad Intel Xeon CPUs as well as on a MacBook computer.

2.2 Deterministic simulations

In Chapter 4, I ran deterministic simulations in R [153] while applying the deSolve package (version 1.20) [154]. To this end, I sped up simulations by outsourcing expensive computations to C-code that was dynamically loaded into R. In order to solve ODE equations, I applied the LSODA algorithm [155]. A first template for fast ODE simulations using dynamic loading of C-code into R was provided by Jonas Förster¹. Template scripts can be found on the attached data medium.

In Chapter 5, I ran deterministic simulations in Copasi (Complex Pathway Simulator) [156] which I connected to R by means of CoRC (Copasi R Connector; version 0.4.0)². CoRC is a high-level API allowing for the combination of powerful biochemical modeling tools in Copasi with superior scripting in R. Again, I applied the LSODA algorithm for deterministic simulations.

2.3 Stochastic simulations

I applied Gillespie's Direct Method to run stochastic simulations [157]. Again, I sped up simulations by outsourcing expensive computations to C-code that I dynamically loaded into R.

The standard Direct Method algorithm is defined by the following reaction probability density function:

$$p(\tau, \mu | x, t) = a_{\mu}(x) \cdot \exp \left(- \sum_{1 \dots M} a_{\mu}(x) \cdot \tau \right) \quad (2.1)$$

¹Jonas Förster: Biological Information Processing Group at the BioQuant Center, Heidelberg University

²The most recent version of the CoRC package for R by Jonas Förster and Jürgen Pahle (Biological Information Processing Group at the BioQuant Center, Heidelberg University) can be downloaded from <https://jpahle.github.io/CoRC/>.

The function describes the probability density of the next reaction being of type R_μ (with corresponding propensity a_μ) and being executed at time $t + \tau$ for a system that is currently in state x at time t . The presented probability density function is a homogeneous Poisson process.

In my analysis, I often used time series as model inputs in stochastic simulations. Therefore, as a result of changes in the input time series, propensities could also vary during a time step. This was accounted for by changing Equation 2.1 to an inhomogeneous Poisson process, as reported in [158]. The altered probability density function reads:

$$p(\tau, \mu) = a_\mu(t + \tau) \cdot \exp\left(-\int_t^{t+\tau} \sum_{1 \dots M} a_\mu(t) dt\right) \quad (2.2)$$

A first template for stochastic simulations using Gillespie's Direct Method with an inhomogeneous Poisson process was provided by Jürgen Pahle³. The template can be found on the attached data medium.

2.4 Optimizations

For optimizations, I used the default `optim` function in R. To this end, I employed the Nelder-Mead algorithm [159]. Since the algorithm only detects local optima, I applied a multi-start optimization scheme to approximate a global solution. Thus, I performed up to 50000 optimization runs per optimization problem. Optimization scripts differed from each other in the initial values of optimizable parameters, whereas initial values were drawn out of uniform or log-uniform distributions.

A first template for using R's `optim` function to optimize models according to `deSolve` simulation results was provided by Michael Gabel and Peter Kumberger⁴. The template can be found on the attached data medium.

2.5 Estimations of mutual information

For estimations of mutual information (as defined in Section 1.4.2), I applied a Kraskov-Stoegbauer-Grassberger estimator [160]. In contrast to other estimators, KSG estimators do not employ a constant volume, but rather set the number of data points within a volume to a constant value. Therefore, the volume size adjusts dynamically when scanning through a data set. The superiority of KSG estimators in estimating mutual information was reported in [161].

³Jürgen Pahle: Biological Information Processing Group at the BioQuant Center, Heidelberg University

⁴Michael Gabel and Peter Kumberger: Modelling Infection & Immunity Group at the BioQuant Center, Heidelberg University.

In this work, I set k , i.e., the fixed number of data points within a volume, to 5. Before measuring the mutual information between variables, I normalized variables by z-scoring. Z-scoring sets the mean of a variable distribution to 0 and its standard deviation to 1. Further, I added minuscule amounts of normally-distributed noise to the z-scored data points (mean = 0, standard deviation = 10^{-10}). The addition of noise ensured that data points could be clearly ranked which is a requirement for the KSG estimation process.

A low number of data points may lead to spurious estimates of mutual information. Thus, for every original estimate of mutual information, I performed between 100 and 1000 surrogate estimations. Surrogate estimates were previously applied to validate the significance of mutual information estimates [162] and of estimates of related information-theoretic measures [163]. The method follows the null hypothesis that a permutation of one variable's distribution order should disrupt dependencies to a second variable's distribution. For validation, I compared the mean of the surrogate estimate distribution to a corresponding original estimate.

For all presented estimations of mutual information, I employed a KSG estimator provided by Irina Surovtsova and Martin Zauser⁵. To this end, estimations of mutual information were initiated in R, while expensive computations were outsourced to C-code. The estimator accepts vectors as well as matrices as input variables. It can be found on the attached data medium.

2.6 Estimations of channel capacity

For estimations of channel capacity (as defined in Section 1.4.3), I employed the Blahut-Arimoto (BA) algorithm [164, 165].

For inferring channel capacity, i.e., the maximal mutual information of a channel for a given set of inputs, the relative entropy between $p(x)$ and $p(x|y)$ was iteratively increased until convergence, where X refers to the input variable and Y to the output variable. For calculating $p(x)$ and $p(x|y)$, the following two equations were employed:

$$p_n(x|y) = \frac{p_{n-1}(x) \cdot p(y|x)}{\sum_x p_{n-1}(x) \cdot p(y|x)} \quad (2.3)$$

and

$$p_n(x) = \frac{\prod_y (p_n(x|y))^{p(y|x)}}{\sum_x \prod_x (p_n(x|y))^{p(y|x)}} \quad (2.4)$$

For a detailed derivation of the equations, please refer to [146]. In this study, the cycle was repeated until the Euclidean distance between the new input distribution $p_n(x)$ and the former input distribution $p_{n-1}(x)$ was smaller than a set threshold of $1 \cdot 10^{-50}$ signaling a stop of a significant improvement. By convention, the algorithm was initiated by using a uniform input distribution.

⁵Irina Surovtsova and Martin Zauser: Biological Information Processing Group at the BioQuant Center, Heidelberg University.

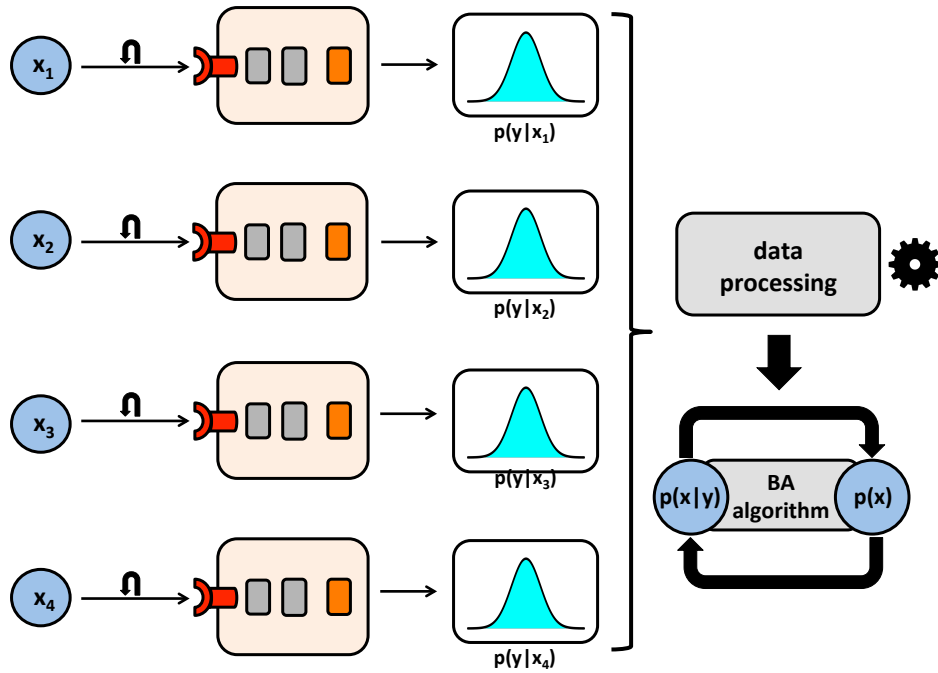


Fig. 2.1. Workflow for acquiring input-signal-specific output probability distributions. First, I defined a set of relevant input signals (x_1, x_2, \dots). By means of stochastic simulations, the repeated application of a particular input signal x_i led to the acquisition of an input-signal-specific output distribution $p(y|x_i)$. Before using the output distributions in the BA algorithm (as defined in Equations 2.3 and 2.4), the data had to be discretized. In my analysis, I defined the output measure as the average number of particles of a biochemical species. I obtained maximal resolution by using a bin width of one particle.

According to Equations 2.3 and 2.4, the output distribution $p(y|x)$ was required. This distribution represents the variation in the output variable Y in response to the input variable X . In this thesis, I inferred $p(y|x)$ from stochastic simulation results. In particular, I performed the workflow sketched in Figure 2.1. First, I defined a set of relevant input signals. Then, I applied these input signals to a communication channel, i.e., a biochemical model. For every input signal x_i , I ran 1000 stochastic simulations in order to obtain a corresponding input-signal-specific output distribution $p(y|x_i)$. Since the BA algorithm only accepts discrete data, I binned the obtained output distributions $p(y|x_i)$. As I defined the output measure as the average number of particles of a biochemical species, I could obtain maximal resolution by setting the bin width to one particle.

The applied BA algorithm script was initialized in R. Expensive computations were outsourced to faster C-code. A first MATLAB template of the algorithm was provided by Aarón Vázquez-Jiménez. This template was converted into R- and C-code by Jürgen Pahle, Arne Schoch and Martin Zauser⁶.

⁶Aarón Vázquez-Jiménez: Centro de Investigación y de Estudios Avanzados del IPN (Cinvestav-IPN), Unidad Monterrey, Mexico; others: Biological Information Processing Group at the BioQuant Center, Heidelberg University.

2.7 Data presentation

For data visualization, I used default functions in R as well as additional functions provided in the R packages `ellipse` and `ggplot2` [166].

Part III

Results

Method development and investigation

3.1 The *OscillatorGenerator* package for R

A large part of this thesis was about a model-based analysis of the frequency-decoding of calcium oscillations by dependent proteins. For the protein models presented in Chapter 4, I described the concentration of calcium over time by means of a predefined input, invariable to any feedback. In most cases, I approximated calcium oscillations by a sine wave function that allowed for an easy modulation of the oscillation amplitude, offset and period. In cells, however, calcium oscillations often differ from sine waves. In particular, experimental time series exhibit a duty cycle, i.e., a clear distinction between an active, above-baseline and an inactive, baseline part within a single oscillation cycle. Further, calcium oscillations are often asymmetric and sometimes possess several minor spikes after a larger primary spike within a single oscillation cycle.

In order to generate more physiological calcium oscillation shapes that featured some of the mentioned characteristics, I implemented several functions into R. In total, discrete time series of seven basic oscillation shapes can be generated by means of seven functions. Parameters defining the time series' duration and resolution as well as overall appearance are set by the user. To this end, due to the incorporation into R, a particular parameter can be readily scanned to test for its impact on a connected protein model. I comprised all functions in the *OscillatorGenerator* package, an official CRAN release (the Comprehensive R Archive Network)¹. The most recent version of the *OscillatorGenerator* package can be found at <https://cran.r-project.org/package=OscillatorGenerator>.

The functions of the *OscillatorGenerator* package can be distinguished into two complexity levels generating either signals resembling spiking or bursting oscillations. In terms of spiking-like oscillations, four functions, i.e., basic shapes, are provided: a sinusoid, a square-wave, a spike with linear increase and decrease dynamics and a spike with exponential increase and decrease dynamics (Figure 3.1). All functions present the user with the option to set baseline and peak levels as well as an oscillation period (Figure 3.1 A-C) and a duty cycle (Figure 3.1 D-F). In addition, a trend parameter can be used to specify a linear growth or decline in the peak level from one oscillation cycle to the next, with decline motions automatically stopping at the set baseline level (Figure 3.1 G-I). The trend parameter can be applied to simulate the depletion or influx of an upstream first messenger that is linked to a change in the calcium oscillation amplitude over time (as observed in fish [47]). Furthermore, for linear and exponential spiking shapes, the peak position in the active phase of an oscillation

¹I generated all time series with package version 0.1.0.

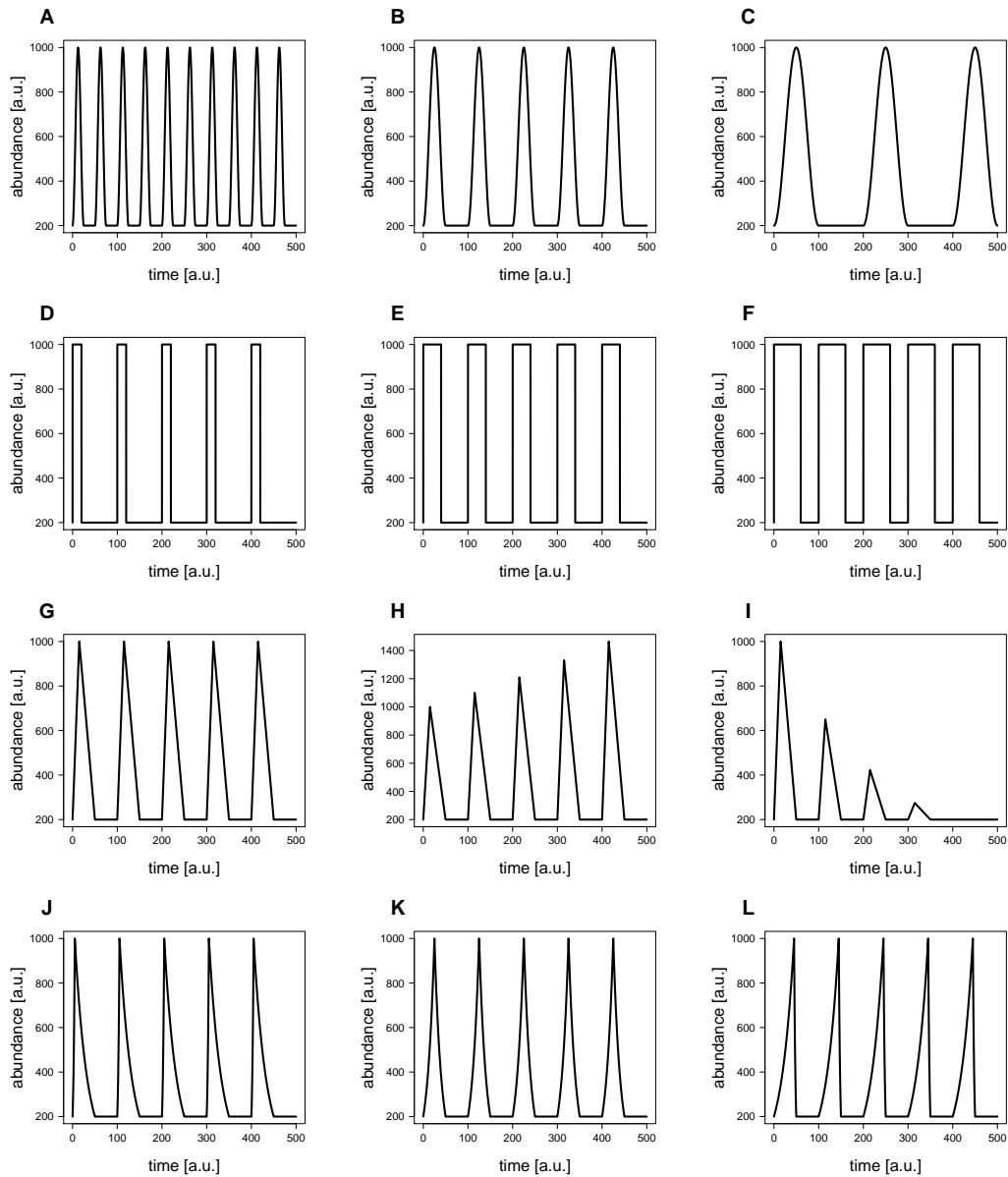


Fig. 3.1. Time series resembling spiking oscillations generated with the *OscillatorGenerator* package. The *OscillatorGenerator* package provides four basic shapes resembling spiking oscillations: a sinusoid (A-C), a square-wave (D-F) and a spike-shape with either linear (G-I) or exponential dynamics (J-L). The user can specify the oscillation period, the duty cycle, baseline and peak levels as well as the evolution of the oscillation amplitude: (A) period = 50, (B) period = 100, (C) period = 200. (D) duty cycle = 0.2, (E) duty cycle = 0.4, (F) duty cycle = 0.6. (G) trend = 1 (peak level does not change), (H) trend = 1.1, (I) trend = 0.9. For spiking oscillations with linear or exponential dynamics, the peak position in the active phase of an oscillation cycle is also customizable: (J) position = 0.1, (K) position = 0.5, (L) position = 0.9. For the presented data, I applied the following standard parameters: baseline = 200, peak = 1000, duration = 500, resolution = 0.1. If not explicitly mentioned: period = 100, duty cycle = 0.5, trend = 1, peak position = 0.3.

cycle is user-defined as well (Figure 3.1 J-L), whereas the active phase is the above-baseline part of an oscillation cycle.

Dependent on the first messenger and the cell-line in question, bursting oscillations arise [50]. Bursting oscillations are characterized by the presence of a primary peak succeeded by minor

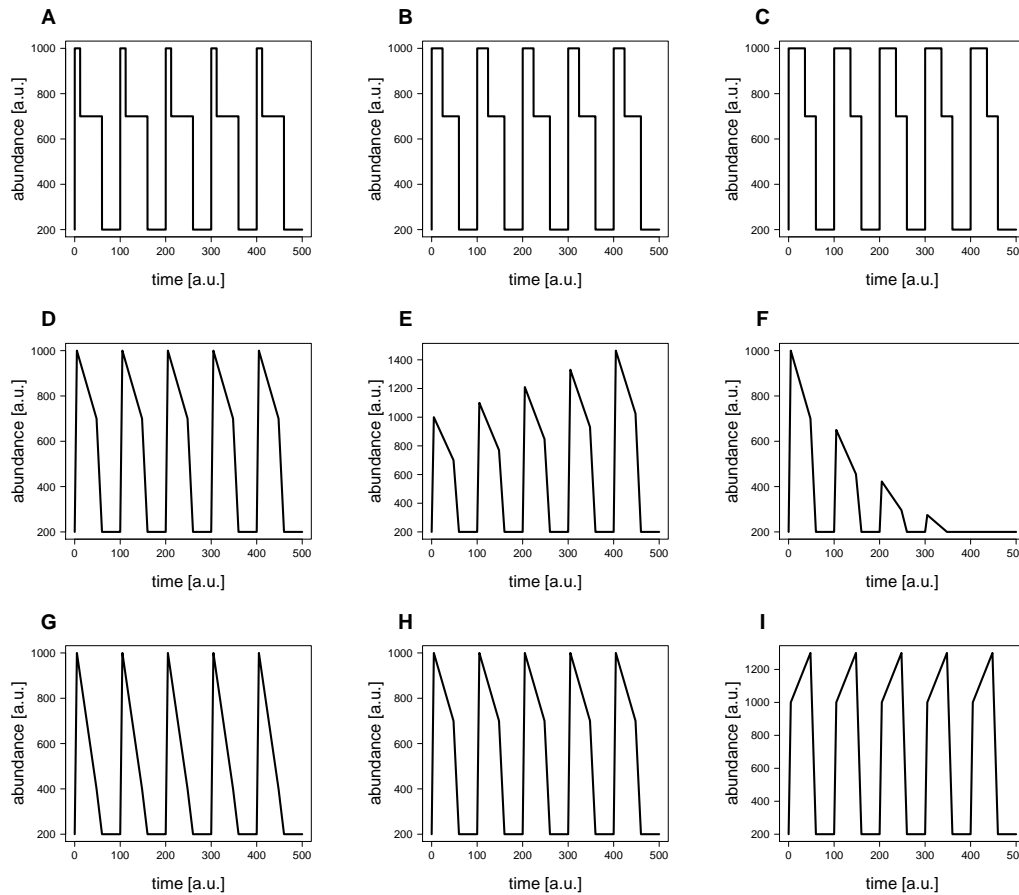
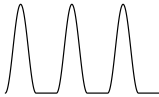
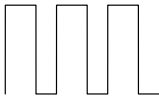


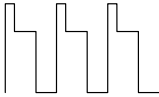




Fig. 3.2. Time series resembling bursting oscillations generated with the *OscillatorGenerator* package. The *OscillatorGenerator* package provides three basic shapes resembling bursting oscillations: a bursting-like oscillation shape composed of two superimposed square-waves (A-C) or bursting-like shapes for which baseline, peak and secondary peak levels are connected by either linear (D-F) or exponential dynamics (G-I). In addition to the characteristics shown in Figure 3.1, the secondary duty cycle as well as the secondary peak level can be modulated for bursting-like oscillation shapes as well. The trend parameter now determines the evolution of peak and secondary peak levels: (A) secondary duty cycle = 0.2, (B) secondary duty cycle = 0.4, (C) secondary duty cycle = 0.6. (D) trend = 1 (peak level unchanged), (E) trend = 1.1, (F) trend = 0.65. (G) secondary peak level = 400, (H) secondary peak level = 700, (I) secondary peak level = 1300. For the presented data, I applied the following standard parameters: baseline = 200, peak = 1000, period = 100, duty cycle = 0.6, duration = 500, resolution = 0.1. If not explicitly mentioned: secondary duty cycle = 0.8, secondary peak level = 700, trend = 1.

secondary peaks, within a single oscillation cycle. In the following, the presented artificial oscillation shapes represent coarse outlines of these bursting dynamics. Bursting-like oscillation shapes can be generated by means of three distinct functions in the *OscillatorGenerator* package, the simplest being a bursting-like shape composed of two superimposed squares for which primary and secondary peak levels are set by the user. For the other two functions, baseline, primary peak and secondary peak levels are connected by either linear or exponential dynamics (Figure 3.2). Again, a duty cycle parameter defines the ratio of the general active phase to the total oscillation period. However, in contrast to the previously presented spiking-like oscillations, a secondary duty cycle parameter is also customizable. This parameter determines the ratio of the primary active phase to the total active phase (Figure 3.2 A-C), whereas the primary active phase spans from the beginning of an oscillation cycle until the secondary peak level is reached. The trend parameter now determines the change in peak and in secondary

Tab. 3.1. Function calls in the *OscillatorGenerator* package.

Function call	Output example
<code>Sinusoid(baseline, peak, period, duty_cycle, trend, duration, resolution)</code>	
<code>SquareSpike(baseline, peak, period, duty_cycle, trend, duration, resolution)</code>	
<code>LinSpike(baseline, peak, period, duty_cycle, peak_pos, trend, duration, resolution)</code>	
<code>ExpSpike(baseline, peak, period, duty_cycle, peak_pos, trend, duration, resolution)</code>	
<code>SquareBurst(baseline, peak, period, duty_cycle, sec_duty_cycle, sec_peak, trend, duration, resolution)</code>	
<code>LinBurst(baseline, peak, period, duty_cycle, sec_duty_cycle, sec_peak, trend, peak_pos, duration, resolution)</code>	
<code>ExpBurst(baseline, peak, period, duty_cycle, sec_duty_cycle, sec_peak, trend, peak_pos, duration, resolution)</code>	

The *OscillatorGenerator* package provides seven functions resembling seven basic oscillation shapes. Each function exhibits multiple arguments for further customization.

peak levels from one oscillation cycle to the next (Figure 3.2 D-F). The initial secondary peak level is also customizable (Figure 3.2 G-I).

A full list of function calls as well as detailed descriptions of function arguments are provided in Tables 3.1 and 3.2.

Tab. 3.2. Function arguments used in the *OscillatorGenerator* package for R.

Argument	Description
duration	duration of the generated time series
resolution	resolution of the generated time series
baseline	minimal value of the oscillator
peak	maximal value of the oscillator
sec_peak	for bursting modes only: intermediary value targeted between peak and return to baseline
period	oscillation period (reciprocal of the frequency)
duty_cycle	ratio of the active phase (oscillator above baseline) to the total oscillation period
sec_duty_cycle	for bursting modes only: ratio of the primary active phase (time interval from cycle start until sec_peak) to the total active phase
peak_pos	for linear and exponential modes only: position of the peak in the (primary) active phase of an oscillation cycle
trend	percental linear increase or decrease in peak and if available sec_peak between oscillation cycles; for trend = 1, values remain unchanged

Arguments listed above apply for the function calls presented in Table 3.1.

3.2 A theoretical analysis of channel capacity estimates

3.2.1 A measure for quantifying the discriminability of input signals in the presence of fluctuations

In biological signal transduction, information transmission must be highly reliable, since the spurious interpretation of input signals can lead to the emergence of severe malfunctions [5]. To this end, information transmission must be unambiguous, despite the presence of stochastic effects adding uncertainty to a system's response after a stimulation with a particular input. In particular, due to stochastic effects, several distinct responses can be linked to a particular input signal. In order to investigate the discrimination of input signals under realistic stochastic conditions, I employed a stochastic simulation algorithm, i.e., Gillespie's Direct Method [157] in the second half of Chapter 4. By means of a repeated stimulation of a system with the same input signal, I could infer input-signal-specific output distributions.

I then applied channel capacity estimations [17] to quantify the discriminability of the input-signal-specific output distributions. Channel capacity C is defined as the maximal mutual information I of a channel for a set of given input signals x_i , whereas the analyzed channel is assumed to be memoryless. It can be inferred by optimizing the input distribution $p(x)$:

$$C(X;Y) = \sup_{p(x)} I(X;Y), \quad (3.1)$$

where mutual information is defined as

$$I(X;Y) = \sum_{y \in Y} \sum_{x \in X} p(x,y) \cdot \log_2 \left(\frac{p(x,y)}{p(x) \cdot p(y)} \right) = H(X) - H(X|Y) = H(Y) - H(Y|X), \quad (3.2)$$

and $H(X)$ is the Shannon entropy of X and $H(X|Y)$ is the conditional entropy of X given Y . For mathematical notations of $H(X)$ and $H(X|Y)$, please refer to Equations 1.3 and 1.4 in Section 1.4.2.

For estimations of channel capacity, i.e., for maximizations of the mutual information, I applied the Blahut-Arimoto algorithm, as presented in Section 2.6. In previous studies, channel capacity was already used to define an upper boundary to information transmission in biological signal transduction pathways [147, 167, 150, 151].

Since the interpretation of channel capacity estimates can be challenging, in the following, I discuss simple example cases to provide a better understanding on the meaning of the measure, as it is applied here.

3.2.2 Channel capacity is limited by the number of input signals considered

For this section, I approximated input-signal-specific output distributions as normal distributions $\mathcal{N}(\mu; \sigma^2)$, with mean μ and variance σ^2 . In the first example case, I considered two output distributions, $p(y|x_1)$ and $p(y|x_2)$, to arbitrary input signals x_1 and x_2 .

Both distributions exhibited a variance of 1. While I set the mean of the first distribution to a constant value, I incrementally increased the mean of the second distribution (Figure 3.3 A). After every change in the second distribution's mean, I performed an estimation of channel capacity to study the effect of varying degrees of discriminability between output distributions on the channel capacity estimate.

In case both distributions shared the same mean value, thus, were practically identical, estimations yielded 0 bits. Hence, the 0-bits-mark can be associated with absolutely no distinctness between output distributions. In more detail, 0 bits can be interpreted as $2^0 = 1$ distinguishable input set. Therefore, an observer of the output could only tell, whether any of the two input signals was applied, but was not able to specify which one. When iteratively increasing the difference between the distributions' mean values, channel capacity estimates rose until a maximum of 1 bit was reached (Figure 3.3 B). The less overlap between the output distributions, the more likely it became that an observer of the output could reliably discriminate between the applied input signals. Only when the two output distributions were

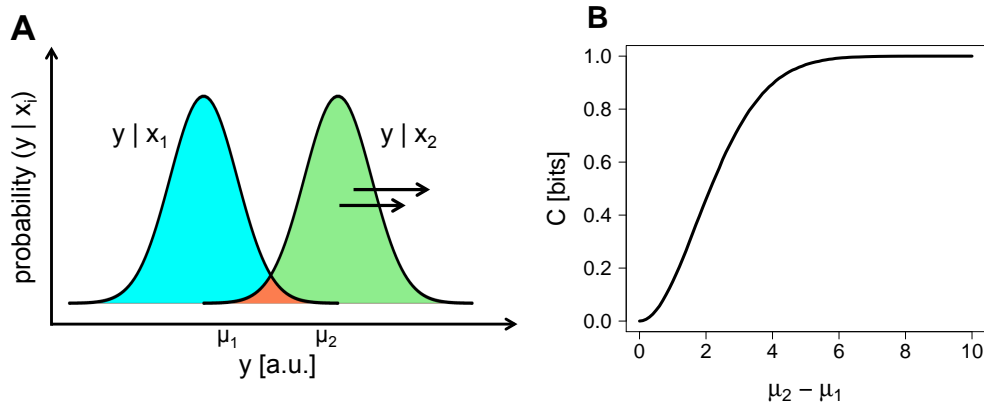


Fig. 3.3. Measuring the channel capacity between two output distributions with variable distinctness. (A) Schematic depicting two output distributions to arbitrary input signals x_1 and x_2 . I raised the second distribution's mean μ_2 between channel capacity estimations to iteratively increase the distinctness between output distributions. As a result, channel capacity increased as well (B). When output distributions were identical, channel capacity estimations yielded 0 bits, i.e., an observer could recognize $2^0 = 1$ input set, thus, was only able to tell whether any of the considered input signals was applied, but could not specify which one. In contrast, if output distributions were completely distinct, 1 bit was reached. In this case, an observer of the output could clearly discriminate between $2^1 = 2$ input signals based on the fact that distinct parts of the output range were clearly related to the action of either one of the two input signals. Here, "input set" can refer to a batch of input signals or a single input signal. With $\mathcal{N}_1(\mu_1 = 0; \sigma_1^2 = 1)$ and $\mathcal{N}_2(\mu_2; \sigma_2^2 = 1)$, whereas μ_2 was scanned from 10 to 20.

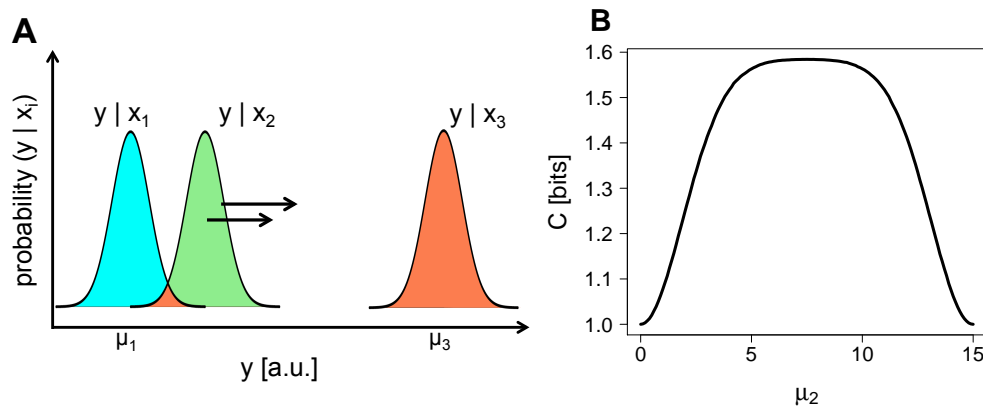


Fig. 3.4. Measuring the channel capacity between three output distributions with variable distinctness. (A) Schematic depicting three output distributions to three arbitrary input signals x_1 , x_2 and x_3 . I iteratively increased the second distribution's mean μ_2 between channel capacity estimations from 0 (which is equal to the first distribution's mean μ_1) to 15 (which is equal to the third distribution's mean μ_3). (B) A sigmoidal increase in channel capacity followed up by a sigmoidal decrease was the result. When two output distributions were identical to each other, channel capacity estimates yielded 1 bit, for the third distribution was always absolutely distinct to the other two. When distancing the second output distribution from the first and the third output distribution, thus, creating three entirely distinct distributions, channel capacity increased to 1.58 bits. This can be interpreted as $2^{1.58} = 3$ input sets that can be clearly discriminated based on the channel's output. With $\mathcal{N}_1 (\mu_1 = 0; \sigma_1^2 = 1)$, $\mathcal{N}_2 (\mu_2; \sigma_2^2 = 1)$, where μ_2 was scanned from 0 to 15, and $\mathcal{N}_3 (\mu_3 = 15; \sigma_3^2 = 1)$.

entirely distinct, the 1-bit-mark was touched². 1 bit can be interpreted as $2^1 = 2$ input sets that are distinguishable beyond any doubt based on the output measure. Now, entirely distinct output states could be clearly related to either one of the two input signals.

In the second example, I considered three output distributions to three distinct input signals, all exhibiting identical variances of 1. While the first and the third output distribution were always entirely distinct to each other, the second output distribution was shifted from the first to the third distribution in an iterative manner. Once again, after every change in the second distribution's mean, I performed estimations of channel capacity. The described experiment resulted in a sigmoidal rise in channel capacity from 1 bit to 1.58 bits, followed by a sigmoidal decline from 1.58 bits back to 1 bit (Figure 3.4). Only in case the second distribution's mean μ_2 was identical to the first distribution's mean μ_1 or the third distribution's mean μ_3 , I received 1 bit pointing at two distinguishable input sets. This time the 1-bit-mark did not refer to two single input signals being clearly distinguishable, but instead to a single input signal and a combination of two input signals being clearly distinguishable; if μ_1 was identical to μ_2 , the range of output states could be divided into two distinct parts, one referring to the action of input signal three, the other to the action of either input signal one or two. Thus, input signals one and two were grouped into a shared category. In case all three output distributions were entirely distinct to each other, I received 1.58 bits pointing at $2^{1.58} = 3$ clearly distinguishable input sets. This time, the three distinguishable input sets were actually composed of single

²Exactly 1 bit was only reached, since there were no shared elements between the distributions that were composed of a finite number of elements. When applying Gaussian distributions with an infinite number of elements, outliers would always interfere with a perfect distinction, thus, capacity would never reach 1 bit but rather converge to 1 bit, when iteratively increasing the difference between the mean values of the output distributions.

input signals x_1 , x_2 and x_3 . In consequence, the range of output states could be divided into three distinct parts, each part clearly linked to the action of one of the three input signals.

In conclusion, when considering a group of input signals x_1, x_2, \dots, x_n , one can attest, without knowledge of any input-specific output distribution, that the capacity has to lie between 0 bits, meaning that all input-signal-specific output distributions are identical, and $\log_2(n)$ bits, meaning that every single output distribution is entirely distinct to the others, thus, there are no overlaps between single output distributions. The upper boundary can also be inferred from the mathematical notation of mutual information (see Equation 3.2). $I(X; Y)$ is the difference between the Shannon entropy $H(X)$ and the conditional entropy $H(X|Y)$. $H(X|Y)$ refers to the uncertainty in the input X given the output Y . If there are no overlaps between output distributions, this uncertainty, i.e., $H(X|Y)$, is equal to 0 bits. In this case, $I(X; Y)$ is equal to $H(X)$ and the maximum of $H(X)$ is obtained with a uniform input distribution $p(x)$ resulting in $\log_2(n)$ bits (see Equation 1.3 in Section 1.4.2).

3.2.3 Input recurrence in channel capacity estimates

For the example presented in Figure 3.4, the 1-bit-mark was associated with two distinct parts of the output range being linked to the actions of entirely distinct input sets. However, when considering an example case in which output distributions $p(y|x_1)$ and $p(y|x_3)$ were entirely distinct to each other and the output distribution $p(y|x_2)$ covered all output values that were already covered by $p(y|x_1)$ and $p(y|x_3)$, channel capacity still amounted to 1 bit despite the lack of two entirely distinct input sets.

I sketched a corresponding set-up in Figure 3.5 A. Since the applied Blahut-Arimoto algorithm requires discretized input-signal-specific output data, output states can be imagined as squares. In case an output distribution $p(y|x_i)$ covered an output square, it was highlighted in red. If the presented "overlap pattern" in Figure 3.5 A was applied, independent of the underlying probability values for the occurrence of particular output state upon stimulation with a particular input signal (for example $p(y_1|x_1)$), channel capacity always amounted to 1 bit. In general terms, this means that an observer of the output could divide the range of output states into $2^1 = 2$ parts, both being clearly linked to the actions of a distinct input set. However, while input sets might be distinguishable, not all elements of the input sets have to be distinct. In case an observer received the outer left output square, input signal three could be dismissed, while the observer could be certain that either input signal one or two was applied. In case an observer received the outer right output square, input signal one could be dismissed, while the observer could be certain that either input signal three or, once again, two was applied. Therefore, an observer was able to distinguish between the actions of two input sets, whereas input sets shared input signal two as a mutual, recurring component.

Similarly, for the set-up sketched in Figure 3.5 B, independent of the underlying, input-specific output distributions within the red squares, channel capacity always amounted to 1.58 bits. Thus, an observer could divide the range of output states into $2^{1.58} = 3$ parts, each part being clearly linked to the action of a distinct input set. For the outer left square, input signals three and four could be clearly dismissed, while it was certain that either input signal one or two was applied. For the squares in the middle, input signals one and three could be

clearly dismissed, while it was certain that either input signal two or four was applied. And for the outer right square, input signals one or four could be clearly dismissed, while it was certain that either input signal two or three was applied. In summary, three distinct input sets could be recognized, with all input sets sharing input signal two as a mutual, recurring component.

Hence, channel capacity estimates seem to provide an answer to the following question: Into how many parts can a range of output states be divided, with every part clearly referring to

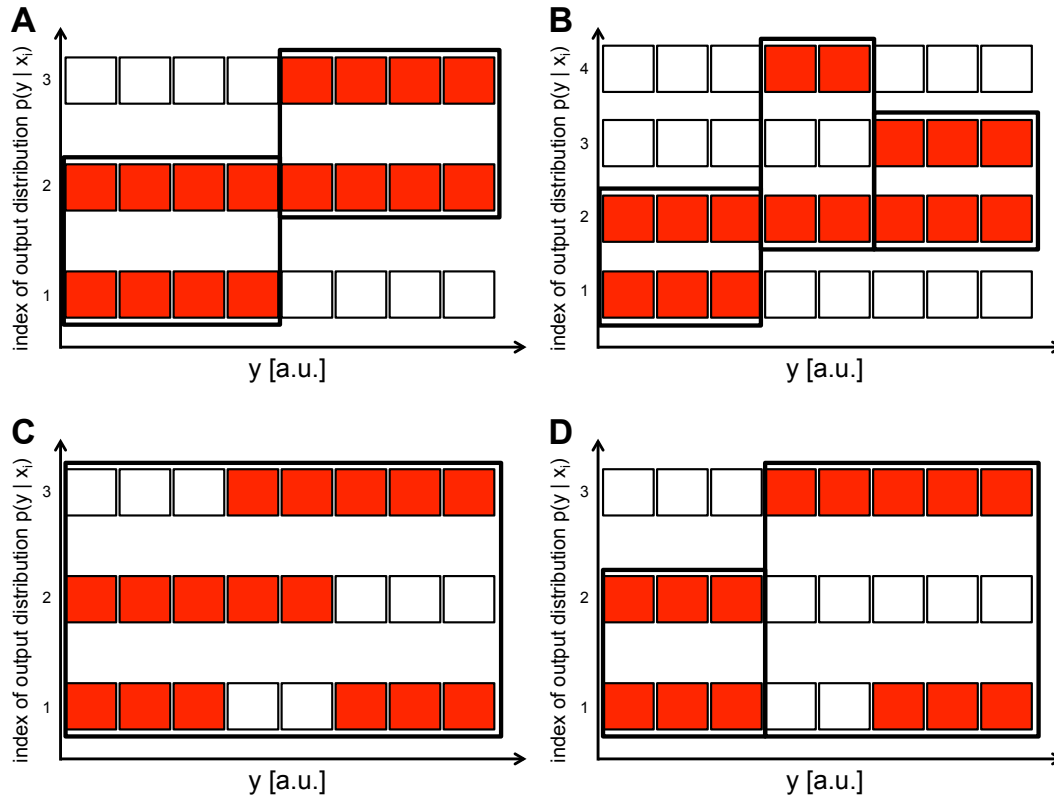


Fig. 3.5. Channel capacity estimates refer to the number of distinct input sets characterized by at least one set-exclusive element. For the applied Blahut-Arimoto algorithm, output values had to be discretized. In the panels above, discretized output values are represented as squares. In case an input-signal-specific output distribution covered a discretized output value, the corresponding square was highlighted in red. (A): When employing the presented "overlap pattern" between three input-signal-specific output distributions, channel capacity estimates always amounted to 1 bit, independent of the underlying probabilities within the red squares. Thus, the output range could be divided into $2^1 = 2$ parts, with each part referring to different input sets. Here, input signal two was part of both input sets. (B): Similarly, when employing this overlap pattern, channel capacity always amounted to 1.58 bits. Thus, the range of output states could be divided into $2^{1.58} = 3$ parts, with each part referring to different input sets. Again, input signal two was part of all input sets. (C): While distinct input sets can share single input signals with each other, at least one input signal has to be set-exclusive. Here, the output range could be divided into three parts, with each part referring to a different input set; set one composed of input signals one and two, set two composed of input signals two and three and set three composed of input signals one and three (from left to right). Nonetheless, channel capacity actually amounted to less than 1 bit. This was because none of the aforementioned input sets included a set-exclusive element. When changing to overlap pattern (D), channel capacity amounted to at least 1 bit, while it never reached 1.58 bits. Now, the output range could be divided into two parts, with each part referring to input sets that included at least one set-exclusive element. Correct input sets are marked by thick black outlines.

the action of a distinct input set? However, also this interpretation is not entirely correct, as demonstrated in Figure 3.5 C. In this example case, the range of output states could be divided into three separate parts, with each part referring to the action of a distinct input set; input set one composed of input signals one and two, input set two composed of input signals two and three and input set three composed of input signals one and three (from left to right in the sketch). According to the initial interpretation of channel capacity, independent of the underlying, input-specific probability distributions within the red squares, channel capacity should always amount to 1.58 bits. In reality, however, channel capacity was very much dependent on these probabilities and did not even amount to 1 bit. To add to the confusion, when changing the pattern in Figure 3.5 C to the one in Figure 3.5 D, channel capacity estimates were larger than or equal to 1 bit but smaller than 1.58 bits, although the range of output states could be divided into three parts referring to three distinct input sets (input set one composed of input signals one and two, input set two composed of input signal three and input set three composed of input signals one and three).

While for the overlap pattern in Figure 3.5 C, one cannot find two distinct input sets that exhibit at least one element, i.e., one single input signal, that is set-exclusive, in Figure 3.5 D, only two input sets can be identified, that include at least one set-exclusive input signal: input set one composed of input signals one and two and input set two composed of input signals one and three (marked by black outlines). Therefore, one has to add: Into how many parts can a range of output states be divided, with every part clearly referring to the action of a distinct input set that is characterized by at least one set-exclusive input signal?

3.2.4 Reducing overlaps between output distributions increases channel capacity estimates

In Section 3.2.2, I stated that the channel capacity is inherently limited by the number of input signals considered. If all n considered input signals lead to entirely distinct output distributions, channel capacity amounts to $\log_2(n)$ bits. In other words, the distinctness between a given number of output distributions is maximized, if the overlaps between output distributions is minimized. There are two ways this can be achieved: by either spreading out individual output distributions, i.e., maintaining the distributions' variances but distributing them over a larger output range, or narrowing down single output distributions, i.e., maintaining the output range but decreasing the distributions' variances. In both cases, overlaps between output distributions can be reduced.

In an artificial set-up, I added one new output distribution round by round, while keeping all previously generated output distributions. After every round, I proceeded to estimate the channel capacity between the growing number of output distributions. In particular, I drew the mean of each new output distribution from a uniform distribution with finite boundaries. When measuring the channel capacity after every iteration cycle, channel capacity either increased or stayed constant until convergence to a cap value. The addition of more input-signal-specific output distributions never led to a decrease in channel capacity due to the phenomenon of input recurrence (see Section 3.2.3). As expected, increases in the output range or decreases in the variance of output distributions led to larger channel capacity caps (see Figure 3.6).

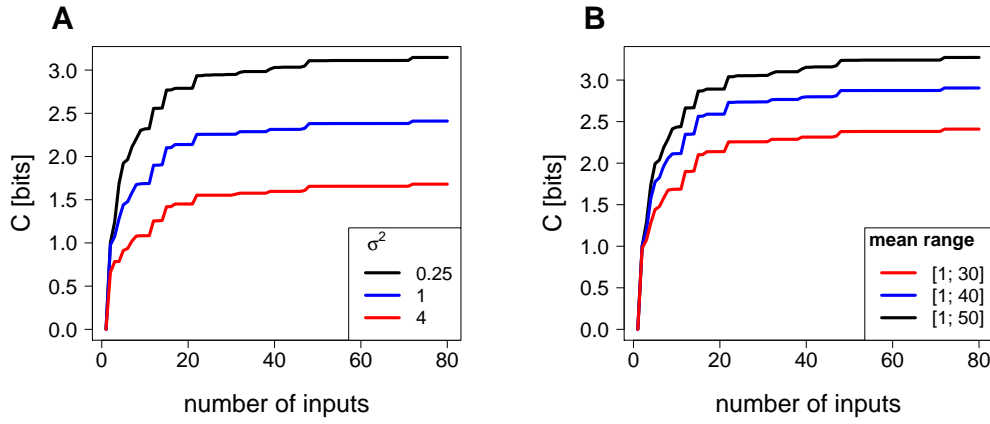


Fig. 3.6. Effect of spreading out or narrowing down output distributions on channel capacity estimates. To obtain the presented results, I ran multiple input addition assays varying either the variance σ^2 of the input-signal-specific output distributions (A) or the output range (B). In the input addition assays, per round, a new output distribution was added to the mix of already present ones. In each round, I estimated the channel capacity between the growing number of output distributions. In all instances, channel capacity grew or remained constant when adding more output distributions. Eventually, channel capacity converged to a cap value. The cap value was increased for larger output ranges or smaller variances, with both variations leading to less overlaps between output distributions. (A): With $\mathcal{N}_i(\mu_i; \sigma_i^2)$, where μ_i was drawn out of uniform distributions ranging from 10 to 30 and σ_i^2 was set to either 0.5 (black curve), 1 (blue curve) or 2 (red curve). (B): With $\mathcal{N}_i(\mu_i; \sigma_i^2 = 1)$, where μ_i was drawn out of uniform distributions ranging from 10 to 50 (black curve), from 10 to 40 (blue curve) or from 10 to 30 (red curve).

In the second half of Chapter 4, I used channel capacity estimations to quantify the discriminability of calcium oscillation frequencies based on the average concentration of a calcium-dependent protein. The presented example studies in this chapter were meant to clarify the meaning of channel capacity and to point out the ambiguity of the measure.

Analyzing the frequency-decoding of calcium oscillations

4.1 Chapter introduction

4.1.1 About this chapter

Several proteins, directly or indirectly regulated by calcium, are sensitive to modulations of the calcium oscillation frequency. A list of examples is provided in Section 1.2.3. In most cases, it was found that a dependent protein's activity is positively correlated with the calcium oscillation frequency, i.e., faster oscillations result in an increased protein activity [62]. Opposed to this high-pass activation mechanism, for the transcription factor NFAT, experimental studies suggest a more complex decoding behavior. NFAT was reported to exhibit an optimal frequency for maximal activity. Thus, oscillations slower or faster than the optimal frequency only result in a reduced activity [62, 64]. In the following, I call this kind of frequency-decoding band-pass activation.

Here, I present a reproduction and analysis of high-pass (Section 4.2) and band-pass activation (Section 4.3) using simple kinetic protein models. To this end, I defined a molecular communication channel in which the calcium oscillation frequency served as an input and the average concentration of a dependent model species acted as the channel output. I attested frequency-decoding in case significant changes in the output arose upon stimulating a protein model with different input signals, i.e., in case the applied calcium frequencies could be clearly discriminated by means of the output measure. Further, on the basis of the aforementioned protein models, I constructed a more specific model for the calcium-dependent activation of the transcription factor NFAT (Section 4.6). I used the NFAT model to probe for the possibility of band-pass activation of the transcription factor, as reported in literature [62, 64].

In order to probe for high-pass or band-pass activation in a given protein model, I employed optimization algorithms (Section 4.4). To this end, I optimized selected model parameters to maximize the distinctness in high-pass or band-pass activation. In case optimizations did not yield significant high-pass or band-pass activation, I concluded that a model was not able to perform this kind of frequency-decoding.

Strikingly often, proteins bind calcium ions in a positive-cooperative manner (Table 4.1). Positive-cooperative protein activation is characterized by ligands, here calcium ions, exhibiting a higher affinity for a protein once other ligands have already bound. As a result, the fraction of ligand-saturated protein as a function of the ligand's concentration takes on a sigmoidal, ultrasensitive shape that can be described by a Hill equation [168]. In order to represent

Tab. 4.1. List of calcium-dependent proteins activated in a positive-cooperative manner.

Protein	Coop. coefficient	Experimental details
CaM	1.7; 1.1 4	for binding of Ca^{2+} to high-affinity and low-affinity binding sites <i>in vitro</i> , respectively [169] for binding of Ca^{2+} to unspecified sites in a mathematical model [69]
CaMKII	3; 1.8; 4	for binding of CaM- Ca^{2+} in <i>C. elegans</i> ; phosphorylation assays with respect to WT-enzyme and syntide substrate, $\Delta 17$ -enzyme and autocamid substrate and $\Delta 17$ -enzyme and syntide substrate [170]
Cn	1.88	in an <i>in vitro</i> phosphatase assay with respect to CaM- Ca^{2+} [171]
PKC- α PKC- β PKC- γ	1.3 1.8 1.4	in an <i>in vitro</i> FRET assay using isolated C2-domains; with respect to Ca^{2+} in the presence of phosphatidylserine-containing vesicles [172]

Several proteins bind calcium ions in a positive-cooperative manner. In Section 4.7, I examined the relationship between cooperativity coefficient parameterization, i.e., the degree of ultrasensitivity, and the frequency-decoding distinctness in kinetic models of calcium-dependent protein activation.

different levels of ultrasensitivity, a parameter in the Hill equation, the cooperativity coefficient, can be modulated, with steeper more ultrasensitive shapes being linked to larger cooperativity coefficients.

By maximizing a model’s frequency-decoding distinctness with regards to either high-pass or band-pass activation, for a given, i.e., non-optimizable parameterization of cooperativity coefficients, I examined the influence of cooperativity strength on frequency-decoding (Section 4.7). To this end, I used a multi-start optimization scheme. Thus, per optimization problem, I obtained a multitude of parameter sets associated with distinct frequency-decoding. Subsequently, I analyzed these optimized parameter sets for conserved characteristics that allowed for highly efficient high-pass or band-pass activation given a particular parameterization of cooperativity coefficients (Section 4.8). In addition, constrained optimizations, i.e., optimizations in which single parameters could only be varied in confined intervals revealed the consequences of an unfavorable model parameterization on frequency-decoding (Section 4.9).

I also applied the optimization-based method to investigate the impact of the calcium oscillation amplitude on the optimal parameterization of binding constants for distinct frequency-decoding (Section 4.10). Furthermore, I analyzed the effect of a higher degree of specificity in band-pass activation on optimization results in Section 4.11.

In the first part of this chapter, I examined frequency-decoding under deterministic conditions. In particular, I was interested in the consequence of given conditions, for example a particular parameterization of cooperativity coefficients, on the maximal distinctness of high-pass or band-pass activation. In contrast, in the second part of this chapter, I changed my objective. Now, I focused on a protein's ability to discriminate between given frequencies in the presence of more realistic stochastic conditions.

For the inclusion of stochastic effects, I employed Gillespie's Direct Method for model simulations [157]. While in deterministic simulations, even slight differences in the output can be reliably mapped to particular input signals, fluctuations blur out links between input and output signals. In order to quantify a protein's ability to discriminate between given frequencies, I applied the information-theoretic measure of channel capacity [17], whereas I estimated channel capacity (as introduced in Sections 1.4.3 and 3.2) based on the Blahut-Arimoto algorithm (as introduced in Section 2.6) [164, 165].

At first, in Section 4.13, I applied channel capacity to analyze the impact of system responsiveness on the discrimination of frequencies situated in a given bandwidth. Further, I discovered a positive relationship between cooperativity strength and the maximal frequency-decoding distinctness. I assumed that, in particularly distinct frequency-decoding, already minor variations in the oscillation frequency can be recognized based on the output measure despite the presence of fluctuations. Therefore, in Section 4.14.2, I quantified the effect of increases in the parameterization of cooperativity coefficients on a protein model's ability to resolve given oscillation frequencies.

In summary, I identified requirements in model parameterization and network structure for frequency-decoding under deterministic and stochastic conditions. In the past, frequency-decoding of calcium oscillations was investigated in several other *in silico* studies [56, 69, 75, 76, 77, 83, 86, 87]. In this regard, I would like to highlight the publications by Dupont and Goldbeter as well as Salazar *et al.* who also described parametric requirements for successful frequency-decoding [76, 87]. The presented analysis is unique in terms of its methodology and its emphasis on band-pass activation that was not investigated in detail before. Furthermore, there are a few studies comprising an information-theoretic analysis of calcium signaling, for instance Nakano and Liu, Keshelava *et al.* and Pahle *et al.* [149, 151, 173]. The presented analysis distinguishes itself from these publication by focusing on the application of information theory, i.e., channel capacity, for an analysis of frequency-decoding of calcium oscillations. Parts of this chapter, in particular Sections 4.2 to 4.9, were published in Schoch and Pahle (2019) [152].

4.1.2 Outside assistance

A first template for fast ODE simulations using dynamic loading of C-code into R was provided by Jonas Förster¹. A first template for using R's `optim` function to optimize model parameters was provided by Michael Gabel and Peter Kumberger². The employed rate law for cooperative protein activation was taken from [79].

¹Biological Information Processing Group at the BioQuant Center, Heidelberg University.

²Modelling Infection & Immunity Group at the BioQuant Center, Heidelberg University.

A first script for estimating channel capacity based on the Blahut-Arimoto algorithm [164, 165] was provided by Aarón Vásquez-Jiménez³. Conversion into C-code coupled to R as well as an optimization of the algorithm's performance were carried out by Jürgen Pahle, Martin Zauser and myself¹. A first template for fast stochastic simulations by means of Gillespie's Direct Method was provided by Jürgen Pahle [157].

³Centro de Investigación y de Estudios Avanzados del IPN (Cinvestav-IPN), Unidad Monterrey, Mexico.

4.2 The high-pass activation model

Previously, Goldbeter *et al.* presented a protein model capable of performing high-pass activation [56]. In the Goldbeter model, a frequency-decoding protein is regulated by a fixed deactivating force and an activating force which in turn is directly stimulated by calcium oscillations. For the following analysis of high-pass activation, I modified the model by Goldbeter *et al.* In particular, I substituted kinetic rate laws to allow for a cooperative activation of the activator by calcium as well as a cooperative conversion of the decoder by competent activator and deactivator molecules. The underlying model network structure was kept. Reaction rate laws are shown in Table 4.2. An overview of the model's network structure is given in Figure 4.1.

In order to analyze frequency-decoding, I defined a molecular communication channel, whereas the calcium oscillation period T (the reciprocal of the oscillation frequency) served as an input and the average concentration of the active decoder $\overline{\text{Pr}}$ served as an output. To this end, the average concentration of the active decoder protein can be interpreted as a proxy of its average activity. Its use is a common practice in the analysis of frequency-decoding (see for instance [56, 79]).

$$\overline{\text{Pr}}(T) = \frac{1}{t} \cdot \int_0^t \text{Pr}(T) dt, \quad (4.1)$$

in which $\overline{\text{Pr}}$ and Pr are functions of the calcium oscillation period T .

In simulations, $\overline{\text{Pr}}$ approached convergence upon increasing the observed time window $\{0; t\}$. Thus, only after the passing of several calcium oscillation cycles, $\overline{\text{Pr}}$ ceased to alter significantly. I paid close attention to t being large enough to retrieve a quasi-converged value of $\overline{\text{Pr}}$.

Upon stimulating the high-pass model with various oscillation periods, it was revealed that the model was able to perform high-pass activation. For very fast calcium oscillations, the decoder

Tab. 4.2. Overview of the high-pass model's structure and kinetics.

Reactions	Kinetics
$\text{Act}_i \xrightarrow{\text{Ca}} \text{Act}$	$v_{H1} = \frac{k_{A1} \cdot \text{Act}_i \cdot \text{Ca}^a}{K_A^a + \text{Ca}^a}$
$\text{Act} \rightarrow \text{Act}_i$	$v_{H2} = k_{A2} \cdot \text{Act}$
$\text{Pr}_i \xrightarrow{\text{Act}} \text{Pr}$	$v_{H3} = \frac{k_{P1} \cdot \text{Pr}_i \cdot \text{Act}^{p1}}{K_{P1}^{p1} + \text{Act}^{p1}}$
$\text{Pr} \xrightarrow{\text{Deact}} \text{Pr}_i$	$v_{H4} = \frac{k_{P2} \cdot \text{Pr} \cdot \text{Deact}^{p2}}{K_{P2}^{p2} + \text{Deact}^{p2}}$

The cooperative binding of calcium ions Ca to the inactive activator Act_i results in the formation of competent activator Act . In turn, Act is able to activate the frequency-decoding protein Pr . A constant deactivating force Deact counteracts Pr 's activation. By default, Deact is fixed to 5000 nM and Ca is defined as a sine wave oscillating between 200 nM and 1000 nM. The index i refers to inactive counterparts of molecular species. k -parameters refer to rate constants, while K -parameters refer to binding constants. a , p_1 and p_2 represent cooperativity coefficients.

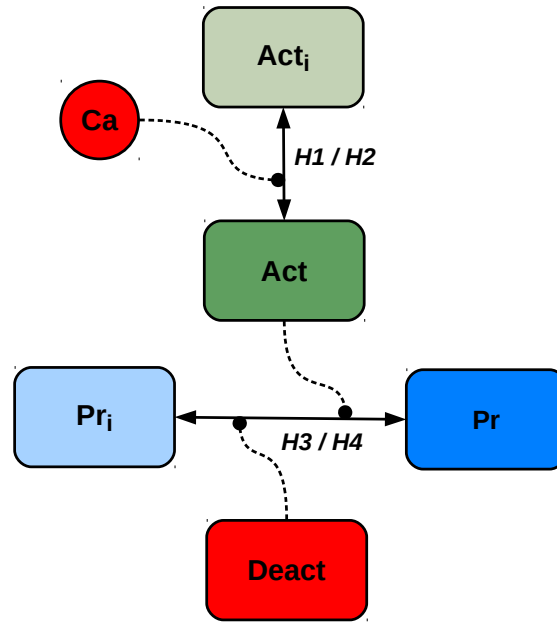


Fig. 4.1. Overview of the high-pass model's network structure. Act_i is activated by the binding of calcium ions Ca . In turn, competent Act can then activate the inactive decoder protein Pr_i . A fixed deactivating force $Deact$ returns the active decoder Pr to its inactive conformation Pr_i . Round-shaped arrowheads with dashed lines refer to activation events. Reaction names refer to the kinetic rate laws presented in Table 4.2.

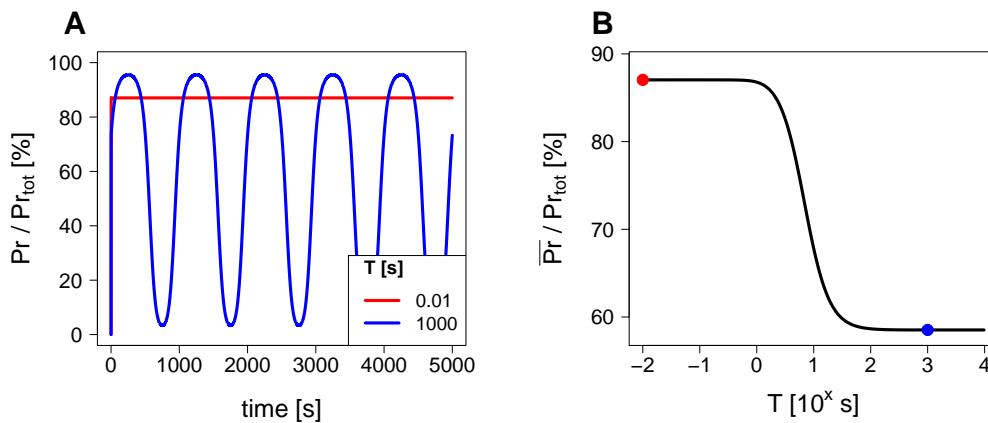


Fig. 4.2. Frequency-decoding in the high-pass model. (A) A stimulation with very fast sine waves ($T = 0.01$ s) resulted in an accumulation of Pr (red line). Slower input oscillations ($T = 1000$ s) led to oscillations in Pr levels (blue line). (B) By computing \overline{Pr} (Equation 4.1), high-pass activation of the decoder protein became apparent. Color-coded points refer to the time courses shown in the left panel. Information about the applied parameter set can be found in the appendix in Table A.3. I defined input sine waves to oscillate between a baseline level of 200 nM and a peak level of 1000 nM. Pr_{tot} refers to the total amount of decoder, i.e., the sum of Pr_i and Pr which I set to 5000 nM by default.

protein Pr could only integrate the upstream signal. In consequence, the concentration of Pr increased to a plateau level (Figure 4.2 A, red line). In contrast, for slower calcium oscillations, the average concentration of the active decoder decreased, since the decoder was now able

to closely follow the upstream oscillation dynamics. Therefore, P_r fell below the previously described plateau level for a large fraction of the observed time window (Figure 4.2 A, blue line).

A computation of the output measure $\overline{P_r}$ according to Equation 4.1, confirmed distinct frequency-decoding. The decoder's average activity dropped from a maximum at 87 % to a minimum at 59 % upon increasing the calcium oscillation period T (Figure 4.2 B), whereas percentage values refer to the average concentration of $\overline{P_r}$ in the observed time window to the total concentration of decoder molecules (the sum of P_{r_i} and P_r).

Importantly, the high-pass model cannot perform high-pass activation for all possible combinations of parameter values. The system has to be sensitive to changes in the calcium oscillation frequency. Information on the applied parameter set can be found in the appendix in Table A.3. More information on parameterization criteria for distinct high-pass activation can be found in Sections 4.8 and 4.9.

4.3 The band-pass activation model

Based on observations in Section 4.2, I concluded that band-pass activation can be achieved in case the decoder protein is regulated by a calcium-dependent activator as well as a calcium-dependent deactivator. Assuming the activator is less responsive and has a weaker control on the decoder compared to the deactivator, I expected the following behavior: For fast oscillations, neither one of the regulators are able to follow the rapid calcium oscillations. In consequence, both active regulators rise to a plateau level, as previously observed in Figure 4.2 A (red line). Since the deactivator has a stronger control on the decoder, the decoder's activity declines. When iteratively decreasing the oscillation period, the more responsive deactivator is the first to oscillate, while the less responsive activator remains close to its plateau level. Therefore, the activator is able to compensate for its lesser control on the decoder, since it is on average more abundant than the deactivator. As a result, the decoder's activity increases for intermediate oscillations. However, for slower oscillations, both of the regulators are expected to heavily oscillate and the previously observed concentration advantage in favor of the activator is abolished. Due to the deactivator's stronger control on the decoder, the deactivator's dominance is restored and, consequentially, the decoder's activity is decreased once again.

According to this blueprint, I extended the high-pass model to build the band-pass model, as presented in Table 4.3 and in Figure 4.3. The deactivator Deact was now modeled as a variable. Like the activator Act, Deact was activated by the cooperative binding of calcium ions. Upon applying a standard parameter set in which Act was less responsive and weaker in the control of Pr in comparison to Deact, I could recreate band-pass activation, as shown in Figure 4.4 (information about the applied parameter set can be found in the appendix in

Tab. 4.3. Overview of the band-pass model's structure and kinetics.

Reactions	Kinetics
$\text{Act}_i \xrightarrow{\text{Ca}} \text{Act}$	$v_{B1} = \frac{k_{A1} \cdot \text{Act}_i \cdot \text{Ca}^a}{K_A^a + \text{Ca}^a}$
$\text{Act} \rightarrow \text{Act}_i$	$v_{B2} = k_{A2} \cdot \text{Act}$
$\text{Deact}_i \xrightarrow{\text{Ca}} \text{Deact}$	$v_{B3} = \frac{k_{D1} \cdot \text{Deact}_i \cdot \text{Ca}^d}{K_D^d + \text{Ca}^d}$
$\text{Deact} \rightarrow \text{Deact}_i$	$v_{B4} = k_{D2} \cdot \text{Deact}$
$\text{Pr}_i \xrightarrow{\text{Act}} \text{Pr}$	$v_{B5} = \frac{k_{P1} \cdot \text{Pr}_i \cdot \text{Act}^{p1}}{K_{P1}^{p1} + \text{Act}^{p1}}$
$\text{Pr} \xrightarrow{\text{Deact}} \text{Pr}_i$	$v_{B6} = \frac{k_{P2} \cdot \text{Pr} \cdot \text{Deact}^{p2}}{K_{P2}^{p2} + \text{Deact}^{p2}}$

The cooperative binding of calcium ions Ca to inactive activator Act_i and inactive deactivator Deact_i leads to the formation of competent activator Act and competent deactivator Deact. The competent regulators control the conversion of the decoder protein Pr. By default, Ca is defined as a sine wave oscillating between 200 nM and 1000 nM. The index *i* refers to inactive counterparts of molecular species. *k*-parameters refer to rate constants, while *K*-parameters refer to binding constants. *a*, *d*, *p*₁ and *p*₂ represent cooperativity coefficients.

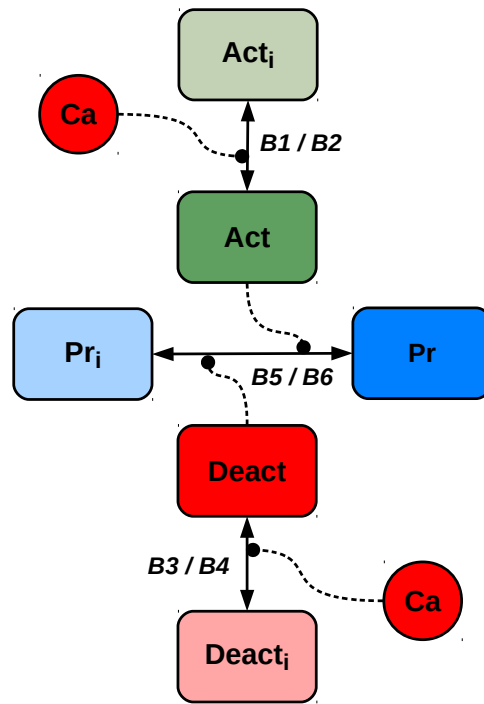


Fig. 4.3. Overview of the band-pass model's network structure. Inactive activator Act_i and inactive deactivator $Deact_i$ are activated by the binding of calcium ions Ca . Competent regulators Act and $Deact$ can activate and deactivate the decoder protein Pr . Round-shaped arrowheads with dashed lines refer to activation events. Reaction names refer to the kinetics presented in Table 4.3.

Table A.5). For fast oscillation, Pr only integrated the upstream calcium dynamics and rose to a low-level plateau (Figure 4.4 G). Pr was suppressed, since the deactivator $Deact$ was about as abundant as the activator Act , but $Deact$ had a stronger control on Pr (Figure 4.4 A and D). For slow calcium oscillations, Pr responded with dampened oscillations of its own. On average, Pr was as abundant as in response to fast calcium oscillations (Figure 4.4 I). Again, Act and $Deact$ were available in similar abundances and Pr was suppressed due to $Deact$'s stronger control (Figure 4.4 C and F). Only the application of intermediate oscillations caused Pr to exhibit high-amplitude oscillations of its own (Figure 4.4 H) leading to a rise in Pr 's average activity. As expected, this was induced by an on average more abundant Act compared to $Deact$ (Figure 4.4 B and E).

A model sharing the presented network structure, i.e., a decoder protein controlled by an oscillator-dependent activator-deactivator couple that is able to perform band-pass activation, was developed independently by Aguilera *et al.* [48]. The kinetics of the model presented in Table 4.3 distinguish themselves from the model by Aguilera *et al.* only with regards to the cooperative binding of activator and deactivator molecules to the decoder Pr . Further, I employed the presented band-pass model for a different research question, i.e., an analysis of the requirements for distinct band-pass activation.

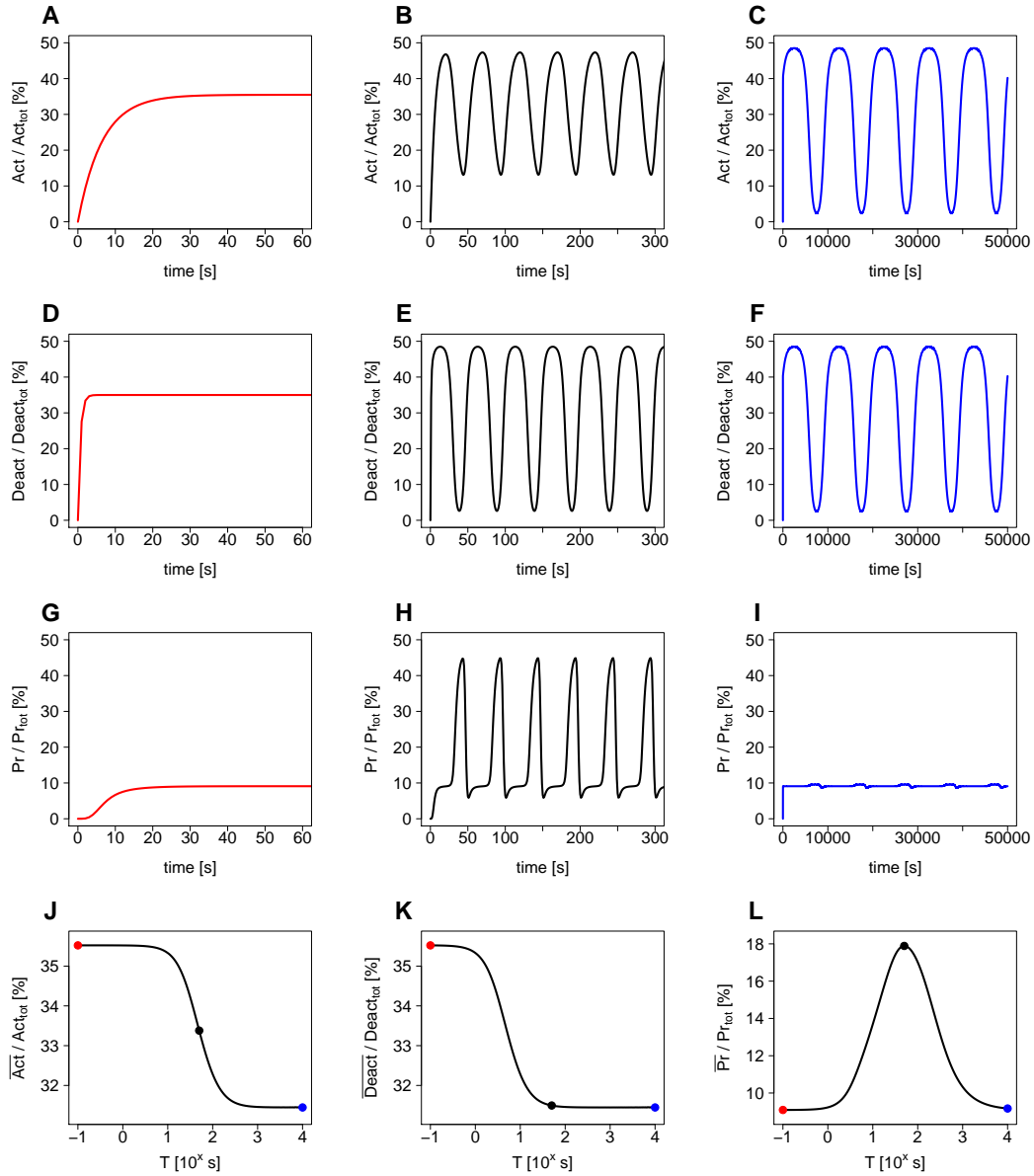


Fig. 4.4. Frequency-decoding in the band-pass model. To obtain the presented results, I stimulated the band-pass model with fast ($T = 0.1$ s) (A, D, G), intermediately fast ($T = 50$ s) (B, E, H) and slow ($T = 10000$ s) calcium sine waves (C, F, I). \bar{Pr} was maximal after a stimulation with intermediately fast oscillations (L). This effect was accomplished by an on average higher abundance of Act compared to Deact (J, K). Color-coded points in the bottom row refer to the calcium oscillation periods used in the simulations in the panels above. All applied calcium sine waves exhibited baseline and peak levels of 200 nM and 1000 nM, respectively. The applied model parameters are listed in the appendix in Table A.5.

4.4 A framework for maximizing frequency-decoding efficiencies

In the following sections, I probed for high-pass and band-pass activation given particular conditions in models of calcium-dependent protein activation. To this end, I ran optimizations to maximize frequency-decoding efficiencies, i.e., the distinctness of either high-pass or band-pass activation. In doing so, I could test whether certain conditions, i.e., particular model network structures or a particular parameterization of non-optimizable parameters, benefited the frequency-decoding distinctness in high-pass or band-pass activation.

First, I defined mathematical notations for high-pass and band-pass activation efficiencies. In terms of high-pass activation, I described the corresponding high-pass activation efficiency Eff_H as the difference between \overline{Pr} in response to fast oscillations and \overline{Pr} in response to slow oscillations (Figure 4.5 A; definition of \overline{Pr} according to Equation 4.1):

$$Eff_H := \overline{Pr}(T_{fast}) - \overline{Pr}(T_{slow}) \quad (4.2)$$

By default, I set the calcium oscillation periods T_{fast} and T_{slow} to 0.1 s and 1000 s. Any deviation from these default values are explicitly mentioned in the text.

By optimizing Eff_H over a subset of a model's parameters Θ_H , the high-pass activation potential E_H , i.e., the maximal high-pass activation efficiency, can be returned:

$$E_H := \max_{\Theta_H} \{Eff_H(\Theta_H)\} \quad (4.3)$$

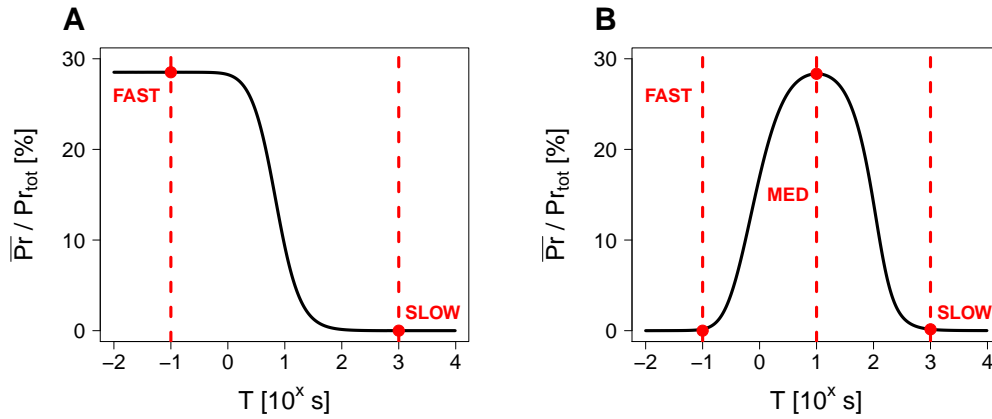


Fig. 4.5. Definition of decoding efficiencies in high-pass and band-pass activation. (A) For high-pass activation, I defined the decoding efficiency Eff_H to be equal to \overline{Pr} given a fast oscillation input minus \overline{Pr} given a slow oscillation input. (B) For band-pass activation, I defined the efficiency Eff_B to be equal to the difference in \overline{Pr} at an intermediate oscillation period and the maximum of \overline{Pr} at a fast and a slow oscillation period (both being smaller than the former). Red dashed lines refer to the default period lengths employed for the optimization algorithms (T_{fast} , T_{med} and T_{slow}). Red points refer to the corresponding \overline{Pr} -values applicable for the quantification of high-pass and band-pass activation efficiencies.

In terms of band-pass activation, I defined the corresponding band-pass activation efficiency Eff_B as the difference between \overline{Pr} in response to an intermediate oscillation $\overline{Pr}(T_{med})$ and the maximum of $\overline{Pr}(T_{fast})$ and $\overline{Pr}(T_{slow})$, both being smaller than $\overline{Pr}(T_{med})$ (Figure 4.5 B):

$$Eff_B := \overline{Pr}(T_{med}) - \max\left(\overline{Pr}(T_{slow}), \overline{Pr}(T_{fast})\right), \quad (4.4)$$

with T_{med} being set to 1 s by default.

By maximizing Eff_B over a subset of a model's parameters Θ_B , the band-pass activation potential E_B can be returned:

$$E_B := \max_{\Theta_B} \{Eff_B(\Theta_B)\} \quad (4.5)$$

Therefore, when maximizing the band-pass activation efficiency, \overline{Pr} is maximized at an intermediate oscillation period T_{med} , while it is minimized at faster and slower oscillation periods T_{fast} and T_{slow} .

In contrast to rate and binding constants, I did not optimize cooperativity coefficients but instead set them to fixed values. Further, I also set the total concentrations of model species, i.e., the sum of active and inactive counterparts, to a constant value of 5000 nM by default. To this end, I set initial concentration values of model species to the corresponding steady state values for a constant calcium input of 600 nM that is the mean concentration of the actually applied calcium sine waves oscillating between 200 nM and 1000 nM. By starting off from these steady states, I observed a significant reduction in the transient phase. Since the transient phase extends the time needed for \overline{Pr} to reach convergence, its reduction was wanted.

I calculated steady states according to the following equations:

$$Act_{ss} = \frac{k_{A1} \cdot Act_{tot} \cdot Ca^a}{k_{A2} \cdot K_A^a + k_{A2} \cdot Ca^a + k_{A1} \cdot Ca^a} \quad (4.6)$$

$$Pr_{ss} = \frac{k_{P1} \cdot Pr_{tot} \cdot \overline{Act}^{p1}}{k_{P1} \cdot \overline{Act}^{p1} + \frac{k_{P2} \cdot \overline{Deact}^{p2} \cdot (K_{P1}^{p1} + \overline{Act}^{p1})}{K_{P2}^{p2} + \overline{Deact}^{p2}}} \quad (4.7)$$

In contrast to the high-pass model, in the band-pass model, also the deactivator $Deact$ is a variable. $Deact$'s steady state was computed according to:

$$Deact_{ss} = \frac{k_{D1} \cdot Deact_{tot} \cdot Ca^d}{k_{D2} \cdot K_D^d + k_{D2} \cdot Ca^d + k_{D1} \cdot Ca^d} \quad (4.8)$$

4.5 Testing for basic frequency-decoding functionalities

In this section, I employed maximizations of frequency-decoding efficiencies to probe for the possibility of different forms of frequency-decoding in the simple kinetic protein models presented in Sections 4.2 and 4.3. I already demonstrated that the high-pass model was able to perform high-pass activation (see Figure 4.2) and that the band-pass model was able to perform band-pass activation (see Figure 4.4). It remained open whether the models were also able to perform other forms of frequency-decoding. In addition to high-pass and band-pass activation, I also tested for low-pass activation, with the low-pass activation efficiency Eff_L being defined as:

$$Eff_L := \overline{\Pr}(T_{slow}) - \overline{\Pr}(T_{fast}) \quad (4.9)$$

and the corresponding low-pass activation potential E_L being defined as:

$$E_L := \max_{\Theta_L} \{Eff_L(\Theta_L)\}, \quad (4.10)$$

where Θ_L is the subset of a model's parameters selected for optimization.

Any attempt to induce low-pass or band-pass activation in the high-pass model by means of maximizations of the corresponding frequency-decoding efficiencies according to Equations 4.3 or 4.10 remained unsuccessful (Figure 4.6 A). In contrast, the band-pass model was capable of recreating all three forms of frequency-decoding (Figure 4.6 B).

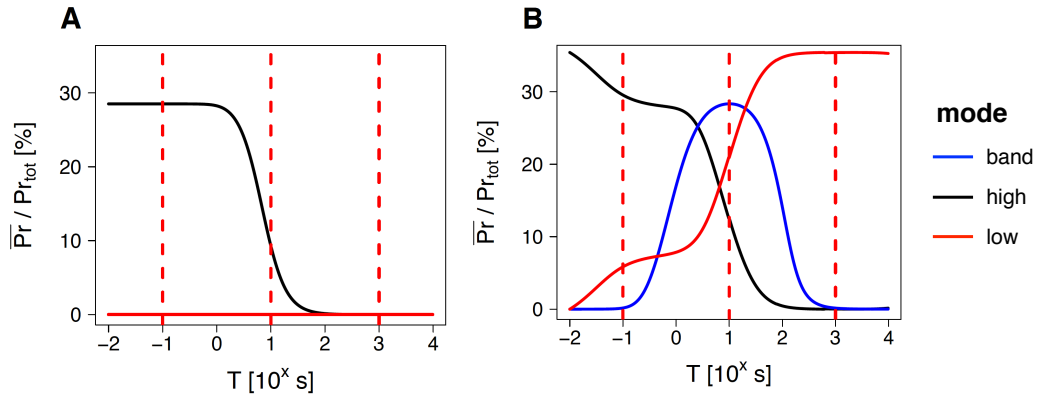


Fig. 4.6. Recreation of different forms of frequency-decoding in the high-pass and band-pass model. I optimized rate and binding constants of either the high-pass or band-pass model for a maximization of Eff_H , Eff_B or Eff_L . Next, I used the optimized parameter sets to compute the presented results. To this end, I scanned the calcium oscillation period T and measured $\overline{\Pr}$, the average activity of the decoder protein. (A) The high-pass model was only capable of performing high-pass activation. Low- and band-pass activation could not be recreated (overlapping lines at 0 %). (B) The band-pass model was capable of recreating all three forms of frequency-decoding. I scaled the minimal concentration of each curve to 0 % to allow for a better comparison. For the optimizations, I employed default values of T_{fast} , T_{med} and T_{slow} that are marked by red dashed lines. All optimized parameter sets are provided in the appendix in Tables A.1 and A.2.

4.6 Band-pass activation of the transcription factor NFAT

4.6.1 The NFAT model

Previously, in Section 4.3, I presented a protein model that was capable of performing band-pass activation. As suggested in [62], the ability to perform band-pass activation seemed to be linked to an antagonistic, oscillator-dependent regulation of the decoder protein (see also Section 4.5). Here, I extended the band-pass model to construct a model particularly for the calcium-dependent activation of NFAT. Subsequently, I probed for the possibility of band-pass activation in this NFAT model.

According to experimental data, the transcription factor NFAT exhibits a peak activity in case cells are stimulated by calcium oscillations of a particular frequency, whereas calcium

Tab. 4.4. The NFAT model's structure and kinetics.

Reaction	Kinetics
$\text{CaMKII} \xrightarrow{\text{Ca}} \text{CaMKII}^*$	$v_{N1} = \frac{k_{N1} \cdot \text{CaMKII} \cdot \text{Ca}^m}{K_{N1}^m + \text{Ca}^m}$
$\text{CaMKII}^* \rightarrow \text{CaMKII}$	$v_{N2} = k_{N2} \cdot \text{CaMKII}^*$
$\text{Cn} \xrightarrow{\text{Ca}} \text{Cn}^*$	$v_{N3} = \frac{k_{N3} \cdot \text{Cn} \cdot \text{Ca}^n}{K_{N2}^n + \text{Ca}^n}$
$\text{Cn}^* \rightarrow \text{Cn}$	$v_{N4} = k_{N4} \cdot \text{Cn}^*$
$\text{Cn} \xrightarrow{\text{CaMKII}^*} \text{CnP}$	$v_{N5} = k_{N5} \cdot \text{CaMKII}^* \cdot \text{Cn}$
$\text{CnP} \rightarrow \text{Cn}$	$v_{N6} = k_{N6} \cdot \text{CnP}$
$\text{CnP} \xrightarrow{\text{Ca}} \text{CnP}^*$	$v_{N7} = \frac{k_{N3} \cdot \text{CnP} \cdot \text{Ca}^n}{K_{N2}^n + \text{Ca}^n}$
$\text{CnP}^* \rightarrow \text{CnP}$	$v_{N8} = k_{N4} \cdot \text{CnP}^*$
$\text{Cn}^* + \text{NFAT} \rightarrow \text{NFAT} : \text{Cn}^*$	$v_{N9} = k_{N7} \cdot \text{Cn}^* \cdot \text{NFAT}$
$\text{NFAT} : \text{Cn}^* \rightarrow \text{Cn}^* + \text{NFAT}$	$v_{N10} = k_{N8} \cdot \text{NFAT} : \text{Cn}^*$
$\text{CnP}^* + \text{NFAT} \rightarrow \text{NFAT} : \text{CnP}^*$	$v_{N11} = \frac{k_{N7} \cdot \text{CnP}^* \cdot \text{NFAT}}{\delta}$
$\text{NFAT} : \text{CnP}^* \rightarrow \text{CnP}^* + \text{NFAT}$	$v_{N12} = k_{N8} \cdot \text{NFAT} : \text{CnP}^*$

Calcineurin (Cn) is activated by the cooperative binding of calcium, Ca. Cn can also change to a phosphorylated form CnP. To this end, the phosphorylation is carried out by calcium-bound Ca^{2+} /calmodulin-dependent protein kinase II (CaMKII*). After binding of Ca, CnP* as well as Cn* are able to form active complexes with NFAT, however, CnP*'s activity is reduced, as modeled by the introduction of δ . δ is defined to be always larger than 1. k -parameters refer to rate constants, K -parameters to binding constants. m and n represent cooperativity coefficients.

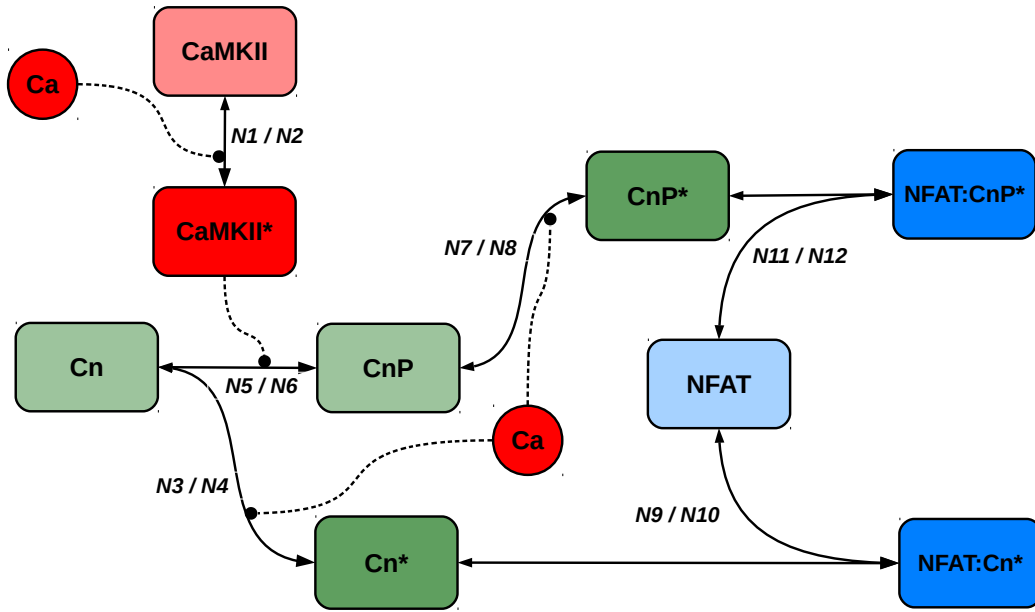


Fig. 4.7. Overview of the NFAT model's network structure. CaMKII and Cn are activated by Ca. Active CaMKII* can convert inactive Cn to the phosphorylated form CnP. After binding of calcium ions, CnP* as well as Cn* are able to form active complexes with NFAT. The ability of CnP* to form an active NFAT complex is reduced compared to Cn*'s. Thus, CaMKII* inhibits the creation of active NFAT complexes by fostering the production of less potent variants of calcineurin, CnP*. Round-shaped arrowheads with dashed lines refer to activation events. Reaction names refer to the kinetics presented in Table 4.4.

frequencies slower or faster than this optimal frequency only lead to a reduced activity. This was observed in RBL-2H3 cells [64]. More commonly, a decline in NFAT activity was detected for increasingly slow calcium oscillations (in Jurkat cells from 10 mHz downwards [63], in BHK and again Jurkat cells from 11 mHz downwards [174] and in rat neonatal cardiomyocytes from 83 mHz downwards [175]), while a decrease in activity was found in cardiac cells upon stimulation with increasingly fast calcium oscillations (from 20 mHz upwards) [176] providing additional evidence for a band-pass activation mechanism. For a review that comprises these reports, please refer to [62].

NFAT exhibits the necessary premises for the previously described band-pass activation mechanism that appeared to be linked to an antagonistic, oscillator-dependent control (see Sections 4.3 and 4.5). In particular, NFAT's transcriptional activity is positively regulated by the calcium-dependent phosphatase calcineurin [177] and negatively regulated by the calcium-dependent kinase CaMKII [178, 179]. To this end, NFAT is largely existent in its inactive, phosphorylated form in the cytosol of a resting cell. In the presence of calcium oscillations, the activity of the calcium-dependent phosphatase calcineurin is increased. Subsequent dephosphorylations of NFAT, that are mediated by active calcineurin, result in conformational changes allowing for NFAT's transportation into the nucleus by uncovering nuclear localization sequences [180]. NFAT's presence in the nucleus is countered by direct phosphorylations causing the transcription factor's export out of the nucleus, for instance by glycogen synthase kinase 3 (GSK-3) [181], or by blocking its import into the nucleus in the first place, for instance by c-Jun N-terminal kinases (JNKs) and extracellular signal-regulated kinases (ERK) [182]. As mentioned before, there is also a calcium-dependent inhibition of NFAT activity that is

mediated by the calcium-dependent kinase CaMKII. CaMKII does not directly interact with NFAT. Instead CaMKII phosphorylates calcineurin, the calcium-dependent activator of NFAT, which in its phosphorylated form exhibits a decreased affinity for the transcription factor. As a result, dephosphorylation and import of NFAT into the nucleus are impaired [178, 179]. After the binding of calcium to calcineurin, a phosphorylation of calcineurin is improbable due to allosteric constraints. However, calcium binding to phosphorylated calcineurin remains possible [179]. Based on these information, I designed a kinetic model that comprised a calcium-dependent, antagonistic regulation of NFAT by calcineurin and CaMKII in the cytosol. I assumed that the calcium oscillation frequency determines, whether calcium-dependent kinases or phosphatases are dominant, as previously discussed in [62, 75]. Importantly, the model was not built for a quantitative analysis, but first and foremost to probe for the possibility of band-pass activation of the transcription factor NFAT.

In the model, calcium-dependent regulator proteins are cooperatively activated by calcium ions Ca. Activated CaMKII* is able to induce the phosphorylation of inactive Cn which leads to the production of the phosphorylated calcineurin form CnP. Calcium-bound CnP* as well as Cn* can mediate a dephosphorylation of inactive NFAT forming active NFAT compounds ready for a transportation into the nucleus. I modeled a decreased activity of CnP* compared to Cn* by introducing the inhibition factor δ . For δ larger than 1, NFAT's activation by means of CnP* is slower compared to its activation by means of Cn*. I considered both active NFAT compounds, NFAT : CnP* and NFAT : Cn*, as equally potent (Table 4.4 and Figure 4.7). Thus, I defined the sum of the average activities $\overline{\text{NFAT} : \text{CnP}^*}$ and $\overline{\text{NFAT} : \text{Cn}^*}$ as the model output $\overline{\text{NFAT}^*}$:

$$\overline{\text{NFAT}^*} := \overline{\text{NFAT} : \text{CnP}^*} + \overline{\text{NFAT} : \text{Cn}^*} \quad (4.11)$$

4.6.2 Definition of an objective function for an optimization of the NFAT model

In the following, I optimized the NFAT model (Table 4.4) in order to recreate experimentally observed frequency-decoding behavior. In particular, I aimed at recreating the band-pass activation of NFAT, while, at the same time, fitting the model output to experimental data by Dolmetsch *et al.*. Dolmetsch *et al.* quantified the frequency-dependent gene expression mediated by NFAT [63]. With respect to the recreation of band-pass activation, I defined the optimal frequency for maximal NFAT activity T_{med} to be equal to 60 mHz, as reported in [62, 64].

Dolmetsch *et al.* employed Jurkat cells to measure the effect of modulations in the calcium oscillation frequency on the expression of an NFAT/*lacZ* reporter gene. By rapidly washing store-depleted cells with a high-concentration calcium solution and a calcium-free solution in an alternating manner, they could induce cytosolic calcium oscillations with a "uniform frequency" and an amplitude "that [was] relatively constant" [63]. Importantly, Dolmetsch *et al.*'s data (presented in Figure 3b in [63]) refers to gene expression, while the model output refers to the average active transcription factor concentration in the cytosol. Therefore, I only

performed a qualitative fit assuming a simple linear relationship between both measures. In consequence, I employed a scaling factor β as well as an offset factor γ :

$$\rho = (A_{data} - (A_{NFAT} \cdot \beta + \gamma))^2 + (B_{data} - (B_{NFAT} \cdot \beta + \gamma))^2 + (C_{data} - (C_{NFAT} \cdot \beta + \gamma))^2 + (D_{data} - (D_{NFAT} \cdot \beta + \gamma))^2, \quad (4.12)$$

with A_{data} to D_{data} referring to the experimental frequency-dependent measurements of NFAT-mediated gene expression as presented in Figure 3b in [63] and A_{NFAT} to D_{NFAT} referring to the model output in response to the same calcium oscillation frequencies (model output as described in Equation 4.11).

In simulations, I defined calcium oscillations as square-waves, since these shapes closely resembled the oscillations employed by Dolmetsch *et al.* To this end, I set baseline and peak levels of the square-waves to 100 nM and 1000 nM. Upon changes in the square-wave oscillation period, only the duration of the inactive baseline phase was varied, while I maintained the active peak phase duration of 10 s, as previously shown for a similar fit to the same experimental dataset in Fisher *et al.* [183].

In order to achieve band-pass activation, I maximized the NFAT model's band-pass activation efficiency Eff_B according to Equation 4.4, with $T_{fast} = 25$ s, $T_{med} = 60$ s and, by default, $T_{slow} = 500$ s. Again, I employed square-wave inputs for stimulating the model. This time I set the active phase to 20 s. I chose T_{med} as well as the active phase duration in reference to information provided in [62, 64].

I generated all input time series of the square-wave oscillations by means of the *Oscillator-Generator* package (see Section 3.1). Details about the parameterization of the employed square-waves can be found in the appendix in Section A.2.1.

The objective function Ψ_{NFAT} links the least-squares function in Equation 4.12 to the maximization of Eff_B , as presented in Equation 4.5:

$$\Psi_{NFAT} = \max_{\Theta_{NFAT}} \left(Eff_B(\Theta_{NFAT}) + \frac{1}{\rho}(\Theta_{NFAT}) \right), \quad (4.13)$$

with $\Theta_{NFAT} = (k_{N1-8}, K_{N1-2}, m, n, \beta, \gamma, \delta)$.

4.6.3 Antagonistic, oscillator-dependent regulation enables band-pass activation of NFAT

In this section, I optimized the original NFAT model (Table 4.4) as well as two truncated versions according to Equation 4.13. Truncated versions differed from the original model in exhibiting either no CaMKII-mediated inhibition (only reactions $N3$ to $N4$ and $N9$ to $N10$ applied) or a constant, calcium-independent CaMKII-mediated inhibition (removal of reactions $N1$ to $N2$). For the latter, I introduced a constant concentration value of CaMKII* that I optimized as well.

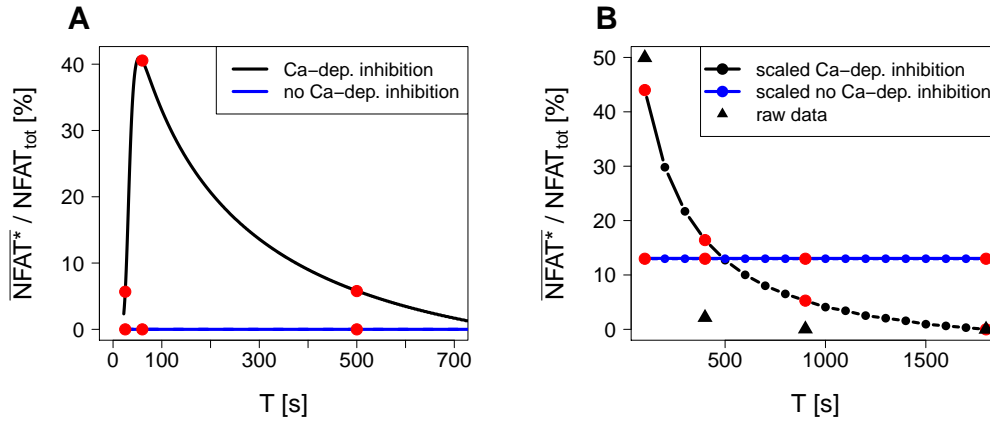


Fig. 4.8. Frequency-decoding in optimized versions of the NFAT model. I conducted optimizations of different versions of the NFAT model according to Ψ_{NFAT} (Equation 4.13) in order to induce band-pass activation as well as to perform a qualitative fit to gene expression data from Dolmetsch *et al.* [63]. In particular, I optimized the original NFAT model (Table 4.4) as well as model versions lacking an antagonistic, oscillator-dependent regulation of NFAT. (A) Only when employing the original model version with antagonistic, oscillator-dependent regulation of the transcription factor, I could recreate band-pass activation. Red points mark the model output \overline{NFAT}^* given period lengths used in the optimization algorithm ($T_{fast} = 25$ s, $T_{med} = 60$ s, $T_{slow} = 500$ s). I scaled each curve's minimal value to 0 %. (B) By means of optimizations, I also performed qualitative fits of the model output to gene expression data presented in Figure 3b in [63]. Only the default model's transformed output (i.e., data points times β plus γ) showed a resemblance to the original dataset. Red points mark model output values in response to calcium oscillations exhibiting period lengths used in the optimization algorithm. Corresponding period lengths were identical to those employed in [63] (100 s, 400 s, 900 s and 1800 s). Black triangles refer to the original gene expression data. All optimized parameters can be found in the appendix (Section A.2.2, Tables A.21 to A.23).

When employing the original version of the NFAT model exhibiting antagonistic, oscillator-dependent regulation, I could recreate band-pass activation over a physiological bandwidth. Furthermore, with the same optimized parameter set, a resemblance to gene expression data from Dolmetsch *et al.* was recognizable [63] (Figure 4.8, black lines). In contrast, the truncated model versions without antagonistic, oscillator-dependent control failed in reproducing band-pass activation as well as in showing a resemblance to experimental gene expression data. In Figure 4.8, the simulation results of the truncated model versions were almost identical (overlapping blue lines). In conclusion, the NFAT model was able to perform band-pass activation over a physiological bandwidth in case NFAT was regulated in an antagonistic, oscillator-dependent manner.

4.6.4 Effect of variations in T_{slow} on optimization results

In Section 4.6.3, I optimized different versions of the NFAT model with $T_{fast} = 25$ s, $T_{med} = 60$ s and $T_{slow} = 500$ s (parameters refer to Equations 4.4 and 4.5). While I chose T_{med} , the optimal oscillation period associated with a maximal NFAT activity, in reference to an experimental report [64], there were only limited options for a parameterization of T_{fast} , since T_{fast} had to be smaller than T_{med} but larger than the constant active phase duration of 20 s. In contrast, there was a wide range of possibilities for the parameterization of T_{slow} .

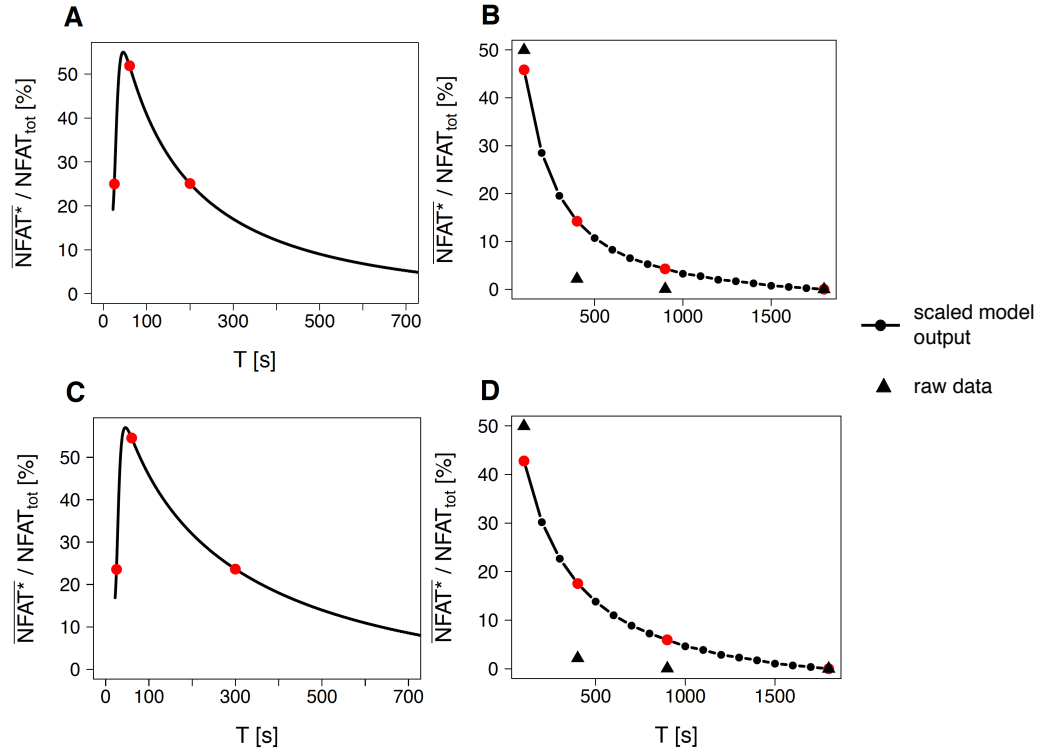


Fig. 4.9. Frequency-decoding in the original NFAT model with alternative parameterizations of T_{slow} . Here, I optimized the original NFAT model (Table 4.4) according to Ψ_{NFAT} (Equation 4.13) in order to generate band-pass activation as well as to perform a qualitative fit to gene expression data from Dolmetsch *et al.* [63]. In the optimizations, T_{slow} was either set to 200 s (A and B) or to 300 s (C and D). For both tested parameterizations of T_{slow} , optimized models exhibited a reduced band-pass activation potential E_B compared to the model optimized with $T_{slow} = 500$ s (Figure 4.8). Further, calcium oscillations exhibiting a period length of T_{med} did no longer lead to maximal NFAT activity (A and C). Red points mark \overline{NFAT}^* in response to calcium oscillations exhibiting period lengths used in the optimization algorithm (T_{fast} , T_{med} and T_{slow}). Optimizations also included a qualitative fit of the NFAT model to gene expression data presented in Figure 3b in [63] (B). Here, a smaller parameterization of T_{slow} resulted in a steeper decline in NFAT* for increasingly slow calcium oscillations. As a consequence, the model output resembled the gene expression data from Dolmetsch *et al.* more closely. Red points mark model output values in response to periods lengths used in the optimization algorithm. Corresponding period lengths were identical to those employed in [63] (100 s, 400 s, 900 s and 1800 s). Black triangles refer to the original gene expression data points. All optimized parameter sets can be found in the appendix (Section A.2.2, Tables A.24 and A.25).

I found that a decrease in T_{slow} from its default parameterization of 500 s led to a closer resemblance of the model output to gene expression data from Dolmetsch *et al.* However, this effect came at the expense of a reduced band-pass activation potential E_B . Further, T_{med} did not quite lead to maximal NFAT activity (for $T_{slow} = 500$ s, $E_B = 35\%$; for $T_{slow} = 300$ s, $E_B = 31\%$; for $T_{slow} = 200$ s, $E_B = 27\%$) (Figure 4.9).

4.7 The importance of being cooperative in frequency-decoding

Several proteins bind calcium ions in a positive-cooperative manner (see Table 4.1 for a list of examples). Therefore, I implemented Hill kinetics in the high-pass and band-pass model describing the activation of the regulator species as well as the conversion of the decoder protein from its inactive to its active conformation and vice versa. The latter was motivated by the observation that, after calcium ions bind to calmodulin in a cooperative manner, also calmodulin-calcium complexes were found to cooperatively bind to substrate proteins [170, 171]. In this section, the aim was to analyze the relationship between cooperativity strength and frequency-decoding distinctness. While a corresponding link was previously reported (for instance in [76]), a quantitative analysis was still missing. By means of optimizations, I quantified the frequency-decoding potential, i.e., the maximal frequency-decoding efficiency, in protein models with a set parameterization of cooperativity coefficients. Upon changing the parameterization of cooperativity coefficients between optimizations, I could assess the resultant impact on the frequency-decoding potential.

For the high-pass activation model, I observed a clear rise in the high-pass activation potential E_H upon increases in the cooperativity coefficient a , as shown in Figures 4.10 A and 4.11 A (red line). Similarly, for the band-pass activation model, simultaneous increases in the cooperativity coefficients a and d resulted in a rise in the band-pass activation potential E_B (Figures 4.10 B and 4.11 B, black line). Also simultaneous increases in p_1 and p_2 led to a rise in E_B in the band-pass model (Figure 4.11 B, grey line). However, there was no increase in

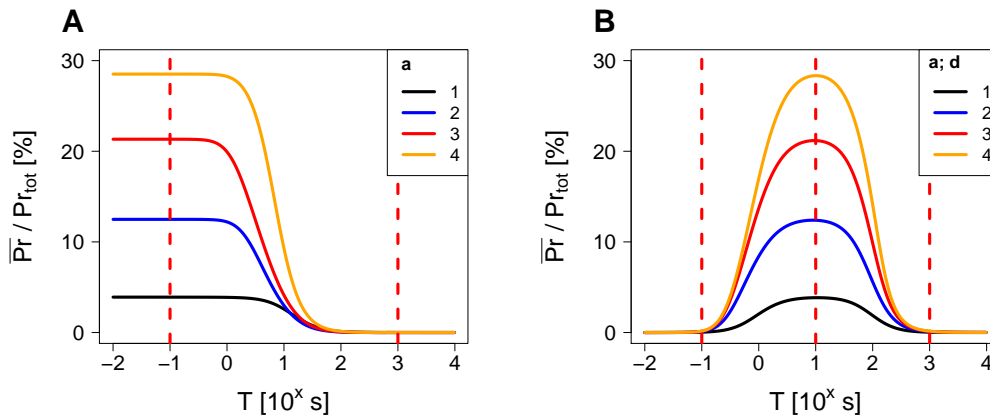


Fig. 4.10. Increases in cooperativity coefficients describing the binding of calcium to regulator species lead to a rise in frequency-decoding potentials. I optimized binding and rate constants in order to compute the high-pass activation potential E_H (Equation 4.3) in the high-pass model (Table 4.2) and the band-pass activation potential E_B (Equations 4.5) in the band-pass model (Table 4.3) given a set parameterization of cooperativity coefficients. (A) For high-pass activation in the high-pass model, an increase in a clearly increased the high-pass activation potential E_H . (B) For band-pass activation in the band-pass model, simultaneous increases in a and d led to a rise in the band-pass activation potential E_B . I scaled the minimal concentration of each curve to 0% to allow for a better comparison. Red dashed lines mark calcium oscillation periods used in the optimization algorithms (T_{fast} , T_{med} and T_{slow}). Optimized parameter sets are provided in the appendix in Tables A.3 and A.5.

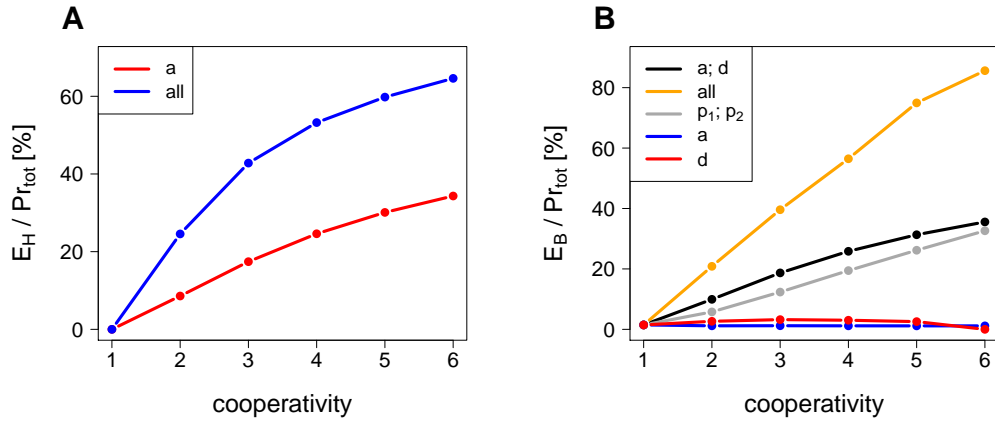


Fig. 4.11. High-pass and band-pass activation potentials for different parameterizations of cooperativity coefficients. I optimized binding and rate constants to maximize E_H (Equation 4.3) in the high-pass model (Table 4.2) and E_B (Equation 4.5) in the band-pass model (Table 4.3). **(A)** As already presented in Figure 4.10 A, increases in a led to a rise in E_H in the high-pass model (red line). E_H was raised even higher in case I simultaneously increased all of the high-pass model's cooperativity coefficients (a , p_1 and p_2) (blue line). **(B)** For band-pass activation in the band-pass model, simultaneous increases in the cooperativity coefficients of the deactivating and of the activating model branch led to a rise in E_B (orange, black and grey lines). Again, a concatenation of cooperative events was most effective (orange line, simultaneous increases in a , d , p_1 and p_2). When disrupting the balance between the activating and deactivating model branch by increasing only the cooperativity coefficients in either one of them, E_B was not raised (red and blue lines). I scaled the minimal concentration of each line to 0 % to allow for a better comparison. Optimized parameter sets are provided in the appendix in Tables A.3 to A.9.

E_B in case only a or only d was raised (Figure 4.11 B, red and blue lines). Hence, band-pass activation seemed to be the result of a balanced interplay between activating and deactivating forces.

For both, high-pass and band-pass activation, a concatenation of cooperative events, i.e., a cooperative activation succeeded by yet another cooperative activation, was found to be most effective in increasing the high-pass and band-pass activation potential (Figure 4.11 A, blue line and B, orange line).

4.8 Detecting conserved parameter margins for efficient frequency-decoding

4.8.1 Isolating the best parameter sets for particular optimization problems

For the optimizations used in Section 4.7, I employed the local Nelder-Mead algorithm [159]. In order to approximate a global solution, I conducted hundreds to thousands of local optimization runs for a particular optimization problem, with single runs differing from each other in the initial parameterization of optimizable parameters. As a consequence, I regularly found a multitude of parameter sets linked to objective values close to the overall best objective value per optimization problem.

I isolated these parameter sets and analyzed them for conserved parameterization characteristics that were crucial for inducing highly efficient high-pass or band-pass activation given a set parameterization of cooperativity coefficients. In particular, I isolated all parameter sets leading to objective values within a 2-nM-margin to an overall best objective value for a maximization of Eff_H in the high-pass model given several parameterizations of a and for a maximization of Eff_B in the band-pass model given several parameterizations of a and d . In Figure 4.12, I show that all of the isolated parameter sets truly induced the intended decoding behavior with very similar frequency-decoding efficiencies (in Figure 4.12 A $a = 4$ in the high-pass model, in B $a = d = 4$ in the band-pass model).

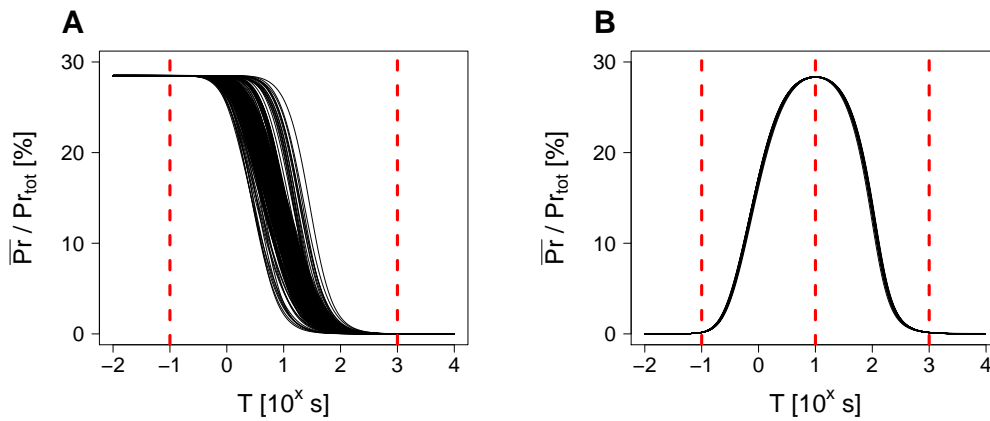


Fig. 4.12. Isolated parameter sets reliably induced efficient high-pass and band-pass activation. For the identification of parametric requirements for efficient high-pass and band-pass activation, I isolated optimized parameter sets associated with objective values within a 2-nM-margin to an overall best objective value per optimization problem. In particular, the optimizations targeted a maximization of Eff_H in the high-pass model or a maximization of Eff_B in the band-pass model given a set parameterization of cooperativity coefficients. Here, I demonstrate that, for a parameterization of $a = 4$ in the high-pass model (A) as well as of $a = d = 4$ in the band-pass model (B), all isolated parameter sets in the 2-nM-margin were clearly capable of efficient high-pass or band-pass activation. I scaled the minimal concentration of each line to 0% to allow for a better comparison. Red dashed lines mark calcium oscillation periods used in the optimization algorithms (T_{fast} , T_{med} and T_{slow}).

All of the analyzed parameter sets in this section are provided on the attached data medium. Further, all analyzed parameter sets were obtained by employing previously introduced objective functions (Equations 4.3 and 4.5) while applying default period lengths in the optimization algorithms ($T_{fast} = 0.1$ s, $T_{med} = 1$ s and $T_{slow} = 1000$ s).

4.8.2 Single parameter analysis

In the following, I analyzed parameter sets that induced efficient high-pass activation for different parameterizations of the cooperativity coefficient a in the high-pass model (Table 4.2) as well as efficient band-pass activation for different parameterizations of the cooperativity coefficients a and d in the band-pass model (Table 4.3).

By visualizing the high-pass model's parameter distributions, common characteristics of parameter sets capable of inducing efficient high-pass activation were revealed (Figure 4.13). With respect to the model's rate constants, k_{P2} was by far the most confined parameter, mostly ranging between 0.1 s^{-1} and 10 s^{-1} for all tested values of a (Figure 4.13 D). Also the activator's degradation rate k_{A2} was strongly confined for larger values of a (Figure 4.13 B). In contrast, the production rate constants k_{A1} and k_{P1} exhibited less confinements (Figure 4.13 A and C). In terms of the model's binding constants, most of them lay in a range spanning from 10^3 nM to 10^6 nM. Particularly, K_A appeared to be strongly confined to this margin. Further, K_A 's parameterization margin decreased upon increases in a , with mean values shifting from about $10^{5.5}$ nM for a equal to 1 to about $10^{3.75}$ nM for a equal to 6 (Figure 4.13 E). Also for the remaining two binding constants K_{P1} and K_{P2} , a minor drop in the mean values of the distributions was recognizable (Figure 4.13 F and G).

Similarly, parameter sets capable of efficient band-pass activation in the band-pass model exhibited some common characteristics (Figure 4.14). For one, the deactivation rate constants of the regulator species, k_{A2} and k_{D2} , both indicated severely confined margins for all tested parameterizations of a and d (Figure 4.14 B and D). The corresponding production rate constants k_{A1} and k_{D1} were found to exhibit much broader margins (Figure 4.14 A and C). Also k_{P1} 's and k_{P2} 's distributions ranged over broader margins (Figure 4.14 E and F). In terms of binding constants, once more a drop was recognizable upon increases in the model's cooperativity coefficients (Figure 4.14 G-J). Again, this drop was the most pronounced for binding constants describing calcium-binding reactions, i.e., for K_A and K_D (Figure 4.14 G and H). The majority of the isolated binding constants lay between 10^3 nM and 10^6 nM.

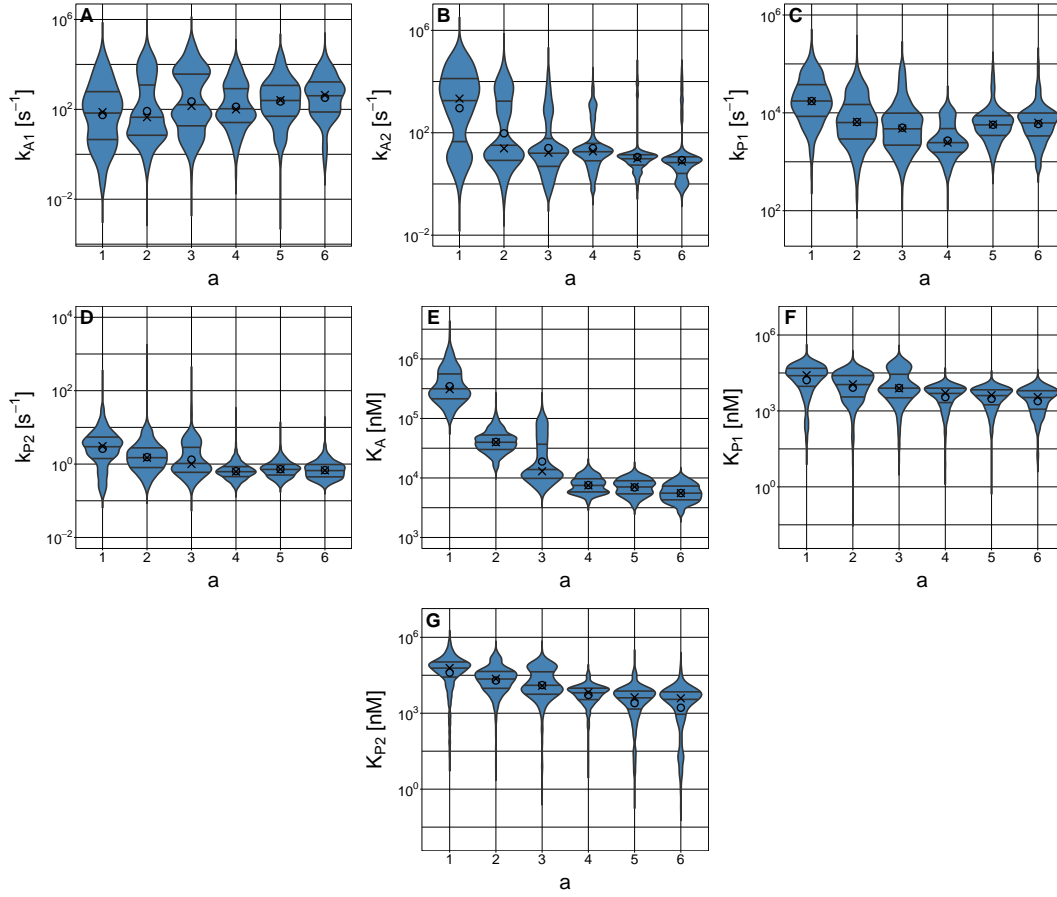


Fig. 4.13. Parameter distributions of parameter sets capable of inducing efficient high-pass activation. For this analysis, I isolated parameter sets leading to objective values within a 2-nM-margin of an overall best objective value per optimization problem. The optimizations targeted a maximization of the high-pass activation efficiency Eff_H for set parameterizations of the cooperativity coefficient a in the high-pass model (Table 4.2). Circles refer to the mean, crosses to the median of parameter distributions. K_A 's distributions indicated a decrease upon increases in a (E). All of the optimized binding constants, K_A , K_{P1} and K_{P2} , mostly resided between 10^3 nM and 10^6 nM (E to G). The degradation rate constants k_{P2} and, for higher cooperativity values, also k_{A2} were the most confined parameters (B and D). Number of isolated parameter sets for $a = 1, 2, \dots, 6$: 638, 982, 981, 483, 408, 344. Number of isolated fits relative to the overall number of fits for $a = 1, 2, \dots, 6$: 13.13 %, 50.51 %, 52.43 %, 65.27 %, 29.96 %, 44.73 %. 2 nM relative to the leading objective value for $a = 1, 2, \dots, 6$: 1.02 %, 0.32 %, 0.19 %, 0.14 %, 0.12 %, 0.1 %.

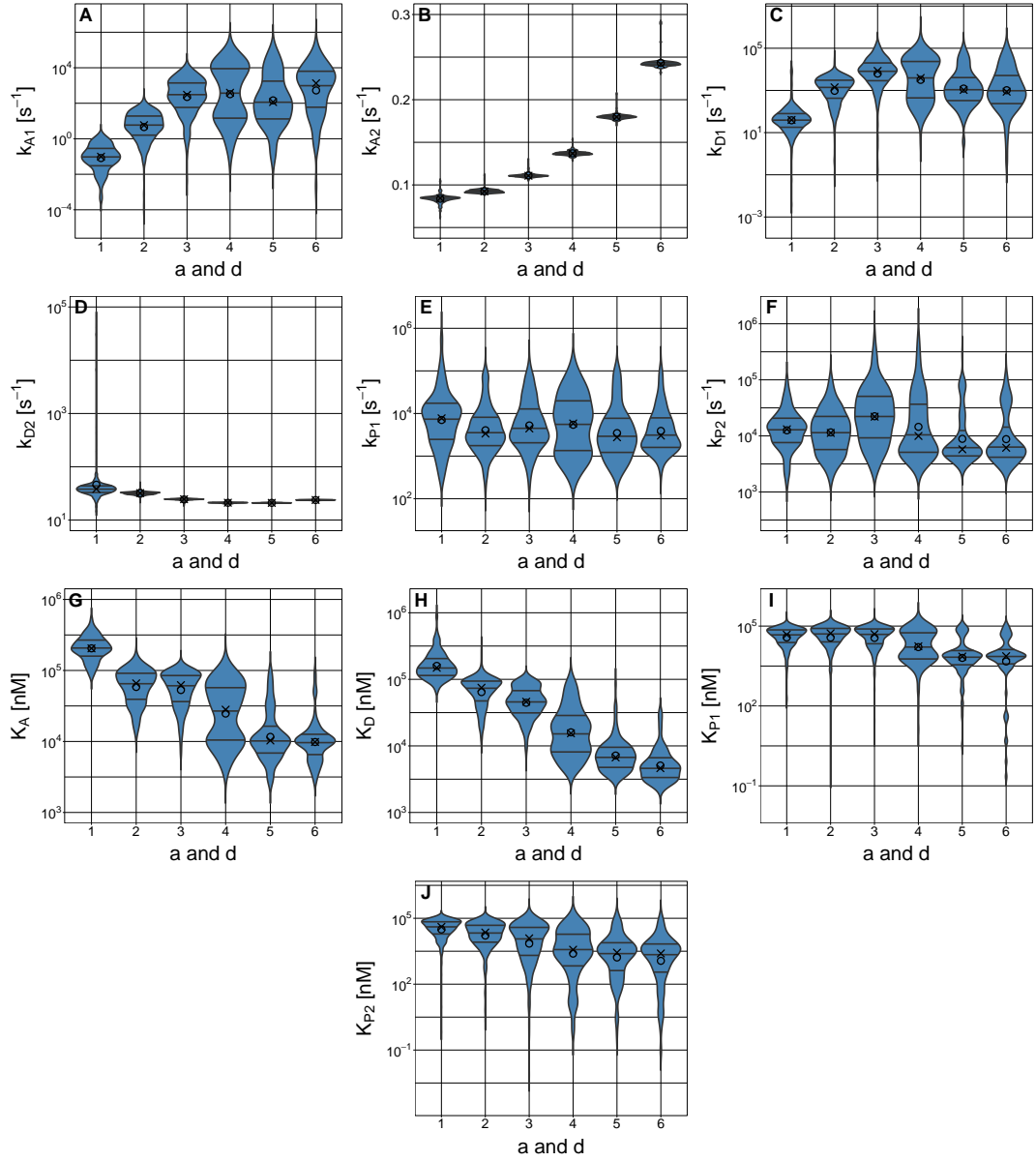


Fig. 4.14. Parameter distributions of parameter sets capable of inducing efficient band-pass activation. For this analysis, I isolated parameter sets leading to objective values within a 2-nM-margin of an overall best objective value per optimization problem. The optimizations targeted a maximization of the band-pass activation efficiency Eff_B for set parameterizations of the cooperativity coefficients a and d in the band-pass model. Circles refer to the mean, crosses to the median of parameter distributions. I found that the degradation rate constants of the regulator species k_{A2} and k_{D2} were the most confined parameters (B and D). With regards to the binding constants, a drop in the optimal parameterization margins was recognizable upon increases in a and d . This was most apparent for the regulators' binding constants (K_A and K_D) (G - J). Number of isolated parameter sets for $a = d = 1, 2, \dots, 6$: 254, 431, 416, 152, 121, 79. Number of isolated fits relative to the overall number of fits for $a = d = 1, 2, \dots, 6$: 3.12%, 5.88%, 6.28%, 1.88%, 0.76%, 0.28%. 2 nM relative to the leading objective value for $a = d = 1, 2, \dots, 6$: 1.04%, 0.33%, 0.19%, 0.14%, 0.12%, 0.11%.

4.8.3 Analysis of parameter couples

Next, I used the optimized parameter sets to investigate the dependence among parameter couples for inducing efficient frequency-decoding. To this end, I quantified linear dependencies by means of correlation analyses and linear as well as nonlinear dependencies by means of estimations of mutual information between parameter distributions. Both methods detected relationships between parameters, many of which were highly sensitive to changes in the parameterization of cooperativity coefficients. For instance, in the high-pass model, k_{A1} and k_{A2} shared a recognizable dependence for a equal to 1. However, this dependence deteriorated upon further increases in a . Also between k_{P2} and K_{P2} as well as between k_{A1} and K_A both methods identified close relationships in the high-pass model that were once again sensitive to changes in a (Figure 4.15 A and B). Most strikingly, the degradation rate constant of the decoder protein k_{P2} was found to be always smaller than the corresponding production rate constant k_{P1} . A visualization of the ratio distributions shows that the distributions' mean

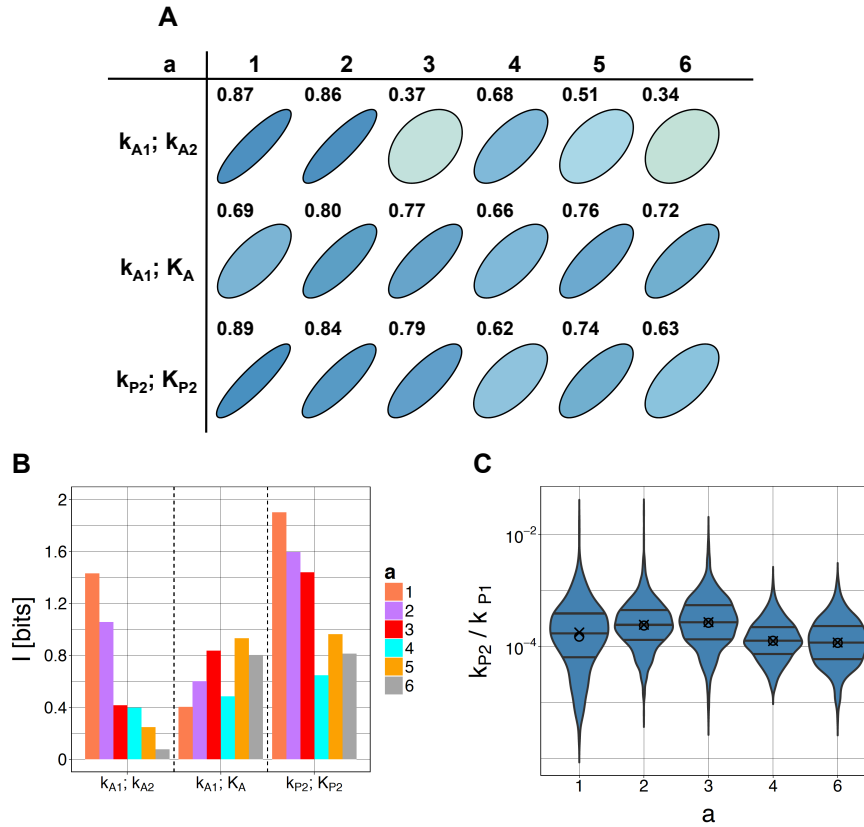


Fig. 4.15. Noticeable relationships between parameters in parameter sets capable of inducing efficient high-pass activation in the high-pass model. For this analysis, I isolated parameter sets leading to objective values within a 2-nM-margin of an overall best objective value. The optimizations targeted a maximization of Eff_H for several parameterizations of the cooperativity coefficient a in the high-pass model. (A): Correlation coefficients were visualized by means of the plotcorr function of the ellipse package. (B): Surrogate-corrected mutual information estimates as described in Section 2.5. k_{A1} and k_{A2} shared a strong dependence for a equal to 1. The dependency deteriorated upon further increases in a . The dependencies between k_{A1} and K_A as well as between k_{P2} and K_{P2} seemed to be more robust to changes in a , yet were also found to be sensitive to them. (C): In all isolated parameter sets, k_{P2} was smaller than k_{P1} . Additional correlation and mutual information results between parameter couples can be found in the appendix in Section A.1.2.

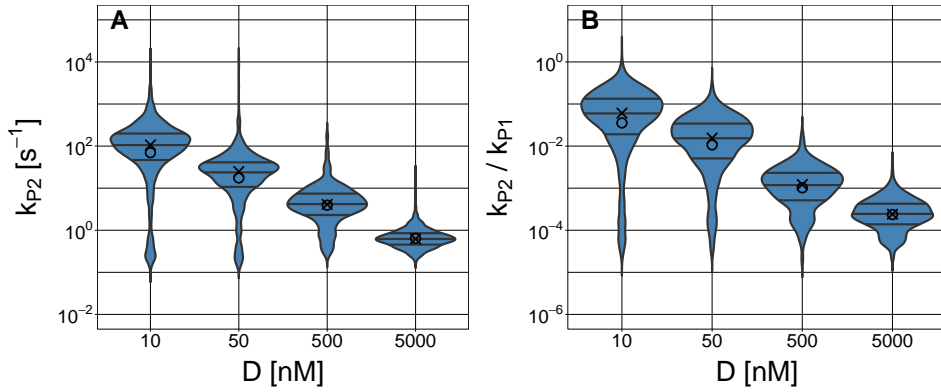


Fig. 4.16. Decreases in the fixed concentration of Deact led to visible increases in k_{P2} and in the k_{P2} -to- k_{P1} ratio in the high-pass model. I isolated parameter sets leading to objective values within a 2-nM-margin of an overall best objective value per optimization problem. The optimizations targeted a maximization of the high-pass activation efficiency Eff_H for several parameterizations of Deact's fixed concentration in the high-pass model. For all optimizations, a was set to 4. Circles refer to the mean, crosses to the median of the parameter distributions. Decreases in the fixed concentration of Deact induced a recognizable rise in k_{P2} (A). As a consequence, k_{P2} was occasionally larger than k_{P1} (B). However, even for the smallest applied parameterization of Deact, in most instances, k_{P1} was still larger than k_{P2} . Irrespective of the applied changes in Deact, I observed no significant changes in E_H (not shown). Number of isolated parameter sets for Deact = 10, 50, 500 and 5000 nM: 1155, 961, 158 and 483. Number of isolated fits relative to the overall number of fits for Deact = 10, 50, 500 and 5000 nM: 27.04 %, 45.83 %, 5.85 %, 65.27 %. 2 nM relative to the leading objective value for Deact = 10, 50, 500 and 5000 nM: 0.14 %, 0.14 %, 0.14 %, 0.14 %.

value stayed on a relatively constant level for several parameterizations of a (Figure 4.15 C).

I assumed that the default setup of the high-pass model led to k_{P1} being always smaller than k_{P2} . In the high-pass model, the competent activator Act is defined as a variable and can range between 0 nM and 5000 nM, whereas the competent deactivator Deact is fixed to a concentration of 5000 nM. I expected that, in order to compensate for the strong deactivating force, the activator-dependent rate constant governing decoder production k_{P1} was optimized to be larger than its counterpart k_{P2} . In accordance to this assumption, upon decreasing Deact's fixed concentration, k_{P2} distributions increased (Figure 4.16). However, even for very small levels of Deact, only in rare instances k_{P1} was indeed smaller than k_{P2} .

With regards to the band-pass model, correlation and mutual information analyses detected relationships between parameter distributions that were highly sensitive to changes in the cooperativity coefficients a and d . I discovered the strongest and most consistent relationships between rate constants and corresponding binding constants, with the exception of k_{P1} and K_{P1} (Figure 4.17 A and B). Furthermore, I found that the degradation rate constant of the activator k_{A2} was always smaller than the degradation rate constant of the deactivator k_{D2} (Figure 4.17 C). This observation was in agreement with my initial hypothesis stated in Section 4.3. In particular, I assumed that band-pass activation was only possible in case the activator was less responsive than the deactivator.

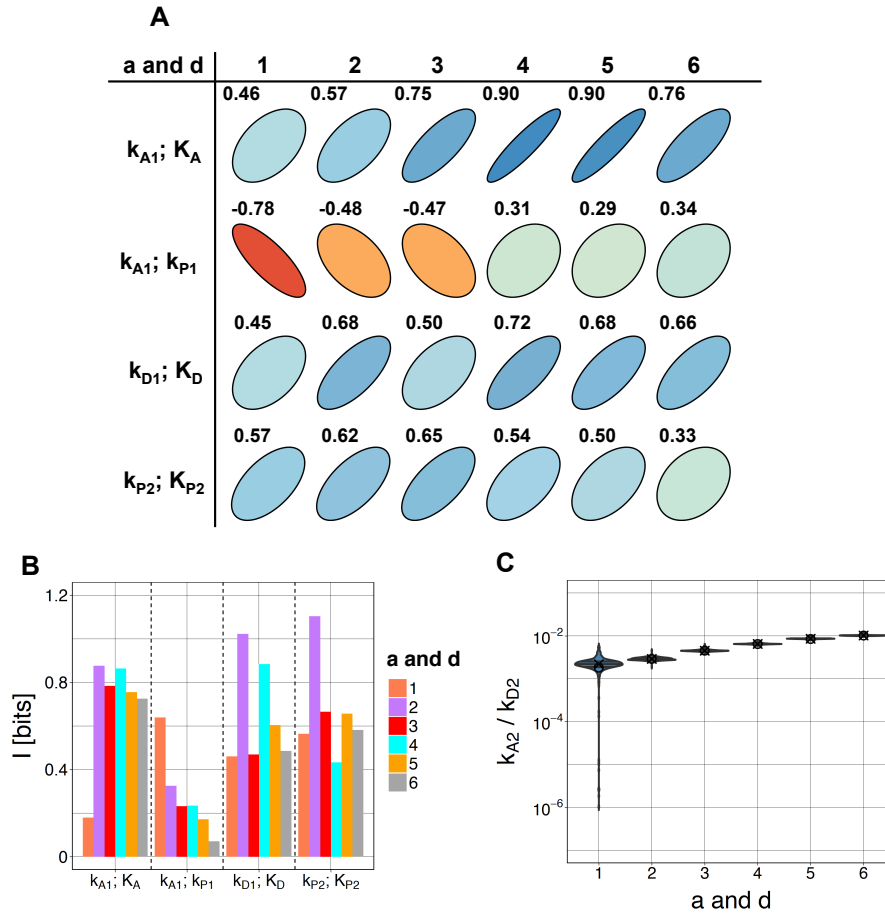


Fig. 4.17. Noticeable relationships between parameters in parameter sets capable of inducing efficient band-pass activation in the band-pass model. For this analysis, I isolated parameter sets leading to objective values within a 2-nM-margin of an overall best objective value. The optimizations targeted a maximization of Eff_B for several parameterizations of the cooperativity coefficients a and d in the band-pass model. (A): Correlation coefficients were visualized by means of the `plotcorr` function of the `ellipse` package. (B): Surrogate-corrected mutual information estimates as described in Section 2.5. The correlation and mutual information results between parameter distributions indicated a high sensitivity of parameter dependencies to changes in the model's cooperativity coefficients. The dependencies between rate constants and corresponding binding constants were most noticeable. Additionally, a relationship between k_{A1} and k_{P1} fully deteriorated upon increases in a and d . (C): For all isolated parameter sets, k_{A2} was smaller than k_{D2} . Further correlation and mutual information results can be found in the appendix in Section A.1.2.

4.9 Constraint optimizations reveal consequences of unfavorable parameterization margins

According to results presented in Section 4.8.2, most parameters were constraint to particular ranges of values in order to induce efficient high-pass or band-pass activation. Further, interdependent constraints between parameter couples were found (Section 4.8.3). As a follow-up to these results, I analyzed the effect of unfavorable parametrization margins on the models' frequency-decoding capabilities. Again, I performed optimizations targeting a maximization of the high-pass activation efficiency Eff_H in the high-pass model and a maximization of the band-pass activation efficiency Eff_B in the band-pass model given set parameterizations of cooperativity coefficients (in the high-pass model $a = 4$, in the band-pass model $a = d = 4$; I set all remaining cooperativity coefficients to 1). For all optimizations, I applied default period lengths ($T_{fast} = 0.1$ s, $T_{med} = 10$ s and $T_{slow} = 1000$ s).

In previous optimizations, I constrained rate constants to an interval of $[0; 10^6]$ s⁻¹ and binding constants to an interval of $[0; 10^6]$ nM. I chose these optimization intervals in reference to Bar-Even *et al.* [184]. In particular, Bar-Even *et al.* scanned through enzyme databases to analyze the distributions of kinetic parameters. In the following, I varied the parameterization constraints by either raising the default lower boundary or lowering the default upper boundary of either rate or binding constants.

Iterative increases in the lower rate constant boundary L_R eventually resulted in systems being too fast to perform frequency-decoding over the intended bandwidth as defined by T_{fast} , T_{med}

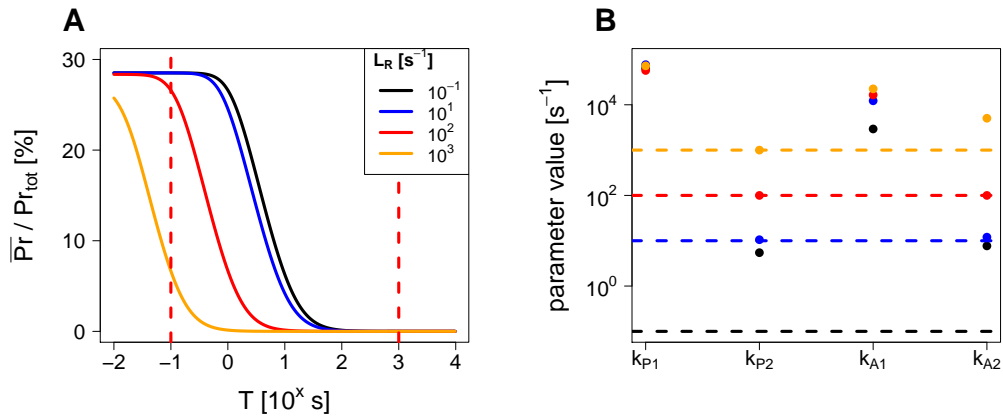


Fig. 4.18. Effect of an increased lower rate constant boundary L_R on optimization results for high-pass activation. Here, I optimized the high-pass activation efficiency Eff_H , with all rate constants in the high-pass model being constrained to $[L_R; 10^5]$ s⁻¹. Per optimization problem, I isolated the most efficient parameter set associated with the best objective value and applied it to compute the presented simulation results. (A) When forced to adapt to larger rate constant values, the system could no longer set the optimum at the intended T_{fast} (left red dashed line). The optimum shifted towards smaller, thus faster, calcium oscillation periods. Red dashed lines mark the input period lengths T_{fast} and T_{slow} that I used in the optimization algorithm. In (B), I present the rate constants applied in (A). For strongly raised values of L_R , the degradation rates were close to the imposed lower limit as marked by dashed lines (orange, red and blue). Colors match the fits presented in the left panel.

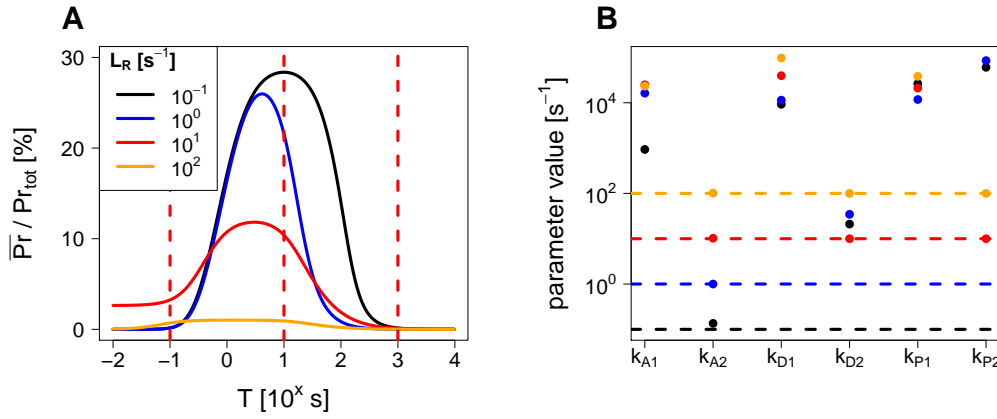


Fig. 4.19. Effect of an increased lower rate constant boundary L_R on optimization results for band-pass activation. Here, I optimized the band-pass activation efficiency Eff_B in the band-pass model, with all rate constants being constrained to $[L_R; 10^5] \text{ s}^{-1}$. Per optimization problem, I isolated the most efficient parameter set associated with the best objective value and applied it to compute the simulation results presented in (A). When forced to adapt to larger rate constant values, the system's frequency-decoding shifted towards faster bandwidths, i.e., smaller period lengths. Red dashed lines mark the oscillation period lengths used in the optimization algorithm (T_{fast} , T_{med} and T_{slow}). In (B), I present the rate constants applied in (A). For a strongly raised L_R , the degradation rates were close to the imposed lower limit as marked by dashed lines (orange, red and blue). Colors match the fits presented in the left panel.

and T_{slow} . The systems were forced to become faster and, in consequence, frequency-decoding shifted towards faster bandwidths. With respect to the band-pass model, a decrease in the band-pass activation potential E_B could be observed upon increases in L_R (Figures 4.18 A and 4.19 A). After isolating the best parameter sets for particular optimization problems, it was revealed that the degradation rate constants converged to the imposed L_R in case it was raised significantly. Thus, the optimization algorithm tried to slow down the system as much as possible to induce efficient frequency-decoding over the intended bandwidth (Figures 4.18 B and 4.19 B).

Vice versa, maintaining the default L_R while decreasing the upper rate constant boundary U_R forced the high-pass and band-pass models to slow down. In both instances, frequency-decoding shifted towards slower bandwidths, i.e., larger period lengths. This effect was accompanied by reduced frequency-decoding potentials (Figures 4.20 A and C). When visualizing the rate constant parameterizations of the best fits, I found that the production rate constants had converged to the imposed upper limit U_R in case U_R was particularly low (Figures 4.20 B and D).

Decreases in the upper binding boundary U_B induced a decline in the frequency-decoding potentials for both, high-pass and band-pass activation (Figures 4.21 A and C). Restricting the allowed margin to different orders of magnitude revealed, also a lower binding boundary L_B was crucial for establishing efficient frequency-decoding (Figures 4.21 B and D). If L_B was set too high, frequency-decoding potentials declined as well and, for L_B larger than 10^5 nM , frequency-decoding collapsed entirely. In both instances, I detected an optimal parameterization range of binding constants between 10^3 nM and 10^5 nM that is in agreement with results presented in Section 4.8.2 (for $a = d = 4$). Upon modulations of L_B or U_B , I could observe no shift of frequency-decoding shapes towards slower or faster bandwidths.

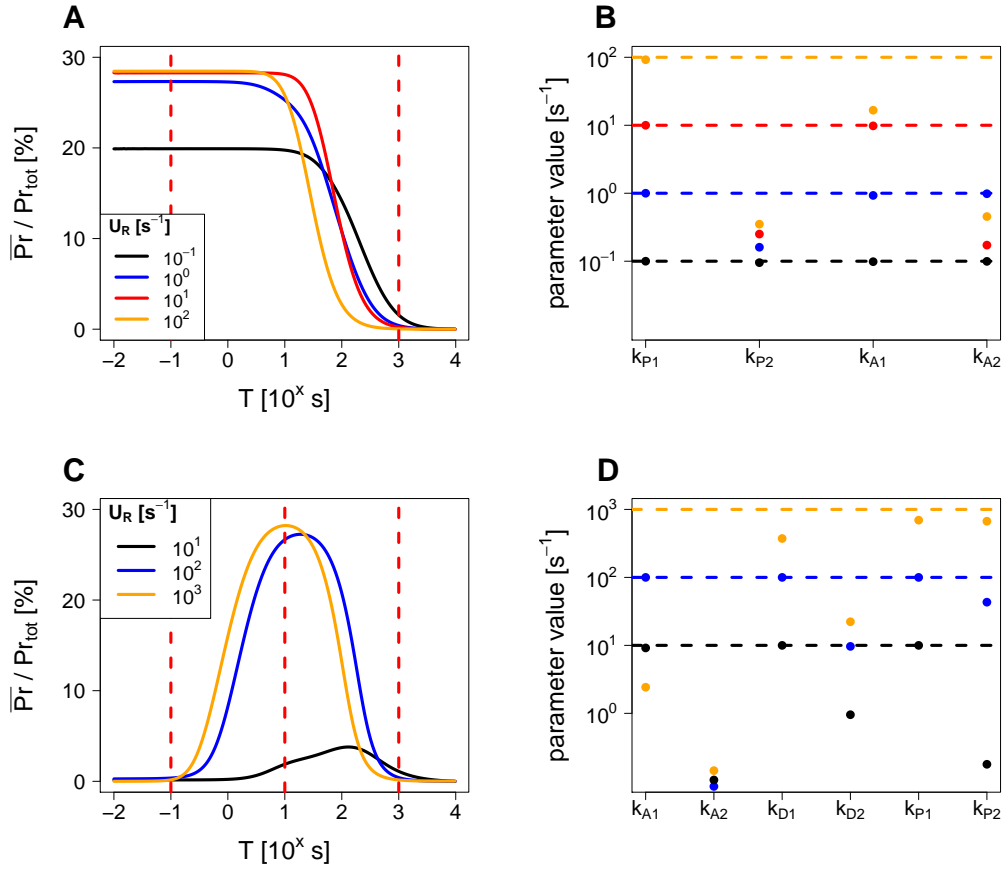


Fig. 4.20. Effect of a decreased upper rate constant boundary U_R on optimization results in high-pass and band-pass activation. For this analysis, I optimized either Eff_H in the high-pass model or Eff_B in the band-pass model, with all rate constants being constrained to $[0; U_R] s^{-1}$. In both instances, frequency-decoding shifted towards slower oscillations, i.e., larger period lengths, for particularly low values of U_R . This was accompanied by a loss in the frequency-decoding potentials (**A**;**C**). Red dashed lines mark the period lengths used in the optimization algorithms, T_{fast} , T_{med} and T_{slow} . In (**B**) and (**D**), I present the rate constants applied in (**A**) and (**C**). For particularly low values of U_R , the production rate constants converged to the imposed upper limit. Colors match the fits presented in the left panels.

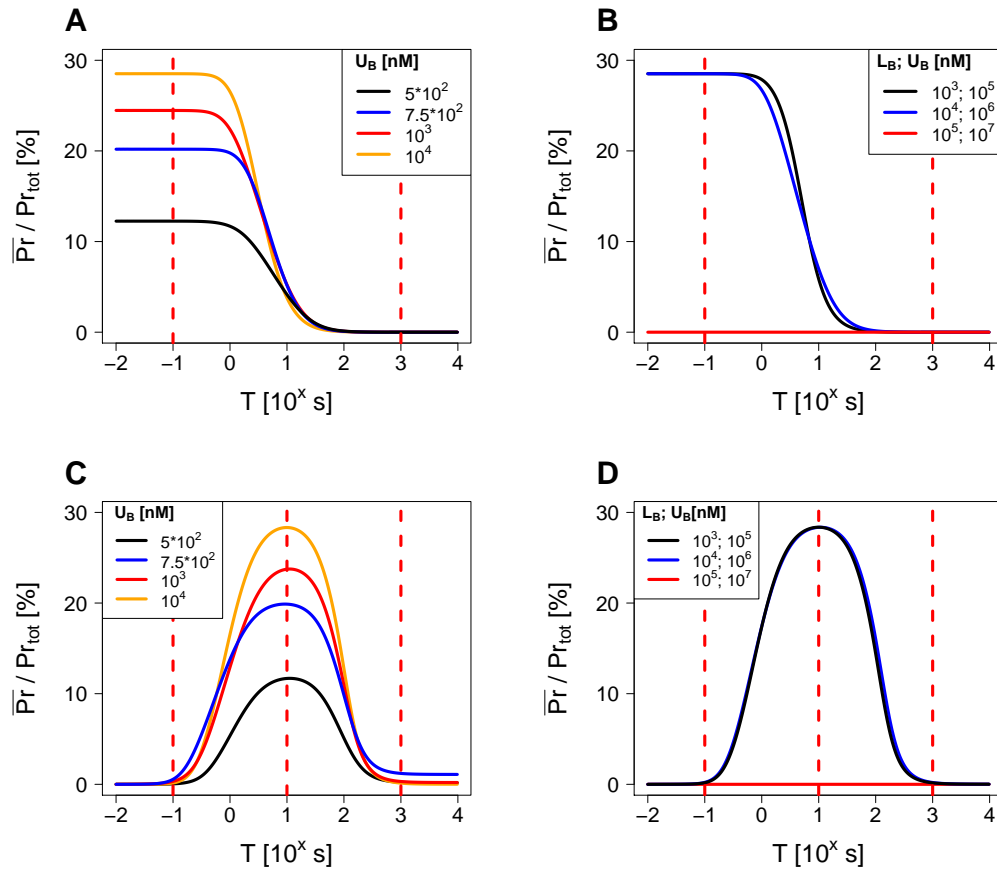


Fig. 4.21. Effect of constraint binding constant parameterizations on optimization results in high-pass and band-pass activation. (A) and (C): A decreased upper binding boundary U_B led to a clear decrease in the high-pass and band-pass activation potential. (B) and (D): Confinements, introduced by lowering U_B as well as by raising the lower binding boundary L_B , revealed an optimal margin for binding constants that seemed to lie between 10^3 nM and 10^5 nM. The applied changes in L_B and U_B did not lead to significant shifts in the period spectrum.

4.10 Dependence of the binding constant parameterization on the calcium oscillation amplitude

In Sections 4.8.2 and 4.9, I identified parameterization margins of binding constants in which protein models could perform highly efficient frequency-decoding. To this end, the parameterization margins of calcium-binding constants K_A and K_D appeared to be almost identical for high-pass activation in the high-pass model and band-pass activation in the band-pass model. In both instances, I defined the calcium input as a sine wave oscillating between 200 nM and 1000 nM. Thus, I assumed that the amplitude of the calcium oscillations likely impacted the parameterization margins of calcium-dependent binding constants.

To test this hypothesis, I considered multiple optimization problems aiming at a maximization of Eff_B in the band-pass model. The optimization problems differed from each other in the calcium sine wave's peak level. The baseline level of the sine waves was always set to 200 nM. Once again, I isolated parameter sets leading to objective values within a 2-nM-margin to an overall best objective value per optimization problem. Upon increases in the peak level of the calcium oscillations, thus, increases in the oscillation amplitude, I observed an increase in K_A and K_D supporting my initial hypothesis. For a peak level of only 500 nM, a considerable number of optimized binding constants lay between 10^3 nM and $10^{3.5}$ nM. For a peak level of 1500 nM and larger, only a minority remained in this range of values (Figure 4.22). Also other

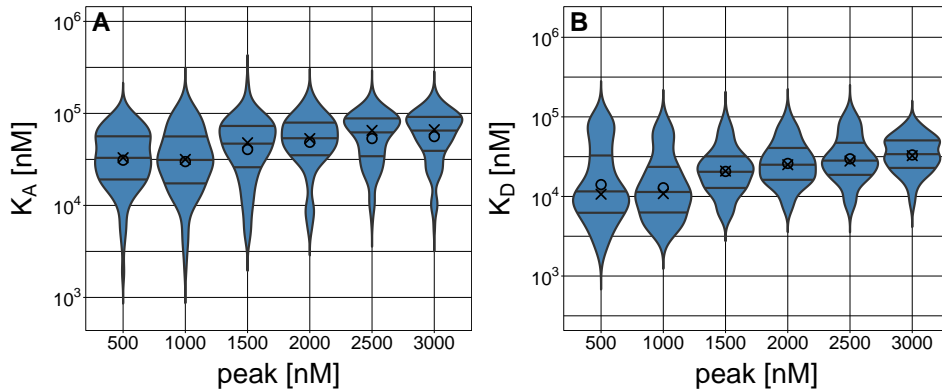


Fig. 4.22. Increases in the calcium oscillation peak level led to increases in the optimal parameterization margins of K_A and K_D for efficient band-pass activation. Here, I isolated parameter sets leading to objective values within a 2-nM-margin of an overall best objective value per optimization problem. The optimizations targeted a maximization of Eff_B in the band-pass model for several peak levels of the sine wave calcium oscillations. While I scanned the peak level, I set the baseline level to 200 nM. The cooperativity coefficients a and d were set to 4 in all optimizations (the remaining cooperativity coefficients were set to 1). Both binding constants, K_A and K_D , describe the binding of calcium to the regulator species. A clear increase in the binding constants' optimal parameterization margins can be observed upon increases in the calcium oscillation peak level. Remaining parameter distributions can be found in the appendix in Section A.1.3. Number of isolated parameter sets for peak = 500, 1000, ..., 3000 nM: 180, 96, 70, 98, 104, 120. Number of isolated fits relative to the overall number of fits for peak = 500, 1000, ..., 3000 nM: 4.18 %, 2.38 %, 2.12 %, 3.36 %, 4.08 %, 4.82 %. 2 nM relative to the leading objective value for peak = 500, 1000, ..., 3000 nM: 0.25 %, 0.14 %, 0.13 %, 0.12 %, 0.12 %, 0.12 %.

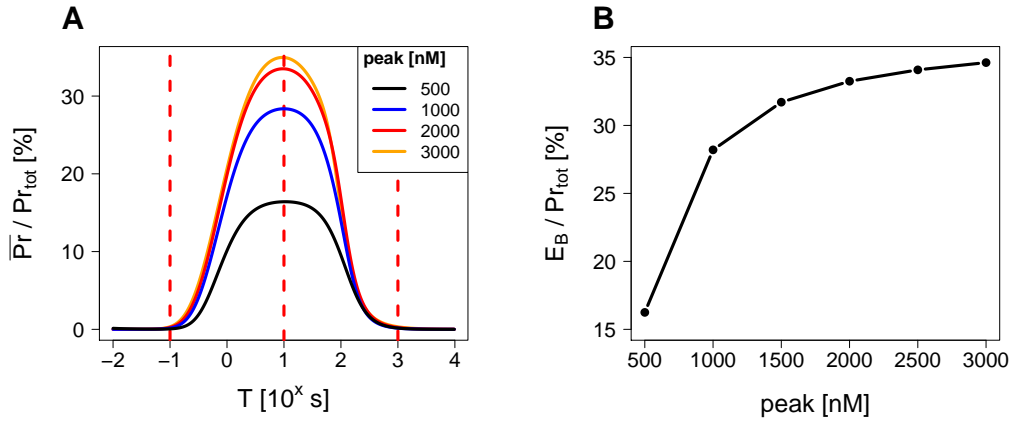


Fig. 4.23. Increases in the calcium oscillation amplitude led to an increased E_B . I maximized Eff_B in the band-pass model for different amplitudes of the calcium sine wave. While I fixed the sine wave's base level to 200 nM, I varied the peak level between optimization problems. For all optimization problems, I set a and d to 4 (the remaining cooperativity coefficients were set to 1). Increases in the oscillation amplitude clearly led to increases in the band-pass activation potential E_B . A saturation of this effect became visible for larger peak values. Applied parameter sets can be found in appendix A in Table A.14.

parameters were sensitive to the applied changes, with k_{A1} indicating a minor decrease and k_{A2} indicating a minor increase upon increases in the peak level (all parameter distributions that are not presented here can be found in the appendix in Section A.1.3).

Further, I observed that increases in the calcium oscillation amplitude led to a rise in the band-pass activation potential E_B . However, increases in E_B as a result of increases in the calcium oscillation amplitude appeared to be restricted, as visible by the onset of a saturation in Figure 4.23.

4.11 Precision versus efficiency in frequency-decoding

As a result of a maximization of Eff_B according to Equation 4.5, a decoder protein's average activity \overline{Pr} is increased in the bandwidth between T_{fast} and T_{slow} (as visualized in Figure 4.10 B). Since, in cellular pathways, precision is a crucial factor, I investigated the effect of changes in the size of the filter bandwidth on band-pass activation.

In more detail, I assessed the effect of changes in T_{fast} and T_{slow} on the band-pass activation potential E_B . For each applied filter bandwidth, I ran optimizations targeting a maximization of Eff_B for different parameterizations of the cooperativity coefficients a and d in the band-pass

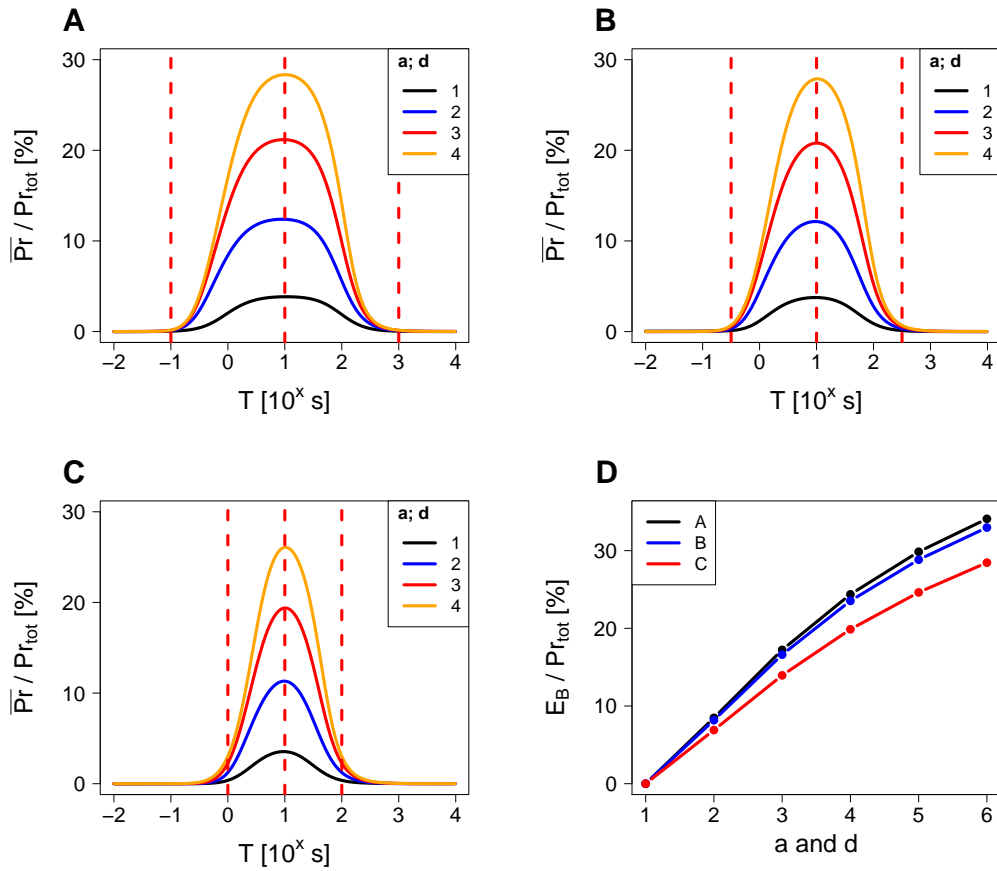


Fig. 4.24. Effect of modulating the filter bandwidth on the distinctness of band-pass activation. For the presented results, I optimized binding and rate constants in the band-pass model aiming at a maximization of E_B (according to Equation 4.5) for various parameterizations of the cooperativity coefficients a and d . To this end, I performed optimizations of Eff_B for differently narrow band-pass filters, as defined by T_{fast} and T_{slow} (see red dashed lines in the panels above or Table 4.5). With the optimized parameter sets (presented in the appendix in Tables A.5, A.15 and A.16), I computed the results shown above. (A) $T_{fast} = 10^{-1} s$ and $T_{slow} = 10^3 s$. (B) $T_{fast} = 10^{-0.5} s$ and $T_{slow} = 10^{2.5} s$. (C) $T_{fast} = 10^0 s$ and $T_{slow} = 10^2 s$. (D) Upon decreasing the difference between T_{fast} and T_{slow} , the band-pass activation potential E_B was clearly reduced. The larger the cooperativity coefficients a and d were, the larger became the potential gap between the installed band-pass filters.

Tab. 4.5. Filter bandwidths applied in this section.

Setting	T_{fast} [s]	T_{med} [s]	T_{slow} [s]
A	10^{-1}	10^1	10^3
B	$10^{-0.5}$	10^1	$10^{2.5}$
C	10^0	10^1	10^2

In this section, I ran optimizations for differently narrow band-pass filters. Setting A is identical to the default filter introduced in Section 4.4. I applied the period lengths in optimizations targeting a maximization of the band-pass activation efficiency Eff_B in the band-pass model (see Equations 4.4 and 4.5).

model (Table 4.3). I set all of the remaining cooperativity coefficients to 1. For a full list of the applied parameterizations of T_{fast} and T_{slow} , please refer to Table 4.5.

As shown in Figure 4.24, for each of the applied filter bandwidths, an increase in a and d led to an increase in E_B , as previously shown in Section 4.7. A direct comparison between the resultant frequency-decoding potentials revealed a clear decrease in E_B upon applying narrower filter bandwidths for band-pass activation. The larger the cooperativity coefficients a and d were, the larger became the potential gap between differently narrow band-pass filters (Figure 4.24 D). Furthermore, while for the broader band-pass filters the decoder protein's average activity \overline{Pr} was only increased in the defined filter bandwidth spanning between T_{fast} and T_{slow} (Figure 4.24 A, B), for the narrowest of the applied band-pass filters \overline{Pr} was also slightly elevated outside of the intended filter bandwidth (Figure 4.24 C).

4.12 Recreating high-pass activation under stochastic conditions

In my analysis of frequency-decoding, I found pronounced high-pass activation shapes to be particularly interesting. I assumed that, for calcium oscillation periods leading to output responses in the quasi-linear part of the high-pass activation shape, already minor changes in the calcium oscillation period would be linked to large changes in the output measure that could be clearly discriminated even in the presence of stochastic fluctuations.

In order to test for this effect, first, I had to recreate high-pass activation under stochastic conditions. To this end, I employed the Direct Method algorithm by Gillespie to run stochastic simulations [157]. For the algorithm's application, I defined time-dependent propensity terms for every reaction of the deterministic high-pass model (Table 4.2). Reaction-specific propensity terms were derived from the current abundances of substrate and modifier species as well as the deterministic reaction rates. All propensity terms of the stochastic version of the high-pass model are presented in Table 4.6.

I found that a deterministically optimized parameter set (optimizations targeting a maximization of Eff_H according to Equation 4.3) frequently resulted in a successful recreation of high-pass activation also under stochastic conditions. However, in case rate constants were too small, a recreation of high-pass activation failed. I assumed that, in these instances, fluctuation dynamics overshadowed model dynamics. In addition, in case rate constants or the abundances of substrate or modifier species were too large, an extensive number of reaction events were fired throughout the course of the simulation leading to large computational expenses. Therefore, I was only able to recreate high-pass activation under stochastic conditions in case rate constants and particle numbers were kept on a moderate level.

Tab. 4.6. Propensity terms of the high-pass activation model.

Reaction	Propensity term
$Act_i \xrightarrow{Ca} Act$	$a_{H1} = \frac{k_{A1} \cdot N(Act_i) \cdot N(Ca)^a}{K_A^a \cdot \epsilon + N(Ca)^a}$
$Act \rightarrow Act_i$	$a_{H2} = k_{A2} \cdot N(Act)$
$Pr_i \xrightarrow{Act} Pr$	$a_{H3} = \frac{k_{P1} \cdot N(Pr_i) \cdot N(Act)^{p1}}{K_{P1}^{p1} \cdot \epsilon + N(Act)^{p1}}$
$Pr \xrightarrow{Deact} Pr_i$	$a_{H4} = \frac{k_{P2} \cdot N(Pr) \cdot N(Deact)^{p2}}{K_{P2}^{p2} \cdot \epsilon + N(Deact)^{p2}}$

I derived reaction-specific propensity terms from the corresponding reaction rates of the deterministic high-pass model (Table 4.2) as well as from the current abundances of substrates and modifiers. The scaling factor ϵ is the product of the Avogadro constant N_A and the system volume V that I set to 10^{-15} L by default. The application of ϵ allowed for the conversion of concentration values to particle numbers.

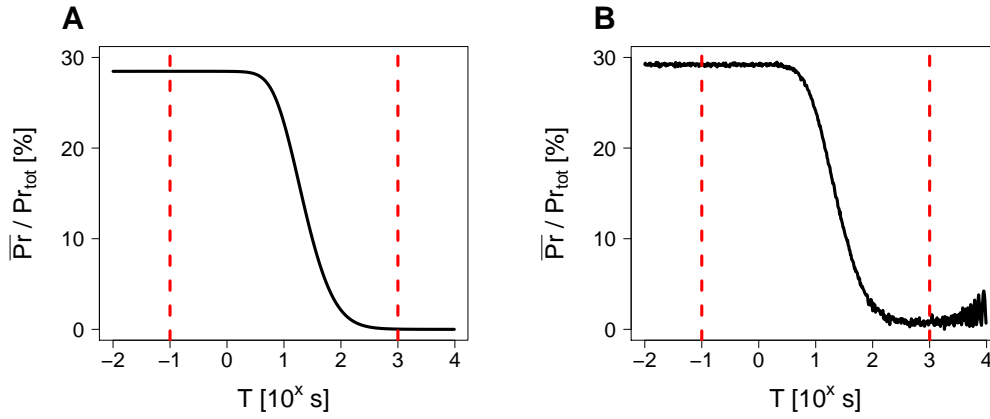


Fig. 4.25. Recreation of high-pass activation under stochastic conditions. First, I deterministically optimized the high-pass activation efficiency Eff_H in the deterministic high-pass model (Table 4.2). To this end, I applied default parameterizations of T_{fast} and T_{slow} , here marked by red dashed lines (A). With the optimized parameter set, I could successfully transfer high-pass activation to a stochastic version of the high-pass model (Table 4.6) (B). I found that the obtained high-pass activation shape of the stochastic version of the high-pass model became noisier for larger values of T , since I measured \overline{Pr} within a fixed window of time. Thus, for slower calcium oscillations, simulations covered a lesser number of oscillation cycles compared to faster oscillations. Importantly, the recreation of high-pass activation under stochastic conditions failed, if parameter sets exhibited particularly small rate constants. In these cases, fluctuation dynamics overshadowed model dynamics. Also in case rate constants or particle numbers were too large, high computational expenses impaired stochastic simulations. The applied parameter set can be found in the appendix in Table A.17.

In Figure 4.25, I present stochastic simulation results that I obtained by applying a parameter set satisfying this condition. In detail, I set $N(Act_{tot})$ and $N(Pr_{tot})$ to 602 particles each, while I constrained rate constants to an interval of $[1; 100] s^{-1}$ in deterministic optimizations. The optimized parameter set can be found in the appendix in Table A.17.

4.13 Impact of model responsiveness on frequency-decoding under stochastic conditions

As previously mentioned, for calcium oscillation periods leading to responses in the quasi-linear part of the high-pass activation shape (see Figure 4.25), I assumed that already minor changes in the oscillation period led to large changes in the average activity of the decoder protein $\overline{\text{Pr}}$ that could be discriminated in the presence of stochastic fluctuations.

In this section, I investigated the effect of variations in the responsiveness of the decoder protein on the discrimination of a fixed set of calcium oscillation periods. To this end, I employed simple sine wave functions to mimic calcium oscillations and modulated the responsiveness of the decoder protein Pr by introducing a new parameter ω . The propensity terms a_{H3} and a_{H4} from Table 4.6 changed to

$$a_{H3}^* = \left(\frac{k_{P1} \cdot N(\text{Pr}_i) \cdot N(\text{Act})^{p_1}}{K_{P1}^{p_1} \cdot \epsilon + N(\text{Act})^{p_1}} \right) \cdot \frac{1}{\omega} \quad (4.14)$$

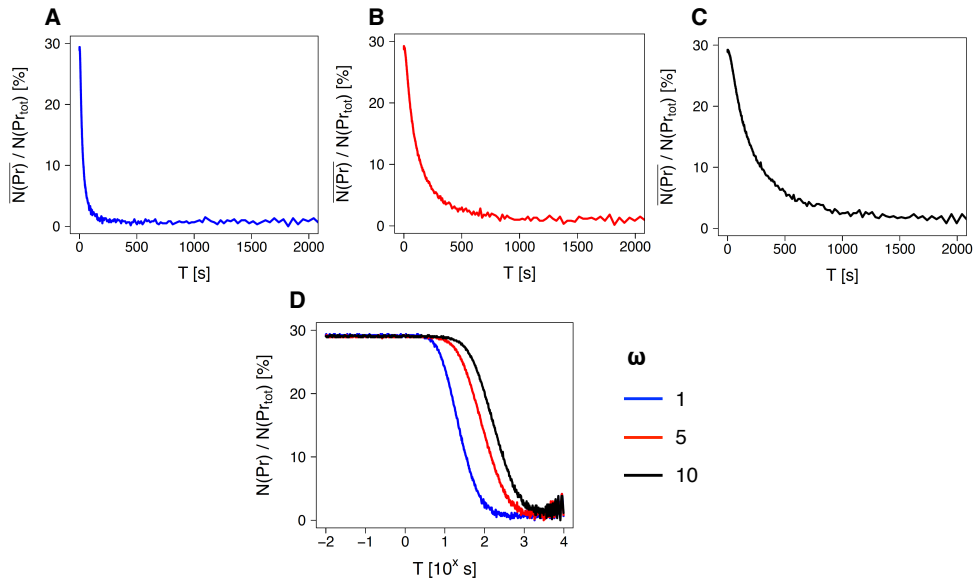


Fig. 4.26. Effect of variations in the decoder protein's responsiveness on high-pass activation under stochastic conditions. For differently responsive versions of the high-pass model, I applied a parameter set capable of inducing high-pass activation under stochastic conditions. The applied parameter set originated from an optimization of the deterministic high-pass model (Table 4.2) for $\omega = 1$. Increases in ω led to decreases in the decoder protein's responsiveness. This caused a shift of the high-pass activation shape towards slower oscillations, i.e., larger values of T (D). The width of the quasi-linear part of the resultant high-pass activation shapes remained constant on a log-scale. Therefore, on a linear scale, the quasi-linear part of the high-pass activation shape of the least responsive model version covered a larger range of period lengths (C) compared to the quasi-linear parts of the more responsive model versions (A, B). I measured the decoder's average activity, i.e. the average number of active decoder particles $\overline{N}(\text{Pr})$, after a simulation time of 40000 s.

and

$$a_{H4}^* = \left(\frac{k_{P2} \cdot N(\text{Pr}) \cdot N(\text{Deact})^{p_2}}{K_{P2}^{p_2} \cdot \epsilon + N(\text{Deact})^{p_2}} \right) \cdot \frac{1}{\omega} \quad (4.15)$$

For ω -values larger than 1, Pr was slowed down, while, for ω -values smaller than 1, Pr was accelerated compared to the original model version. As shown in Figure 4.26 D, increases in ω led to a shift in the high-pass activation shape towards larger values of T without a loss in the high-pass activation efficiency Eff_H . Interestingly, upon modulations of ω , the width of the quasi-linear part of the high-pass activation shape did not vary on a log-scale. Thus, on a linear scale, the quasi-linear part of the high-pass activation shape of the least responsive model version ($\omega = 10$) covered the largest range of period lengths (Figure 4.26 A-C). For the other model parameters, I always applied the parameter set presented in the appendix in Table A.17.

Since variations in Pr's responsiveness resulted in a shift of the quasi-linear part of the high-pass activation shape, I concluded that also the ability to discriminate between a set of period lengths should be affected. In order to confirm this hypothesis, I performed estimations of channel capacity, as introduced in Section 3.2, to quantify a protein model's ability to discriminate between a set of calcium oscillation period lengths. To this end, for every parameterization of ω and every analyzed period length T , I ran 1000 simulations allowing for the acquisition of T - and ω -specific distributions of $\overline{N(\text{Pr})}$. Next, I estimated the channel capacity in high-pass model versions differing in the responsiveness of Pr for an increasing number of T 's, iteratively adding slower T 's to the set of already present ones (as previously shown in Section 3.2.4). In this way, I could assess a model version's ability to discriminate fast oscillations only compared to its ability to discriminate between a mix of fast and slow oscillations. The maximal set of T 's comprised a uniform sequence of 300 period lengths spanning from 5 s to 1500 s ($\{T_1 = 5 \text{ s}; T_2 = 10 \text{ s}; \dots; T_{300} = 1500 \text{ s}\}$). Thus, for the first estimation of channel capacity in each model version, I included only two inputs, $\{T_1 = 5 \text{ s}; T_2 = 10 \text{ s}\}$, while, in the next round, I included three inputs, $\{T_1 = 5 \text{ s}; T_2 = 10 \text{ s}; T_3 = 15 \text{ s}\}$, until, in the 299th round, I included all 300 inputs.

The addition of more and more calcium oscillation period lengths led to a rise in channel capacity until convergence to a cap value. To this end, the fast responsive model version ($\omega = 1$) was inferior in discriminating between input period lengths, when incorporating fast as well as slow period lengths into the channel capacity estimation (Figure 4.27 D). A visualization of the T -specific distributions of $\overline{N(\text{Pr})}$ in different model versions showed that, for the less responsive model versions ($\omega = 5$ and $\omega = 10$), mean values were distributed over a larger range of output values. Thus, for the less responsive model versions, output distributions were more distinct to each other compared to the output distributions of the fast responsive model version ($\omega = 1$) (Figure 4.27 A to C). A comparison between Figure 4.26 and Figure 4.27 confirmed that, for T larger than 100 s and ω equal to 1, the average activity levels ceased to vary in a significant manner. Therefore, it was impossible to discriminate between single period lengths. In contrast, for the less responsive model versions, increases in T beyond 100 s still continued to result in significantly different values of $\overline{N(\text{Pr})}$ for a while. Considering all 300 inputs, the model version with $\omega = 10$ could clearly discriminate between 12 input sets, the model version with $\omega = 5$ could discriminate between 9 input sets and the model version with $\omega = 1$ could discriminate between 5 input sets.

As shown in Figure 4.27 D, upon only considering small T 's, the fast responsive model version ($\omega = 1$) held a clear advantage over the other model versions. Only when adding a number of larger T 's, the less responsive model versions ($\omega = 5$ and $\omega = 10$) became superior in discriminating between given input period lengths. This observation was also in agreement with Figure 4.26 in which, for the model version with $\omega = 1$, responses to the smallest of the applied period lengths lay in the quasi-linear part of the high-pass shape, while this was not the case with regards to responses in the less responsive model versions.

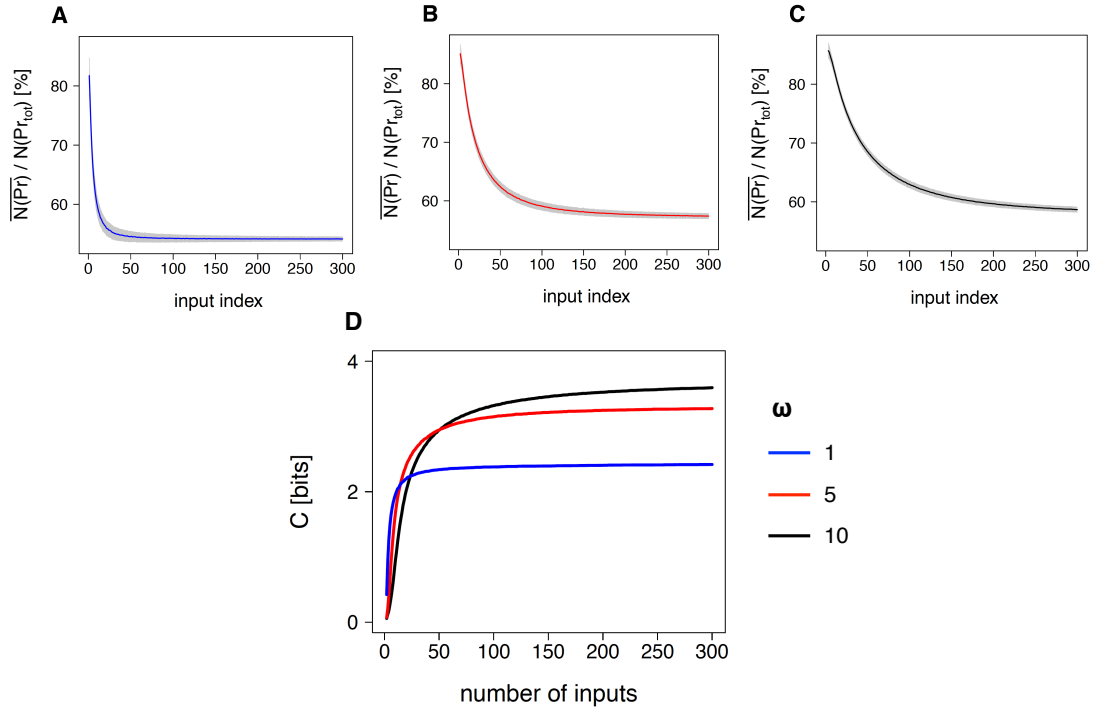


Fig. 4.27. Channel capacity estimates for a growing number of input period lengths and various levels of decoder responsiveness. For quantifying the ability of different versions of the stochastic high-pass model (Table 4.6) to discriminate between a set of calcium oscillation period lengths, I employed the information-theoretic measure of channel capacity. To this end, I ran stochastic simulations in which I stimulated the model versions with calcium sine waves exhibiting different period lengths T . In particular, for every model version and value of T , I ran 1000 stochastic simulations to collect condition-specific distributions of the model output $\overline{N}(\text{Pr})$. In total, I analyzed 300 different values of T ($T_{all} = \{T_1 = 5 \text{ s}; T_2 = 10 \text{ s}; \dots; T_{300} = 1500 \text{ s}\}$). Model versions differed from each other in the responsiveness of the decoder protein Pr, as modulated by variations in ω (Equations 4.14 and 4.15). In (A) to (C), I present the mean values and standard deviations of T -specific output distributions for different model versions. For $\omega = 1$ (A), the mean values of T -specific output distributions faster converged to a minimum compared to the output distributions for $\omega = 5$ and $\omega = 10$ (B and C). Thus, I expected that the model version with $\omega = 1$ was the least capable of discriminating between all 300 period lengths. Next, I employed the T -specific output distributions for estimations of channel capacity, iteratively adding output distributions referring to larger values of T to the set of already present ones. After every iteration, I estimated the channel capacity for a growing number of input period lengths. As a consequence of more distinct output distributions, the less responsive model versions exhibited larger channel capacity values after almost all iterations. Only for a very low number of T -values, thus only small values of T 's, the fast responsive model version exhibited a larger channel capacity (D). Maximal channel capacity values: for $\omega = 1$, 2.42 bits, for $\omega = 5$, 3.27 bits and, for $\omega = 10$, 3.6 bits. The applied parameter set can be found in the appendix Table A.17. $\overline{N}(\text{Pr})$, i.e., the average number of active decoder particles, was computed after 10 oscillation cycles.

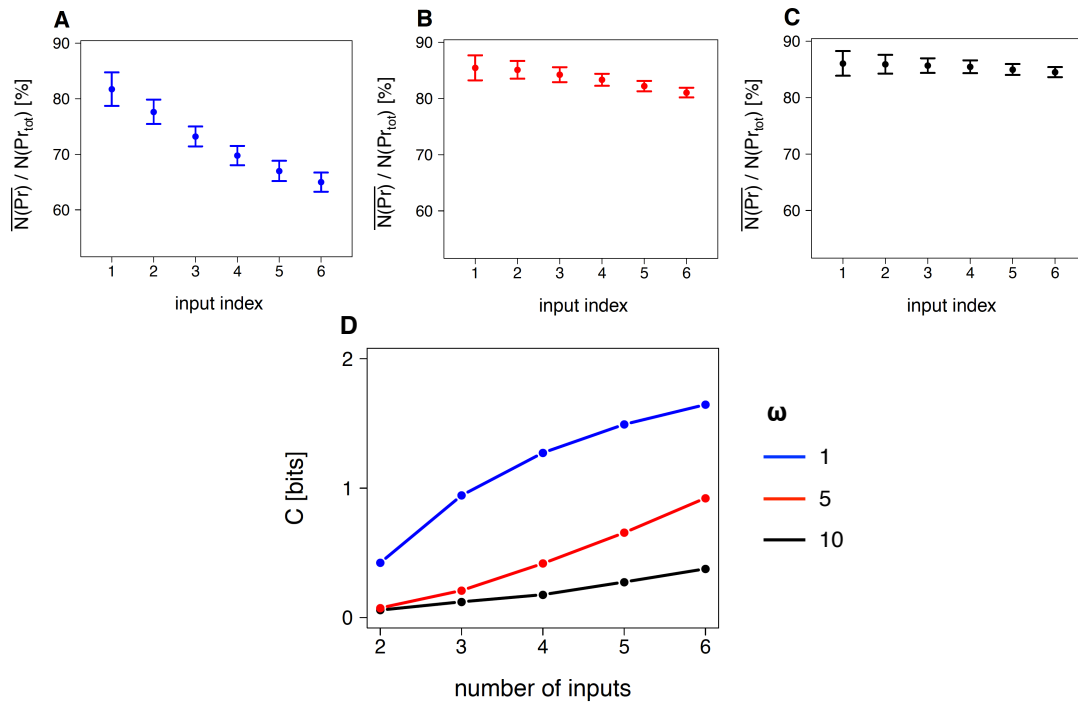


Fig. 4.28. Channel capacity estimates for a growing number of fast input period lengths and various levels of decoder responsiveness. Once again, I stimulated three versions of the high-pass model exhibiting different levels of decoder responsiveness with calcium sine waves of various period lengths. In particular, I modulated the responsiveness of the decoder protein by variations in ω (Equations 4.14 and 4.15). For every model version and value of T , I ran 1000 stochastic simulations to collect condition-specific distributions of the model output $\overline{N(Pr)}$. In total, I employed 6 values of T : $T_{all} = \{T_1 = 5 \text{ s}; T_2 = 10 \text{ s}; \dots; T_6 = 30 \text{ s}\}$. In (A) to (C), I present the mean values and standard deviations of T -specific output distributions for different model versions. For $\omega = 1$ (A), period-specific output distributions appeared to be more distinct to each other compared to output distributions of model versions with $\omega = 5$ and $\omega = 10$ (B and C). I employed these period-specific output distributions to compute channel capacity estimates. As in Figure 4.27, I iteratively added slower input period lengths to the mix of already present ones and estimated the channel capacity in different model versions after every iteration. As expected, the channel capacity estimates were larger for the fast responsive model version in the observed bandwidths (D). Maximal channel capacity values: for $\omega = 1$, 1.65 bits, for $\omega = 5$, 0.92 bits and, for $\omega = 10$, 0.38 bits. The applied parameter set can be found in the appendix in Table A.17. $\overline{N(Pr)}$, i.e., the average number of active decoder particles, was computed after 10 oscillation cycles.

To investigate this further, I repeated the described routine another time. However, this time I analyzed period lengths that spanned a much smaller bandwidth and consisted of smaller values of T ($\{T_1 = 5 \text{ s}; T_2 = 10 \text{ s}; \dots; T_6 = 30 \text{ s}\}$). As presented in Figure 4.28 D, the fast responsive model version ($\omega = 1$) was by far the most capable in discriminating between the applied period lengths. Many of the applied values of T were converted into distinct output distributions, while, for the less responsive model versions ($\omega = 5$ and $\omega = 10$), less of the output range was utilized and output distributions severely overlapped, thus, were less distinct to each other (Figure 4.28 A to C). Considering all 6 input period lengths, the model versions with $\omega = 5$ and $\omega = 10$ could discriminate between less than 2 input sets, while the model version with $\omega = 1$ could discriminate between 3 input sets.

In conclusion, the applied changes in the responsiveness of a model led to shifts in the optimal bandwidth for the discrimination between given input period lengths. It was demonstrated

that a model could be too fast (Figure 4.27 A) or too slow (Figure 4.28 B and C) to properly discriminate between a set of given period lengths.

4.14 Effect of cooperativity strength on frequency-decoding under stochastic conditions

4.14.1 Increases in the cooperativity strength lead to increases in the frequency-decoding distinctness under stochastic conditions

Previously, I demonstrated that, under deterministic conditions, increases in the high-pass model's cooperativity coefficients allowed for increases in the high-pass activation potential E_H . In particular, while the quasi-linear part of the high-pass activation shape covered the same bandwidth of input period lengths, it extended over a much larger range of output values upon increases in cooperativity coefficients (see Figure 4.10 A in Section 4.7). In conclusion, I assumed that increases in cooperativity coefficients leading to more pronounced high-pass activation shapes could allow for an improved discrimination between period lengths situated in the quasi-linear part of the high-pass activation shape under stochastic conditions.

In Section 4.7, I used deterministic optimizations to demonstrate that increases in the parameterization of cooperativity coefficients fostered the maximal distinctness of frequency-decoding in high-pass as well as band-pass activation. Upon applying such optimized parameter sets in stochastic simulations, it became clear that the described effect could be transferred: Increases in the cooperativity coefficient a could lead to increases in the high-pass activation efficiency also under stochastic conditions (Figure 4.29).

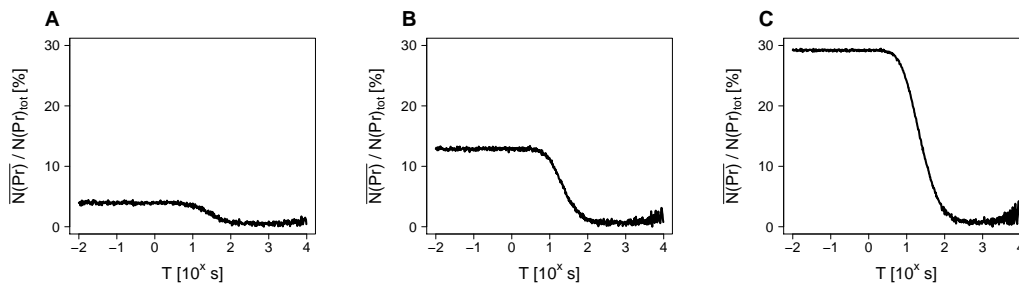


Fig. 4.29. Increases in cooperativity coefficients allowed for more pronounced high-pass activation also under stochastic conditions. For the presented results, I deterministically optimized rate and binding constants in the high-pass model (Table 4.2) for a maximization of the high-pass activation efficiency Eff_H given different parameterizations of the cooperativity coefficient a . Upon applying the optimized parameter sets to the stochastic version of the high-pass model (Table 4.6), it became clear that the positive correlation between cooperativity strength and high-pass activation distinctness was conserved. (A): $a = 1$; (B): $a = 2$, (C): $a = 4$. In this section, I analyzed the effect of the cooperativity strength on the discrimination between period lengths situated in quasi-linear part of the high-pass activation shapes. Therefore, the bandwidth of interest spanned from 10^1 s to 10^2 s . The applied optimized parameter sets can be found in the appendix in Tables A.17, A.18 and A.19.

4.14.2 Increases in cooperativity coefficients foster the robustness against noise

In this section, I quantified the ability of different versions of the high-pass model to discriminate between calcium oscillation period lengths ranging from 10^1 s to 10^2 s, whereas calcium oscillations exhibited different levels of distortion. In particular, model versions differed from each other with respect to their high-pass activation efficiency, as determined by variations in the cooperativity coefficient a (see Figure 4.29). For larger parameterizations of a , the high-pass activation efficiency increased. Further, I modeled a distortion of the calcium oscillation input by drawing numbers out of Gaussian distributions $\mathcal{N}(\mu = 0; \sigma^2)$ and adding these numbers to the concentration values of discretized time series of calcium sine waves. Variations in the distribution's standard deviation σ readily allowed for a modulation of the extrinsic noise magnitude. In case a transformed sine wave value was smaller than 0, the corresponding value was discarded and the transformation was repeated.

For every model version, distortion level σ and calcium oscillation period length T , I acquired distributions of the output measure $\overline{N}(\text{Pr})$ by means of repeated stochastic simulations. To get a first glance of the impact of increases in input distortion and cooperativity coefficients, I conducted a - and σ -specific input addition assays (as introduced in Figure 3.6 in Section 3.2). More information about the selected input period lengths can be found in the caption of Figure 4.30. Clearly, larger degrees of input distortion, i.e., larger values of σ , led to a decline in channel capacity in all model versions. Thus, larger levels of input distortion impaired

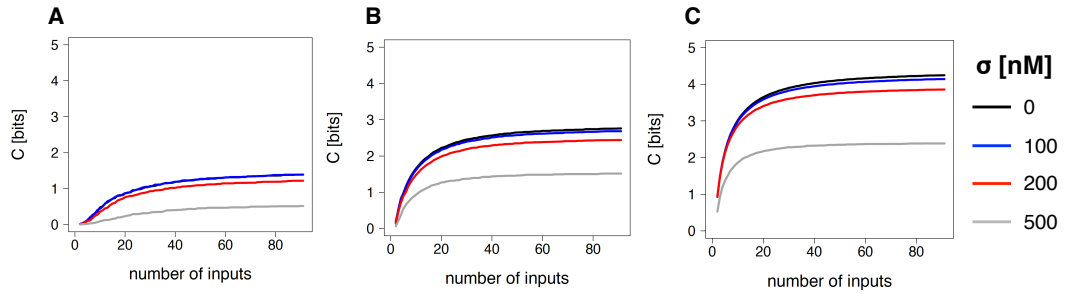


Fig. 4.30. Impact of modulations of the extrinsic noise amplitude and the high-pass model's cooperativity strength on the discrimination of period lengths. For this analysis, I applied three versions of the high-pass model and stimulated all three model versions with calcium sine waves exhibiting different period lengths T and different levels of distortion (as modulated by the magnitude of the standard deviation σ of the Gaussian distributions added to the discretized time series values of the calcium input). The model versions differed from each other in the parameterization of the cooperativity coefficient a that impacted the high-pass activation efficiency E_H (see also Figure 4.29). (A) $a = 1$; (B) $a = 2$; (C) $a = 4$. For every combination of σ and T , I ran 1000 stochastic simulations to collect condition-specific distributions of the output measure $\overline{N}(P)$ in each model version. I then employed these distribution data to perform estimations of channel capacity for different model versions and levels of distortion, iteratively adding larger values of T to the mix of already present ones. In total, I analyzed 91 values of T : $T_{all} = \{T_1 = 10 \text{ s}; T_2 = 11 \text{ s}; \dots; T_{91} = 100 \text{ s}\}$. All of the selected input period lengths led to model responses situated in the quasi-linear part of the high-pass activation shapes (as shown in Figure 4.29). For all applied parameter sets, increases in the distortion of calcium oscillations, as modulated by increases in σ , induced a clear decline in the channel capacity. Model versions exhibiting larger cooperativity coefficients were more potent in discriminating between the selected input period lengths for all levels of distortion. I computed $\overline{N}(P)$ within a simulation time window of 10^4 s. The applied parameter sets can be found in the appendix in Tables A.17, A.18 and A.19.

Tab. 4.7. Overview of input period lengths applied in the resolution assay presented in Figure 4.31.

input periods [s]	N	ΔT [s]
$T_1 = 10; T_2 = 100$	2	90
$T_1 = 10; T_2 = 55; T_3 = 100$	3	45
$T_1 = 10; T_2 = 40; \dots; T_4 = 100$	4	30
$T_1 = 10; T_2 = 25; \dots; T_7 = 100$	7	15
$T_1 = 10; T_2 = 20; \dots; T_{10} = 100$	10	10
$T_1 = 10; T_2 = 15; \dots; T_{19} = 100$	19	5
$T_1 = 10; T_2 = 12.5; \dots; T_{37} = 100$	37	2.5
$T_1 = 10; T_2 = 11; \dots; T_{91} = 100$	91	1
$T_1 = 10; T_2 = 10.5; \dots; T_{181} = 100$	181	0.5
$T_1 = 10; T_2 = 10.1; \dots; T_{901} = 100$	901	0.1

In order to determine a model's resolution limit with regards to discriminating between period lengths in the range from 10 s to 100 s, I estimated the channel capacity in this bandwidth using different scanning resolution levels ΔT . Here, I provide information about the input period lengths that I applied in estimations of channel capacity presented in Figure 4.31.

the discrimination between calcium period lengths (Figure 4.30). Model versions exhibiting smaller parameterizations of the cooperativity coefficient a , thus, less pronounced high-pass activation shapes, were less capable of discriminating between the applied calcium period lengths for all analyzed levels of distortion (Figure 4.30 A).

Next, I examined whether an increase in the cooperativity coefficient a as well as a decrease in the distortion level σ could lead to an improvement of the resolution limit with regards to discriminating between period lengths in the range from 10 s to 100 s. For this, I scanned the bandwidth of interest between 10 s and 100 s with various levels of resolution ΔT . Subsequently, I performed channel capacity estimations for every model version, input distortion level σ and resolution level ΔT . In Table 4.7, I provide an overview of the applied input period lengths in the resolution assay.

As shown in Figure 4.31, larger parameterizations of the cooperativity coefficient a led to an improved discrimination between input period lengths for almost all tested values of ΔT and σ . Only for a very low resolution level, for instance for $\Delta T = 90$ s, model versions performed equally well. In model versions exhibiting smaller parameterizations of a , the gain in additional information upon iterative decreases in ΔT stopped earlier for the same level of input distortion σ . Furthermore, for all model versions, larger levels of distortion (i.e., larger values of σ) went hand in hand with smaller channel capacity estimates in most cases. Only for particularly low scanning resolutions (i.e., large values of ΔT), there was no negative effect of large values of σ on a model's ability to discriminate between input period lengths. Also, when increasing the level of input distortion, models stopped earlier in gaining additional information upon iterative decreases in ΔT . Therefore, decreases in the input

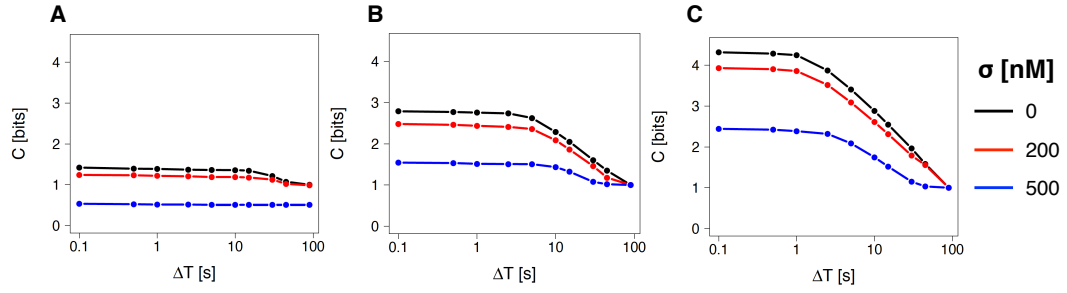


Fig. 4.31. Increases in cooperativity coefficients leading to increases in the high-pass activation efficiency allowed for an improvement of the resolution limit. By means of channel capacity estimations, I quantified the ability of different versions of the high-pass model (Table 4.6) to discriminate between input period lengths ranging from 10 s to 100 s. To this end, I scanned the bandwidth of interest with different resolution levels performing channel capacity estimations for every model version, distortion level σ and level of resolution ΔT (details on the applied input period lengths for each resolution level are given in Table 4.7). The model versions differed from each other in the efficiency of high-pass activation. In particular, model versions exhibiting larger parameterizations of the cooperativity coefficient a displayed more pronounced high-pass activation shapes (see Figure 4.29). $a = 1$ in (A), $a = 2$ in (B) and $a = 4$ in (C). Parameterizations exhibiting larger values of a performed better for almost all analyzed resolution levels (except for very large values of ΔT). Additionally, models exhibiting a larger parameterization of a stopped later in gaining additional information upon iteratively decreasing ΔT . Higher levels of input distortion reduced the model versions' decoding capabilities. The higher the level of distortion was, the sooner there was a stop to the additional gain in information upon iteratively decreasing ΔT . In conclusion, decreases in the input distortion level σ and increases in the cooperativity coefficient a allowed for a rise of the resolution limit in the high-pass model. The applied optimized parameter sets can be found in the appendix in Tables A.17, A.18 and A.19.

distortion level as well as increases in the parameterization of the cooperativity coefficient a clearly raised the resolution limit in the high-pass model.

4.15 Chapter discussion

4.15.1 Summary and conclusions

In this chapter, I presented kinetic models capable of performing two distinct forms of frequency-decoding, i.e., high-pass and band-pass activation. In high-pass activation, the activity of an oscillator-dependent protein is increased for fast frequencies, whereas it is decreased for slower frequencies. In band-pass activation, an oscillator-dependent protein exhibits an optimal frequency for maximal protein activity with frequencies slower or faster than the optimal frequency leading to a reduced protein activity. Both forms of frequency-decoding were described for calcium-dependent proteins in nature (see Section 1.2.3). Previously, Goldbeter *et al.* also published a model for high-pass activation that was extended for this work [56], while Aguilera *et al.* used a very similar kinetic model capable of performing band-pass activation in [48].

In the high-pass model, a decoding protein is regulated by a calcium-dependent activator and a constant calcium-independent deactivator. In contrast, in the band-pass model, the deactivator is calcium-dependent as well (Sections 4.2 and 4.3). The true nature of the protein modifications mediated by the regulators is left open, but several reversible protein modifications are known that are delivered by opposing enzyme entities, most prominently methylation-demethylation and phosphorylation-dephosphorylation modifications. Building on this, examples of calcium-dependent kinases and phosphatases do exist, for instance, conventional isoforms of PKC, CaMKII and calcineurin.

The transcription factor NFAT is targeted by both, a calcium-dependent kinase and a calcium-dependent phosphatase. In experiments, it was shown that NFAT exhibits band-pass activation [62, 64]. To this end, I assumed that the antagonistic, oscillator-dependent regulation was essential for the band-pass activation mechanism. And indeed, with the band-pass model, band-pass activation could be successfully recreated, while the same was not possible for the high-pass model that exhibited a calcium-dependent activator but lacked a calcium-dependent deactivator (Section 4.5, Figure 4.6). I proceeded to construct a more complex model featuring the calcium-dependent activation of NFAT to probe for band-pass activation of the transcription factor (Section 4.6). The model could successfully reproduce band-pass activation over a physiological bandwidth [64], while, at the same time, qualitatively agreeing with gene expression data [63]. Once again, band-pass activation was enabled by an antagonistic, oscillator-dependent regulation, in this case delivered by calcineurin and CaMKII. When removing this kind of regulation, the model failed in reproducing band-pass activation as well as in resembling experimental gene expression data (Figure 4.8).

A literature search on further signaling pathways that are antagonistically regulated by calcium-dependent kinase-phosphatase couples yielded several interesting results. For instance, Runyan *et al.* showed that calcineurin and CaMKII modulate the working memory exhibiting antagonistic roles to each other [185], while Wen *et al.* observed how calcineurin and CaMKII switch growth cone guidance control in axons [186]. Also in skeletal muscle differentiation, a conventional PKC isoform and calcineurin appear to work against each other [187]. This does not necessarily mean that components involved in these pathways exhibit band-pass

activation, yet it shows that antagonistic, calcium-dependent control is a recurring motif in cells increasing the likelihood of further instances of band-pass activation. Further, it needs to be mentioned that the decoding of calcium oscillation frequencies by dependent proteins was often not studied as extensively as necessary to confidently exclude the possibility of band-pass activation for known frequency-decoders currently categorized as high-pass decoders.

A large number of frequency-decoding, calcium-dependent proteins bind multiple calcium ions in a cooperative manner to gain full activity (Section 4.1.1, Table 4.1). Therefore, I implemented cooperative activation kinetics in the presented models. By means of optimizations, I then assessed the effect of the parameterization of cooperativity coefficients on the maximization of the high-pass and band-pass activation efficiency, Eff_H and Eff_B (Equations 4.2 and 4.4), i.e., the distinctness of high-pass and band-pass activation (Section 4.7). I observed that increased cooperativity coefficients fostered distinct high-pass and band-pass activation (Figures 4.10 and 4.11). However, in case of band-pass activation, increases in the model's cooperativity coefficients had to be balanced between the activating and deactivating model branch for an improvement of the frequency-decoding distinctness. Together with the finding that band-pass activation could not be recreated in the high-pass model that lacked a calcium-dependent deactivator (Figure 4.6), this is yet another indication for the necessity of a balanced, antagonistic and oscillator-dependent regulation for the generation of band-pass activation. Additionally, I found that a concatenation of cooperative events was most efficient in maximizing the frequency-decoding distinctness (Figures 4.10 and 4.11). Concatenative effects could play a role in the activation of proteins via calmodulin. For example, in case of calcineurin and CaMKII, two separate cooperative calcium binding events are needed for the proteins to gain full activity; cooperative binding of calcium to calmodulin and, subsequently, cooperative binding of calcium-calmodulin complexes to CaMKII or calcineurin [170, 171]. The overall conclusion that cooperativity was adopted by frequency-decoding proteins in the course of evolution in order to improve their frequency-decoding distinctness seems plausible with respect to the presented simulation data. Importantly, the relationship between cooperativity strength and the distinctness of frequency-decoding was already discussed in two other theoretical studies focusing on calcium signaling. In both, protein models were employed that were capable of performing high-pass activation [76, 87]. To the best of my knowledge, the presented results are unique in terms of the methodology that I used for analyzing the quantitative relationship between cooperativity strength and frequency-decoding distinctness as well as the fact that I included band-pass activation in my analysis.

Analyses of parameter sets capable of inducing distinct high-pass activation in the high-pass model or band-pass activation in the band-pass model allowed for an identification of conserved parameterization characteristics (Section 4.8). In case of high-pass activation in the high-pass model, the parameterization of the rate constants k_{A2} and k_{P2} appeared to be most important for the decoding distinctness at first glance (Figure 4.13 C and D). In contrast to the other rate constants, both of them were confined to particularly narrow parameterization margins. Moreover, for all analyzed parameterizations of the cooperativity coefficient a , k_{P2} was smaller than k_{P1} (Figure 4.15 C). Further analyses, however, revealed that k_{P2} 's parameterization was in fact connected to the model's default setup in which large, constant concentrations of Deact had to be balanced by smaller concentrations of Act. Thus, Deact's influence on the decoder Pr was regulated by decreases in the rate constant k_{P2} (Figure 4.16).

In case of band-pass activation in the band-pass model, the parameterization of the degradation rate constants was most important for distinct frequency-decoding, with k_{A2} and k_{D2} being the most confined parameters in the optimized parameter sets. Further, k_{A2} was always smaller than k_{D2} for all analyzed parameterizations of the cooperativity coefficient a and d (Figure 4.17 C). This observations was in line with my initial hypothesis in Section 4.3 that, for band-pass activation in the band-pass model, the activator had to be less responsive compared to the deactivator (Section 4.3). In this way, for intermediate oscillations, the activator only integrates the input oscillations staying on an elevated plateau, while the more responsive deactivator closely follows the oscillation dynamics exhibiting a lower average concentration. Therefore, the activator has a stronger impact on the decoder protein compared to the deactivator for intermediate oscillations resulting in the decoder's average concentration to peak. The described concentration advantage is lost for very fast input oscillations at which both regulators only integrate the upstream calcium dynamics or very slow oscillations at which both regulators closely follow the calcium oscillation dynamics. The relationship between the calcium oscillation frequency and the dynamics of regulator species is presented in Figure 4.4 in Section 4.3.

I found that, in most optimized parameter sets capable of inducing efficient high-pass or band-pass activation, binding constants lay between 10^3 nM and 10^6 nM (Section 4.13, Figures 4.13 E-G and 4.14 G-J). This margin is well in the reported norm for enzymes [184]. In most simulations, the calcium input was defined as a sine wave function oscillating between 200 nM and 1000 nM. I concluded that, especially for the calcium-binding constants K_A and K_D , the optimal parameterization margins were impacted by the calcium oscillation amplitude. And indeed, upon changes in the calcium oscillation amplitude, the optimal parameterization margins of K_A and K_D exhibited a significant sensitivity to the applied changes, with increases in the peak level of the calcium sine wave leading to a rise in the optimal parameterization margins of the dependent binding constants (Section 4.10, Figure 4.22).

Constrained optimizations, i.e., optimizations in which parameters were only allowed to vary in particularly confined intervals, shed more light on the frequency-decoding mechanisms in the presented models (Section 4.9). In order to perform high-pass or band-pass activation, rate constants needed to be parameterized in a way that allowed a system to be susceptible to changes in the bandwidth of interest (as defined by T_{fast} , T_{med} and T_{slow}). In case a system was forced to adapt to significantly smaller rate constants, frequency-decoding shifted towards slower bandwidths (Figure 4.20). Vice versa, in case a systems was forced to adapt to significantly larger rate constants, frequency-decoding shifted towards faster bandwidths (Figures 4.18 and 4.19). While in simulations rate constants can grow infinitely small or large, in reality there are clear limitations. On the one hand, biological systems need to react fast enough to a stimulation, since information transmission has to occur on a reasonable time scale and signaling components activated in response to a transient stimulation are degraded, eventually. On the other hand, very fast systems are likely linked to large energetic costs, for instance for kinase-catalyzed phosphorylations. Also with respect to binding constants, I conducted constrained optimizations. Again, I could detect an optimal parameterization margin for binding constants that was in line with results presented in Section 4.8.2. When forcing the systems to adapt to increasingly unfavorable binding constant parameterizations, first, I observed a reduction in the frequency-decoding distinctness and, eventually, a total breakdown of frequency-decoding (Figures 4.21). In all optimizations, I allowed rate and

binding constants to vary in physiologically relevant intervals. I chose corresponding intervals in reference to Bar-Even *et al.* who scanned through enzyme databases to analyze the distributions of kinetic enzyme parameters [184].

Furthermore, I identified a trade-off between the frequency-decoding precision and efficiency in band-pass activation (Section 4.11). Here, the precision was defined as the bandwidth size in which protein activity was intended to be increased, i.e., the bandwidth between T_{fast} and T_{slow} . For very narrow bandwidths, the band-pass activation efficiency E_B was clearly reduced and the decoder's average activity was slightly elevated for period lengths larger than T_{slow} or smaller than T_{fast} (Figure 4.24).

Molecular signaling pathways have to function in environments impacted by stochastic fluctuations. In particular, although the transmission of information from input signals is affected by fluctuations, output elements at the end of a signaling pathway have to be able to correctly infer the input signal. With respect to a frequency-decoding protein, the protein has to be able to interpret calcium oscillation frequencies in a reliable manner. Spurious interpretations of molecular signals can be detrimental affecting the survival of a cell and even of the whole organism. Thus, in the last part of this chapter, I analyzed a protein model's ability to discriminate between given calcium oscillation frequencies in the face of fluctuations. While I accounted for the inclusion of realistic fluctuation profiles by applying the Direct Method algorithm by Gillespie [157], I employed the information-theoretic measure of channel capacity to quantify the discriminability between given oscillation frequencies based on the average concentration of active decoder protein [17].

First, I applied channel capacity to investigate the impact of protein responsiveness on the decoding of a given set of frequencies (Section 4.13). For this, I employed the high-pass activation model and created three differently responsive versions of it. Channel capacity estimates showed that model versions performed best in terms of discriminating between fine differences in input frequencies in particular bandwidths (Figures 4.27 and 4.28). Thus, for a particular level of responsiveness there was a particular bandwidth best suited for the discrimination between input frequencies. This effect could be traced back to output proteins rising to plateau values in response to fast oscillations, while exhibiting almost identical oscillation amplitudes in response to slow oscillations. Since the output was defined as the average concentration of an active protein in a defined window of time, outputs to particularly fast or slow oscillations became indiscriminable. The same conclusion could also be drawn from visualizations of the model versions' high-pass activation shapes in Figure 4.29. A frequency-dependent, selective activation of proteins that is based on differences in protein responsiveness is imaginable, since calcium-dependent proteins were in fact shown to differ in their rate constants for calcium binding [85].

Further, I found that increases in the high-pass model's cooperativity coefficient a were linked to increases in the distinctness of high-pass activation under stochastic conditions. In Section 4.14, I applied channel capacity to examine whether particularly distinct high-pass activation shapes were more robust against fluctuations as well as could account for a finer frequency-decoding resolution with respect to the discrimination between frequencies in the quasi-linear part of the high-pass activation shape (Figure 4.31). To this end, my assumptions were based on the fact that, in particularly distinct high-pass activation, minor

changes in the calcium oscillation frequency resulted in large changes in the output measure. I observed that an increase in the amplitude of stochastic fluctuations led to more overlaps between input-signal-specific output distributions. Due to the more generous spacing between input-signal-specific output distributions, model versions exhibiting particularly pronounced high-pass activation were less affected. In conclusion, the cooperative activation of calcium-dependent proteins does not only allow for a clear discrimination between fast and slow frequencies, but also for an improved discrimination between fine differences in oscillation frequencies in an intermediate bandwidth in the presence of fluctuations.

4.15.2 Pitfalls for the application of channel capacity

In this chapter, I applied channel capacity to analyze stochastic simulation data. In particular, I defined a communication channel in which the calcium oscillation frequency served as an input and the average concentration of a calcium-dependent protein served as an output. To this end, I applied the information-theoretic measure for the following research questions: How well can a calcium-dependent protein discriminate between applied oscillation frequencies based on its average activity in the presence of stochastic fluctuations?

In order to estimate the channel capacity in a protein model, I used the Blahut-Arimoto algorithm (see Section 2.6). For this purpose, I had to collect input-signal-specific output distributions. Therefore, it had to be known which calcium oscillation frequencies were of relevance. Instead of assessing the discrimination of oscillation frequencies in general, channel capacity estimates can only shed light on the discriminability of selected oscillation frequencies. The generation of fast calcium oscillations might require large energetic costs, while very slow calcium oscillations might be impractical, since the transmission and decoding of the signal might require a lot of time. Thus, while an incorporation of extreme frequencies into the input alphabet could potentially lead to an increase in channel capacity, under physiological conditions, they might still not be considered due to competing interests. Vice versa, the application of channel capacity for the assessment of a system's decoding performance might lead to an underestimation, because the system might utilize input signals that were not considered.

In this chapter, the application of channel capacity was facilitated by the fact that it was applied to simulation data. In contrast, the application of channel capacity to experimental data is coupled to larger efforts. After all, relevant inputs need to be reapplied several times to the system of interest in order to allow for an assessment of stochastic effects on the output measure [148].

4.15.3 Simplifications in the applied communication channel

As mentioned before, in order to analyze frequency-decoding, I defined a molecular communication channel. While I declared the calcium oscillation frequency as the channel's input, I used the average concentration of a calcium-dependent protein as the channel's output. For large parts of this chapter, I employed sine wave functions to mimic calcium oscillations. In reality, however, calcium oscillations often exhibit more complex shapes. For instance,

physiological oscillation dynamics frequently exhibit a duty cycle, i.e., a separation into an active, above-baseline and an inactive, baseline part within a single oscillation cycle. Further, oscillation amplitude and frequency slightly vary between oscillation cycles.

In Section 4.6, I also successfully recreated band-pass activation upon using a square-wave function to resemble calcium oscillations. To this end, changes in the oscillation period T went hand in hand with changes in the duty cycle. Thus, the absolute duration of the active phase remained constant when changing the oscillation period. Additionally, band-pass activation could also be recreated in the NFAT model upon employing square-waves for which frequency modulations did not cause a change in the duty cycle (data not shown).

I measured the channel's output by measuring the average concentration of active, calcium-dependent protein in a defined window of time. Therefore, the output did not directly arise out of the model. This is justified by the assumption that downstream processes are slower than the model reactions, thus, dynamics of the output protein get integrated. However, when employing a particularly large time window for the computation of the output, a cellular integration mechanism becomes increasingly unrealistic, since proteins of the signaling pathway would be degraded, eventually. In this work, I employed physiologically plausible time spans for the computation of the output. In general, the usage of the average concentration of an active protein as a proxy of its average activity is a common practice in the analysis of calcium-dependent frequency-decoding (see for instance [79, 56]).

4.15.4 Simplifications in the NFAT model

In Section 4.6, I introduced an NFAT model to test whether the transcription factor could perform band-pass activation, while agreeing with gene expression data presented in [63]. For the latter, I employed a qualitative fitting procedure since the model's output, the average concentration of NFAT compounds competent for the transfer into the nucleus, was not directly comparable to the product of NFAT-mediated gene expression. Related to that, I assumed that frequency-decoding was already established in the cytosol and maintained in the nucleus. With this said, other decoding mechanisms are imaginable that, for instance, might introduce distinct frequency-decoding only after the transportation of NFAT into the nucleus.

Besides the exclusion of a nuclear compartment, the model's complexity was also reduced in terms of the calcium-dependent activation of calcineurin and CaMKII. Both proteins are activated via calmodulin. In case of CaMKII, around twelve sub-units form a super complex in which all sub-units can be existent in various forms that are characterized by different degrees of kinase activity [69]. Also in case of calcineurin, the protein can exist in different conformations that vary in their phosphatase activity [188]. By using a strongly simplified model structure, computational expenses were reduced.

In summary, the presented model was not intended to be an exact quantitative representation of NFAT activation. It has to be understood as a simplification for the purpose of probing for a possible band-pass activation mechanism of the transcription factor.

4.15.5 On the efficiency of the applied optimization workflow

Many of the results presented in this chapter were based on optimizations. Since I employed a local optimization algorithm, per optimization problem, a multitude of runs had to be launched to approximate a global solution. Especially for large cooperativity coefficients, the identification of the global optimum was associated with great computational efforts. In total, I executed and analyzed several hundreds of thousands of local optimization runs for this chapter alone leading to long queue times until final results could be obtained.

Initially, I tested faster local as well as global optimization algorithms in the intention of either accelerating or slimming down the workflow. Ultimately, only the Nelder-Mead algorithm, as implemented in R's `optim` function, provided the necessary reliability, however, at the expense of large computational expenses. Long computation times were countered by using multiple nodes on a computation cluster to run a large number of local optimizations in parallel. Further, I applied an automatic submission script to achieve a seamless transition from the execution of one optimization script to the next. Example scripts are provided on the attached data medium.

Despite its drawbacks, the applied workflow offered also unique advantages for the analysis of frequency-decoding. Due to the detection of multiple, quasi-optimal parameter sets for particular optimization problems, corresponding sets could be analyzed for shared traits that enabled peak performance. I concluded that strongly conserved parameterization characteristics or dependencies between parameters were crucial for the generation of distinct frequency-decoding.

Analyzing the encoding of attractant levels in the chemotaxis of *E. coli*

5.1 Chapter introduction

5.1.1 About this chapter

In this chapter, I present an analysis of signal transduction in another prominent example system: the chemotaxis pathway of *Escherichia coli*. Based on an established kinetic model by Kollmann *et al.* [3] (model details provided in Section 5.2), I focused my analysis on the encoding of ambient attractant levels into receptor methylation levels, as observed experimentally [134]. To this end, I identified requirements for the broad dynamic range in chemotaxis [109, 112] as well as reasons behind failures in the chemotactic behavior for attractant levels outside of the dynamic range.

In the chemotaxis pathway, information about absolute attractant levels is encoded into the methylation levels of chemoreceptors, with smaller attractant levels leading to fewer receptor methylations and vice versa [134]. Upon encountering a variation in attractant levels, a cell's receptor methylation status is changing. It is this transition that drives temporary responses in connected effector proteins culminating in directed cell locomotion [134]. In more detail, in case attractant levels are rising, the number of receptor methylations gradually increases. In this period of change, the concentration of active motor effector CheYp is decreased and the cell's tumbling frequency is reduced, thus, longer stretches of straight runs occur. In case attractant levels are declining, the number of receptor methylations gradually decreases. In consequence, CheYp levels temporarily increase along with the cell's tumbling frequency. Now, the average duration of straight runs is shortened [97, 98, 99, 100, 101, 102].

The chemotaxis system of *Escherichia coli* is characterized by a high sensitivity to relative changes in attractant levels for a broad dynamic range spanning several orders of magnitude [109, 112]. In response to variations in ambient attractant levels, effector proteins such as CheY change, initially, but recover back to pre-stimulation standard values, eventually [93, 113, 189]. In case adaptation is impaired, cells exhibit excessive tumbling or running that prevents a biased locomotion towards increasing attractant levels or away from increasing repellent levels [105, 106, 107]. In terms of time scales for adaptation, it is believed that pathway dynamics in chemotactic cells adapted to common living environments [93, 104, 190, 191]. In Section 5.3, I used the described hallmarks of chemotaxis to define the

model's dynamic range, i.e., the range of attractant levels, for which chemotaxis remained functional.

Next, I investigated whether the limitations in the model's dynamic range were already imposed by upstream limitations in the encoding of attractant levels into receptor methylation levels. To this end, I employed novel methods for the characterization of encoding in the chemotaxis system. For one, in Section 5.4, in cooperation with Jonas Förster¹, I inferred attractant levels from present receptor methylation levels to identify possible discrepancies between actually present and perceived attractant levels. Secondly, in Section 5.5, I employed delayed mutual information estimations to monitor the dynamical processes of memory formation and memory loss, whereas both processes related to directed changes in receptor methylation levels in response to changes in ambient attractant levels. While mutual information had been previously applied for the analysis of chemotaxis, for example, to measure information transmission between input ligand trajectories and output flagellar motor trajectories [192] or between input ligand trajectories and output motility directions [193], to the best of my knowledge, this was the first time it was used for characterizing the methylation-based chemotactic memory.

In *Escherichia coli* chemotaxis, receptor molecules can be methylated several times [194, 195]. Recently, experimentators attested a reduction in the dynamic range of the chemotaxis system in mutants exhibiting a lesser number of methylation sites per receptor molecule [196]. The same was suggested earlier on the basis of computational models by Tu *et al.* as well as Endres and Wingreen [197, 198]. Based on the aforementioned methods, I provide additional insights into the consequences of a reduced number of methylation sites on the system's encoding capabilities (see Section 5.6).

5.1.2 Outside assistance

I performed all estimations of mutual information by means of a KSG estimator provided by Irina Surovtsova and Martin Zauser.

Some of the presented results are reproductions of my colleagues', in particular of Jonas Förster and Aarón Vásquez-Jiménez. Reproductions are clearly highlighted as such in the captions of corresponding plots. Further, the idea of and the methodology for inferring attractant levels from present receptor methylation levels is credited to Jonas Förster¹.

¹Aarón Vásquez-Jiménez: Centro de Investigación y de Estudios Avanzados del IPN (Cinvestav-IPN), Unidad Monterrey, Mexico; others: Biological Information Processing Group at the BioQuant Center, Heidelberg University.

5.2 The employed model for *Escherichia coli* chemotaxis

For my analysis, I applied an *Escherichia coli* chemotaxis model from Kollmann *et al.* that is partly based on another model by Rao *et al.* [3, 128]. The model describes the response in the chemotaxis pathway upon changes in attractant levels. The authors of the model either adopted parameter values from published measurements [199] or optimized parameters, as described in the supplementary information in [3].

In Table 5.1, an overview of the model's kinetics and standard parameterization is given. In the model, the methyltransferase CheR leads to the emergence of methylated variants of the receptor T. More precisely, CheR can methylate T up to four times, whereas methylated receptor proteins are labeled as T_i . Here, the index denotes the number of methylations of the receptor protein. Only methylated receptor proteins can become active. To this end, the more methylations a receptor holds, the higher are the chances for its activation. In contrast, increases in the attractant level L result in a reduction of a receptor's activation probability. Both points are accounted for in Equations 5.1 to 5.4 that specify the activation probabilities of receptors exhibiting different numbers of methylations.

Active receptors T_{act} are able to cause the phosphorylation of the histidine kinase CheA that, in its phosphorylated state, can induce the phosphorylation of the motor regulator CheY. Phosphorylated CheYp is deactivated by means of an autodephosphorylation reaction as well as the constitutively active phosphatase CheZ. Since CheAp does not only phosphorylate CheY but also the methylesterase CheB, the model exhibits a negative feedback loop that culminates

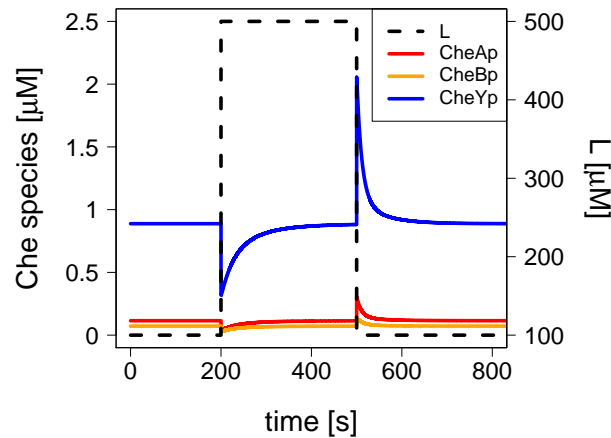


Fig. 5.1. Adaptation in the chemotaxis model after changes in attractant levels. Deterministic simulation results of the chemotaxis model from Kollmann *et al.* [3] showing the response in CheAp, CheBp and CheYp to assigned changes in attractant L . Immediately after an increase in L , a decline in the concentration levels of all three dependent variables can be observed. Subsequently, concentration levels return to pre-stimulation standard values. Conversely, after a decrease in L , the concentration levels of the three dependent variables briefly increase, before returning to their standard values. For model details, please refer to Table 5.1.

in the demethylation of active receptors via CheBp. Importantly, the phosphorylation of CheB is slower than the phosphorylation of CheY.

Therefore, in case the model is stimulated by an increase in attractant L , CheYp temporarily declines. In experiments, it was observed that a decrease in CheYp translates to longer stretches of straight runs that are less frequently interrupted by tumbles [97, 200, 98]. In the opposite case, after a decrease in L , CheYp temporarily increases. In experiments, this could be linked to an increase in the tumbling frequency and shorter stretches of straight runs [201, 202].

For a large range of attractant levels, the concentration levels of species of the phosphorylation cascade return to pre-stimulation standard values, as long as attractant levels stay constant. This sensory adaptation is crucial for the bacterium to retain a high sensitivity to further changes in attractant levels and to prevent the cell from prolonged running or tumbling motions [105, 106, 107, 203, 204]. The dynamics of downstream model species in response to variations in L are shown in Figure 5.1.

Tab. 5.1. Overview of the chemotaxis model's structure and kinetics.

Reactions	Kinetics	Parameterization
$T_0 \xrightarrow{\text{CheR}; T_{\text{tot}}} T_1$	$v_{C1} = \frac{k_{M1} \cdot \text{CheR} \cdot T_0}{K_{M1} + T_{\text{tot}}}$	$k_{M1} = 0.39 \text{ s}^{-1}; K_{M1} = 99.9 \text{ nM}$
$T_1 \xrightarrow{\text{CheBp}; T_{\text{act}}; T_{\text{act}1}} T_0$	$v_{C2} = \frac{k_{D1} \cdot \text{CheBp} \cdot T_{\text{act}1}}{K_{D1} + T_{\text{act}}}$	$k_{D1} = 6.3 \text{ s}^{-1}; K_{D1} = 2500 \text{ nM}$
$T_1 \xrightarrow{\text{CheR}; T_{\text{tot}}} T_2$	$v_{C3} = \frac{k_{M2} \cdot \text{CheR} \cdot T_1}{K_{M2} + T_{\text{tot}}}$	$k_{M2} = 0.39 \text{ s}^{-1}; K_{M2} = 99.9 \text{ nM}$
$T_2 \xrightarrow{\text{CheBp}; T_{\text{act}}; T_{\text{act}2}} T_1$	$v_{C4} = \frac{k_{D2} \cdot \text{CheBp} \cdot T_{\text{act}2}}{K_{D2} + T_{\text{act}}}$	$k_{D2} = 6.3 \text{ s}^{-1}; K_{D2} = 2500 \text{ nM}$
$T_2 \xrightarrow{\text{CheR}; T_{\text{tot}}} T_3$	$v_{C5} = \frac{k_{M3} \cdot \text{CheR} \cdot T_2}{K_{M3} + T_{\text{tot}}}$	$k_{M3} = 0.39 \text{ s}^{-1}; K_{M3} = 99.9 \text{ nM}$
$T_3 \xrightarrow{\text{CheBp}; T_{\text{act}}; T_{\text{act}3}} T_2$	$v_{C6} = \frac{k_{D3} \cdot \text{CheBp} \cdot T_{\text{act}3}}{K_{D3} + T_{\text{act}}}$	$k_{D3} = 6.3 \text{ s}^{-1}; K_{D3} = 2500 \text{ nM}$
$T_3 \xrightarrow{\text{CheR}; T_{\text{tot}}} T_4$	$v_{C7} = \frac{k_{M4} \cdot \text{CheR} \cdot T_3}{K_{M4} + T_{\text{tot}}}$	$k_{M4} = 0.39 \text{ s}^{-1}; K_{M4} = 99.9 \text{ nM}$
$T_4 \xrightarrow{\text{CheBp}; T_{\text{act}}; T_{\text{act}4}} T_3$	$v_{C8} = \frac{k_{D4} \cdot \text{CheBp} \cdot T_{\text{act}4}}{K_{D4} + T_{\text{act}}}$	$k_{D4} = 6.3 \text{ s}^{-1}; K_{D4} = 2500 \text{ nM}$
$\text{CheA} \xrightarrow{T_{\text{act}}} \text{CheAp}$	$v_{C9} = k_A \cdot \text{CheA} \cdot T_{\text{act}}$	$k_{A1} = 0.05 \frac{1}{\text{nM} \cdot \text{s}}$
$\text{CheAp} + \text{CheB} \rightarrow \text{CheA} + \text{CheBp}$	$v_{C10} = k_{B1} \cdot \text{CheAp} \cdot \text{CheB}$	$k_{B1} = 0.003 \frac{1}{\text{nM} \cdot \text{s}}$
$\text{CheBp} \rightarrow \text{CheB}$	$v_{C11} = k_{B2} \cdot \text{CheBp}$	$k_{B2} = 1 \text{ s}^{-1}$
$\text{CheAp} + \text{CheY} \rightarrow \text{CheA} + \text{CheYp}$	$v_{C12} = k_{Y1} \cdot \text{CheAp} \cdot \text{CheY}$	$k_{Y1} = 0.1 \frac{1}{\text{nM} \cdot \text{s}}$
$\text{CheYp} \xrightarrow{\text{CheZ}} \text{CheY}$	$v_{C13} = k_{Y2} \cdot \text{CheYp} \cdot \text{CheZ}$	$k_{Y2} = 0.03 \frac{1}{\text{nM} \cdot \text{s}}$
$\text{CheYp} \rightarrow \text{CheY}$	$v_{C14} = k_{Y3} \cdot \text{CheYp}$	$k_{Y3} = 0.1 \text{ s}^{-1}$

where concentrations of active receptor species are computed according to the following equations:

$$T_{\text{act}1} = 0.25 \cdot \left(1 - \frac{L^{1.2}}{L^{1.2} + 20^{1.2}} \right) \cdot T_1 \quad (5.1)$$

$$T_{\text{act}2} = 0.5 \cdot \left(1 - \frac{L^{1.2}}{L^{1.2} + 150^{1.2}} \right) \cdot T_2 \quad (5.2)$$

$$T_{\text{act}3} = 0.75 \cdot \left(1 - \frac{L^{1.2}}{L^{1.2} + 1500^{1.2}} \right) \cdot T_3 \quad (5.3)$$

$$T_{\text{act}4} = 1 \cdot \left(1 - \frac{L^{1.2}}{L^{1.2} + 60000^{1.2}} \right) \cdot T_4 \quad (5.4)$$

$$T_{\text{act}} = T_{\text{act}1} + T_{\text{act}2} + T_{\text{act}3} + T_{\text{act}4} \quad (5.5)$$

and T_{tot} refers to:

$$T_{\text{tot}} = T_0 + T_1 + T_2 + T_3 + T_4 \quad (5.6)$$

In the model by Kollmann *et al.* [3], CheR methylates the receptor T. Methylated versions of T can acquire an active status, whereas increases in attractant L decrease the chances of T's activation and a higher number of methylations increases them (Equations 5.1 to 5.4). Thus, in response to changes in L, the abundance of active receptors T_{act} temporarily deviates from standard values in adaptation. For decreases in L, T_{act} is briefly increased and vice versa. T_{act} controls the phosphorylation of CheA to CheAp which in turn phosphorylates CheY. Further, CheAp phosphorylates CheB setting off a negative feedback that allows for adaptation. In consequence, after a change in the attractant level, CheA, CheB, CheY, their active counterparts as well as T_{act} return to standard values eventually, as long as L remains constant.

5.3 Defining the chemotaxis model's dynamic range

In this section, I define the dynamic range of the chemotaxis model presented in Section 5.2, whereas the dynamic range is the range of attractant levels for which the following criteria of functional chemotaxis are fulfilled. For one, CheYp should be reasonably sensitive to relative changes in the attractant level. Secondly, CheYp should be able to recover back to a standard value range after a change in the attractant level. And thirdly, the recovery of CheYp should take place in a moderate period of time.

In more detail, Kollmann *et al.* stated that CheYp can only vary one-third from its standard value in fully adapted cells without exhibiting a chemotactic response. Outside of this range a cell "mainly tumbles" for increased CheYp or "swims continuously" for decreased CheYp [3]. To identify the standard value of CheYp in adaptation, I computed steady state concentrations for a range of attractant levels. As shown in Figure 5.2 A, steady state CheYp and T_{act} levels converge to their respective default values upon decreases in the constant attractant level. To this end, CheYp converges towards $0.89 \mu\text{M}$. and, for attractant levels larger than $10^{5.6} \mu\text{M}$, steady state CheYp levels dropped more than one-third from this standard value of $0.89 \mu\text{M}$. Thus, according to Kollmann *et al.*, for attractant levels larger than $10^{5.6} \mu\text{M}$, the cell would run indiscriminately. In Figure 5.2 A, I marked the corresponding threshold attractant level with a red dashed line. In contrast, for variations in the attractant level below the threshold, CheYp levels might temporarily rise or fall, as shown in Figure 5.1, but ultimately return to an

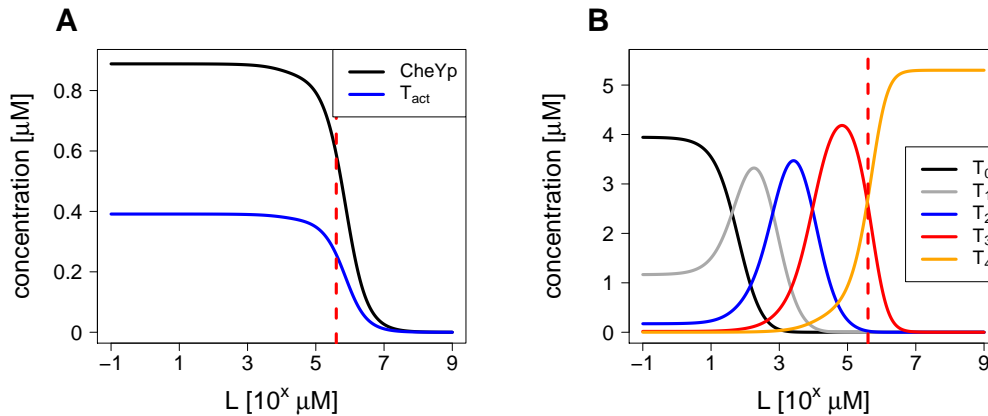


Fig. 5.2. Steady state behavior of biochemical species in the chemotaxis pathway to a broad range of constant attractant levels. Steady state results of the chemotaxis model from Kollmann *et al.* [3] in response to constant attractant level spanning from $10^{-1} \mu\text{M}$ to $10^9 \mu\text{M}$. For model details, please refer to Table 5.1. (A) Steady state CheYp levels mimicked those of T_{act} . For a large range of L , CheYp's adaptation remained functional. Only for ligand levels larger than $10^{5.6} \mu\text{M}$, steady state CheYp dropped more than 33 % from its standard value of $0.89 \mu\text{M}$ (boundary marked by a red dashed line). As a conclusion, for attractant levels larger than $10^{5.6} \mu\text{M}$, constantly low CheYp levels would translate into indiscriminable runs even in continuous environments or environments exhibiting negative attractant gradients. (B) Ambient levels of L are encoded into the methylation levels of the receptor T . For very small and very large levels of L , the ratio of methylation levels remained constant. Here, the system could not discriminate between variations in L . Shown are reproductions of plots by Jonas Förster.

adapted level allowing for a termination of the chemotactic response. In other words, sensory adaptation would be functional.

While the sensory adaptation was functional up to attractant levels of $10^{5.6} \mu\text{M}$, it remained open whether relative changes in L could lead to significant changes in CheYp levels that allowed for a chemotactic response. To get an idea of the model's sensitivity to variations in L , I increased L up to 300 % from a range of baseline levels spanning from $10^{-1} \mu\text{M}$ to $10^9 \mu\text{M}$. To this end, before increasing L , the system was always adapted to the selected attractant baseline level. In Figure 5.3 A, I captured the chemotactic response by measuring the absolute decline in CheYp from its baseline-adapted level in response to an increase in L . For very large attractant baseline levels, CheYp did not decline upon further increases in L . This result was consistent with Figure 5.2 A in which, for levels of L larger than $10^7 \mu\text{M}$, adapted CheYp was already close to zero. Thus, upon an increase in L , a further decrease in CheYp was impossible. Also for very small attractant baseline levels, no significant drop in CheYp was observed upon percental increases in L of up to 300 %.

According to Vladimirow *et al.*, a 20 % decrease in CheYp from its standard value of $0.89 \mu\text{M}$ results in a large 30 % increase in the CCW motor bias that should already drive a recognizable chemotactic response [129]. In Figure 5.3 B, I present, by means of a binary heatmap, the necessary magnitude of a percental increase in L to cause CheYp to temporarily fall below this threshold for a range of attractant baseline levels. Again, for particularly large baseline levels, even without further increases in L , CheYp was always below the 20 % threshold due to an

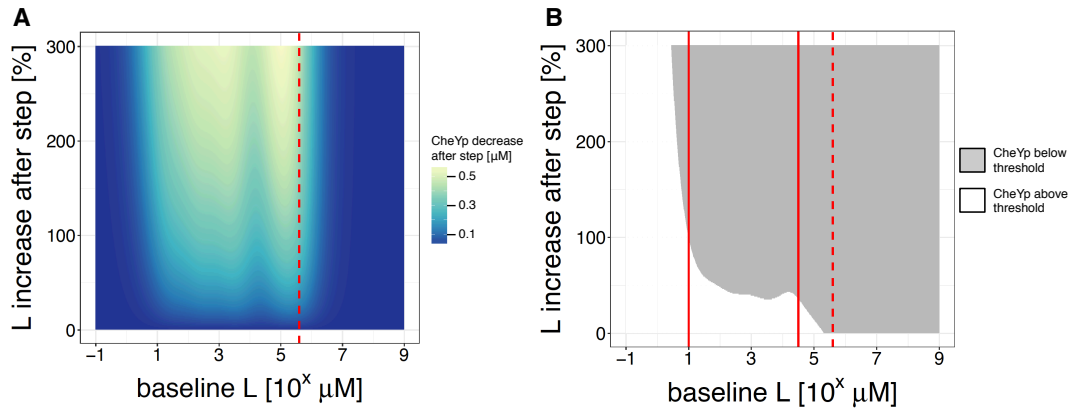


Fig. 5.3. Decreases in CheYp in response to sudden increases in L . In deterministic simulations, the chemotaxis model was first adapted to a baseline level of L , prior to being confronted with a sudden increase in L . Increases in L could result in a temporary drop in CheYp. In (A), I present the absolute magnitude of the drop in CheYp from its baseline-adapted value. For very small baseline levels, the system was not sensitive enough to react to the applied increases in L . Also for very large baseline levels, the system could not react to increases in L , this time due to an incomplete adaptation (see Figure 5.2 A; for large baseline levels, CheYp was already at a very low concentration and, thus, could not decrease any further). In (B), I identified all heatmap cells for which CheYp dropped more than 20 % from its standard value of $0.89 \mu\text{M}$. According to Vladimirow *et al.*, below the 20 % threshold of CheYp the CCW motor bias of the flagella is changed significantly making a chemotactic response very likely [129]. In the baseline level range spanning from $10^1 \mu\text{M}$ to $10^{4.5} \mu\text{M}$, the system exhibited a functional adaptation as well as a reasonable sensitivity to percental increases in L . Here, increases in attractant levels as small as 36 % would lead to a chemotactic response. The red dashed line marks the boundary at which adaptation started to fail. Red continuous lines confine the area between $10^1 \mu\text{M}$ to $10^{4.5} \mu\text{M}$ in which adaptation was functional and system sensitivity reasonable. (A) is a reproduction of a plot by Jonas Förster.

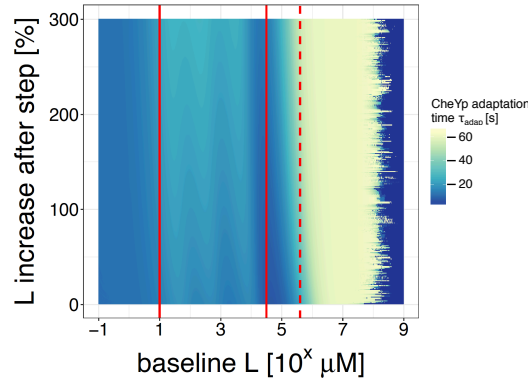


Fig. 5.4. Measurements of τ_{adap} after sudden increases in L. In deterministic simulations, the chemotaxis model was first adapted to a baseline level of L, prior to being confronted with a sudden increase in L. Increases in L could result in a drop in CheYp followed by its adaptation. Here, I measured the adaptation time τ_{adap} that was defined as the time period spanning from the moment the increase in L was applied to the moment CheYp rose to half of its new steady state value (that, for large parts of the analyzed baseline range, was very close to the standard value of $0.89 \mu\text{M}$). Between the baseline levels of $10^1 \mu\text{M}$ and $10^{4.5} \mu\text{M}$ (marked by red continuous lines), τ_{adap} was moderately large. For baseline levels larger than $10^{5.6} \mu\text{M}$ (marked by a red dashed line), adaptation was incomplete and partly required much more time. For extremely large baseline levels, measurements of τ_{adap} failed, since no drops in CheYp could be attested upon further increases in L. Shown is a reproduction of plots by Jonas Förster and Aarón Vásquez-Jiménez.

incomplete adaptation (see Figure 5.2 A). For baseline levels slightly smaller than $10^{5.6} \mu\text{M}$, adaptation barely worked, but even small increases in L could cause the system to surpass the adaptation threshold possibly leading to long stretches of indiscriminate running. In contrast, for a range of attractant levels spanning between $10^1 \mu\text{M}$ and $10^{4.5} \mu\text{M}$, adaptation was functional, while the system was also sensitive enough to react to increases in attractant levels as small as 36 % with a significant increase in the CCW motor bias.

In conclusion, the dynamic range of the chemotaxis model was confined by a lower boundary due to a finite system sensitivity and by an upper boundary due to a finite adaptation capacity. Limitations in the system's sensitivity could be also inferred from Figure 5.2 B. As mentioned in the chapter introduction, absolute attractant levels are encoded into receptor methylation levels. A chemotactic response, i.e., a change in the tumbling frequency of the cell, is driven by changes in attractant levels that cause a reorganization of these receptor methylation levels. However, in the model, for attractant levels smaller than $10^{-1} \mu\text{M}$ or attractant levels larger than $10^7 \mu\text{M}$, receptor methylation levels barely changed upon variations in L. For instance, in case L was increased from $10^{-1} \mu\text{M}$ to $10^{-0.5} \mu\text{M}$, receptor methylation levels would remain almost unchanged. Without a clear reorganization of receptor methylation levels, no signal is transmitted to the downstream effector module encompassing CheYp.

Still it needed to be determined whether the process of adaptation occurred on a reasonable time scale for changes in ambient attractant levels in the dynamic range. If adaptation was completed too soon, the cell would not have enough time to translate changes in CheYp into changes in cell locomotion. If adaptation was completed too late, the cell would not be flexible enough to react to new changes in attractant levels in time [93, 104, 190, 191]. To investigate the time scale for the adaptation process, I defined the measure τ_{adap} . To this end, τ_{adap} was

equal to the time period spanning from the moment L was increased to the moment CheYp reached half of its new steady state concentration.

As shown in Figure 5.4, τ_{adap} was very insensitive to the step size, but predominantly determined by the baseline level of L . For particularly large baseline levels of L , measurements of τ_{adap} failed due to the fact that CheYp was already at zero and could no longer respond to further increases in L . In the range of attractant baseline levels between $10^1 \mu\text{M}$ and $10^{4.5} \mu\text{M}$, the adaptation process required a moderate amount of time with a minimal τ_{adap} of 7.1 s and a maximal τ_{adap} of 26.9 s. In comparison, in experiments, Koshland quantified the persistence time, i.e., the time period a bacterium spends going up or down a gradient, to lie between 1 s and 10 s for *Salmonella* [190], suggesting a similar time scale for a related measure in a relative of *Escherichia coli* [205].

In conclusion, attractant levels between $10^1 \mu\text{M}$ and $10^{4.5} \mu\text{M}$ can be viewed as the model's ideal dynamic range, since all three hallmarks of chemotaxis, functional adaptation, reasonable sensitivity to relative changes in attractant levels and a moderate time scale for the adaptation process, are in check. In the following sections, I investigated how the system's dynamic range is dependent on the encoding of attractant levels into receptor methylation levels.

5.4 Inferring attractant levels from receptor methylation levels

5.4.1 Inferring attractant levels in continuous environments

Ambient attractant levels are encoded into receptor methylation levels in the chemotaxis of *Escherichia coli*. While downstream effector proteins such as CheAp and CheYp along with the abundance of active receptors T_{act} return to standard values after initially responding to changes in ambient attractant levels, receptor methylation levels do not (see Figure 5.2). Instead, for a large range of attractant levels, particular combinations of receptor methylation levels T_0 to T_4 arise.

In this section, based on the expected amount of active receptors T_{act} in adapted cells, that I defined to be equal to $0.39 \mu\text{M}$ as concluded from Figure 5.2 A, and present receptor methylation levels, I inferred the perceived attractant level L_{exp} . To this end, L_{exp} represents an approximation of the actually applied attractant level L . L_{exp} was computed according to the following equation:

$$T_{\text{act}1}(L_{\text{exp}}; T_1) + T_{\text{act}2}(L_{\text{exp}}; T_2) + T_{\text{act}3}(L_{\text{exp}}; T_3) + T_{\text{act}4}(L_{\text{exp}}; T_4) - \lambda = 0, \quad (5.7)$$

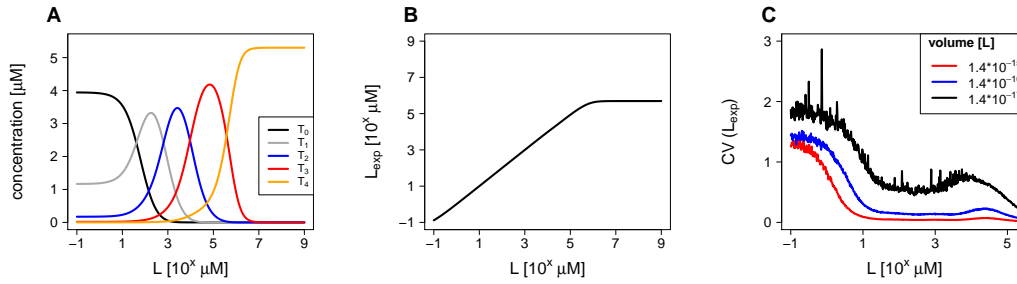


Fig. 5.5. Inferring L_{exp} in continuous environments given deterministic and stochastic conditions. (A) (B) I employed the steady state concentrations of the methylated receptor species T_1 to T_4 as inputs for Equation 5.7 to infer L_{exp} , an approximation of the actually applied attractant level L . The approximation was highly accurate for attractant levels between $10^{-1} \mu\text{M}$ and $10^6 \mu\text{M}$. For larger levels of L , L_{exp} did no longer resemble L . In conclusion, the system was unable to distinguish between levels of L that were larger than roughly $10^6 \mu\text{M}$. (C) To investigate the approximation of L under more realistic conditions, I ran stochastic simulations. In detail, per attractant level L , I ran 1000 stochastic simulations in order to compute 1000 L_{exp} values at a defined point in time. I used the obtained values to calculate L -specific coefficients of variation of L_{exp} . The described procedure was repeated several times for different system sizes. A decrease in the system size led to an increase in the relative fluctuation amplitude, thus, enhanced the impact of stochastic fluctuations. For L smaller than $10 \mu\text{M}$, the uncertainty in inferring the correct attractant level rapidly grew imposing a clear lower boundary for functional encoding in the chemotaxis system. A decrease in the relative fluctuation amplitude led to an overall increase in the coefficients of variation. Shown are reproductions of plots by Jonas Förster.

where T_{act1} to T_{act4} refer to Equations 5.1 to 5.4, that are functions of the present receptor methylation levels as well as L_{exp} , and λ is the standard value of active receptors in adapted cells. The equation was solved by employing the root finder function `uniroot()` in R. According to Equation 5.7, L_{exp} is synonymous to the attractant level for which T_{act} can return to its standard value λ . The original idea of and first implementations for inferring perceived attractant levels from the current state of the cell's methylation-based working memory are credited to Jonas Förster.

Upon using the steady state concentrations of the receptor species T_1 to T_4 as inputs for Equation 5.7, it was observable that the inferred L_{exp} levels were close to identical to the actually applied L levels for a large range of attractant levels spanning from 10^{-1} μ M to about 10^6 μ M (Figure 5.2 A and B). Therefore, in this range, an applied attractant level could be correctly inferred from present receptor methylation levels given deterministic noise-free conditions. For even larger attractant levels, however, L could no longer be correctly inferred. Since particularly large levels of L were associated with the same combination of receptor methylation levels, also L_{exp} did not vary. Therefore, for particularly large attractant levels, it appears that, based on present receptor methylation levels, a cell would only be able to recognize that an ambient attractant level is larger than roughly 10^6 μ M, but could not narrow down the actually applied attractant level more precisely.

To investigate the approximation of L under more realistic conditions, I employed stochastic simulations. In particular, per applied attractant level L , I obtained 1000 concentration samples of the receptor species T_1 to T_4 from 1000 stochastic simulations. These concentration values were used to compute 1000 values of L_{exp} according to Equation 5.7. Then, I used L -specific batches of L_{exp} values to calculate coefficients of variation of the L_{exp} estimates. I repeated the described procedure for different relative fluctuation amplitudes that I modulated by varying the system size. As shown in Figure 5.5 B, the coefficient of variation rose significantly for L levels smaller than 10 μ M indicating a growth in the uncertainty of L_{exp} . In other words, for particularly small attractant levels, fluctuations in receptor methylation levels severely impaired a reliable inference of L imposing a clear lower boundary of encoding in the chemotaxis system.

5.4.2 Inferring attractant levels in changing environments

Once a cell encounters a variation in ambient attractant levels, receptor methylation levels start to reorganize. It is this reorganization that drives a chemotactic response. For the results presented in Figure 5.6, I applied a rapid increase from 1 μ M to 10^5 μ M. Shown are transient responses in receptor methylation levels and the effector species T_{act} and CheYp. During the time receptor methylation levels were in transition, the effector species were still in the process of adaptation. The completion of the reorganization of receptor methylation levels roughly coincided with the completion of the adaptation process.

Here, I investigated what attractant level can be inferred from receptor methylation levels that are in transition. Thus, I applied an increase in L to a system that had been adapted to a baseline level of L . For different time points during the reorganization process, I isolated receptor methylation levels and used these concentrations as inputs for Equation 5.7 to infer

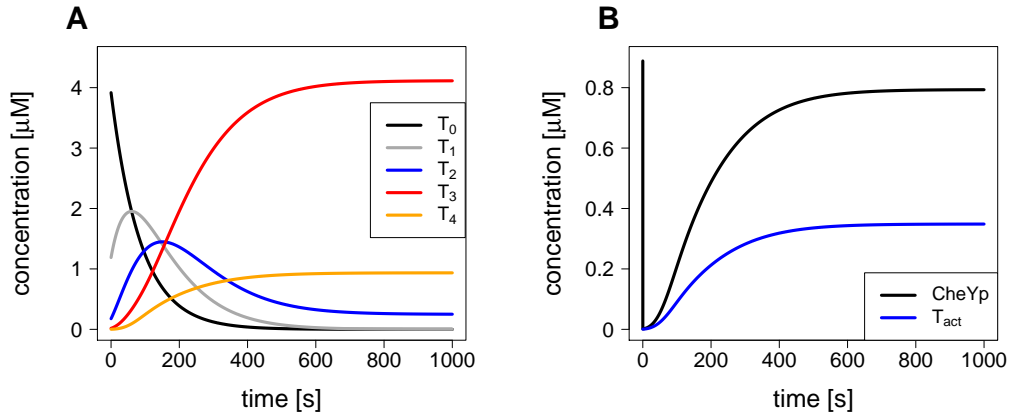


Fig. 5.6. Model response to a sudden increase in the attractant level from 1 μM to $10^5 \mu\text{M}$. Deterministic simulation results of the chemotaxis model from Kollmann *et al.* [3] showing the response to a sudden increase in the attractant level from 1 μM to $10^5 \mu\text{M}$. (A) The receptor methylation levels encode information about the absolute attractant level. The employed change in the attractant level led to a reorganization of receptor methylation levels. Thus, the previously encoded information was gradually overwritten. (B) While the methylation module was in transition, the connected effector module was, too. The full recovery of the effector module roughly coincided with the completion of the reorganization of receptor methylation levels.

transient estimates of L_{exp} . In Figure 5.6 A, the transition in L_{exp} is shown for an increase in L from 1 μM to $10^5 \mu\text{M}$. The rapid switch in L was interpreted as a gradual increase. Once receptor methylation levels stopped to vary, also L_{exp} stopped to change.

I defined $\tau_{L_{\text{exp}}}$, that is marked in Figure 5.7 A, as a measure of the build-up time of L_{exp} after an increase in L . $\tau_{L_{\text{exp}}}$ is the time period spanning from the moment L was raised to its

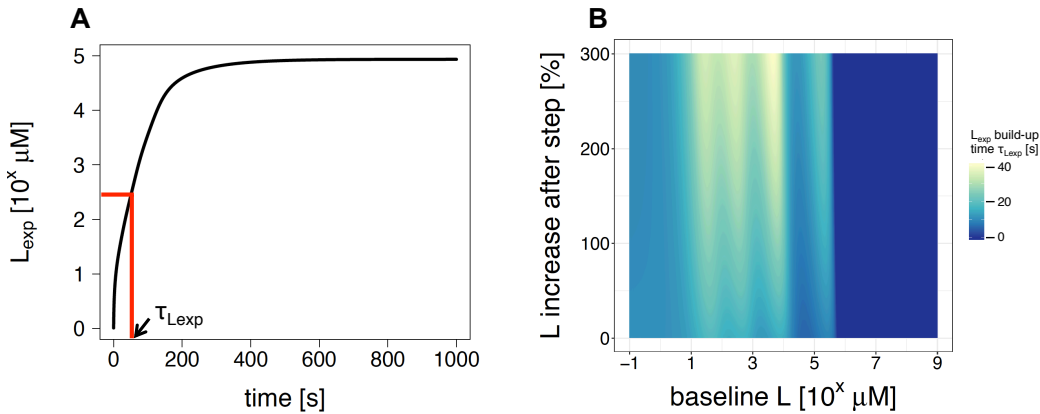


Fig. 5.7. Quantification of transient dynamics of L_{exp} build-up. (A) In a deterministic simulation, I stimulated the chemotaxis model, that was adapted to an attractant level of 1 μM , by suddenly increasing the attractant level to $10^5 \mu\text{M}$ at time point 0 s. Due to the reorganization of receptor methylation levels, also L_{exp} was changing. The sudden increase in L was interpreted as a gradual increase. L_{exp} was computed according to Equation 5.7. (B) I defined $\tau_{L_{\text{exp}}}$ as a measure of the build-up time of L_{exp} . It is the time period spanning from the moment L was increased to the moment L_{exp} reached half of its new steady state. A strong resemblance between measurements of $\tau_{L_{\text{exp}}}$ and τ_{adap} became apparent (see Figure 5.4). Therefore, I concluded a close relationship between the process of reorganization of receptor methylation levels and of adaptation of CheYp.

step level to the moment L_{exp} reached half of its new steady state value. Again, I increased L up to 300 % from a range of attractant baseline levels, this time measuring $\tau_{L_{\text{exp}}}$. As shown in Figure 5.7 B, there was a very strong resemblance between measurements of $\tau_{L_{\text{exp}}}$ and τ_{adap} that I defined as a time measure for the adaptation process of CheYp (see Figure 5.4). Both measures were very insensitive to the step size, but predominantly determined by the baseline level of L . Further, in both figures, four stripes, i.e., confined margins of L , were recognizable in which the measures exhibited particularly large values. Thus, the process of CheYp adaptation appears to be closely controlled by the process of reorganization of receptor methylation levels.

5.5 Analyzing the methylation-based memory by means of mutual information

Upon applying an increase in attractant levels, receptor methylation levels reorganize until they are adjusted to the new attractant level (see Figure 5.6 B). Since receptor methylation levels store information about ambient attractant levels, thus, function as a molecular memory of sort, the process of reorganization can be viewed as memory formation with regards to information about the new attractant level or memory loss with regards to information about the old attractant level. In this section, I describe the size of the methylation-based memory as well as time scales for memory formation and memory loss by means of estimations of mutual information. The presented methodology was applied to characterize further limitations in the encoding in the chemotaxis system. Since it can be used for the analysis of stochastic

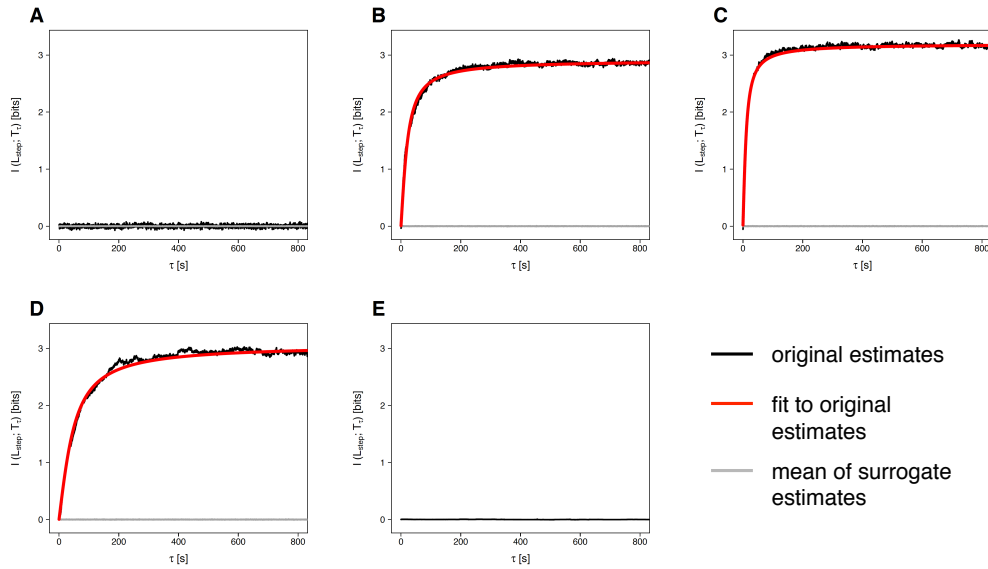


Fig. 5.8. Quantification of memory formation by means of estimates of mutual information between attractant step levels and receptor methylation levels at a given point in time. Per attractant baseline level (10^{-1} μ M, 10^0 μ M, 10^1 μ M, \dots , 10^8 μ M), I ran 1000 stochastic simulations in which the attractant level was increased to a step level at $\tau = 0$. Attractant step levels were drawn out of a uniform distribution spanning from the selected baseline level to the baseline level plus 200 %. Here, I present mutual information estimates between the baseline-specific batch of attractant step levels and the corresponding receptor methylation levels at a given point in time τ . Plots refer to the following attractant baseline levels: (A) 10^{-1} μ M, (B) 10^4 μ M, (C) 10^5 μ M, (D) 10^6 μ M, (E) 10^8 μ M. By changing τ , the process of memory formation could be visualized. Information about attractant step levels increased until convergence to a plateau level for intermediate attractant baseline levels (B, C, D). For very small or large attractant baseline levels, no memory formation could be detected (A and E). I employed surrogate estimations of mutual information to validate original estimates. For surrogate estimates, the L_{step} variable was permuted to disrupt original dependencies to T_τ , the matrix of receptor methylation levels at a given time point τ . Per original estimate, I performed 100 surrogate estimates. Shown are the mean values of such surrogate distributions in darkgrey. Further, in order to quantify the time period for memory formation, I fitted the original estimate data (black) to Equation 5.8 if memory formation was present. Fitted curves are presented in red. Applied system size: $1.4 \cdot 10^{-15}$ L. All remaining curves can be found in the appendix in Section B.1.

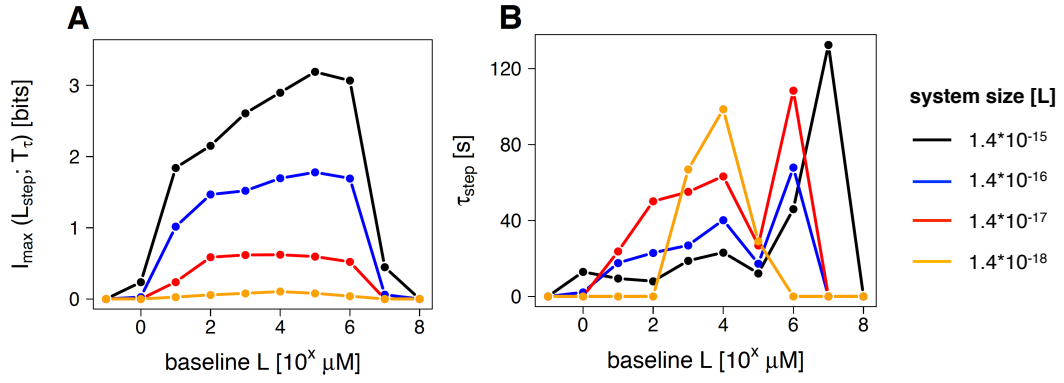


Fig. 5.9. System-size- and baseline-specific maximal estimates of mutual information and time scales for memory formation. For various system sizes and attractant baseline levels, I quantified the process of memory formation by means of estimations of mutual information. (A) For the largest system sizes, the most information about attractant step levels could be stored in the receptor methylation levels at an attractant baseline level of $10^5 \mu\text{M}$. Decreases in the system size, thus, increases in the relative amplitude of fluctuations, clearly led to a reduced memory size. (B) As shown in Figure 5.8, for intermediate attractant baseline levels, information about applied attractant step levels built up gradually. I fitted the obtained curves of mutual information estimates in dependence of τ to Equation 5.8. This allowed for measurements of τ_{step} that I defined as the time period spanning from the moment the attractant level was raised until the moment the fitted function reached half of its maximum. For very small and very large attractant baseline levels, no memory formation could be detected. Therefore, τ_{step} could not be measured for these baseline levels. For decreases in the system size, τ_{step} seemed to increase with regards to intermediate baseline levels. τ_{step} peaked at the largest analyzed baseline level for which memory could still be built up. All fits that I used for the presented results in (B) can be found in the appendix in Section B.1.

simulation data, it grants particularly valuable insights. For a mathematical notation of mutual information, please refer to Section 1.4.2.

For analyzing memory formation by means of mutual information, I stimulated the chemotaxis model by increasing the attractant level from a defined baseline level. In particular, I selected multiple baseline levels covering several orders of magnitude and, per baseline level, I drew 1000 attractant step levels out of a uniform distribution spanning from the selected baseline level to the baseline level plus 200 %. Per attractant baseline level, I applied the 1000 step attractant levels to the baseline-adapted system in 1000 stochastic simulations. Then, I monitored the model response by taking time-conditioned cross-sections of the receptor methylation levels T_0 to T_4 . Thus, per baseline level and per observed time point, I obtained 1000 concentration values of each receptor species in response to 1000 stimulations characterized by increases in the attractant level to different plateaus. I proceeded to estimate the mutual information between the applied batch of attractant step levels L_{step} and the corresponding receptor methylation levels at a given time point after model stimulation T_{τ} . Therefore, the estimates provided information on the discriminability of different attractant step levels based on receptor methylation levels at a given time point τ .

Increases in τ resulted in a rise in mutual information until convergence to a plateau level for intermediate attractant baseline levels (Figure 5.8 B, C and D). In conclusion, it took time until the maximal number of attractant step levels could be inferred from snapshots of receptor methylation levels. When repeating the experiment with very small attractant baseline levels ($10^{-1} \mu\text{M}$ in Figure 5.8 A) or very large attractant baseline levels ($10^8 \mu\text{M}$ in

Figure 5.8 E), no attractant step level could be identified by means of snapshots of receptor methylation levels and there was no measurable formation of memory. These results agree with previous observations that receptor methylation levels barely reorganized in response to a two-fold rise in attractant levels from very small or very large attractant baseline levels (see Figure 5.5 A).

In order to validate mutual information estimates, I performed surrogate estimations of mutual information by permutating L_{step} , thus, disrupting original dependencies between L_{step} and T_{τ} . Per original estimate, I performed 100 surrogate estimates. In Figure 5.8, darkgrey lines refer to the mean values of these surrogate estimate distributions. For more information about the application of surrogate estimates of mutual information, please refer to Section 2.5.

As observable in Figure 5.8, not only the maximal mutual information varied between analyzed attractant baseline levels, but also the time period required for memory formation. To obtain baseline-specific time scales for memory formation, I fitted the mutual information curves to the following function:

$$I(\tau) = a \cdot \frac{\arctan(\tau \cdot b^{-1})}{b} \quad (5.8)$$

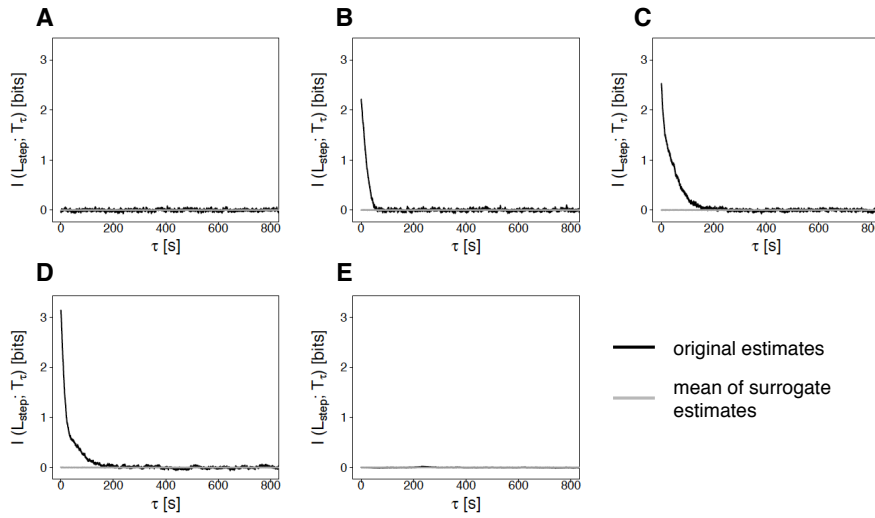


Fig. 5.10. Quantification of memory loss by means of estimates of mutual information between attractant step levels and receptor methylation levels at a given point in time. Per attractant baseline level ($10^{-1} \mu\text{M}$, $10^0 \mu\text{M}$, $10^1 \mu\text{M}$, \dots , $10^8 \mu\text{M}$), I ran 1000 stochastic simulations in which the attractant level was decreased from a step level to the selected baseline level at $\tau = 0$. Attractant step levels were drawn out of a uniform distribution spanning from the selected baseline level to the baseline level plus 200 %. Here, I present mutual information estimates between the baseline-specific batch of attractant step levels and the corresponding receptor methylation levels at a given point in time τ . Plots refer to the following attractant baseline levels: (A) $10^{-1} \mu\text{M}$, (B) $10^1 \mu\text{M}$, (C) $10^3 \mu\text{M}$, (D) $10^5 \mu\text{M}$, (E) $10^8 \mu\text{M}$. By scanning τ , the process of memory loss could be visualized. Information about attractant step levels gradually decreased until it was completely lost for intermediate attractant baseline levels (B, C, D). For very small or large attractant baseline levels, no memory loss could be detected, since there was no information about attractant step levels at $\tau = 0$ to begin with (A and E). I employed surrogate estimations of mutual information to validate original estimates. For surrogate estimates, the L_{step} variable was permuted to disrupt original dependencies to T_{τ} , the matrix of receptor methylation levels at a given time point. Per original estimate, I performed 100 surrogate estimates. Shown are the mean values of such surrogate distributions in darkgrey. Applied system size: $1.4 \cdot 10^{-15} \text{ L}$. All remaining curves can be found in the appendix in Section B.1.

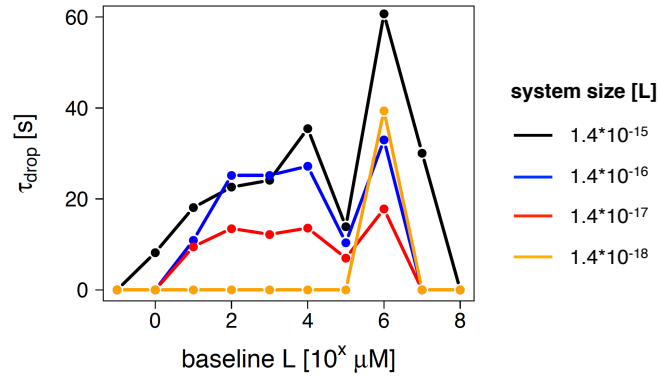


Fig. 5.11. System-size- and baseline-specific time scales for memory loss. For various system sizes and attractant baseline levels, I quantified the process of memory loss by means of estimations of mutual information. Based on data sets representing time-dependent mutual information estimates, as presented in Figure 5.10, I quantified τ_{drop} . To this end, I defined τ_{drop} as the time period spanning from the moment attractant levels were decreased at $\tau = 0$ to the moment time-dependent mutual information estimates fell below half of their initial information content. For very small or large attractant baseline levels, τ_{drop} could not be measured, since there was no information about attractant step levels at $\tau = 0$ to begin with. Generally, measurements of τ_{drop} were smaller than corresponding measurements of τ_{step} . Thus, memory loss appeared to be faster than memory formation in the analyzed chemotaxis system. All data sets that I used for the presented results can be found in the appendix in Section B.2.

in which I optimized parameters a and b to match the data at hand. I defined τ_{step} as the time period spanning from the moment the attractant level was raised (at $\tau = 0$) until the moment the fitted function reached half of its maximal value. Example fits can be found in Figure 5.8 B, C and D (red lines). For a full list of fitted parameters and corresponding curves, please refer to the appendix, Section B.1.

I repeated the described routine for several system sizes, thus, modulating the relative amplitude of fluctuations. In Figure 5.9, I present volume- and baseline-specific maximal estimates of mutual information $I_{max}(L_{step}; T_\tau)$ and time scale measurements for memory formation. When increasing the relative amplitude of fluctuations by decreasing the system size, maximal mutual information clearly decreased. Therefore, less attractant step levels could be discriminated by receptor methylation levels. For the largest employed system sizes, the methylation-based memory stored most information about attractant step levels for an attractant baseline level of $10^5 \mu M$. With regards to time scale measurements, for intermediate attractant baseline levels, decreases in the system size resulted in a slight increase in the required time for memory formation. Further, memory formation failed for particularly small or large attractant baseline levels, while τ_{step} peaked at the largest baseline level for which memory could still be built up. For smaller system sizes, the peak occurred at smaller attractant baseline levels.

In order to quantify memory loss by means of estimations of mutual information, per selected attractant baseline level, I ran 1000 stochastic simulations in which I decreased the attractant level from a step level to the selected baseline level at time point $\tau = 0$. Once again, I drew 1000 step levels from a uniform distribution spanning from the selected baseline level to the baseline level plus 200 %. Subsequently, I estimated the mutual information between the baseline-specific batch of step levels L_{step} and the matrix T_τ storing the corresponding receptor methylation levels T_0 to T_4 at a given point in time. As shown in Figure 5.10 B,

C and D, when increasing τ , previously stored information about attractant step levels was gradually lost for intermediate baseline levels. For particularly small or large baseline levels, no information about step levels was stored in the methylation-based memory at $\tau = 0$ (in agreement to results presented in Figure 5.8). Therefore, no information could be lost after a decrease in attractant levels given these extreme baseline levels (see Figure 5.10 A and E).

I repeated the described routine for several system sizes and attractant step levels. This time, I defined a time measure for memory loss τ_{drop} . To this end, τ_{drop} is the time period starting at $\tau = 0$, the moment in which I decreased attractant levels, and ending in the moment τ -dependent mutual information estimates fell below half of their initial information for $\tau = 0$. According to my measurements, the process of memory loss appeared to be faster than the process of memory formation (Figure 5.11).

5.6 Consequences of reducing the maximal number of receptor methylations

5.6.1 Loss in the dimensions of the dynamic range

In *Escherichia coli*, chemoreceptors possess multiple methylation sites. While Tar receptors can be methylated up to four times, Tsr and Tsg receptors exhibit even five methylation sites [206, 207, 208, 209]. In experimental as well as computational studies, researchers attested that, upon reducing the maximal number of receptor methylations, the dynamic range of the chemotaxis system is reduced [196, 197, 198]. In this section, I apply the previously introduced methodology (see Sections 5.3 to 5.5) to gain additional insights into the consequences of a reduction in the maximal number of receptor methylations on the system's encoding capabilities.

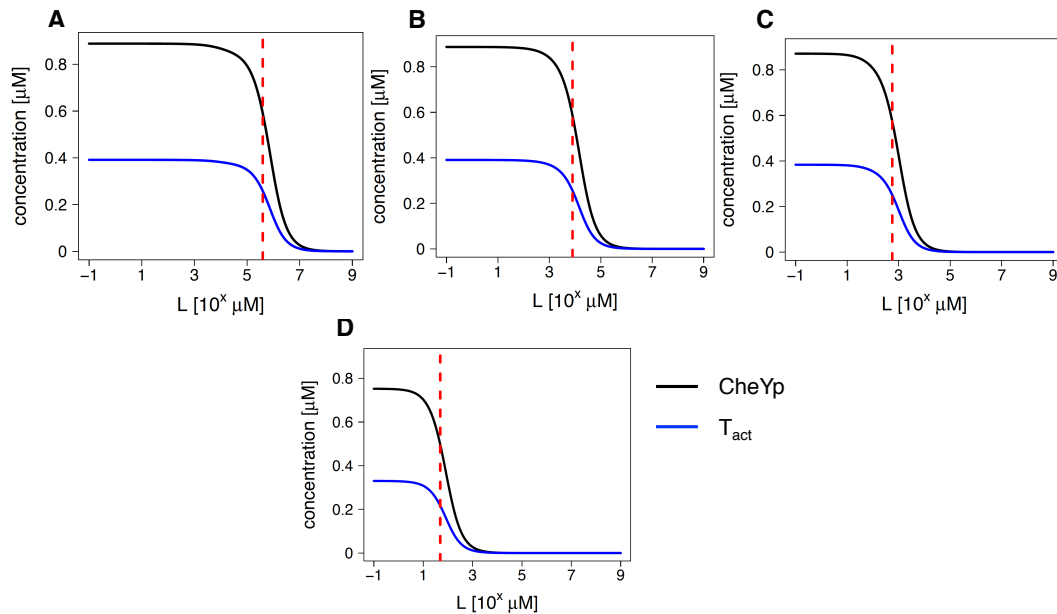


Fig. 5.12. Steady state behavior in the effector module for a range of attractant levels in model versions differing in the maximal number of receptor methylations. Deterministic simulations results showing the steady states of the effector species CheYp and T_{act} for a range of attractant levels in model versions differing in the maximal number of receptor methylations: in (A) up to four, in (B) up to three, in (C) up to two and in (D) up to one methylation(s) allowed per receptor. The standard value of CheYp in adapted cells was highly robust to changes in the maximal number of receptor methylations. A clear decline was only recognizable upon reducing the maximal methylation number to one. Standard CheYp values for different model versions: in (A) $0.89 \mu\text{M}$, in (B) $0.89 \mu\text{M}$, in (C) $0.87 \mu\text{M}$ and in (D) $0.75 \mu\text{M}$. In contrast, the range of attractant levels in which adaptation remained functional was very much sensitive to the applied changes. The smallest attractant level at which CheYp dropped more than 33 % from version-specific standard values: in (A) $10^{5.6} \mu\text{M}$, in (B) $10^{3.9} \mu\text{M}$, in (C) $10^{2.75} \mu\text{M}$ and in (D) $10^{1.69} \mu\text{M}$. In environments with attractant levels larger than these thresholds, I assumed that cells would exhibit indiscriminate runs, therefore failing in exhibiting functional chemotaxis. Version-specific threshold attractant levels are marked by red dashed lines.

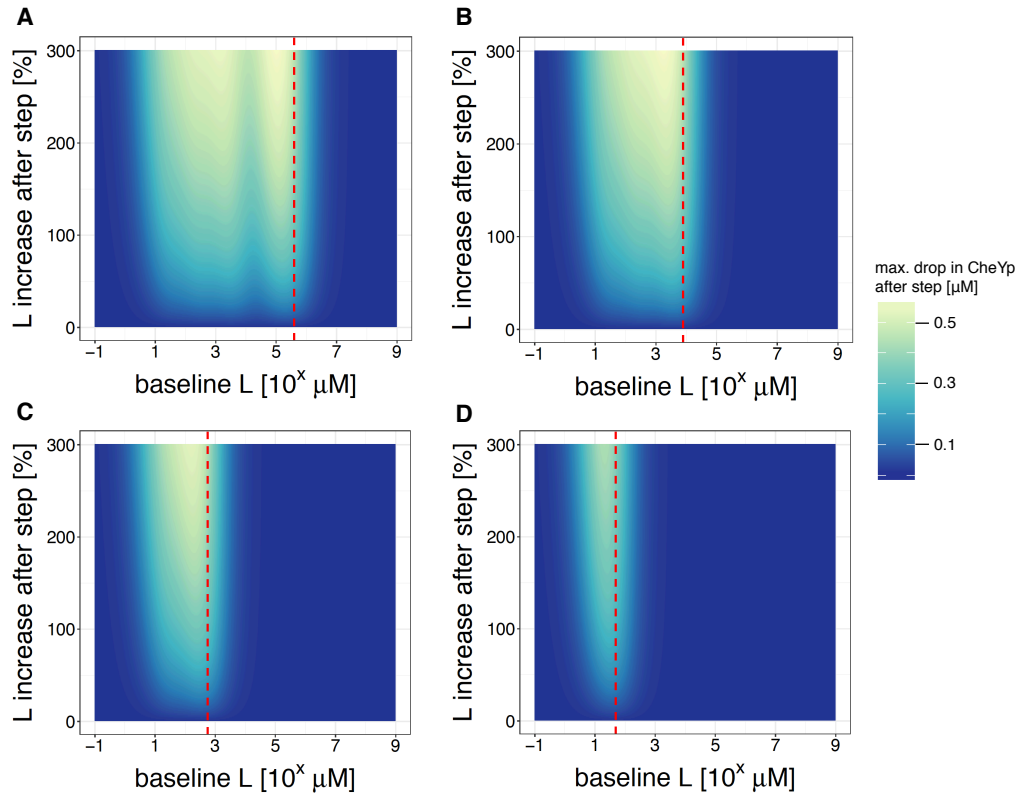


Fig. 5.13. Decreases in CheYp as a response to increases in L in model versions differing in the maximal number of receptor methylations. In deterministic simulations, several versions of the chemotaxis model were first adapted to a baseline level of L before being confronted with a sudden increase in the attractant level. Model versions differed from each other in the maximal number of receptor methylations: in (A) four, in (B) three, in (C) two and in (D) one methylation(s) allowed per receptor. Here, I present measurements of the absolute magnitude of the drop in CheYp from its baseline-adapted value in response to an increase in L. Clearly, decreases in the maximal number of receptor methylations caused a decrease in the upper boundary of attractant baseline levels at which CheYp responded with a drop. In contrast, the lower boundary of the dynamic range seemed to be stable to the applied changes. Overall, I could link a decrease in the maximal number of receptor methylations to a minor decrease in the CheYp drop amplitude. Maximal decrease in CheYp: in (A) 0.58 μM , in (B) 0.58 μM , in (C) 0.54 μM and in (D) 0.44 μM . Red dashed lines refer to the smallest baseline levels of L at which adaptation failed (as shown in Figure 5.5).

First, I needed to verify that the chemotaxis model by Kollmann *et al.* could confirm published reports, i.e., that a reduction in the maximal number of receptor methylations decreased the model's dynamic range. To this end, I generated three additional model versions that differed from each other in the maximal number of receptor methylations. For a maximal methylation number of three I deleted reactions v_{C7} and v_{C8} plus Equation 6.4, for a maximal methylation number of two I deleted reactions v_{C5} to v_{C8} plus Equations 6.3 and 6.4 and for a maximal methylation number of one I deleted reactions v_{C3} to v_{C8} plus Equations 6.2 to 6.4. I also edited Equations 5.5 and 5.6 by deleting corresponding receptor methylation levels. A full list of reactions and equations of the original model can be found in Table 5.1.

In a first analysis, I examined adaptation in the effector module given continuous environments. In Figure 5.12, I present model-version-specific steady state concentrations of CheYp and T_{act} for a range of constant attractant levels. The standard values of CheYp and T_{act} in adapted cells, i.e., the steady state concentrations of the effector species for particularly low attractant

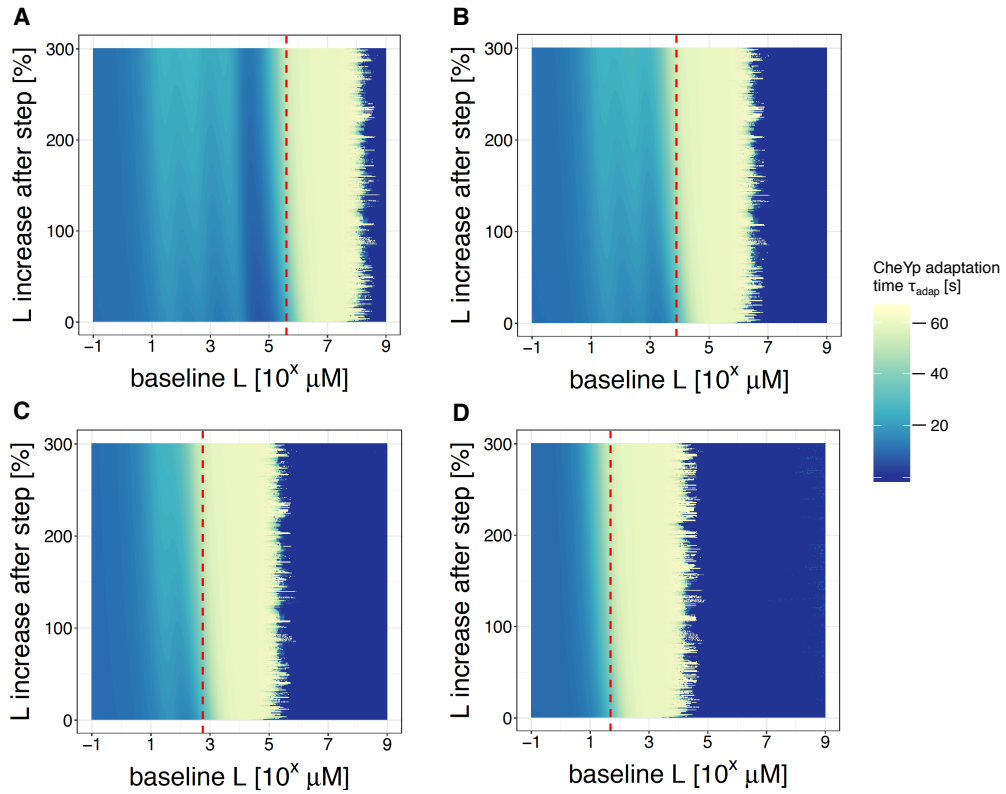


Fig. 5.14. Measurements of τ_{adap} after sudden increases in L in model versions differing in the maximal number of receptor methylations. In deterministic simulations, several versions of the chemotaxis model were first adapted to a baseline level of L before being confronted with a sudden increase in the attractant level. Model versions differed from each other in the maximal number of receptor methylations: in (A) four, in (B) three, in (C) two and in (D) one methylation(s) allowed per receptor. Here, I present measurements of the CheYp adaptation time τ_{adap} that I defined as the time period spanning from the moment the increase in L was applied until the moment CheYp recovered to half of its new steady state. As in Figure 5.13, the upper boundary of attractant baseline levels was highly sensitive to the applied changes, while the lower boundary was not. In each panel, stripes were recognizable, i.e., short confined margins of baseline levels in which τ_{adap} was particularly increased. The number of stripes was equal to the maximal number of receptor methylations.

levels, turned out to be very robust to the applied changes. Only for a maximal methylation number of one, standard values indicated a clear decrease. In contrast, the applied changes had a much stronger impact on the range of attractant levels in which adaptation remained functional. As mentioned in Section 5.3, for a 33 % decrease in CheYp from its standard value, a cell was expected to exhibit indiscriminable runs (according to [3]). Upon reducing the maximal receptor methylation number, the 33 % threshold was reached for increasingly lower attractant levels (thresholds marked by red dashed lines in Figure 5.12). For this and the following analyses, I assumed model-version-specific standard values of CheYp and T_{act} . Thus, I considered a scenario in which the bacterium evolved given a particular maximal receptor methylation number, rather than a scenario in which mutations caused a reduction in the maximal methylation number in some cells.

Based on Figure 5.12, I could attest that decreases in the maximal number of receptor methylations led to a clear reduction in the dynamic range. In particular, the applied changes led to decreases in the upper boundary of the dynamic range. According to additional results

presented in Figure 5.13, the lower boundary of the dynamic range was more robust to the applied changes. All model versions seemed to be similarly sensitive to percental increases from particularly low attractant baseline levels. Upon reducing the maximal number of receptor methylations, I could only attest a minor overall decrease in the magnitude of the CheYp response (quantitative information provided in the caption of Figure 5.13).

With regards to the CheYp adaptation time measure τ_{adap} (first defined in Section 5.3), all model versions exhibited moderate values between attractant baseline levels of $10^1 \mu\text{M}$ and the version-specific 33% threshold (marked by red dashed lines in Figure 5.14). Within the mentioned intervals, narrow margins of attractant baseline levels were recognizable in which τ_{adap} was slightly increased. The number of these stripe-like margins was equal to the maximal number of receptor methylations.

5.6.2 Loss in the dimensions of the encoding range

Previously, in Section 5.4, I found that limitations in the dynamic range of the original chemotaxis model were imposed by limitations in the encoding of attractant levels into receptor methylation levels. As decreases in the maximal number of receptor methylations further affected the dimensions of the dynamic range (see Section 5.6.1), I assumed that this was connected to stronger limitations in the encoding of attractant levels. And indeed, in Figure 5.15 A-D, it became evident that the range in which attractant levels could be uniquely mapped to specific combinations of receptor methylation levels was increasingly confined upon reductions in the the maximal number of receptor methylations.

I could draw the same conclusions from model-version-specific computations of L_{exp} (as introduced in Section 5.4.1). When computing L_{exp} based on steady state concentrations of receptor methylation levels for a number of attractant levels (Figure 5.15 E), the upper boundary of the range in which attractant levels were correctly inferred was gradually lowered upon decreases in the maximal number of receptor methylations. I computed L_{exp} according to version-specific variations of Equation 5.7. In particular, I deleted obsolete summands from the equation and adapted the parameterization of λ to a version-specific value (model-version-specific parameterizations of λ are provided in the caption of Figure 5.15).

In Section 5.4.1, I also investigated the robustness of estimations of L_{exp} in the presence of stochastic fluctuations. In particular, per constant attractant level L , I ran 1000 stochastic simulations to compute 1000 estimates of L_{exp} . Similarly, in Figure 5.16, I present the coefficients of variations of baseline-specific L_{exp} distributions in each model version. All model versions behaved very similar. Only for very large relative fluctuation amplitudes, as modulated by reductions in the system size, differences between model versions became apparent. The model version exhibiting a maximal receptor methylation number of only one appeared to be slightly less affected by the applied fluctuations with respect to estimations of L_{exp} for particularly low attractant levels (Figure 5.16 D).

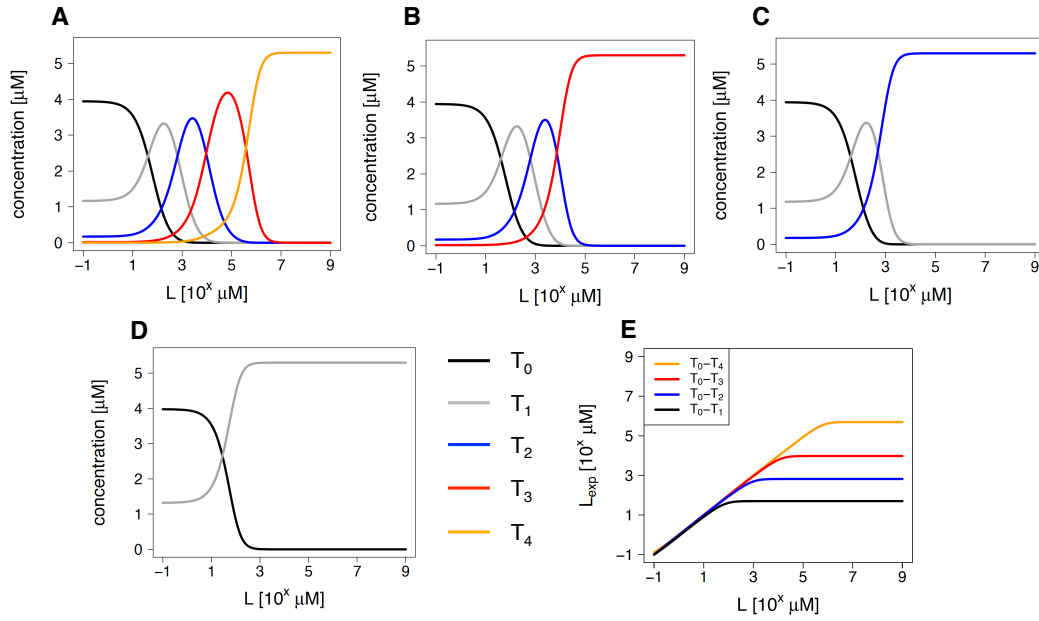


Fig. 5.15. Encoding of attractant levels into receptor methylation levels in model versions differing in the maximal number of receptor methylations. Panels (A-D): Deterministic simulations results showing the steady states of receptor species in response to a range of constant attractant levels in model versions differing in the maximal number of receptor methylations: in (A) up to four, in (B) up to three, in (C) up to two and in (D) up to one methylation(s) allowed per receptor. For E, I computed expected attractant levels L_{exp} based on steady state receptor methylation levels shown in panels (A-D). In particular, for the computation of L_{exp} , I employed Equation 5.7 which I adapted for specific model versions by deleting obsolete summands and updating the parameterization of λ : for a maximal methylation number of four or three (orange and red lines in (E)), λ was set equal to $0.39 \mu\text{M}$, for a maximal methylation number of two (blue line), λ was set equal to $0.38 \mu\text{M}$ and, for a maximal methylation number of one (black line), λ was set equal to $0.33 \mu\text{M}$. λ is the standard value of T_{act} in adapted cells and can be derived from Figure 5.12. The obtained results suggest that particularly large attractant levels could not be distinguished based on receptor methylation levels. Reducing the maximal number of receptor methylations led to an earlier onset of this failure.

5.6.3 Shifts in the optimal attractant baseline level for memory formation

As changes in the maximal number of receptor methylations clearly impacted the encoding of attractant levels (see Section 5.6.2), here, I analyzed the effect of these changes on memory formation. To this end, I applied the methodology introduced in Section 5.5 using delayed mutual information estimates.

More precisely, per model version exhibiting different maximal numbers of receptor methylation and per analyzed attractant baseline level, I ran 1000 stochastic simulations in which I increased the attractant level to specific step levels at time point $\tau = 0$. Again, step levels were drawn from uniform distributions spanning between the selected baseline level to the baseline level plus 200 %. I then measured the mutual information between the model-version- and baseline-specific batch of step levels L_{step} and corresponding receptor methylation levels which were summarized in the matrix T_τ , whereas columns of T_τ contained receptor-methylation-level-specific concentration values at a time point τ . Thus, for a model version with a maximal receptor methylation number of two, T_τ comprised three columns for T_0 , T_1 and T_2 . By

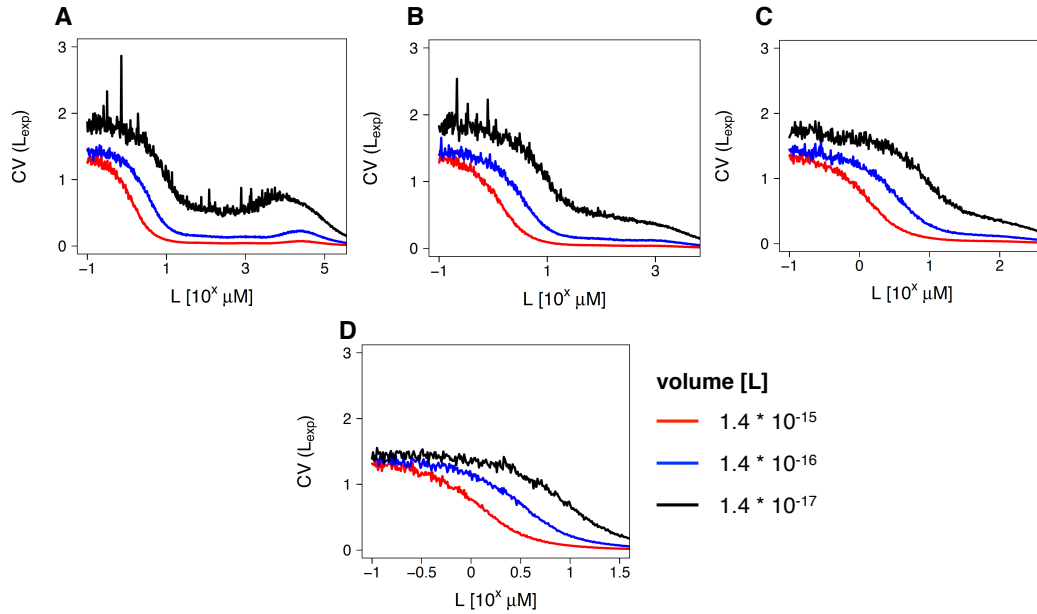


Fig. 5.16. Robustness against fluctuations in inferring L in model versions differing in the maximal number of receptor methylations. In stochastic simulations, I stimulated different versions of the chemotaxis model with constant attractant levels L . Model versions differed from each other with respect to the maximal number of receptor methylations: in (A) up to four, in (B) up to three, in (C) up to two and in (D) up to one methylation(s) allowed per receptor. Per constant attractant level, I repeated stochastic simulations 1000 times in order to be able to compute L -specific coefficients of variation of L_{exp} distributions. In particular, I analyzed a range of attractant levels L spanning from $10^{-1} \mu\text{M}$ to the version-specific threshold value, as presented in Figure 5.12. To this end, I computed L_{exp} according to model-version-specific adaptations of Equation 5.7. For more details, please refer to the caption of Figure 5.15. In turn, the described procedure was repeated for various relative fluctuation amplitudes, as modulated by alterations in the system size. For L smaller than $10 \mu\text{M}$, the uncertainty in inferring L from receptor methylation levels rapidly grew in all model versions. For particularly large relative fluctuation amplitudes (small system sizes) and small attractant levels, the model version with a maximal receptor methylation number of one appeared to be less affected by stochastic fluctuations (D).

scanning τ , I could visualize the process of memory formation, as shown in Figure 5.8. The obtained mutual information estimates informed about the discriminability of step levels based on snapshots of the methylation-based memory.

In Figure 5.17, I present the maximal memory size in different model versions, for various attractant baseline levels and system sizes. To this end, decreases in the system size enhanced the relative amplitude of stochastic fluctuations. Thus, it was to be expected that a decrease in the system size impaired information transmission. Once again, I could determine a reduction in the encoding range upon decreases in the maximal number of receptor methylations, i.e., for model versions exhibiting a smaller number of maximal receptor methylations, memory formation failed for smaller attractant baseline levels. Further, the optimal attractant baseline level associated with the maximal memory size shifted towards smaller baseline levels upon decreases in the maximal number of receptor methylations. Interestingly, the maximal memory size was highly robust against the applied changes in the maximal number of receptor methylations. All model versions appeared to be similarly affected by increases in the relative amplitude of fluctuations.

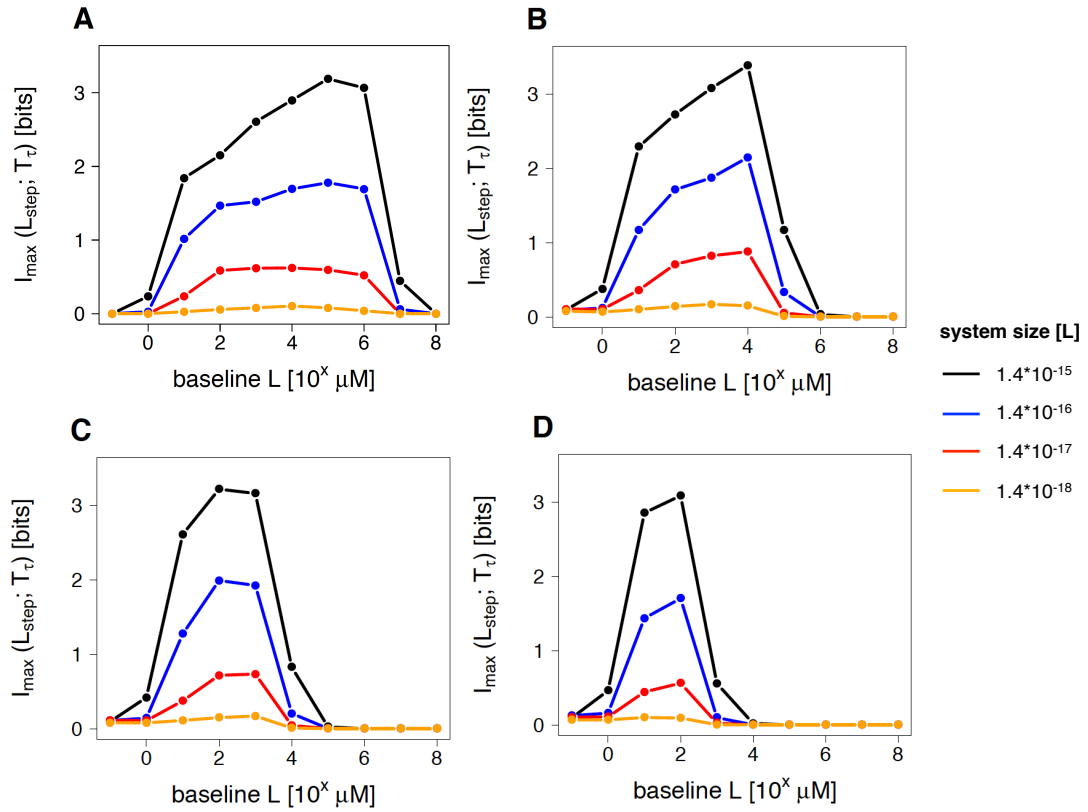


Fig. 5.17. Maximal estimates of mutual information between batches of attractant step levels and snapshots of receptor methylation levels in model versions differing in the maximal number of receptor methylations. For various model versions, system sizes and attractant baseline levels, I quantified the maximal mutual information in memory formation, as previously shown in Figure 5.8. Model versions differed from each other in the maximal number of receptor methylations: in (A) four, in (B) three, in (C) two and in (D) one methylation(s) allowed per receptor. Decreases in the maximal number of receptor methylations clearly reduced the encoding range, i.e., model versions with a lower maximal number of receptor methylations failed to build up a memory on attractant step levels for smaller attractant baseline levels. The optimal baseline level related to the maximal memory size shifted towards smaller baseline levels upon decreases in the maximal number of receptor methylations. All model versions were similarly affected by increases in the relative amplitude of stochastic fluctuations.

For additional information about measurements of τ_{step} and τ_{drop} in the presented model versions, please refer to the appendix, Section B.3.

5.7 Chapter discussion

5.7.1 Summary and conclusions

In this chapter, I investigated the encoding of absolute attractant levels into receptor methylation levels by means of an established kinetic model by Kollmann *et al.* [3]. The model, that is described in Section 5.2, allowed for an analysis of responses in the chemotaxis pathway of *Escherichia coli* upon changes in ambient attractant levels. It is of note that the model does not include cell movement. Thus, statements on cell locomotion had to be inferred from levels of phosphorylated motor effector CheYp. In experiments, CheYp levels were found to be sensitive to changes in attractant levels. In particular, increases in attractant levels led to temporary decreases in CheYp, while decreases in attractant levels resulted in temporary increases in CheYp. In turn, decreased CheYp levels reduced the tumbling frequency of cells, while increased CheYp levels raised the tumbling frequency [97, 98, 99, 100, 101, 102].

After a change in ambient attractant levels within the dynamic range of the system, CheYp levels return to pre-stimulation standard values, as long as the chemotaxis pathway is not triggered again by another change in attractant levels. If this sensory adaptation mechanism is impaired, cells exhibit excessive tumbling or running and cannot purposefully respond to further changes in attractant levels [105, 106, 107]. In addition, adaptation retains sensitivity to a broad range of attractant or repellent levels covering several orders of magnitude. For example, gradient detection of aspartate was found to be successful with regards to relative changes from nanomolar or millimolar abundances of the attractant [132, 210, 211].

In Section 5.3, I described the dynamic range of the analyzed chemotaxis model, i.e., the range of attractant levels in which chemotaxis was functional. To this end, I defined the dynamic range on the basis of the following criteria: a successful adaptation of the model species CheYp, a high sensitivity to relative changes, as detected by temporary changes in CheYp levels, and an appropriate time window for CheYp adaptation in response to a new attractant level. I found that the dynamic range was confined by a lower boundary due to a finite system sensitivity and by an upper boundary due to a finite adaptation capacity. In particular, I attested unsuccessful adaptation, if CheYp levels deviated more than one-third from a standard value in adapted cells, as Kollmann *et al.* proposed that this would lead to cells being unable to "properly respond to stimuli" [3] (Figure 5.2 A). According to the presented results, a cell would run indiscriminately, when encountering attractant levels larger than $10^{5.6}$ μM , and would not be able to detect gradients, if absolute attractant levels were larger than the aforementioned threshold.

In my analysis, I assessed the sensitivity of the system by applying relative increases in attractant levels, whereas I scanned the attractant baseline level as well as the percental magnitude of the increase (Figure 5.3). Under natural conditions, most chemotactic bacteria do not encounter large singular jumps in ambient attractant levels. It is more likely that, as a bacterium follows an attractant gradient, ambient attractant levels rise incrementally. While a single increase might only lead to a minor deviation in CheYp levels from the standard value in adapted cells, the same increase soon followed up by yet another increase of identical magnitude might result in a much larger drop in CheYp. Additive effects in the chemotaxis

pathway were previously also reported with regards to the adaptation time of CheA [132, 133]. Furthermore, saturating effects might also have to be taken into account, as, based on an *in silico* study, Vladimirov *et al.* reported that linear and Gaussian gradients of attractant levels up to 100 μM initially resulted in a stimulation of CheYp levels. However, with time, CheYp levels started to recover despite the continued presence of the attractant gradient [129]. In conclusion, the dynamic range that I described is valid for a particular scenario in which I used a single sudden increase in attractant levels for model stimulation. It might change for other scenarios, particularly scenarios considering attractant gradients.

In the described dynamic range of the model, the adaptation of CheYp took place in a moderate window of time upon increases in attractant levels of up to 300 %. In contrast, adaptation required much more time for increases from attractant baseline levels between $10^{5.6}$ μM and 10^8 μM (Figure 5.4). I quantified the adaptation time of CheYp by means of the measure τ_{adap} that I defined as the time period spanning from the moment attractant levels were increased until the moment CheYp recovered to half of its steady state level. Within the model's dynamic range, for increases of up to 300 %, τ_{adap} ranged between 7.1 s and 26.9 s. In experiments, the adaptation time is mostly quantified by measuring the time period from cell stimulation until the moment the cell returns to a pre-stimulation tumbling frequency. Therefore, a direct comparison between measurements of τ_{adap} and experimental measurements is complicated. Since τ_{adap} does not even cover the time period for full CheYp adaptation, it should, however, be smaller than the adaptation time of the tumbling frequency. In experimental studies, dependent on the applied stimulation, the tumbling frequency recovered within several seconds or several minutes [132, 133]. Therefore, I assume that the obtained measurements of τ_{adap} are plausible.

I traced back limitations in the dynamic range to limitations in the encoding of attractant levels into receptor methylation levels. In the model, the number of active receptors T_{act} is modulated by the absolute attractant level as well as receptor methylation levels (see Equations 5.1 to 5.4). Upon changes in attractant levels, the effector module comprising CheY is stimulated, since T_{act} is transiently changing in response to transient changes in receptor methylation levels. Soon after receptor methylation levels have adjusted, T_{act} and downstream species including CheYp complete adaptation (Figure 5.6). For a large range of attractant levels, steady state T_{act} levels remain almost constant (Figure 5.2 A), since larger attractant levels are matched by compensating adjustments in receptor methylation levels. However, for particularly large attractant levels, steady state receptor methylation levels do not vary (Figure 5.2 B). Therefore, receptor methylation levels cannot compensate for particularly large attractant levels and the adaptation of T_{act} and of connected effector species like CheYp is incomplete. Similarly, for particularly small attractant levels, steady state receptor methylation levels do not vary. In this case, the effector module remains in an unstimulated state upon changes in attractant levels (Figure 5.3), since neither variations in receptor methylation levels nor variations in absolute attractant levels are large enough to result in significant temporary changes in T_{act} .

In Section 5.4, attractant levels were inferred from present receptor methylation levels. As shown in Figure 5.5 B, particularly large attractant levels significantly differed from inferred attractant levels. In conclusion, based on receptor methylation levels, the chemotaxis system could not discriminate between large attractant levels and adaptation in the effector module

began to fail for reasons discussed in the last paragraph. Further, it was found that the encoding of particularly small attractant levels outside of the system's dynamic range was severely affected by stochastic fluctuations in receptor methylation levels (Figure 5.5 C). Within the dynamic range of the system, receptor methylation levels were ultrasensitive to changes in attractant levels. Therefore, fluctuations in receptor methylation levels only led to small inaccuracies in inferring ambient attractant levels. Outside of the dynamic range, however, fluctuations could lead to much larger inaccuracies (Figure 5.5 A).

Limitations in the encoding of attractant levels could also be detected, when using delayed mutual information estimates to monitor memory formation and memory loss under stochastic conditions in Section 5.5. In more detail, mutual information estimates provided information about the discriminability of several attractant step levels based on snapshots of receptor methylation levels. As sudden increases in attractant levels led to transient changes in receptor methylation levels, information about the applied step levels was gained in a gradual manner (Figure 5.8). Again, the system proved to be unable to distinctly respond to increases to different attractant step level from particularly small or large attractant baseline levels. In both instances, increases in attractant levels did not lead to significant changes in receptor methylation levels, as observable in Figure 5.5 A.

Mutual information estimates could also be used to determine time scales for memory loss and memory formation. In my analysis, I inferred time scales for memory formation from transient changes in receptor methylation levels upon increases in attractant levels from a common baseline level to different step levels. In contrast, I inferred time scales for memory loss from transient changes in receptor methylation levels upon decreases in attractant levels from different step levels to a common baseline level. I found that memory formation appeared to require more time than memory loss (Figures 5.5 B and 5.11). It remains open, whether the same is true for the inverse case, i.e., when memory formation relates to decreases in attractant levels from a common step level to different baseline levels and memory loss relates to increases in attractant levels from different baseline levels to a common step level.

In wild-type *Escherichia coli*, Tar receptors can be methylated up to four times, while Tsr and Tsg receptors exhibit even five methylation sites [206, 207, 208, 209]. Previously, the effects of a reduction in the number of chemoreceptor methylation sites was investigated in *in silico* studies [197, 198] as well as experimentally [196]. It was reported that a reduction in methylation sites decreased the dynamic range of the chemotaxis system. Based on simulation results of model versions differing in the maximal number of receptor methylations, I could confirm these reports, as shown in Section 5.6 in Figures 5.12 to 5.14. In particular, reducing the maximal number of receptor methylations decreased the upper boundary of the dynamic range by affecting the system's adaptation mechanism. Interestingly, the lower boundary of the dynamic range remained unaffected by the applied changes in the maximal number of receptor methylations.

By inferring attractant levels from present methylation levels (Section 5.6.2) and by employing delayed mutual information estimates for monitoring memory formation and memory loss (Section 5.6.3), I could clearly link losses in the dimensions of the dynamic range to losses in the dimensions of the encoding range. A reduction in the maximal number of receptor methylations decreased the upper boundary of the range of attractant levels that were uniquely

mapped to receptor methylation levels. In consequence, I found that the upper boundary of the range of attractant levels that could be correctly inferred from present receptor methylation levels was lowered (Figure 5.15) and that memory formation already failed for lower attractant levels (Figure 5.17) upon decreases in the maximal number of receptor methylations.

To the best of my knowledge, this is the first time encoding in *Escherichia coli* chemotaxis was analyzed by means of the introduced methods in Sections 5.4 and 5.5. While conventional mutual information estimations were applied several times to measure statistical dependencies between variables in chemotaxis (for example in [192, 193]), this is the first time delayed mutual information estimations were applied to measure dynamic processes of information flow in this system. Further, the presented results could explain reasons behind experimental observations describing a link between the number of receptor methylations and the dimensions of the dynamic range in the chemotaxis system.

Recently, Clausznitzer *et al.* published a chemotaxis pathway model including a more detailed adaptation mechanism as well as a Monod-Wyman-Changeux model to describe receptor-receptor interactions [130]. Especially with regards to a quantitative analysis of time scales for memory formation, memory loss or adaptation, the more recent model should be considered to corroborate presented results, since the authors claim that their model features a more realistic representation of adaptation dynamics.

Part IV

Main discussion

Main discussion

6.1 Contributions to the analysis of information transfer in signal transduction

In this thesis, I studied information transfer in two prime examples of signal transduction: calcium signaling in non-excitable cells and *Escherichia coli* chemotaxis.

In calcium signaling, information from a first messenger is encoded into characteristics of calcium oscillations [43]. For instance, in the salivary glands of the blowfly *Calliphora erythrocephala*, the abundance level of the hormone serotonin is encoded into the calcium oscillation frequency, whereas larger abundance levels are linked to faster oscillations [45]. It was reported that changes in calcium oscillation parameters, such as the oscillation frequency, modulate the activities of dependent proteins. In Chapter 4, I introduced methods to analyze the frequency-decoding of calcium oscillations.

In particular, in Section 4.4, I presented an optimization-based method to identify requirements for distinct frequency-decoding. By running different optimizations for different network structures (see for instance Section 4.5) or different parameterizations of non-optimizable parameters (see for instance Section 4.7), I could assess the impact of model conditions on frequency-decoding. Further, due to the application of a local optimization algorithm [159], I defined a multistart routine to identify suitable parameter sets for distinct frequency-decoding. As a result, per optimization problem, I obtained plenty of optimized parameter sets that I could rank according to their associated objective values. In turn, this allowed me to analyze top-ranked parameter sets for conserved characteristics. I concluded that such conserved characteristics were essential for distinct frequency-decoding in particular protein models.

Previous studies already focused on the identification of kinetic requirements for distinct frequency-decoding [76, 87]. However, to the best of my knowledge, this is the first time, optimizations were used to characterize frequency-decoding of calcium oscillations. As shown throughout Chapter 4, the described optimization-based method yielded extensive information about the analyzed systems, making it a valuable tool. While I applied the method to analyze frequency-decoding, it can be easily adapted to investigate other forms of information transmission.

In addition, I analyzed the frequency-decoding of calcium oscillations by means of channel capacity estimations. To this end, channel capacity estimates informed about the discriminability between given oscillation frequencies under stochastic conditions (Sections 4.12 to 4.14.2). Previously, the impact of stochastic effects had been studied in calcium oscillator models [212, 213]. However, to the best of my knowledge, a stochastic analysis of the

decoding of calcium oscillations was still lacking. In Section 1.4.1, I already mentioned that information theory can be used to investigate a wide array of research questions in numerous research areas [140, 141, 142, 143, 144, 145]. In terms of an analysis of biological signal transduction, however, the application of channel capacity is still fairly new (for other studies analyzing signal transduction by means of channel capacity estimations, see [147, 167, 150, 151]). Thus, in order to provide an interpretation of channel capacity estimates and eradicate misconceptions, I also presented simple example cases for the application of channel capacity in Section 3.2.

In summary, with respect to the analysis of frequency-decoding of calcium oscillations, I could apply the presented methods to corroborate published results, for example, about a correlation between the strength of cooperative calcium-dependent protein activation and the distinctness of frequency-decoding (see Section 4.7 and [76, 87]), while also shedding light on novel aspects, such as the requirement of an antagonistic, oscillator-dependent regulation for band-pass activation (see Section 4.5). In the past, the band-pass activation of calcium-dependent proteins had been barely researched. While, in an experimental study, band-pass activation had been attested for the transcription factor NFAT [63, 64], in an *in silico* study, time-limited spikes of a given frequency had been found to induce maximal autonomous activity of CaMKII [69]. In this thesis, I detected requirements in the model network structure and model parameterization for the generation of band-pass activation adding further insights to this particular form of frequency-decoding.

As a second example study, I analyzed information transfer in the chemotaxis of *Escherichia coli*. In particular, I focused on the encoding of information about absolute ambient attractant levels into the methylation levels of chemoreceptors [134], whereas single receptors exhibit four to five methylation sites [206, 207, 208, 209]. Upon encountering changes in ambient attractant levels, receptor methylation levels are changing, too. In consequence, changes in methylation levels drive downstream responses in signaling proteins such as CheA and CheY directing cell locomotion. For my analysis, I employed an established model of the *Escherichia coli* chemotaxis pathway by Kollmann *et al.* [3].

Based on an idea and implementation of Jonas Förster¹, I inferred expected attractant levels from the methylation-based memory (Sections 5.4 and 5.6.2). Further, I employed delayed estimates of mutual information to quantify the size of the methylation-based memory as well as to measure time scales for the dynamic processes of memory formation and memory loss (Sections 5.5 and 5.6.3). While regular estimations of mutual information had been applied before to characterize information transfer in the chemotaxis system [192, 193], to the best of my knowledge, this was the first time delayed mutual information estimates were used to define the molecular memory in this pathway.

I found that boundaries in the dynamic range of the chemotaxis system [109, 112], i.e., the range of absolute attractant levels for which chemotactic behavior remained functional, were predetermined by limitations in the upstream encoding of absolute attractant levels into receptor methylation levels. This became particularly clear after analyzing model versions that differed in the maximal number of receptor methylations (Section 5.6). To this end, decreases in the maximal number of receptor methylations led to enhanced limitations in the encoding

¹Biological Information Processing Group at the BioQuant Center, Heidelberg University.

of absolute attractant levels. In turn, this was clearly linked to reductions in the dynamic range. A link between the maximal number of receptor methylations and the dimensions of the dynamic range had been observed experimentally [196] and *in silico* [197, 198]. By means of the presented methods, I could shed light on the origins of this effect.

In both example studies of signal transduction, I defined molecular communication channels for my analysis. To this end, I declared the variable to be encoded or decoded, i.e., the ambient attractant level or the calcium oscillation frequency, as the channel input and the encoding or decoding variable, i.e., the receptor methylation levels or the average activity of a calcium-dependent protein, as the channel output. In both cases, the output variable was ultrasensitive to changes in the input variable. This greatly benefited the discriminability between output responses to different input signals, as already minor changes in the input could cause major changes in the output variable (see Figures 4.10 and 5.2 B). While, in calcium signaling, ultrasensitive behavior arises due to the cooperative binding of calcium ions to dependent proteins [69, 169, 170, 171, 172], in *Escherichia coli* chemotaxis, attractant binding regulates receptor kinase activity, whereas cooperative interactions between receptor proteins shape the response curve [109, 214, 215]. It is imaginable that cooperative interactions emerged in the course of evolution to enhance the versatility in encoding and decoding in the analyzed signal transduction pathways. In conclusion, similarly complex signal transduction pathways might rely on cooperative interactions as well.

6.2 Outlook

In Chapter 4, I investigated the decoding of the calcium oscillation frequency by dependent proteins. To this end, I used kinetic models to study different forms of frequency-decoding, i.e., high-pass and band-pass activation, both of which were observed experimentally [62]. The presented models of calcium-dependent protein activation have to be understood as simplifications of more complex molecular processes. For instance, with regards to CaMKII, the holoenzyme is composed of several sub-units that can exhibit different degrees of kinase activity dependent on their interactions with calcium-calmodulin complexes and neighboring sub-units [69]. In a next step, it would be crucial to study frequency-decoding in more detailed models that relate to particular calcium-dependent proteins. While I presented a model for the calcium-dependent activation of NFAT (Section 4.6), the model could be extended to include gene expression enabling a direct comparison to existing gene expression data (see [63]).

In my analysis, I identified requirements for distinct frequency-decoding, for instance, positive-cooperative protein activation (see Section 4.7) or, with regards to band-pass activation, antagonistic, oscillator-dependent regulation of the decoder protein (see Sections 4.5 and 4.6.3). However, as of now, experimental validations for these results are missing. While, in experiments, the frequency of calcium oscillations had been artificially modulated to study the effect on a dependent protein's activity [63, 65, 70], with regards to my results, it would be most informative to extend these protocols by additionally manipulating kinetic properties of particular proteins or altering existing network structures. This would allow for a comparison between frequency-decoding in manipulated and wild-type systems.

Further, the presented optimization-based workflow (see Section 4.4) could be applied to perform additional analyses of the decoding of calcium oscillations *in silico*. For example, in Section 4.11, I detected a tradeoff between the precision and the distinctness in band-pass activation. It would be interesting to analyze the best parameters sets capable of inducing distinct band-pass activation for various degrees of precision. This would allow for the identification of conserved characteristics, possibly providing a better understanding on what parametric changes are required for changes in precision in band-pass activation. Additionally, most of my analysis in Chapter 4 was based on sine wave calcium oscillations. However, experimental time series of calcium oscillations in non-excitable cells frequently exhibit a duty cycle and appear asymmetric, unlike sine waves [53]. Therefore, it would be important to confirm that the presented results can be reproduced with more biological oscillation shapes. For the reproduction of different oscillation shapes, the presented *OscillatorGenerator* package for R can be applied (see Section 3.1). Lastly, in fish, the abundance of several agonists is encoded into the amplitude of calcium oscillations [47]. Thus, it seems likely that calcium-dependent proteins perform amplitude-decoding downstream. Due to the versatility of the presented workflow, it could be easily modified to detect requirements for distinct amplitude-decoding *in silico*.

In Chapter 5, I analyzed the encoding of attractant levels into receptor methylation levels in the chemotaxis pathway of *Escherichia coli*. To this end, I used an established model by Kollmann *et al.* [3] and stimulated the system by increasing or decreasing ambient attractant levels. I then proceeded to measure the model response. While the application of sudden changes in

attractant levels might be a common practice in experiments [93, 94, 133, 202], it is more likely that, under natural conditions, bacteria follow attractant gradients. In conclusion, a chemotactic bacterium would frequently encounter multiple increases in attractant levels in a short period of time, as it swims along an attractant gradient. In an *in silico* study, Vladimirow *et al.* reported that the chemotaxis system becomes insensitive to prolonged gradients, eventually [129]. By approximating spatial gradients by dynamic attractant inputs in the the presented chemotaxis model, one could study this effect in more detail. As I could trace back limitations in the dynamic range of the chemotaxis system to upstream limitations in the encoding of absolute attractant levels for simple singular increases in attractant levels (see Sections 5.3 and 5.4), I suspect that the encoding step might be also responsible for the observations in Vladimirow *et al.* [129]. Once again, the methods presented in Sections 5.4 and 5.5 could be applied.

Finally, most of the presented methods are not limited to the analysis of the decoding of calcium oscillations or the encoding of attractant levels in chemotaxis. Recently, more reports on versatile encoding and decoding mechanisms in signal transduction pathways emerged [18, 216]. The methods presented in this thesis could be adapted to study these systems in more detail.

List of Abbreviations

API	application programming interface
ATP	adenosine triphosphate
BRENDA	BRaunschweig ENzyme DAtabase
BA algorithm	Blahut-Arimoto algorithm
BHK	baby hamster kidney
C	channel capacity
Ca / Ca ²⁺	calcium
CaM	calmodulin
CaMKII	Ca ²⁺ /calmodulin-dependent protein kinase II
CBP	calcium-binding protein
CCK1R	cholecystokinin 1 receptor
CCW	counterclockwise
Cn	calcineurin
COPASI	COmplex PAtchway SIMulator (software)
CoRC	Copasi R Connector
CRAN	Comprehensive R Archive Network
CW	clockwise
DAG	diacylglycerol
EGF	epidermal growth factor
ER	endoplasmic reticulum
ERK	extracellular-signal regulated kinase
FRET	Förster resonance energy transfer
GPCR	G protein-coupled receptor
GSK-3	glycogen synthase kinase 3
H	(Shannon) entropy
I	mutual information
IP ₃	inositol 1,4,5-trisphosphate
IP ₃ R	inositol trisphosphate receptor
JNK	c-Jun N-terminal kinase
KSG	Kraskov-Stoegbauer-Grassberger
LSODA	Livermore Solver for Ordinary Differential Equations
MAPK	mitogen-activated protein kinase

MCP	methyl-accepting chemotaxis protein
MCU	mitochondrial calcium uniporter
N_A	Avogadro constant
NCBI	National Center for Biotechnology Information
NCX	sodium-calcium exchanger
NFAT	nuclear factor of activated T cells
NGF	nerve growth factor
NF κ B	nuclear factor kappa-light-chain-enhancer of activated B cells
ODE	ordinary differential equation
PIP ₂	phosphatidylinositol 4,5-bisphosphate
PKC	protein kinase C
PLC	phospholipase C
PMCA	plasma membrane Ca ²⁺ ATPase
R	"The R Project for Statistical Computing"
RBL	rat basophilic leukemia cells
RTK	tyrosine-kinase-coupled receptor
RTL	rainbow trout liver
RYR	ryanodine receptor
SERCA	sarco/endoplasmic reticulum Ca ²⁺ -ATPase
TF	transcription factor
WT	wild-type

List of Figures

1.1	Schematic: Encoding and decoding of biological signals.	5
1.2	Schematic: Emergence of a calcium signal after a GPCR stimulation.	7
1.3	Schematic: Encoding of first messenger characteristics into calcium oscillation parameters.	9
1.4	Selective activation of frequency-decoding proteins exhibiting high-pass or band-pass activation.	10
1.5	Schematic: The chemotaxis pathway of <i>Escherichia coli</i>	14
1.6	Number of publications in the NCBI database PubMed that contain information-theoretic keywords.	18
1.7	Example case: discrimination of agonist types based on the abundance of active transcription factor.	20
2.1	Workflow for acquiring input-signal-specific output probability distributions. . .	30
3.1	Time series resembling spiking oscillations generated with the <i>OscillatorGenerator</i> package.	36
3.2	Time series resembling bursting oscillations generated with the <i>OscillatorGenerator</i> package.	37
3.3	Measuring the channel capacity between two output distributions with variable distinctness.	41
3.4	Measuring the channel capacity between three output distributions with variable distinctness.	42
3.5	Channel capacity estimates refer to the number of distinct input sets characterized by at least one set-exclusive element.	44
3.6	Effect of spreading out or narrowing down output distributions on channel capacity estimates.	46
4.1	Overview of the high-pass model's network structure.	52
4.2	Frequency-decoding in the high-pass model.	52
4.3	Overview of the band-pass model's network structure.	55
4.4	Frequency-decoding in the band-pass model.	56
4.5	Definition of decoding efficiencies in high-pass and band-pass activation. . . .	57
4.6	Recreation of different forms of frequency-decoding in the high-pass and band-pass model.	59
4.7	Overview of the NFAT model's network structure.	61
4.8	Frequency-decoding in optimized versions of the NFAT model.	64
4.9	Frequency-decoding in the original NFAT model with alternative parameterizations of T_{slow}	65

4.10	Increases in cooperativity coefficients describing the binding of calcium to regulator species lead to a rise in frequency-decoding potentials.	66
4.11	High-pass and band-pass activation potentials for different parameterizations of cooperativity coefficients.	67
4.12	Isolated parameter sets reliably induced efficient high-pass and band-pass activation.	68
4.13	Parameter distributions of parameter sets capable of inducing efficient high-pass activation.	70
4.14	Parameter distributions of parameter sets capable of inducing efficient band-pass activation.	71
4.15	Noticeable relationships between parameters in parameter sets capable of inducing efficient high-pass activation in the high-pass model.	72
4.16	Decreases in the fixed concentration of Deact led to visible increases in k_{P2} and in the k_{P2} -to- k_{P1} ratio in the high-pass model.	73
4.17	Noticeable relationships between parameters in parameter sets capable of inducing efficient band-pass activation in the band-pass model.	74
4.18	Effect of an increased lower rate constant boundary L_R on optimization results for high-pass activation.	75
4.19	Effect of an increased lower rate constant boundary L_R on optimization results for band-pass activation.	76
4.20	Effect of a decreased upper rate constant boundary U_R on optimization results in high-pass and band-pass activation.	77
4.21	Effect of constraint binding constant parameterizations on optimization results in high-pass and band-pass activation.	78
4.22	Increases in the calcium oscillation peak level led to increases in the optimal parameterization margins of K_A and K_D for efficient band-pass activation.	79
4.23	Increases in the calcium oscillation amplitude led to an increased E_B	80
4.24	Effect of modulating the filter bandwidth on the distinctness of band-pass activation.	81
4.25	Recreation of high-pass activation under stochastic conditions.	84
4.26	Effect of variations in the decoder protein's responsiveness on high-pass activation under stochastic conditions.	85
4.27	Channel capacity estimates for a growing number of input period lengths and various levels of decoder responsiveness.	87
4.28	Channel capacity estimates for a growing number of fast input period lengths and various levels of decoder responsiveness.	88
4.29	Increases in cooperativity coefficients allowed for more pronounced high-pass activation also under stochastic conditions.	90
4.30	Impact of modulations of the extrinsic noise amplitude and the high-pass model's cooperativity strength on the discrimination of period lengths.	91
4.31	Increases in cooperativity coefficients leading to increases in the high-pass activation efficiency allowed for an improvement of the resolution limit.	93
5.1	Adaptation in the chemotaxis model after changes in attractant levels.	103
5.2	Steady state behavior of biochemical species in the chemotaxis pathway to a broad range of constant attractant levels.	106
5.3	Decreases in CheYp in response to sudden increases in L.	107
5.4	Measurements of τ_{adap} after sudden increases in L.	108

5.5	Inferring L_{exp} in continuous environments given deterministic and stochastic conditions.	110
5.6	Model response to a sudden increase in the attractant level from 1 μM to $10^5 \mu\text{M}$	112
5.7	Quantification of transient dynamics of L_{exp} build-up.	112
5.8	Quantification of memory formation by means of estimates of mutual information between attractant step levels and receptor methylation levels at a given point in time.	114
5.9	System-size- and baseline-specific maximal estimates of mutual information and time scales for memory formation.	115
5.10	Quantification of memory loss by means of estimates of mutual information between attractant step levels and receptor methylation levels at a given point in time.	116
5.11	System-size- and baseline-specific time scales for memory loss.	117
5.12	Steady state behavior in the effector module for a range of attractant levels in model versions differing in the maximal number of receptor methylations.	119
5.13	Decreases in CheYp as a response to increases in L in model versions differing in the maximal number of receptor methylations.	120
5.14	Measurements of τ_{adap} after sudden increases in L in model versions differing in the maximal number of receptor methylations.	121
5.15	Encoding of attractant levels into receptor methylation levels in model versions differing in the maximal number of receptor methylations.	123
5.16	Robustness against fluctuations in inferring L in model versions differing in the maximal number of receptor methylations.	124
5.17	Maximal estimates of mutual information between batches of attractant step levels and snapshots of receptor methylation levels in model versions differing in the maximal number of receptor methylations.	125
A.1	Correlation results between optimized parameter distributions leading to efficient high-pass activation in the high-pass model.	160
A.2	Mutual information estimates between optimized parameter distributions leading to efficient high-pass activation in the high-pass model for different parameterizations of a	161
A.3	Correlation results between optimized parameter distributions leading to efficient high-pass activation in the band-pass model.	162
A.4	Mutual information estimates between optimized parameter distributions leading to pronounced band-pass activation in the band-pass model for different parameterizations of a and d (part 1).	163
A.5	Mutual information estimates between optimized parameter distributions leading to pronounced band-pass activation in the band-pass model for different parameterizations of a and d (part 2).	164
A.6	Parameter distributions of optimized parameter sets capable of pronounced band-pass activation for different calcium oscillation amplitudes.	165
B.1	Mutual information estimates describing the formation of the methylation-based memory in <i>Escherichia coli</i> chemotaxis for a system size of $1.4 \cdot 10^{-15}$ L.	175
B.2	Mutual information estimates describing the formation of the methylation-based memory in <i>Escherichia coli</i> chemotaxis for a system size of $1.4 \cdot 10^{-16}$ L.	176

B.3	Mutual information estimates describing the formation of the methylation-based memory in <i>Escherichia coli</i> chemotaxis for a system size of $1.4 \cdot 10^{-17}$ L.	177
B.4	Mutual information estimates describing the formation of the methylation-based memory in <i>Escherichia coli</i> chemotaxis for a system size of $1.4 \cdot 10^{-18}$ L.	178
B.5	Mutual information estimates describing the loss of the methylation-based memory in <i>Escherichia coli</i> chemotaxis for a system size of $1.4 \cdot 10^{-15}$ L.	180
B.6	Mutual information estimates describing the loss of the methylation-based memory in <i>Escherichia coli</i> chemotaxis for a system size of $1.4 \cdot 10^{-16}$ L.	181
B.7	Mutual information estimates describing the loss of the methylation-based memory in <i>Escherichia coli</i> chemotaxis for a system size of $1.4 \cdot 10^{-17}$ L.	182
B.8	Mutual information estimates describing the loss of the methylation-based memory in <i>Escherichia coli</i> chemotaxis for a system size of $1.4 \cdot 10^{-18}$ L.	183
B.9	Time scales for memory formation in model versions differing in the maximal number of receptor methylations.	184
B.10	Time scales for memory loss in model versions differing in the maximal number of receptor methylations.	185

List of Tables

3.1	Function calls in the <i>OscillatorGenerator</i> package.	38
3.2	Function arguments used in the <i>OscillatorGenerator</i> package for R.	39
4.1	List of calcium-dependent proteins activated in a positive-cooperative manner. .	48
4.2	Overview of the high-pass model's structure and kinetics.	51
4.3	Overview of the band-pass model's structure and kinetics.	54
4.4	The NFAT model's structure and kinetics.	60
4.5	Filter bandwidths applied in this section.	82
4.6	Propensity terms of the high-pass activation model.	83
4.7	Overview of input period lengths applied in the resolution assay presented in Figure 4.31.	92
5.1	Overview of the chemotaxis model's structure and kinetics.	105
A.1	Parameter sets optimized for different forms of distinct frequency-decoding in the high-pass model.	151
A.2	Parameter sets optimized for different forms of distinct frequency-decoding in the band-pass model.	151
A.3	Parameter sets optimized for a maximization of Eff_H given different parameterizations of the cooperativity coefficient a in the high-pass model.	151
A.4	Parameter sets optimized for a maximization of Eff_H given different parameterizations of the cooperativity coefficients a , p_1 and p_2 in the high-pass model. . .	152
A.5	Parameter sets optimized for a maximization of Eff_B given different parameterizations of the cooperativity coefficients a and d in the band-pass model.	152
A.6	Parameter sets optimized for a maximization of Eff_B given different parameterizations of the cooperativity coefficients p_1 and p_2 in the band-pass model. . . .	153
A.7	Parameter sets optimized for a maximization of Eff_B given different parameterizations of the cooperativity coefficients a , d , p_1 and p_2 in the band-pass model. .	153
A.8	Parameter sets optimized for a maximization of Eff_B given different parameterizations of the cooperativity coefficient a in the band-pass model.	154
A.9	Parameter sets optimized for a maximization of Eff_B given different parameterizations of the cooperativity coefficient d in the band-pass model.	154
A.10	Parameter sets optimized for a maximization of Eff_H given different rate constant optimization margins, $[L_R; U_R]$, in the high-pass model.	155
A.11	Parameter sets optimized for a maximization of Eff_B given different rate constant optimization margins, $[L_R; U_R]$, in the band-pass model.	155
A.12	Parameter sets optimized for a maximization of Eff_H given different binding constant optimization margins, $[L_B; U_B]$, in the high-pass model.	156

A.13	Parameter sets optimized for a maximization of Eff_B given different binding constant optimization margins, $[L_B; U_B]$, in the band-pass model.	156
A.14	Parameter sets optimized for a maximization of Eff_B given different calcium oscillation amplitudes in the band-pass model.	157
A.15	Parameter sets optimized for a maximization of Eff_B in the band-pass model given different parameterizations of the cooperativity coefficients a and d with $T_{fast} = 10^{-0.5}$ s and $T_{slow} = 10^{2.5}$ s.	157
A.16	Parameter sets optimized for a maximization of Eff_B in the band-pass model given different parameterizations of the cooperativity coefficients a and d with $T_{fast} = 10^0$ s and $T_{slow} = 10^2$ s.	158
A.17	Standard parameterization of the stochastic version of the high-pass model for $a = 4$	166
A.18	Standard parameterization of the stochastic version of the high-pass model for $a = 1$	167
A.19	Standard parameterization of the stochastic version of the high-pass model for $a = 2$	167
A.20	Description of the applied square-wave inputs used in Section 4.6.	168
A.21	Optimized parameter values of the original NFAT model with antagonistic, oscillator-dependent regulation.	169
A.22	Optimized parameter values of the NFAT model without CaMKII-mediated inhibition.	169
A.23	Optimized parameter values of the NFAT model version with oscillator-independent deactivation.	170
A.24	Optimized parameter values of the NFAT model with $T_{slow} = 200$ s.	170
A.25	Optimized parameter values of the NFAT model with $T_{slow} = 300$ s.	171
B.1	Parameters fitted to mutual information data for memory formation.	174

Part V

Appendix

Additional material to Chapter 4: Analyzing the frequency-decoding of calcium oscillations

A.1 The high-pass and band-pass activation models

A.1.1 List of optimized parameter sets

Throughout Chapter 4.1, I optimized rate and binding constants for a maximization of the high-pass activation efficiency Eff_H (according to Equations 4.2 and 4.3) or the band-pass activation efficiency Eff_B (according to Equations 4.4 and 4.5). In the following, I list all optimized parameter sets. By default, I set cooperativity coefficients to 1 and the total concentrations of Act, Deact and Pr to 5000 nM. During maximizations, rate constants were allowed to vary between 0 s^{-1} and 10^6 s^{-1} , binding constants between 0 nM and 10^6 nM . If not explicitly mentioned otherwise, period lengths T_{fast} , T_{med} and T_{slow} were equal to 0.1 s, 10 s and 1000 s, respectively. Corresponding period lengths were used for the calculation of frequency-decoding efficiencies.

In Section 4.5, I tried to recreate different forms of frequency-decoding in the high-pass (Table 4.2) and band-pass model (Table 4.3). In addition to a maximization of Eff_H and Eff_B , I also performed maximizations of the low-pass activation efficiency Eff_L (according to Equations 4.9 and 4.10). Optimized parameter sets can be found in Tables A.1 and A.2.

Parameter sets in Tables A.3 to A.9 relate to optimization results targeting either a maximization of Eff_H in the high-pass model or a maximization of Eff_B in the band-pass model given different parameterizations of cooperativity coefficients. I used corresponding parameter sets mainly to compute results presented in Section 4.7.

Rate and binding constants were found to be confined to optimal margins in order to induce efficient band-pass or high-pass activation. In conclusion, I ran constrained optimizations to assess the effect of unfavorable model parameterizations on frequency-decoding. In Tables A.12 to A.13, the resultant optimized parameter sets are shown. I used these parameter sets to compute simulation results presented in Section 4.9.

I assumed a relationship between the optimal parameterization margins of calcium-binding constants K_A and K_D and the calcium oscillation amplitude. Hence, I examined the effect of modulations of the oscillation amplitude on optimized parameter sets. To this end, I

maximized Eff_B in the band-pass model in Section 4.10. Optimized parameter sets can be found in Table A.14.

In Section 4.24, I assessed the impact of narrower band-pass activation filters on the band-pass activation potential E_B (the maximized band-pass activation efficiency Eff_B). Hence, I altered default values of T_{fast} and T_{slow} in maximizations of Eff_B in the band-pass model. Corresponding optimized parameter sets are shown in Tables A.15 and A.16.

Tab. A.1. Parameter sets optimized for different forms of distinct frequency-decoding in the high-pass model.

<i>mode</i>	k_{A1}	K_A	k_{A2}	k_{P1}	K_{P1}	k_{P2}	K_{P2}	Figures
band-pass	3785.348	12694.642	0.011	62902.83	23263.46	0.392	76794.552	4.6 A
low-pass	8359.638	3050.243	0.01	22440.495	7819.267	0.01	68878.498	4.6 A

Rate constants (k_i) are given in s^{-1} , binding constants (K_i) in nM. a was set to 4.

Tab. A.2. Parameter sets optimized for different forms of distinct frequency-decoding in the band-pass model.

<i>mode</i>	k_{A1}	K_A	k_{A2}	k_{D1}	K_D	k_{D2}	k_{P1}	K_{P1}	k_{P2}	K_{P2}	Figures
high-pass	12321.117	29199.079	4.161	2.45	27087.615	$9 \cdot 10^{-5}$	17413.126	98423.14	203.134	55480.785	4.6 B
low-pass	0.297	76844.989	$1 \cdot 10^{-4}$	27983.888	30140.077	17.874	47112.649	30163.517	8881.506	29046.398	4.6 B

Rate constants (k_i) are given in s^{-1} , binding constants (K_i) in nM. a and d were set to 4.

Tab. A.3. Parameter sets optimized for a maximization of Eff_H given different parameterizations of the cooperativity coefficient a in the high-pass model.

a	k_{A1}	K_A	k_{A2}	k_{P1}	K_{P1}	k_{P2}	K_{P2}	Figures
1	2.898	280892.518	68.745	484.951	602.388	0.15	34.808	4.10 A; 4.11 A
2	8.965	46535.326	4.834	9096.133	10978.156	1.815	14737.657	4.10 A; 4.11 A
3	1.34	19467.835	7.82	8257.984	127.075	1.053	4436.11	4.10 A; 4.11 A
4	1.632	7692.575	1.592	7332.157	757.634	1.589	7083.233	4.2; 4.10 A; 4.11 A
5	0.428	8349.609	2.806	1757.642	1.175	2.502	8311.716	4.10 A; 4.11 A
6	0.342	4589.627	1.882	3887.501	23.535	0.934	6480.631	4.10 A; 4.11 A

Rate constants (k_i) are given in s^{-1} , binding constants (K_i) in nM.

Tab. A.4. Parameter sets optimized for a maximization of Eff_H given different parameterizations of the cooperativity coefficients a , p_1 and p_2 in the high-pass model.

a, p_1, p_2	k_{A1}	K_A	k_{A2}	k_{P1}	K_{P1}	k_{P2}	K_{P2}	Figures
2	7.886	21279.256	1742.279	6761.899	2.054	1.146	11375.355	4.11 A
3	48.525	5190.013	1947.89	4006.909	6.134	0.174	0.007	4.11 A
4	25.652	11240.698	802.565	1012.011	0.024	262.073	28850.578	4.11 A
5	1.629	3103.76	337.532	732.514	0.155	2.01	8620.044	4.11 A
6	3495.674	3241.618	358.024	680.004	63.797	1.417	7365.096	4.11 A

Rate constants (k_i) are given in s^{-1} , binding constants (K_i) in nM.

Tab. A.5. Parameter sets optimized for a maximization of Eff_B given different parameterizations of the cooperativity coefficients a and d in the band-pass model.

a, d	k_{A1}	K_A	k_{A2}	k_{D1}	K_D	k_{D2}	k_{P1}	K_{P1}	k_{P2}	K_{P2}	Figures
1	0.01	87551.629	0.074	0.057	89628.179	92.386	3617.695	7609.145	2469.961	9.271	4.10 B; 4.11 B
2	19.922	65280.964	0.092	110.86	91398.746	32.445	3067.717	93931.69	7959.079	603.866	4.10 B; 4.11 B
3	60.595	29208.176	0.112	8667.029	79351.866	24.273	9000.985	97637.004	8071.019	610.981	4.10 B; 4.11 B
4	0.1	500	0.1	1	500	1	0.1	1200	1	1200	4.4
4	0.333	5728.448	0.135	85.022	5335.715	21.38	958.343	1039.251	7725.553	2805.14	4.4; 4.10 B; 4.11 B; 4.24 A, D
5	0.127	2945.616	0.181	461.398	5042.912	21.898	4802.849	7229.097	7386.699	2827.689	4.10 B; 4.11 B
6	0.914	3461.619	0.246	145.713	5009.175	23.899	8564.056	9337.516	1753.228	36.273	4.10 B; 4.11 B

Rate constants (k_i) are given in s^{-1} , binding constants (K_i) in nM.

Tab. A.6. Parameter sets optimized for a maximization of Eff_B given different parameterizations of the cooperativity coefficients p_1 and p_2 in the band-pass model.

p_1, p_2	k_{A1}	K_A	k_{A2}	k_{D1}	K_D	k_{D2}	k_{P1}	K_{P1}	k_{P2}	K_{P2}	Figures
2	$7 \cdot 10^{-6}$	8901.795	0.07	130.808	7861.204	206.455	21.149	0.09	2805.519	3869.145	4.11 B
3	0.863	9716.545	3.803	26.984	7873.771	7.259	8259.895	4186.361	0.05	718.831	4.11 B
4	3.168	7575.555	7.423	8.23	8859.426	4.133	516.273	1717.953	0.038	329.33	4.11 B
5	0.007	9204.396	4.997	407.133	9355.337	4.295	535.57	3.195	0.242	6249.779	4.11 B
6	0.914	3461.619	0.246	145.713	5009.175	23.899	8564.056	9337.516	1753.228	36.273	4.11 B

Rate constants (k_i) are given in s^{-1} , binding constants (K_i) in nM.

Tab. A.7. Parameter sets optimized for a maximization of Eff_B given different parameterizations of the cooperativity coefficients a , d , p_1 and p_2 in the band-pass model.

a, d, p_1, p_2	k_{A1}	K_A	k_{A2}	k_{D1}	K_D	k_{D2}	k_{P1}	K_{P1}	k_{P2}	K_{P2}	Figures
2	$2 \cdot 10^{-5}$	7093.606	0.157	639.195	7723.792	345.795	21.608	0.019	1775.083	706.366	4.11 B
3	15.768	4598.348	6.039	161.296	5392.064	5.698	858.324	1523.089	0.047	97.57	4.11 B
4	4.717	3765.99	4.775	0.108	3594.625	0.011	302.931	156.514	48.818	814.78	4.11 B
5	257.782	7512.029	4.707	316.061	9559.174	0.022	482.739	48.901	3215.851	3482.377	4.11 B
6	159.405	3221.113	7.358	13.587	3618.712	0.016	66.403	216.903	159.784	2693.367	4.11 B

Rate constants (k_i) are given in s^{-1} , binding constants (K_i) in nM.

Tab. A.8. Parameter sets optimized for a maximization of Eff_B given different parameterizations of the cooperativity coefficient α in the band-pass model.

α	k_{A1}	K_A	k_{A2}	k_{D1}	K_D	k_{D2}	k_{P1}	K_{P1}	k_{P2}	K_{P2}	Figures
2	$1 \cdot 10^{-4}$	2279.938	0.01	0.089	9052.617	27.56	626.238	1032.94	5003.852	598.215	4.11 B
3	0.06	9499.622	0.006	0.708	9447.338	11.008	381.041	1706.316	1884.872	3144.254	4.11 B
4	0.014	1274.099	0.034	0.292	9168.139	10.559	185.344	9877.172	9038.629	9355.108	4.11 B
5	0.001	1602.904	0.019	0.062	9157.437	6.162	1364.517	1030.891	5019.353	577.505	4.11 B
6	1.607	2714.466	0.007	0.837	9573.026	4.785	51.511	8306.821	1375.833	8730.873	4.11 B

Rate constants (k_i) are given in s^{-1} , binding constants (K_i) in nM.

Tab. A.9. Parameter sets optimized for a maximization of Eff_B given different parameterizations of the cooperativity coefficient d in the band-pass model.

d	k_{A1}	K_A	k_{A2}	k_{D1}	K_D	k_{D2}	k_{P1}	K_{P1}	k_{P2}	K_{P2}	Figures
2	0.009	9180.861	0.084	189.837	8835.445	309.309	678.798	6416.879	786.922	646.092	4.11 B
3	0.001	5821.896	0.081	1524.41	3490.059	195.969	4265.335	2991.353	3012.494	9999.993	4.11 B
4	0.005	7465.33	0.086	3617.427	2452.237	73.36	741	3667.422	1104.04	9604.892	4.11 B
5	0.005	8596.787	0.088	212.709	715.86	131.998	828.05	4460.901	540.7	7367.289	4.11 B
6	0.069	6337.784	0.076	569.756	473.884	10.56	88.42	8839.108	7.793	5581.445	4.11 B

Rate constants (k_i) are given in s^{-1} , binding constants (K_i) in nM.

Tab. A.10. Parameter sets optimized for a maximization of Eff_H given different rate constant optimization margins, $[L_R; U_R]$, in the high-pass model.

$[L_R; U_R]$	k_{A1}	K_A	k_{A2}	k_{P1}	K_{P1}	k_{P2}	K_{P2}	Figures
$[10^{-1}; 10^6]$	2927.612	35510.309	7.692	64249.904	7029.872	5.454	48596.349	4.18
$[10^1; 10^6]$	12249.346	56917.876	12	76767.482	2492.052	10.539	70549.786	4.18
$[10^2; 10^6]$	16505.823	20488.348	100	57153.213	3223.358	100	99451.488	4.18
$[10^3; 10^6]$	22483.119	21091.119	5046.543	72280.299	12.769	1000.002	99999.864	4.18
$[0; 10^{-1}]$	0.098	903.737	0.1	0.1	1951.197	0.095	35906.895	4.20 A, B
$[0; 10^0]$	0.929	1989.241	0.984	1	507.876	0.161	24330.872	4.20 A, B
$[0; 10^1]$	9.799	5239.361	0.173	10	4264.608	0.251	24713.329	4.20 A, B
$[0; 10^2]$	16.649	7875.01	0.454	92.154	1826.532	0.351	10644.174	4.20 A, B

Rate constants (k_i) are given in s^{-1} , binding constants (K_i) in nM.

Tab. A.11. Parameter sets optimized for a maximization of Eff_B given different rate constant optimization margins, $[L_R; U_R]$, in the band-pass model.

$[L_R; U_R]$	k_{A1}	K_A	k_{A2}	k_{D1}	K_D	k_{D2}	k_{P1}	K_{P1}	k_{P2}	K_{P2}	Figures
$[10^{-1}; 10^6]$	932.782	43499.472	0.136	9260.866	29056.134	21.035	26410.091	23472.548	60513.049	2687.133	4.19
$[10^0; 10^6]$	16262.554	55628.449	1	11430.158	34433.485	34.578	11798.947	10788.299	85303.413	3295.219	4.19
$[10^1; 10^6]$	24962.265	58126.14	10.256	39600.153	5935.52	10	21019.961	44206.609	10	90955.234	4.19
$[10^2; 10^6]$	23314.595	70008.937	101.499	97401.572	9469.651	100	38266.024	6752.905	100	97332.934	4.19
$[0; 10^1]$	9.167	12308.184	0.105	10	1984	0.955	10	28191.045	0.178	6715.465	4.20 C, D
$[0; 10^2]$	100	98501.719	0.084	100	2677.427	9.661	99.97	1.196	43.196	1425.122	4.20 C, D
$[0; 10^3]$	2.423	4357.54	0.144	373.564	46661.439	22.254	694.631	17401.736	670.821	0.204	4.20 C, D

Rate constants (k_i) are given in s^{-1} , binding constants (K_i) in nM.

Tab. A.12. Parameter sets optimized for a maximization of Eff_H given different binding constant optimization margins, $[L_B; U_B]$, in the high-pass model.

$[L_B; U_B]$	k_{A1}	K_A	k_{A2}	k_{P1}	K_{P1}	k_{P2}	K_{P2}	Figures
$[0; 5 \cdot 10^2]$	0.001	500	20.569	3690.866	329.916	0.438	169.197	4.21 A
$[0; 7.5 \cdot 10^2]$	$3 \cdot 10^{-4}$	750	2.815	12224.213	653.707	0.682	374.006	4.21 A
$[0; 10^3]$	0.002	999.997	10.422	9158.07	397.303	0.659	979.734	4.21 A
$[0; 10^4]$	5.246	9127.323	4.402	92668.884	4311.2	2.395	8938.783	4.21 A
$[10^3; 10^5]$	8757.972	48690.264	2.167	86641.722	16125.269	3.765	15981.127	4.21 B
$[10^4; 10^6]$	17725.936	41234.34	8.818	99465.649	35048.306	89.693	974481.489	4.21 B
$[10^5; 10^7]$	6269.573	2387346.774	0.002	1550.278	4951795.967	2.15	4819838.485	4.21 B

Rate constants (k_i) are given in s^{-1} , binding constants (K_i) in nM.

Tab. A.13. Parameter sets optimized for a maximization of Eff_B given different binding constant optimization margins, $[L_B; U_B]$, in the band-pass model.

$[L_B; U_B]$	k_{A1}	K_A	k_{A2}	k_{D1}	K_D	k_{D2}	k_{P1}	K_{P1}	k_{P2}	K_{P2}	Figures
$[0; 5 \cdot 10^2]$	0.001	494.022	0.136	0.142	500	16.338	51.93	246.153	117.587	217.224	4.21 C
$[0; 7.5 \cdot 10^2]$	$7 \cdot 10^{-4}$	691.619	0.128	0.043	750	45.224	90.436	140.07	888.632	53.545	4.21 C
$[0; 10^3]$	0.002	975.135	0.144	2.393	1000	29.078	149.932	949.818	137.579	682.724	4.21 C
$[0; 10^4]$	2.676	9443.178	0.148	311.226	8943.726	20.932	2056.32	2328.925	15948.634	2904.349	4.21 C
$[10^3; 10^5]$	2.773	6028.302	0.131	1155.828	11469.257	20.994	5753.228	40999.303	39056.774	8552.435	4.21 D
$[10^4; 10^6]$	92189.844	59217.018	0.117	11044.986	11906.248	24.693	7710.221	232326.73	99995.858	164779.252	4.21 D
$[10^5; 10^7]$	30294.737	8241926.42	10^{-5}	59209.242	7095776.757	0.053	43329.12	1562009.439	35525.493	1467426.303	4.21 D

Rate constants (k_i) are given in s^{-1} , binding constants (K_i) in nM.

Tab. A.14. Parameter sets optimized for a maximization of Eff_B given different calcium oscillation amplitudes in the band-pass model.

peak	k_{A1}	K_A	k_{A2}	k_{D1}	K_D	k_{D2}	k_{P1}	K_{P1}	k_{P2}	K_{P2}	Figures
500	701.418	19158.557	0.074	6738.973	82861.963	18.253	20667.676	50151.997	46750.123	3.519	4.23 A, B
1500	13794.993	96453.215	0.171	42598.647	63427.411	21.364	6275.99	13445.655	24750.483	885.336	4.23 B
2000	32.518	67943.315	0.202	11785.477	113337.553	23.392	71310.22	3876.51	75763.554	189.428	4.23 A, B
2500	444.465	78522.548	0.229	49873.881	87988.686	26.357	42000.684	39151.208	27871.704	1737.119	4.23 B
3000	65.527	46663.966	0.247	7395.239	68378.372	28.365	13768.857	29728.127	68183.347	3287.243	4.23 A, B

Rate constants (k_i) are given in s^{-1} , binding constants (K_i) in nM. Cooperativity coefficients a and d were set to 4. For variations in the amplitude of the calcium sine wave, only the peak concentration was varied, the sine wave's base concentration was fixed to 200 nM. Peak levels are given in nM.

Tab. A.15. Parameter sets optimized for a maximization of Eff_B in the band-pass model given different parameterizations of the cooperativity coefficients a and d with $T_{fast} = 10^{-0.5} s$ and $T_{slow} = 10^{2.5} s$.

a, d	k_{A1}	K_A	k_{A2}	k_{D1}	K_D	k_{D2}	k_{P1}	K_{P1}	k_{P2}	K_{P2}	Figures
1	0.052	89997.97	0.143	17.533	99248.607	16.322	7513.778	56616.317	9047.696	79231.591	4.24 B, D
2	1.163	48419.225	0.159	14.413	33793.923	11.744	6576.259	23112.702	38718.332	14675.814	4.24 B, D
3	101.581	63198.662	0.182	9978.964	98065.849	9.632	34319.782	64447.342	32843.9	6848.599	4.24 B, D
4	5638.754	77884.43	0.219	192.323	13169.223	8.496	10390.075	5087.496	70000.938	6061.151	4.24 B, D
5	34218.007	77929.146	0.27	1806.608	16699.026	8.709	13971.139	397.357	11436.019	152.235	4.24 B, D
6	8814.901	39891.344	0.325	53703.085	11257.384	8.709	17936.391	69.108	52008.308	9762.824	4.24 B, D

Rate constants (k_i) are given in s^{-1} , binding constants (K_i) in nM.

Tab. A.16. Parameter sets optimized for a maximization of Eff_B in the band-pass model given different parameterizations of the cooperativity coefficients a and d with $T_{fast} = 10^0$ s and $T_{slow} = 10^2$ s.

a, d	k_{A1}	K_A	k_{A2}	k_{D1}	K_D	k_{D2}	k_{P1}	K_{P1}	k_{P2}	K_{P2}	Figures
1	0.147	59379.756	0.246	1.14	95247.351	8.446	1157.318	39960.086	4962.287	11341.806	4.24 C, D
2	2.059	64047.922	0.271	5.304	81972.734	5.295	11813.485	42080.494	8606.191	861.43	4.24 C, D
3	242.58	82053.193	0.305	314.229	64403.295	4.263	47095.525	79710.062	9791.253	765.109	4.24 C, D
4	50.248	17686.973	0.344	25974.273	98595.344	3.946	16720.953	17732.304	65498.886	514.127	4.24 C, D
5	3951.692	20641.722	0.402	96599.464	18894.09	4.083	61548.437	87786.803	31995.059	19377.757	4.24 C, D
6	14898.686	15544.037	0.458	2473.427	5602.219	4.256	11228.532	12090.998	7736.081	6044.701	4.24 C, D

Rate constants (k_i) are given in s^{-1} , binding constants (K_i) in mM.

A.1.2 Additional analysis results of parameter couples

In Section 4.8, I analyzed parameter sets leading to pronounced high-pass activation in the high-pass model (with a scanned from 1 to 6) and pronounced band-pass activation in the band-pass model (with a and d scanned from 1 to 6). To this end, I also searched for pairwise relationships between parameter distributions. In particular, I quantified linear dependencies by means of correlation coefficients as well as linear and non-linear dependencies by means of surrogate-corrected estimations of mutual information.

The application of both methods led to the conclusion that dependencies between parameter distributions were majorly cooperativity-dependent. Changes in the parameterizations of cooperativity coefficients led to the emergence or disappearance of clear relationships between parameter distribution pairs. In case of high-pass activation in the high-pass model, both methods detected the most persistent relationships between k_{A1} and K_A as well as between k_{P2} and K_{P2} . For smaller parameterizations of a , I found also a noticeable relationship between k_{A1} and k_{A2} (Figures A.1 and A.2).

In terms of band-pass activation in the band-pass model, both methods detected relationships between k_{A1} and K_A as well as between k_{D1} and K_D . Estimations of mutual information further identified a close relationship between k_{P2} and K_{P2} that was less pronounced in correlation results (Figures A.3 to A.5).

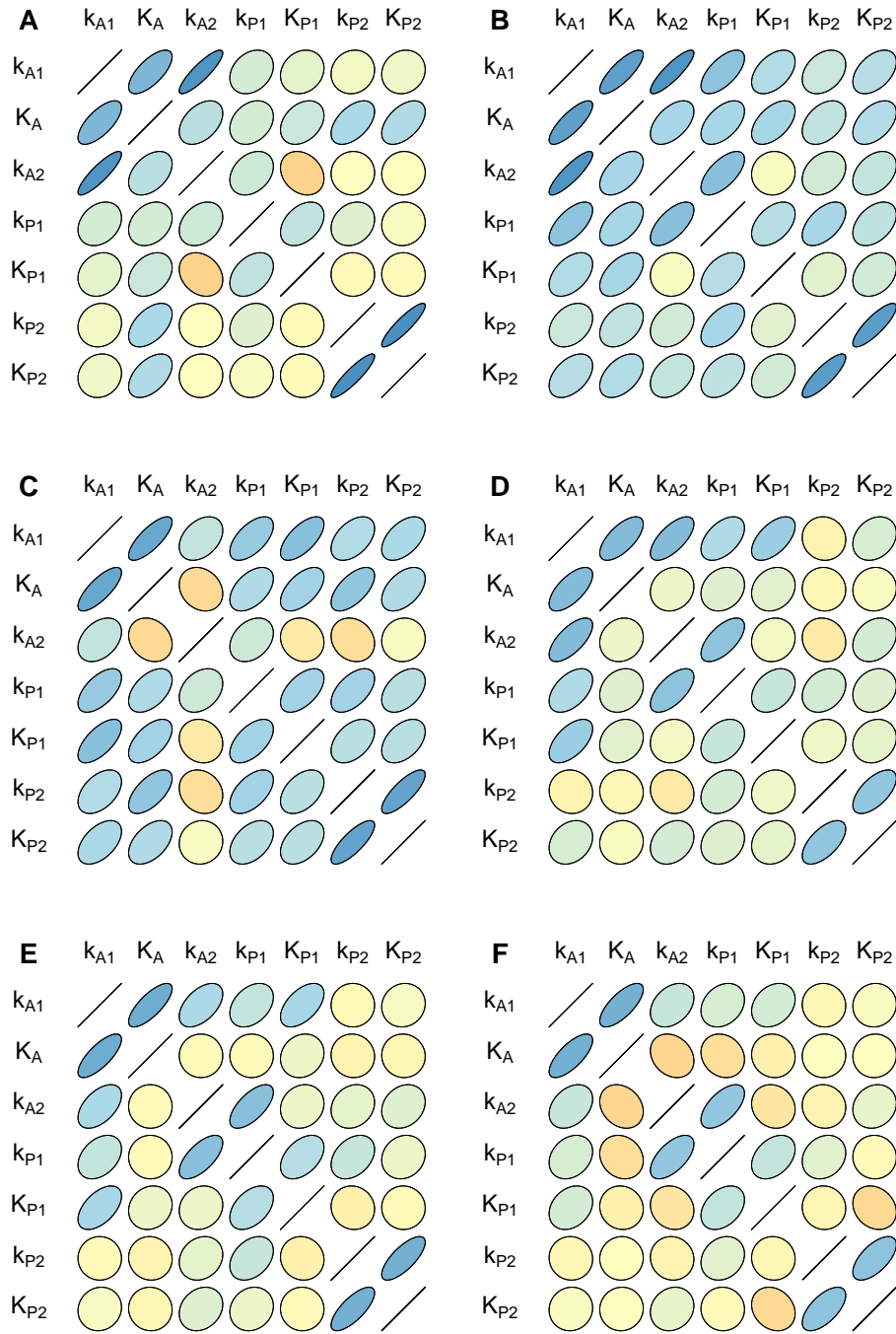


Fig. A.1. Correlation results between optimized parameter distributions leading to efficient high-pass activation in the high-pass model. I isolated optimized parameter sets leading to pronounced high-pass activation in the high-pass model for different parameterizations of the cooperativity coefficient a . In particular, I maximized the high-pass activation efficiency Eff_H and extracted parameter sets linked to an objective value within a 2-nM-margin to the overall best objective value for a specific optimization problem. Most correlation results were highly sensitive to variations in a . Only correlation results between k_{A1} and K_A , k_{P2} and K_{P2} as well as, for smaller values of a , between k_{A1} and k_{A2} were particularly persistent. Plots were generated by means of the plotcorr function in the ellipse package in R. Results for $a = 1$ are shown in (A), for $a = 2$ in (B), ..., for $a = 6$ in (F).

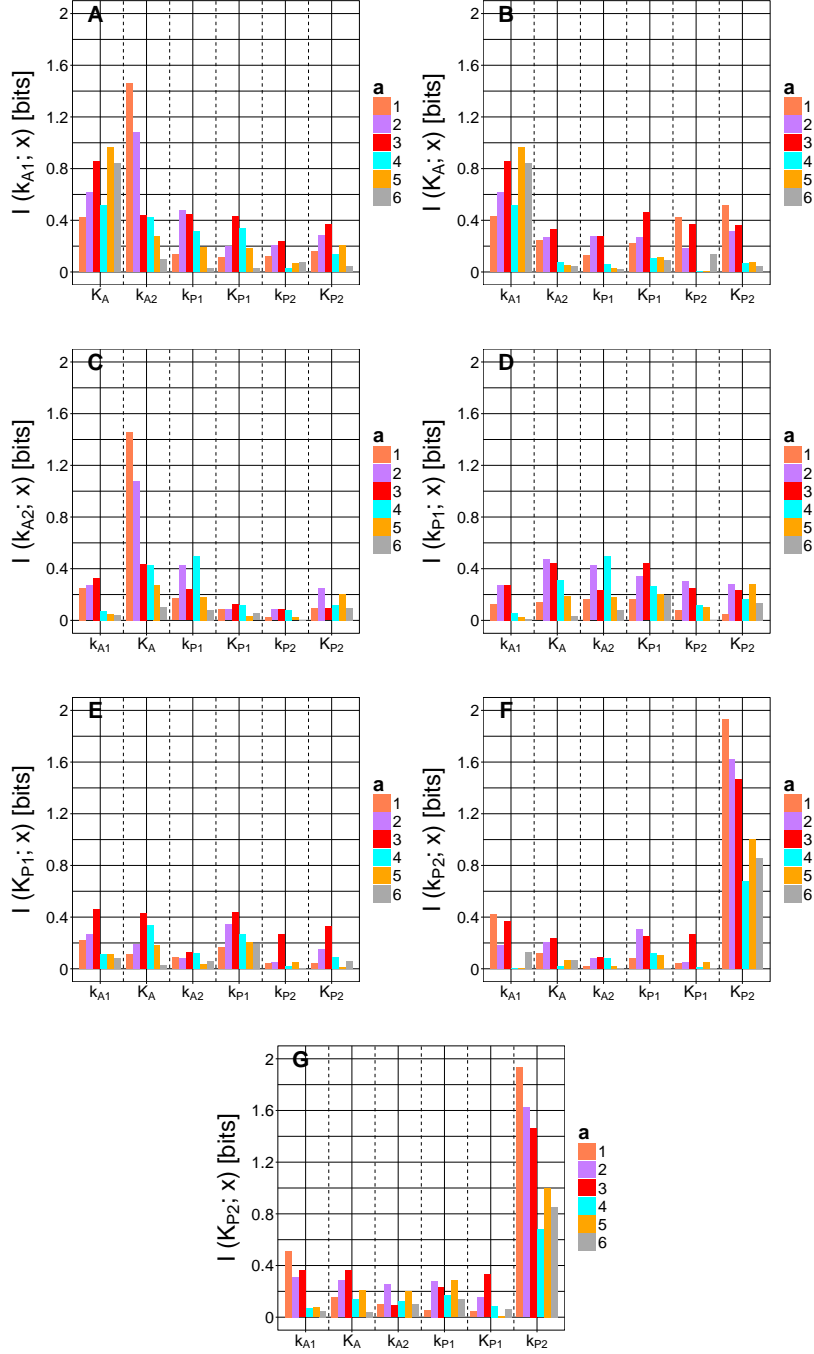


Fig. A.2. Mutual information estimates between optimized parameter distributions leading to efficient high-pass activation in the high-pass model for different parameterizations of a . I isolated optimized parameter sets leading to efficient high-pass activation in the high-pass model for different parameterizations of the cooperativity coefficient a . In particular, I maximized the high-pass activation efficiency Eff_H and extracted parameter sets linked to an objective value within a 2-nM-margin to the overall best objective value per optimization problem. Mutual information estimates between single parameter distributions resembled correlation results (Figure A.1). I found the strongest relationships between k_{A1} and K_A , k_{P2} and K_{P2} as well as, for small parameterizations of a , between k_{A1} and k_{A2} . Presented estimates were bias-corrected by subtracting mean values of surrogate estimate distributions from original estimates (as introduced in Section 2.5). Results for $a = 1$ are shown in (A), for $a = 2$ in (B), ..., for $a = 6$ in (F).

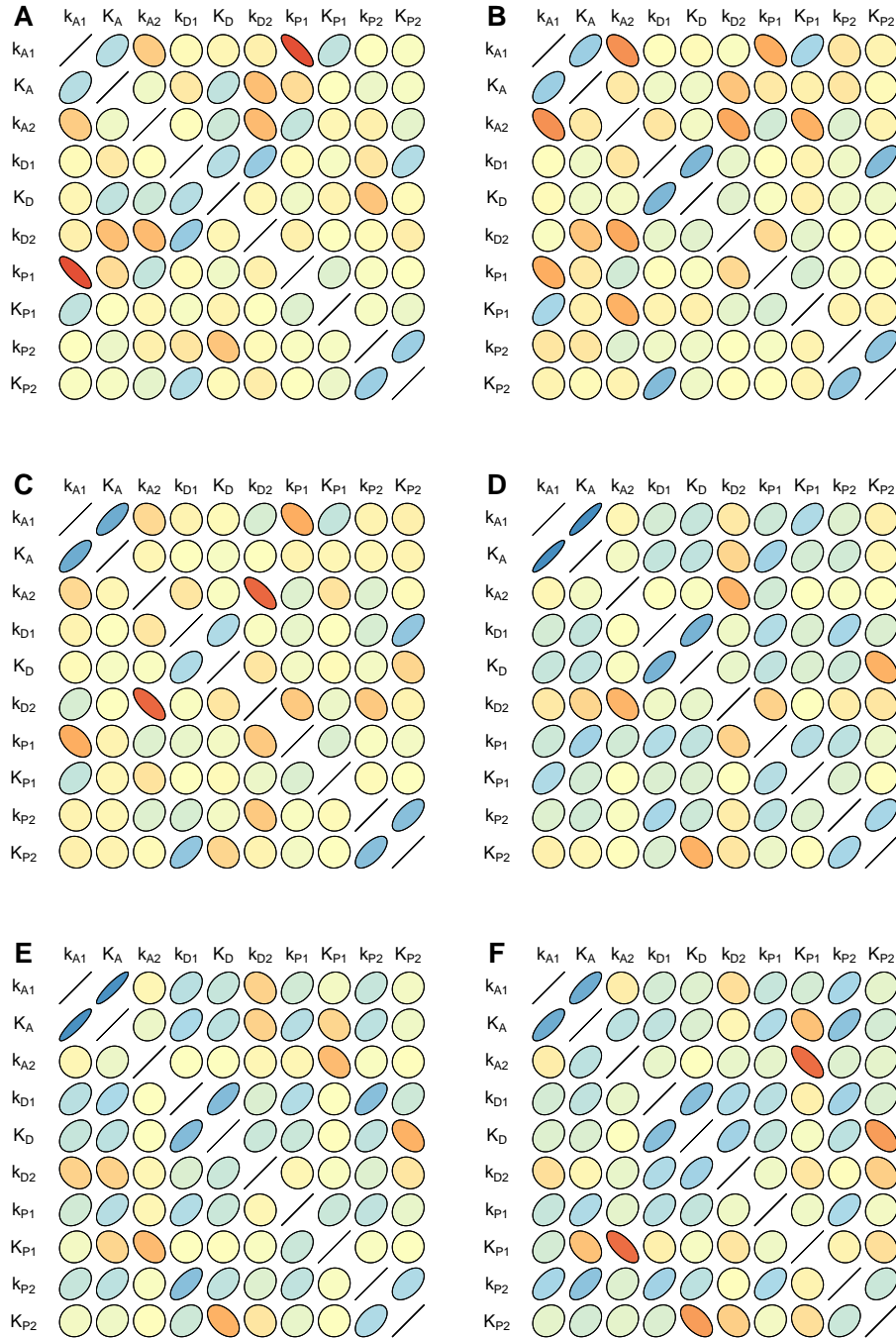


Fig. A.3. Correlation results between optimized parameter distributions leading to efficient high-pass activation in the band-pass model. I isolated optimized parameter sets leading to pronounced band-pass activation in the band-pass model for different parameterizations of a and d . In particular, I maximized the band-pass activation efficiency Eff_B and extracted parameter sets linked to an objective value within a 2-nM-margin to the overall best objective value per optimization problem. As in the high-pass model, correlation results between parameter couples were highly sensitive to changes in the cooperativity coefficients a and d . I found correlation results between k_{A1} and K_A as well as between k_{D1} and K_D to be the most persistent upon changes in a and d . For cooperativity coefficients smaller than 4, a recurring negative correlation between k_{A1} and k_{P1} was found. Plots were generated by means of the `plotcorr` function in the `ellipse` package in R. Results for $a = d = 1$ are presented in (A), for $a = d = 2$ in (B), ..., for $a = d = 6$ in (F).

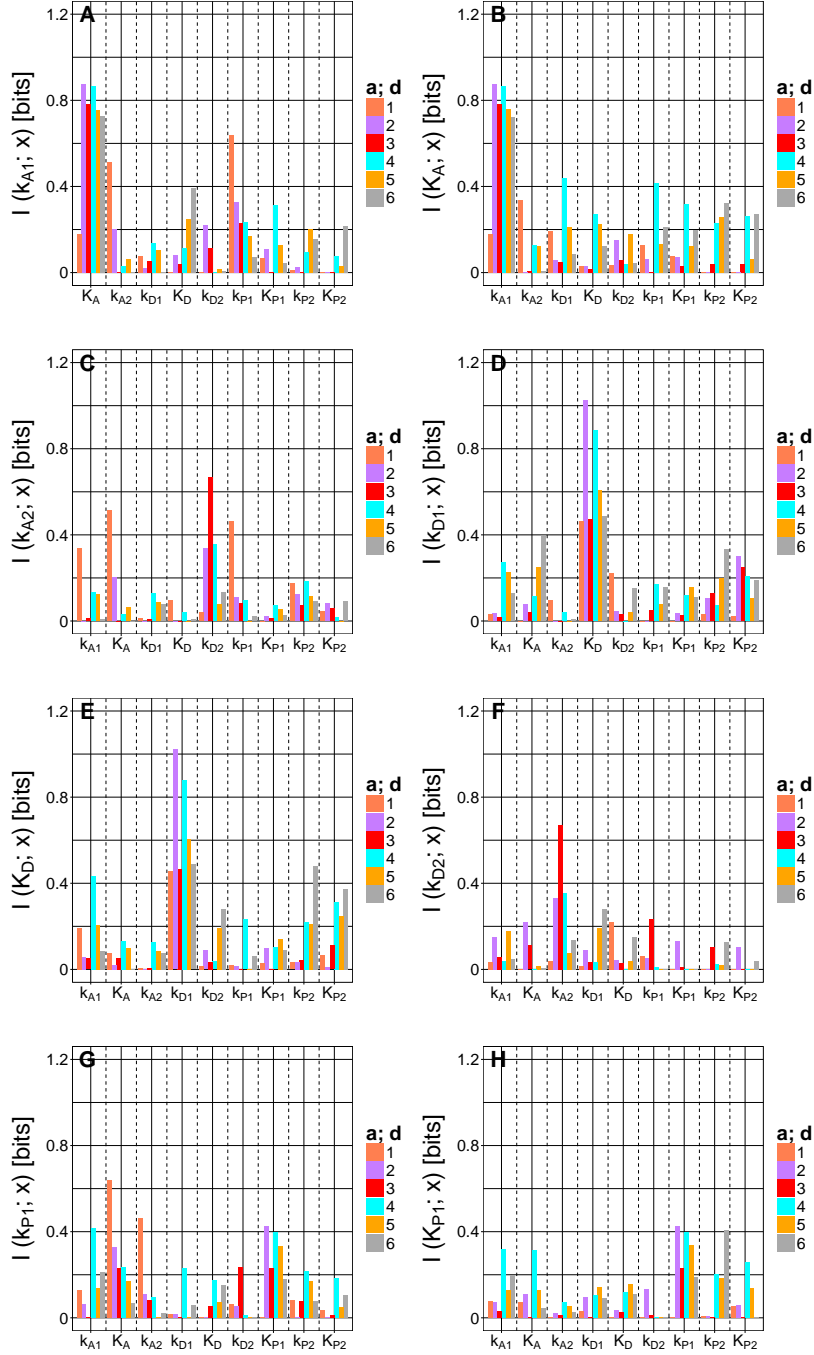


Fig. A.4. Mutual information estimates between optimized parameter distributions leading to pronounced band-pass activation in the band-pass model for different parameterizations of a and d (part 1). I isolated optimized parameter sets leading to pronounced band-pass activation in the band-pass model, for different parameterizations of the cooperativity coefficients a and d . In particular, I maximized the band-pass activation efficiency Eff_B and extracted parameter sets associated with an objective value within a 2-nM-margin to the overall best objective value per optimization problem. Mutual information estimates agree with correlation results presented in Figure A.3 with regards to a clear relationships between k_{A1} and K_A as well as between k_{D1} and K_D . Presented estimates were bias-corrected by subtracting mean values of surrogate estimate distributions from original mutual information estimates (as introduced in Section 2.5).

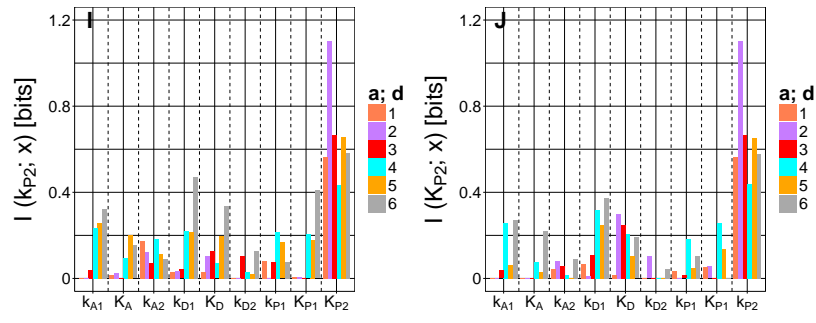


Fig. A.5. Mutual information estimates between optimized parameter distributions leading to pronounced band-pass activation in the band-pass model for different parameterizations of a and d (part 2). Remaining mutual information estimates can be found in Figure A.4.

A.1.3 Dependence of the optimal parameterization of binding constants on the calcium oscillation amplitude - additional parameter distributions

In Section 4.10, I examined the dependence of optimal parameterization margins on the calcium oscillation amplitude in maximizations of the band-pass activation efficiency Eff_B in the band-pass model. While optimized values of the binding constants K_A and K_D indicated a clear sensitivity to the applied changes in the calcium oscillation amplitude (see Figure 4.22 in Section 4.10), the remaining model parameters exhibited no or only a minor sensitivity (Figure A.6). In particular, I could attest a minor sensitivity for k_{A2} and k_{D2} .

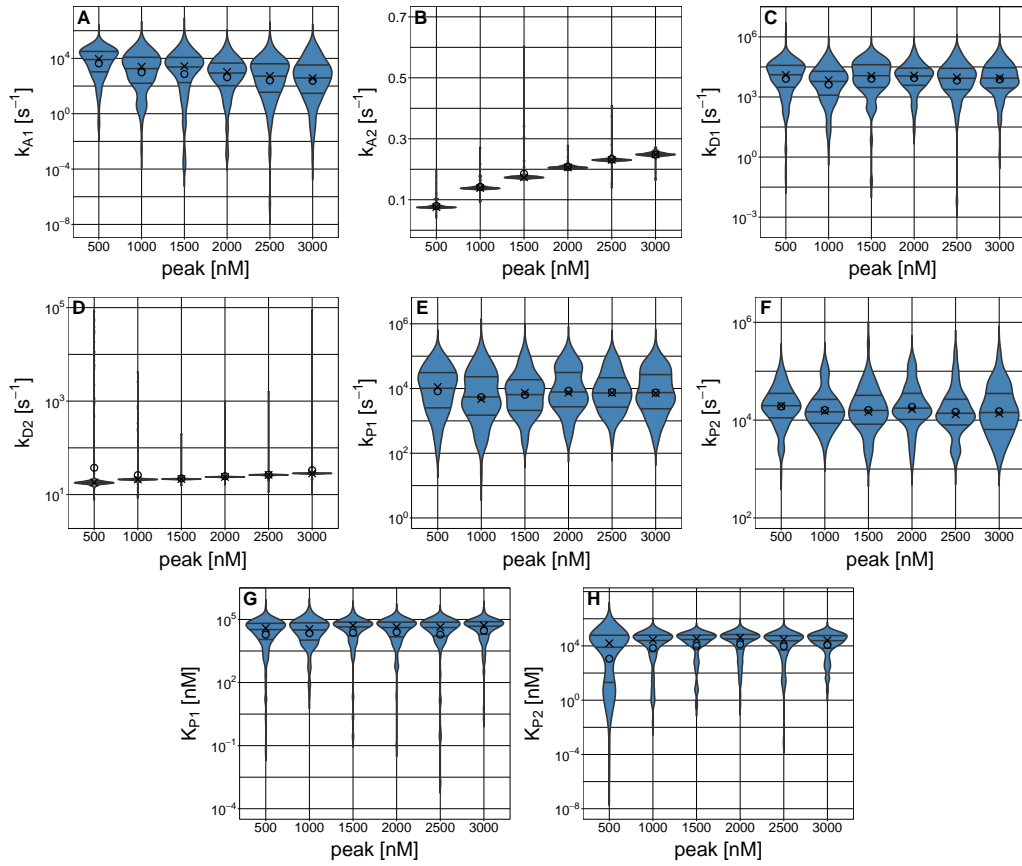


Fig. A.6. Parameter distributions of optimized parameter sets capable of pronounced band-pass activation for different calcium oscillation amplitudes. I isolated optimized parameter sets leading to objective values within a 2-nM-margin to an overall best value. Optimizations targeted a maximization of Eff_B in the band-pass model for different calcium oscillation amplitudes. To this end, I altered the peak level of the calcium oscillations, while setting the base level to a constant value of 200 nM. Further, I set cooperativity coefficients a and d to 4. Rate constants k_{A2} (B) and k_{D2} (D) indicated a minor sensitivity to the applied changes in the oscillation amplitude. Number of isolated parameter sets for peak = 500, 1000, ..., 3000 nM: 180, 96, 70, 98, 104, 120. Number of isolated fits relative to the overall number of fits for peak = 500, 1000, ..., 3000 nM: 4.18 %, 2.38 %, 2.12 %, 3.36 %, 4.08 %, 4.82 %. 2 nM relative to the leading objective value for peak = 500, 1000, ..., 3000 nM: 0.25 %, 0.14 %, 0.13 %, 0.12 %, 0.12 %, 0.12 %.

A.1.4 Applied parameterizations of the stochastic high-pass model

In the second part of Chapter 4, I introduced a stochastic version of the high-pass model (Table 4.6). The standard parameterization of this stochastic version of the high-pass model is given in Table A.17.

In particular, I obtained the standard parameterization by performing optimizations of the deterministic version of the high-pass model (Table 4.2) targeting a maximization of the high-pass activation efficiency Eff_H . To this end, I set the cooperativity coefficient a to 4 and contained model species to a total concentration of 1000 nM each. Only rate and binding constants were allowed to vary in the optimizations. Rate constants, however, were confined to an interval spanning from 0 s^{-1} to 100 s^{-1} during optimizations, since larger values were linked to high computational expenses. In the main text, I demonstrated that the presented standard parameterization also enables distinct high-pass activation under stochastic conditions in the stochastic high-pass model (see Section 4.12).

For Section 4.14, I derived additional parameter sets in a similar manner. First, I employed deterministic optimizations of Eff_H in the high-pass model. Then, I checked whether I could use the optimized parameter set to recreate high-pass activation also under stochastic conditions. This time, however, I set the cooperativity coefficient a to either 1 or 2. The resultant parameter sets are presented in Tables A.18 and A.19.

Tab. A.17. Standard parameterization of the stochastic version of the high-pass model for $a = 4$.

parameter	value	unit	parameter	value	unit
k_{A1}	12.604	s^{-1}	K_A	6687.801	nM
k_{A2}	0.887	s^{-1}	k_{P1}	100	s^{-1}
K_{P1}	287.27	nM	k_{P2}	0.985	s^{-1}
K_{P2}	7549.400	nM	a	4	/
p_1	1	/	p_2	1	/
V	10^{-15}	L	X_{tot}	1000	nM

The presented parameter set was applied for stochastic simulations of the high-pass model in Sections 4.12 to 4.14. X_{tot} refers to the total concentrations of Act, Deact and Pr. Initial concentrations of Act and Pr were computed according to the corresponding steady state equations (Equations 4.6 and 4.7). The presented parameter set originated from a deterministic optimization targeting a maximization of the high-pass activation efficiency Eff_H (Equation 4.3) with default values for T_{fast} and T_{slow} and a set cooperativity coefficient a equal to 4.

Tab. A.18. Standard parameterization of the stochastic version of the high-pass model for $a = 1$.

parameter	value	unit	parameter	value	unit
k_{A1}	0.019	s^{-1}	K_A	9997.111	nM
k_{A2}	1.635	s^{-1}	k_{P1}	99.48	s^{-1}
K_{P1}	269.151	nM	k_{P2}	0.337	s^{-1}
K_{P2}	2448.887	nM	a	1	/
p_1	1	/	p_2	1	/
V	10^{-15}	L	X_{tot}	1000	nM

The presented parameter set was applied for stochastic simulations of the high-pass model in Section 4.14. X_{tot} refers to the total concentrations of Act, Deact and Pr. Initial concentrations of Act and Pr were computed according to the corresponding steady state equations (Equations 4.6 and 4.7). The presented parameter set originated from a deterministic optimization targeting a maximization of the high-pass activation efficiency Eff_H (Equation 4.3) with default values for T_{fast} and T_{slow} and a set cooperativity coefficient a equal to 1.

Tab. A.19. Standard parameterization of the stochastic version of the high-pass model for $a = 2$.

parameter	value	unit	parameter	value	unit
k_{A1}	0.256	s^{-1}	K_A	9999.659	nM
k_{A2}	0.694	s^{-1}	k_{P1}	93.109	s^{-1}
K_{P1}	306.725	nM	k_{P2}	0.942	s^{-1}
K_{P2}	5517.707	nM	a	2	/
p_1	1	/	p_2	1	/
V	10^{-15}	L	X_{tot}	1000	nM

The presented parameter set was applied for stochastic simulations of the high-pass model in Section 4.14. X_{tot} refers to the total concentrations of Act, Deact and Pr. Initial concentrations of Act and Pr were computed according to the corresponding steady state equations (Equations 4.6 and 4.7). The presented parameter set originated from a deterministic optimization targeting a maximization of the high-pass activation efficiency Eff_H (Equation 4.3) with default values for T_{fast} and T_{slow} and a set cooperativity coefficient a equal to 2.

A.2 The NFAT model

A.2.1 Parameterization of square-wave inputs in the NFAT model

For simulations of the NFAT model, I employed square-wave calcium oscillations in Section 4.6. In particular, I used square-waves for fitting the model to gene expression data by Dolmetsch et al. [63] and for a maximization of the band-pass activation efficiency Eff_B . I generated all square-wave time series by means of the SquareSpike function in the *OscillatorGenerator* package for R (see Section 3.1). Details on the parameterization of the square waves can be found in Table A.20.

Tab. A.20. Information on the applied square-wave inputs in Section 4.6.

Task	Period T [s]	Duty cycle [%]	Active phase [s]
fitting	100	10	10
	400	2.5	10
	900	1.11	10
	1800	0.56	10
band-pass	30	66.67	20
activation	60	33.33	20
	500	4	20

I generated square-waves by means of the SquareSpike function of the *OscillatorGenerator* package for R. For all square-waves, I set baseline and peak levels to 100 nM and 1000 nM, respectively, while I set the trend argument to 1. Column "Task" refers to the purpose of the generated input in the optimization process: either for fitting of the model to gene expression data [63] or for recreating band-pass activation. The active phase is the absolute duration within an oscillation period T , in which the square-wave is on its peak level. The duty cycle is defined as the ratio of the active phase to the total oscillation period.

A.2.2 Optimized parameter sets of the NFAT model

In Section 4.8, I optimized different versions of the NFAT model according to Equation 4.13. Model version differed from each other in terms of the presence or absence of a calcium-dependent deactivator. The optimized parameter sets for all applied model versions can be found in Tables A.21 to A.23. I conducted optimizations of Eff_B with $T_{fast} = 25$ s, $T_{med} = 60$ s and $T_{slow} = 500$ s.

In Section 4.6.4, I assessed the effect of alternative parameterizations of T_{slow} . The optimized parameter sets for $T_{slow} = 200$ s and $T_{slow} = 300$ s can be found in Tables A.24 and A.25.

Tab. A.21. Optimized parameter values of the original NFAT model with antagonistic, oscillator-dependent regulation.

parameter	value	unit	parameter	value	unit
k_{N1}	4471.256	s^{-1}	k_{N2}	0.259	s^{-1}
k_{N3}	2351.606	s^{-1}	k_{N4}	0.116	s^{-1}
k_{N5}	0.466	$nM \cdot s^{-1}$	k_{N6}	0.141	s^{-1}
k_{N7}	8.668	$nM \cdot s^{-1}$	k_{N8}	1623.81	s^{-1}
K_{N1}	51359.144	nM	K_{N2}	5963.169	nM
m	3.765	/	n	3.769	/
δ	419.560	/	β	1.164	/
γ	-15.751	/			

I ran optimizations according to the objective function Ψ_{NFAT} (Equation 4.13) in the original NFAT model exhibiting antagonistic, oscillator-dependent regulation, as presented in Table 4.4.

Tab. A.22. Optimized parameter values of the NFAT model without CaMKII-mediated inhibition.

parameter	value	unit	parameter	value	unit
k_{N3}	31204.396	s^{-1}	k_{N4}	0.002	s^{-1}
k_{N7}	3576.947	$nM \cdot s^{-1}$	k_{N8}	17.917	s^{-1}
K_{N2}	1012.038	nM	n	2	/
β	1.131	/	γ	-100	/

I ran optimizations according to the objective function Ψ_{NFAT} (Equation 4.13) in a version of the NFAT model exhibiting no inhibition by means of a phosphorylation of calcineurin by CaMKII. Thus, only reactions $N3$ to $N4$ and $N9$ to $N10$ applied for this model version (model reactions are listed in Table 4.4).

Tab. A.23. Optimized parameter values of the NFAT model version with oscillator-independent deactivation.

parameter	value	unit	parameter	value	unit
k_{N3}	2409.954	s^{-1}	k_{N4}	0.033	s^{-1}
k_{N5}	0.048	$nM \cdot s^{-1}$	k_{N6}	89.201	s^{-1}
k_{N7}	4810.580	$nM \cdot s^{-1}$	k_{N8}	0.086	s^{-1}
K_{N2}	928.155	nM	n	5.241	/
δ	1563.384	/	CaMKII*	2479.653	nM
β	1.131	/	γ	-100	/

I ran optimizations according to the objective function Ψ_{NFAT} (Equation 4.13) in a version of the NFAT model exhibiting a constant, oscillator-independent concentration of active CaMKII. Thus, I cut reactions $N1$ to $N2$ with respect to the model's original form (Table 4.4). Parameter CaMKII* is the constant optimized concentration of active CaMKII.

Tab. A.24. Optimized parameter values of the NFAT model with $T_{slow} = 200$ s.

parameter	value	unit	parameter	value	unit
k_{N1}	93254.118	s^{-1}	k_{N2}	0.326	s^{-1}
k_{N3}	99997.864	s^{-1}	k_{N4}	0.262	s^{-1}
k_{N5}	282.822	$nM \cdot s^{-1}$	k_{N6}	0.127	s^{-1}
k_{N7}	0.014	$nM \cdot s^{-1}$	k_{N8}	2.209	s^{-1}
K_{N1}	78976.966	nM	K_{N2}	6974.387	nM
m	5.596	/	n	4.692	/
δ	1571.038	/	β	1.174	/
γ	-7.315	/			

I ran optimizations according to the objective function Ψ_{NFAT} (Equation 4.13) in the NFAT model, as presented in Table 4.4. For the optimizations, I set T_{fast} to 25 s, T_{med} to 60 s and T_{slow} to 200 s.

Tab. A.25. Optimized parameter values of the NFAT model with $T_{slow} = 300$ s.

parameter	value	unit	parameter	value	unit
k_{N1}	93254.116	s^{-1}	k_{N2}	0.356	s^{-1}
k_{N3}	99995.825	s^{-1}	k_{N4}	0.158	s^{-1}
k_{N5}	282.982	$nM \cdot s^{-1}$	k_{N6}	0.163	s^{-1}
k_{N7}	0.018	$nM \cdot s^{-1}$	k_{N8}	2.441	s^{-1}
K_{N1}	82207.69	nM	K_{N2}	6974.465	nM
m	5.430	/	n	5.053	/
δ	1571.198	/	β	0.931	/
γ	-7.203	/			

I ran optimizations according to the objective function Ψ_{NFAT} (Equation 4.13) in the NFAT model, as presented in Table 4.4. For the optimizations, I set T_{fast} to 25 s, T_{med} to 60 s and T_{slow} to 300 s.

Additional material to Chapter 5: Analyzing the encoding of attractant levels in the chemotaxis of *E. coli*

B.1 Additional estimates of mutual information showing memory formation in the original model

In Section 5.5, per system size and attractant baseline level, I performed 1000 stochastic simulations in which I stimulated the chemotaxis model by Kollmann *et al.* by raising the attractant concentration to different step levels. In particular, I drew 1000 attractant step levels from a uniform distribution spanning between the selected attractant baseline level and the attractant baseline level plus 200 %. For each of the 1000 simulations, I recorded the reorganization of the receptor species T_0 to T_4 that changed in response to the rise in the attractant level.

Then, I monitored the process of memory formation by measuring the mutual information between the batch of attractant step levels L_{step} and the corresponding receptor methylation levels at a time point τ , T_τ . Thus, I estimated the mutual information between a vector of attractant step levels and a five-column matrix of corresponding receptor methylation levels. The process of memory formation could be visualized by performing several estimations of mutual information scanning τ (see Figure 5.8 in Section 5.5). I fitted the obtained curves describing the evolution of mutual information in dependence of τ to the following equation:

$$I(\tau) = a \cdot \frac{\arctan(\tau \cdot b^{-1})}{b} \quad (\text{B.1})$$

By means of the fitted functions, I could derive time measures for memory formation, as presented in Figure 5.9 in Section 5.5. In this section, I present all system-size- and baseline-specific fits to obtained mutual information data. Fitted parameters of Equation B.1 can be found in Table B.1. In Figures B.1 to B.4, mutual information data (black) and corresponding data fits (red) are provided. For more information about the applied workflow, please refer to Section 5.5.

Tab. B.1. Parameters fitted to mutual information data for memory formation.

baseline [μM]	$V = 10^{-15} \text{ L}$		$V = 10^{-16} \text{ L}$		$V = 10^{-17} \text{ L}$		$V = 10^{-18} \text{ L}$	
	a	b	a	b	a	b	a	b
10^{-1}	/	/	/	/	/	/	/	/
10^0	1.95	12.97	0.04	2.19	/	/	/	/
10^1	11.08	9.45	11.42	17.67	3.59	23.55	0.92	52.85
10^2	11.04	8.05	21.46	22.97	18.82	50.42	1.62	44.17
10^3	31.26	18.82	26.09	26.96	21.58	54.79	3.4	66.7
10^4	42.78	23.17	43.46	40.27	25.19	63.66	6.55	98.66
10^5	24.78	12.21	19.53	17.24	10.36	27.28	1.48	29.15
10^6	89.98	46.08	73.23	67.88	36.11	108.59	1.52	59.07
10^7	37.76	132.58	11.12	290.04	/	/	/	/
10^8	/	/	/	/	/	/	/	/

In Section 5.5, I fitted mutual information data showing the dynamic process of memory formation to Equation B.1 for several system sizes (V) and attractant baseline levels in the chemotaxis model by Kollmann *et al.* In this table, I present the fitted parameters of Equation B.1. For cells marked with “/”, a fit to mutual information data was not possible because there was no memory formation, thus, mutual information remained at 0 bits.

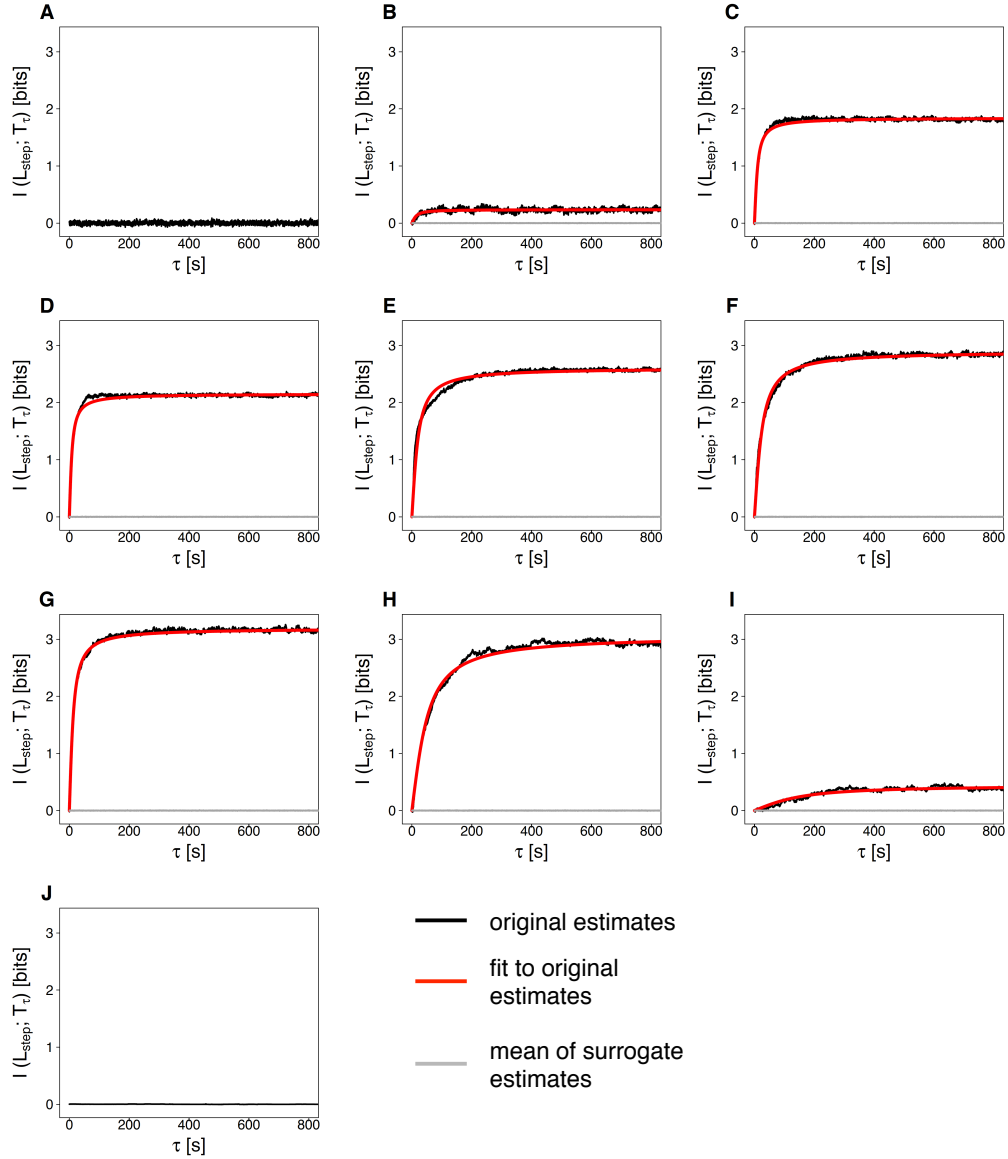


Fig. B.1. Mutual information estimates describing the formation of the methylation-based memory in *Escherichia coli* chemotaxis for a system size of $1.4 \cdot 10^{-15}$ L. Per attractant baseline level, I ran 1000 stochastic simulations in which the attractant level was increased from a baseline level to a step level at $\tau = 0$. To this end, I drew attractant step levels from a uniform distribution spanning from a selected baseline level to the baseline level plus 200 %. Here, I present mutual information estimates between the baseline-specific batch of attractant step levels and the corresponding receptor methylation levels at a time point τ . Presented plots refer to the following attractant baseline levels: (A) 10^{-1} μ M, (B) 10^0 μ M, (C) 10^1 μ M, (D) 10^2 μ M, (E) 10^3 μ M, (F) 10^4 μ M, (G) 10^5 μ M, (H) 10^6 μ M, (I) 10^7 μ M, (J) 10^8 μ M,. By changing τ , I could visualize the process of memory formation. I employed surrogate mutual information estimations to validate original estimates. For surrogate estimates, the L_{step} variable was permuted to disrupt original dependencies. Further, in order to quantify the time period for memory formation, I fitted the original estimate curves (black) to Equation 5.8, in case memory formation was present. Data fits are presented in red. Applied system size: $1.4 \cdot 10^{-15}$ L.

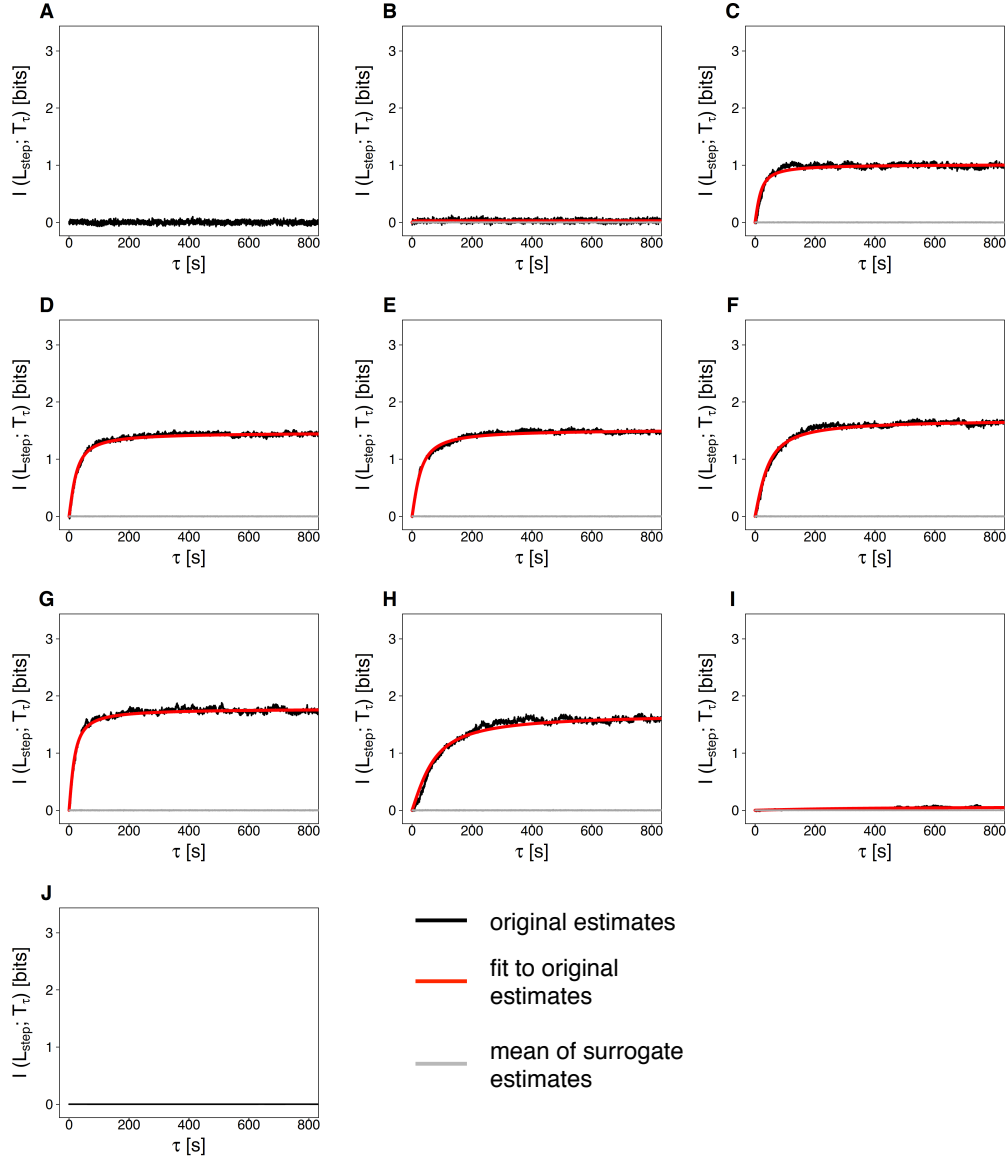


Fig. B.2. Mutual information estimates describing the formation of the methylation-based memory in *Escherichia coli* chemotaxis for a system size of $1.4 \cdot 10^{-16}$ L. Per attractant baseline level, I ran 1000 stochastic simulations in which the attractant level was increased from a baseline level to a step level at $\tau = 0$. To this end, I drew attractant step levels from a uniform distribution spanning from a selected baseline level to the baseline level plus 200 %. Here, I present mutual information estimates between the baseline-specific batch of attractant step levels and the corresponding receptor methylation levels at a time point τ . Presented plots refer to the following attractant baseline levels: (A) 10^{-1} μ M, (B) 10^0 μ M, (C) 10^1 μ M, (D) 10^2 μ M, (E) 10^3 μ M, (F) 10^4 μ M, (G) 10^5 μ M, (H) 10^6 μ M, (I) 10^7 μ M, (J) 10^8 μ M,. By changing τ , I could visualize the process of memory formation. I employed surrogate mutual information estimations to validate original estimates. For surrogate estimates, the L_{step} variable was permuted to disrupt original dependencies. Further, in order to quantify the time period for memory formation, I fitted the original estimate curves (black) to Equation 5.8, in case memory formation was present. Data fits are presented in red. Applied system size: $1.4 \cdot 10^{-16}$ L.

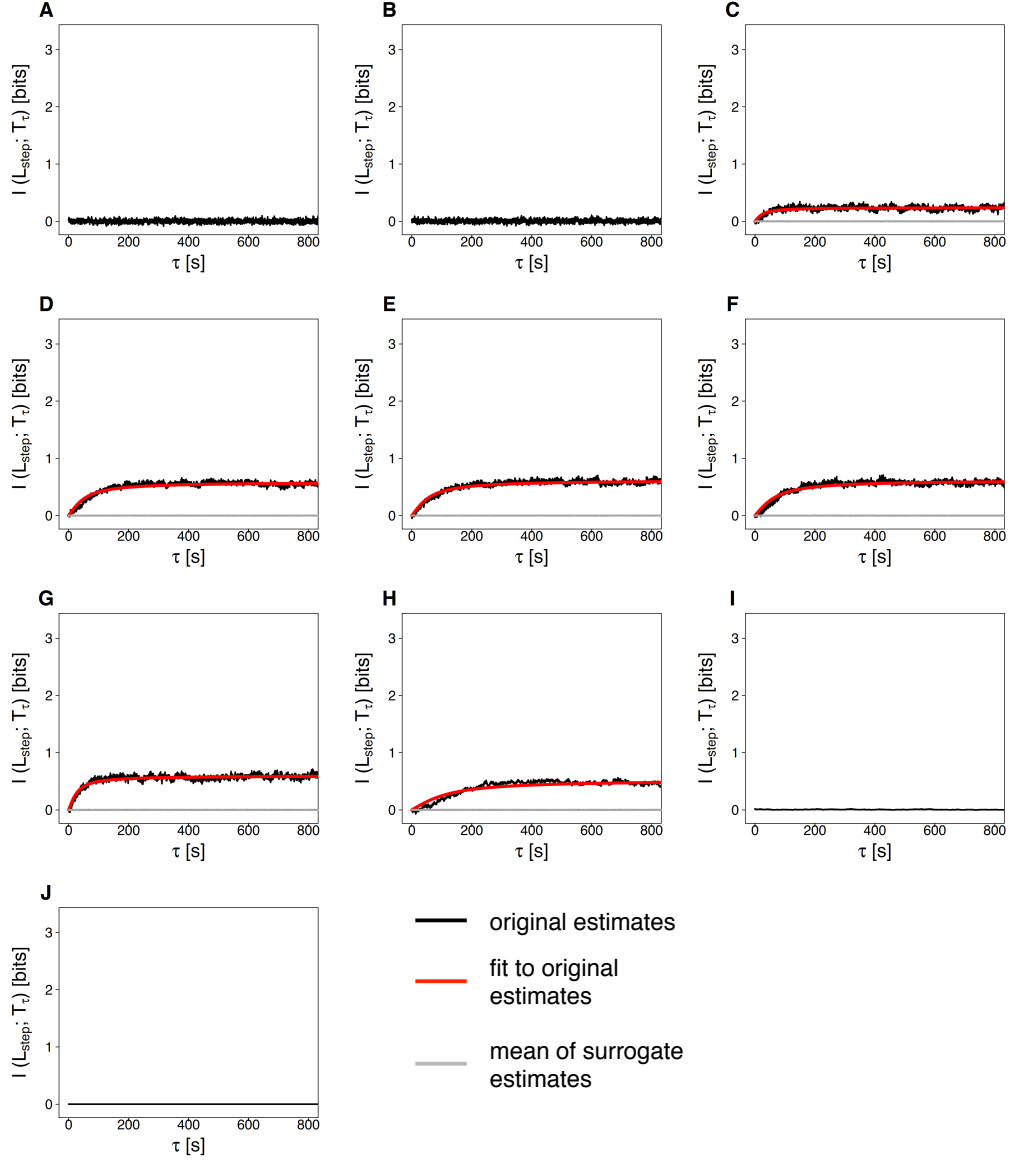


Fig. B.3. Mutual information estimates describing the formation of the methylation-based memory in *Escherichia coli* chemotaxis for a system size of $1.4 \cdot 10^{-17}$ L. Per attractant baseline level, I ran 1000 stochastic simulations in which the attractant level was increased from a baseline level to a step level at $\tau = 0$. To this end, I drew attractant step levels from a uniform distribution spanning from a selected baseline level to the baseline level plus 200 %. Here, I present mutual information estimates between the baseline-specific batch of attractant step levels and the corresponding receptor methylation levels at a time point τ . Presented plots refer to the following attractant baseline levels: (A) 10^{-1} μ M, (B) 10^0 μ M, (C) 10^1 μ M, (D) 10^2 μ M, (E) 10^3 μ M, (F) 10^4 μ M, (G) 10^5 μ M, (H) 10^6 μ M, (I) 10^7 μ M, (J) 10^8 μ M,. By changing τ , I could visualize the process of memory formation. I employed surrogate mutual information estimations to validate original estimates. For surrogate estimates, the L_{step} variable was permuted to disrupt original dependencies. Further, in order to quantify the time period for memory formation, I fitted the original estimate curves (black) to Equation 5.8, in case memory formation was present. Data fits are presented in red. Applied system size: $1.4 \cdot 10^{-17}$ L.

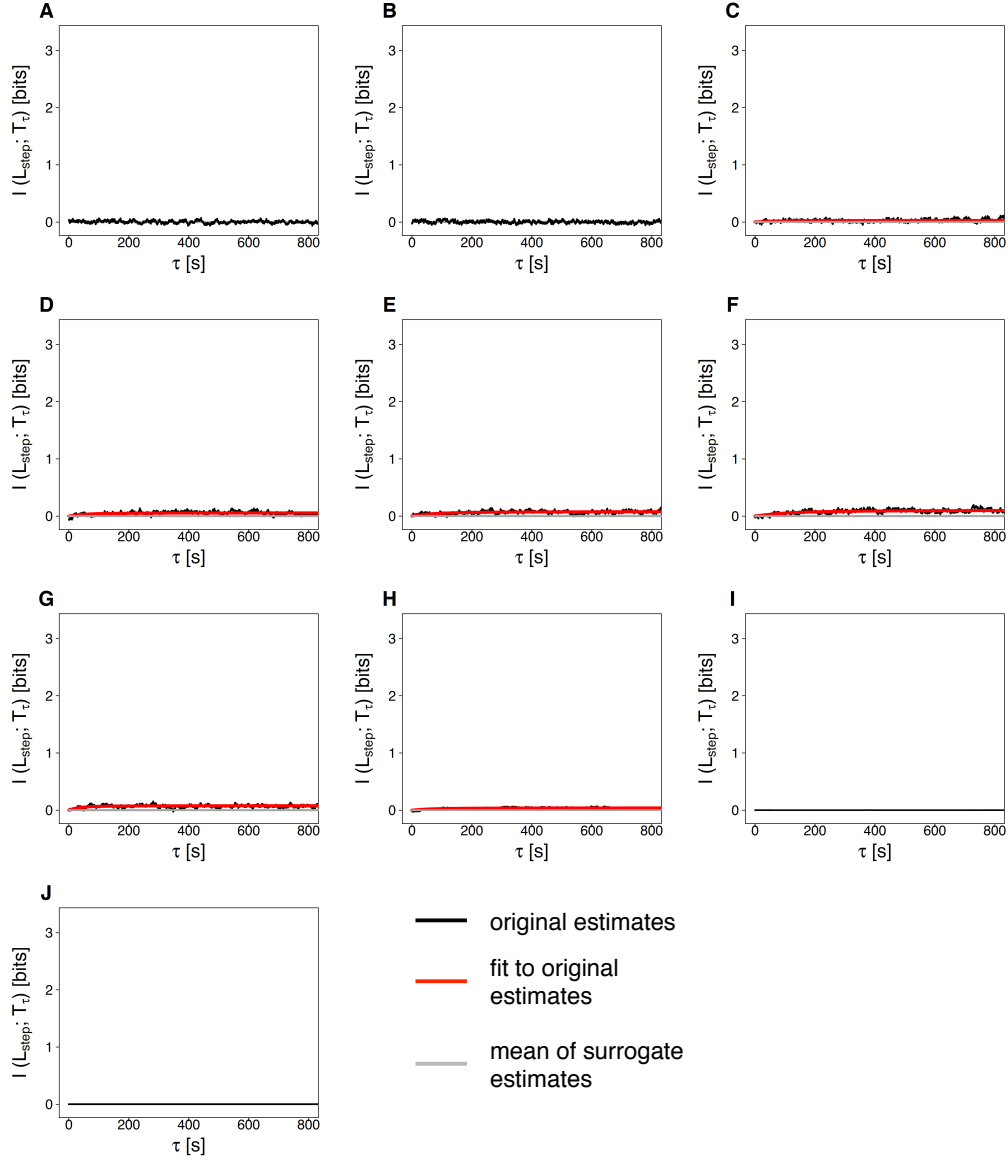


Fig. B.4. Mutual information estimates describing the formation of the methylation-based memory in *Escherichia coli* chemotaxis for a system size of $1.4 \cdot 10^{-18}$ L. Per attractant baseline level, I ran 1000 stochastic simulations in which the attractant level was increased from a baseline level to a step level at $\tau = 0$. To this end, I drew attractant step levels from a uniform distribution spanning from a selected baseline level to the baseline level plus 200 %. Here, I present mutual information estimates between the baseline-specific batch of attractant step levels and the corresponding receptor methylation levels at a time point τ . Presented plots refer to the following attractant baseline levels: (A) 10^{-1} μ M, (B) 10^0 μ M, (C) 10^1 μ M, (D) 10^2 μ M, (E) 10^3 μ M, (F) 10^4 μ M, (G) 10^5 μ M, (H) 10^6 μ M, (I) 10^7 μ M, (J) 10^8 μ M,. By changing τ , I could visualize the process of memory formation. I employed surrogate mutual information estimations to validate original estimates. For surrogate estimates, the L_{step} variable was permuted to disrupt original dependencies. Further, in order to quantify the time period for memory formation, I fitted the original estimate curves (black) to Equation 5.8, in case memory formation was present. Data fits are presented in red. Applied system size: $1.4 \cdot 10^{-18}$ L.

B.2 Additional estimates of mutual information showing memory loss in the original model

In Section 5.5, I also employed estimates of mutual information to show the dynamical process of memory loss. In particular, once a bacterial cell is stimulated by a change in ambient attractant levels, information about the previous attractant level, stored in the receptor methylation levels, is gradually lost.

Per attractant baseline level and system size, I drew 1000 attractant step levels from a uniform distribution spanning from the selected attractant baseline level to the baseline level plus 200 %. Then, per attractant baseline level and system volume, I initialized 1000 stochastic simulations. To this end, I started the simulations with biochemical species being set to their steady state concentrations for the drawn attractant step levels. At time point $\tau = 0$, I decreased the attractant level to the selected baseline level.

Based on the received baseline- and system-size-specific data, I performed estimations of mutual information. To this end, the first variable was composed of the drawn attractant step levels L_{step} and the second variable of the corresponding receptor methylation levels at a time point τ , T_{τ} . Thus, the first variable was composed of a vector, while the second variable was a five-column matrix.

For every original estimate of mutual information, I performed 100 surrogate estimations. In particular, I permuted the attractant step level vector to disrupt dependencies to the receptor methylation level matrix. In Tables B.5 to B.8, I present all obtained time courses of mutual information showing memory loss for different system sizes and attractant baseline levels. Original estimates are shown in black, the mean values of surrogate distributions are shown in darkgrey.

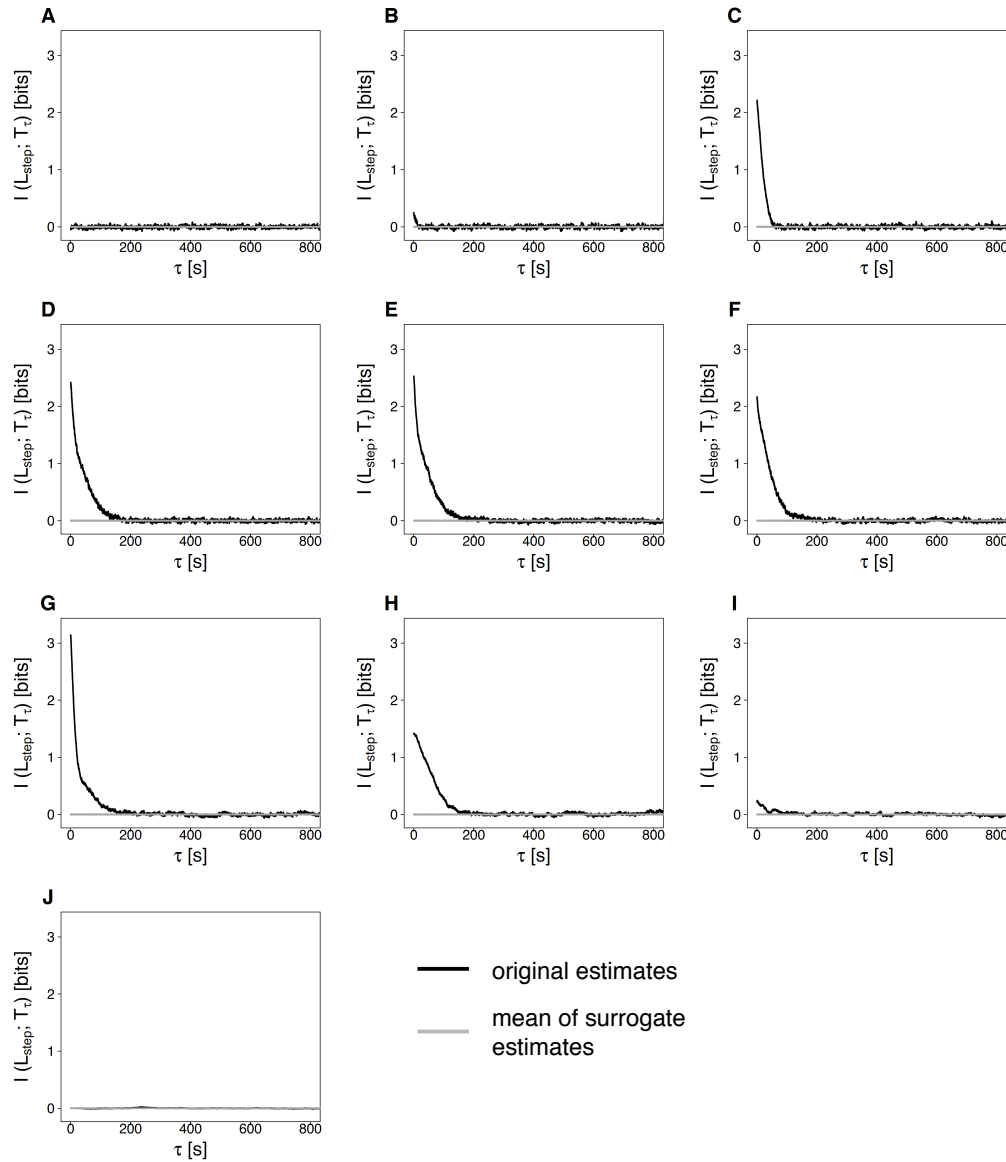


Fig. B.5. Mutual information estimates describing the loss of the methylation-based memory in *Escherichia coli* chemotaxis for a system size of $1.4 \cdot 10^{-15}$ L. Per attractant baseline level, I ran 1000 stochastic simulations. To this end, attractant levels were initialized from a step level and decreased to a baseline level at time point $\tau = 0$. In particular, attractant step levels were drawn out of a uniform distribution spanning from the selected baseline level to the baseline level plus 200 %. Thus, in the 1000 stochastic simulations, attractant levels were initially set to 1000 different step levels and the decreased to the same baseline level. Here, I present mutual information estimates between the baseline-specific batch of attractant step levels and the corresponding receptor methylation levels at a time point τ . Plots refer to the following attractant baseline levels: (A) 10^{-1} μ M, (B) 10^0 μ M, (C) 10^1 μ M, (D) 10^2 μ M, (E) 10^3 μ M, (F) 10^4 μ M, (G) 10^5 μ M, (H) 10^6 μ M, (I) 10^7 μ M, (J) 10^8 μ M,. By changing τ , I could visualize the process of memory loss. I employed surrogate estimations of mutual information to validate the original estimates. For surrogate estimates, I permuted the L_{step} variable to disrupt original dependencies to the receptor methylation level matrix. Per original estimate at a time point τ , I performed 100 surrogate estimates. Shown are the mean values of such τ -specific surrogate distributions in darkgrey. Applied system size: $1.4 \cdot 10^{-15}$ L.

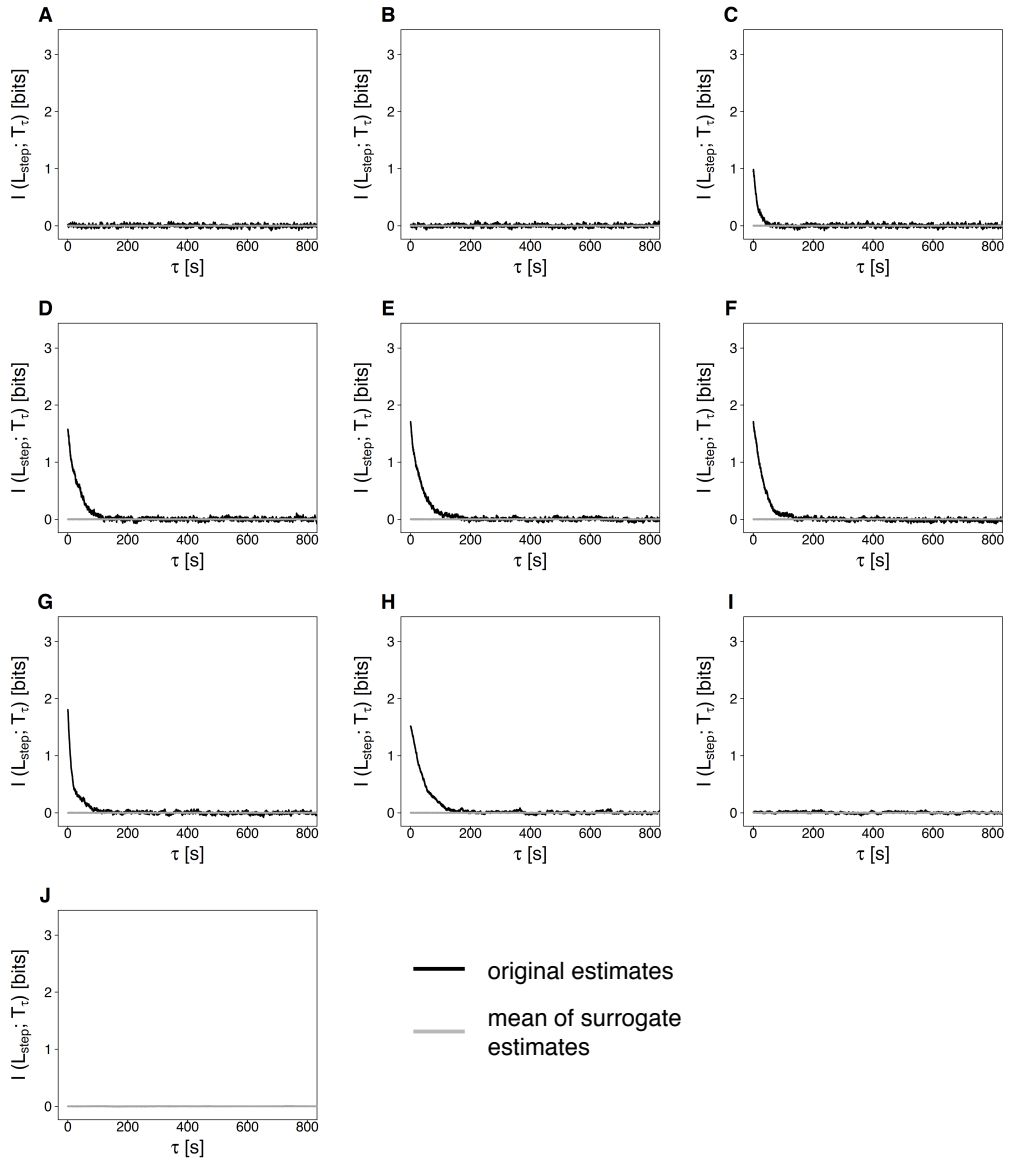


Fig. B.6. Mutual information estimates describing the loss of the methylation-based memory in *Escherichia coli* chemotaxis for a system size of $1.4 \cdot 10^{-16}$ L. Per attractant baseline level, I ran 1000 stochastic simulations. To this end, attractant levels were initialized from a step level and decreased to a baseline level at time point $\tau = 0$. In particular, attractant step levels were drawn out of a uniform distribution spanning from the selected baseline level to the baseline level plus 200 %. Thus, in the 1000 stochastic simulations, attractant levels were initially set to 1000 different step levels and the decreased to the same baseline level. Here, I present mutual information estimates between the baseline-specific batch of attractant step levels and the corresponding receptor methylation levels at a time point τ . Plots refer to the following attractant baseline levels: (A) 10^{-1} μ M, (B) 10^0 μ M, (C) 10^1 μ M, (D) 10^2 μ M, (E) 10^3 μ M, (F) 10^4 μ M, (G) 10^5 μ M, (H) 10^6 μ M, (I) 10^7 μ M, (J) 10^8 μ M,. By changing τ , I could visualize the process of memory loss. I employed surrogate estimations of mutual information to validate the original estimates. For surrogate estimates, I permuted the L_{step} variable to disrupt original dependencies to the receptor methylation level matrix. Per original estimate at a time point τ , I performed 100 surrogate estimates. Shown are the mean values of such τ -specific surrogate distributions in darkgrey. Applied system size: $1.4 \cdot 10^{-16}$ L.

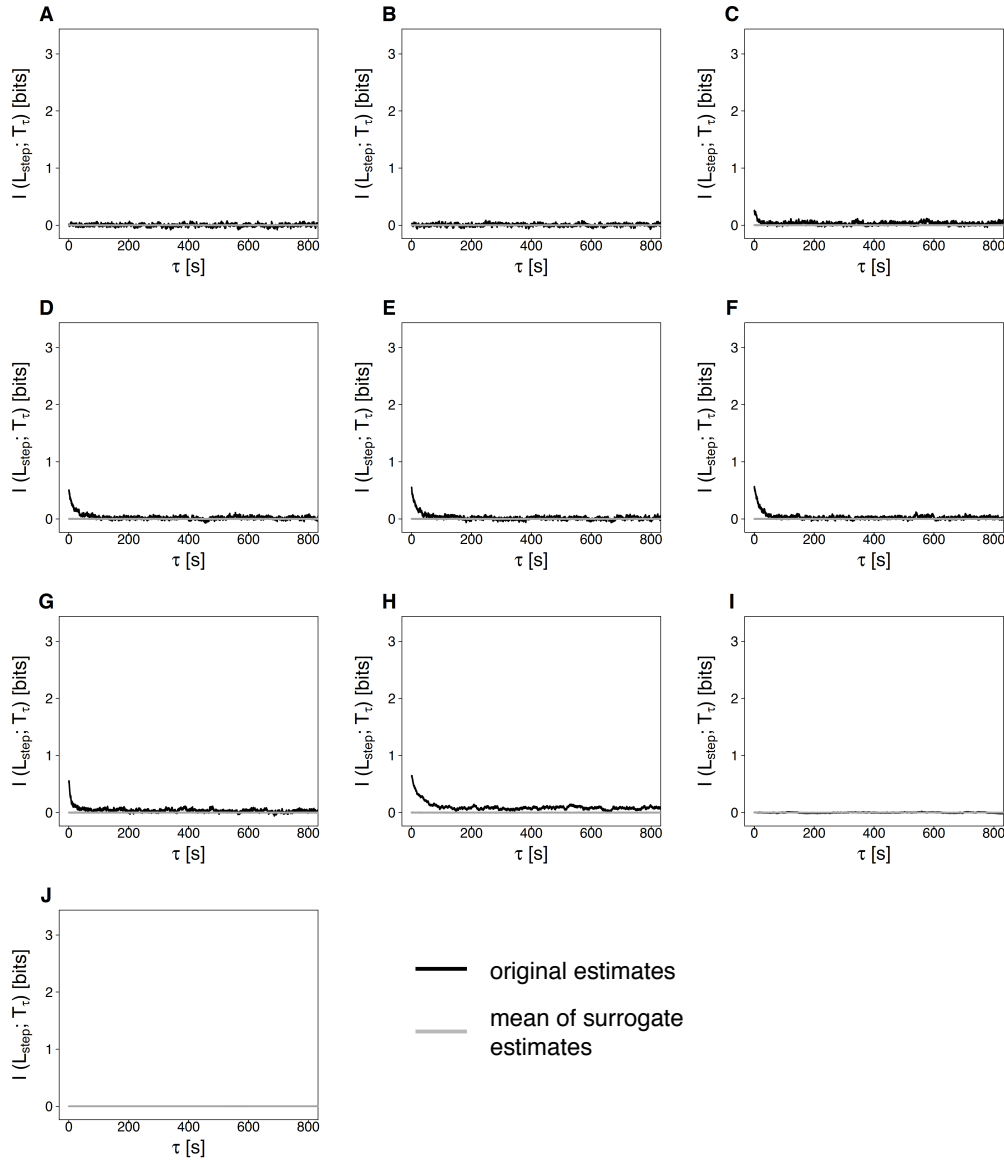


Fig. B.7. Mutual information estimates describing the loss of the methylation-based memory in *Escherichia coli* chemotaxis for a system size of $1.4 \cdot 10^{-17}$ L. Per attractant baseline level, I ran 1000 stochastic simulations. To this end, attractant levels were initialized from a step level and decreased to a baseline level at time point $\tau = 0$. In particular, attractant step levels were drawn out of a uniform distribution spanning from the selected baseline level to the baseline level plus 200 %. Thus, in the 1000 stochastic simulations, attractant levels were initially set to 1000 different step levels and the decreased to the same baseline level. Here, I present mutual information estimates between the baseline-specific batch of attractant step levels and the corresponding receptor methylation levels at a time point τ . Plots refer to the following attractant baseline levels: (A) 10^{-1} μ M, (B) 10^0 μ M, (C) 10^1 μ M, (D) 10^2 μ M, (E) 10^3 μ M, (F) 10^4 μ M, (G) 10^5 μ M, (H) 10^6 μ M, (I) 10^7 μ M, (J) 10^8 μ M,. By changing τ , I could visualize the process of memory loss. I employed surrogate estimations of mutual information to validate the original estimates. For surrogate estimates, I permuted the L_{step} variable to disrupt original dependencies to the receptor methylation level matrix. Per original estimate at a time point τ , I performed 100 surrogate estimates. Shown are the mean values of such τ -specific surrogate distributions in darkgrey. Applied system size: $1.4 \cdot 10^{-17}$ L.

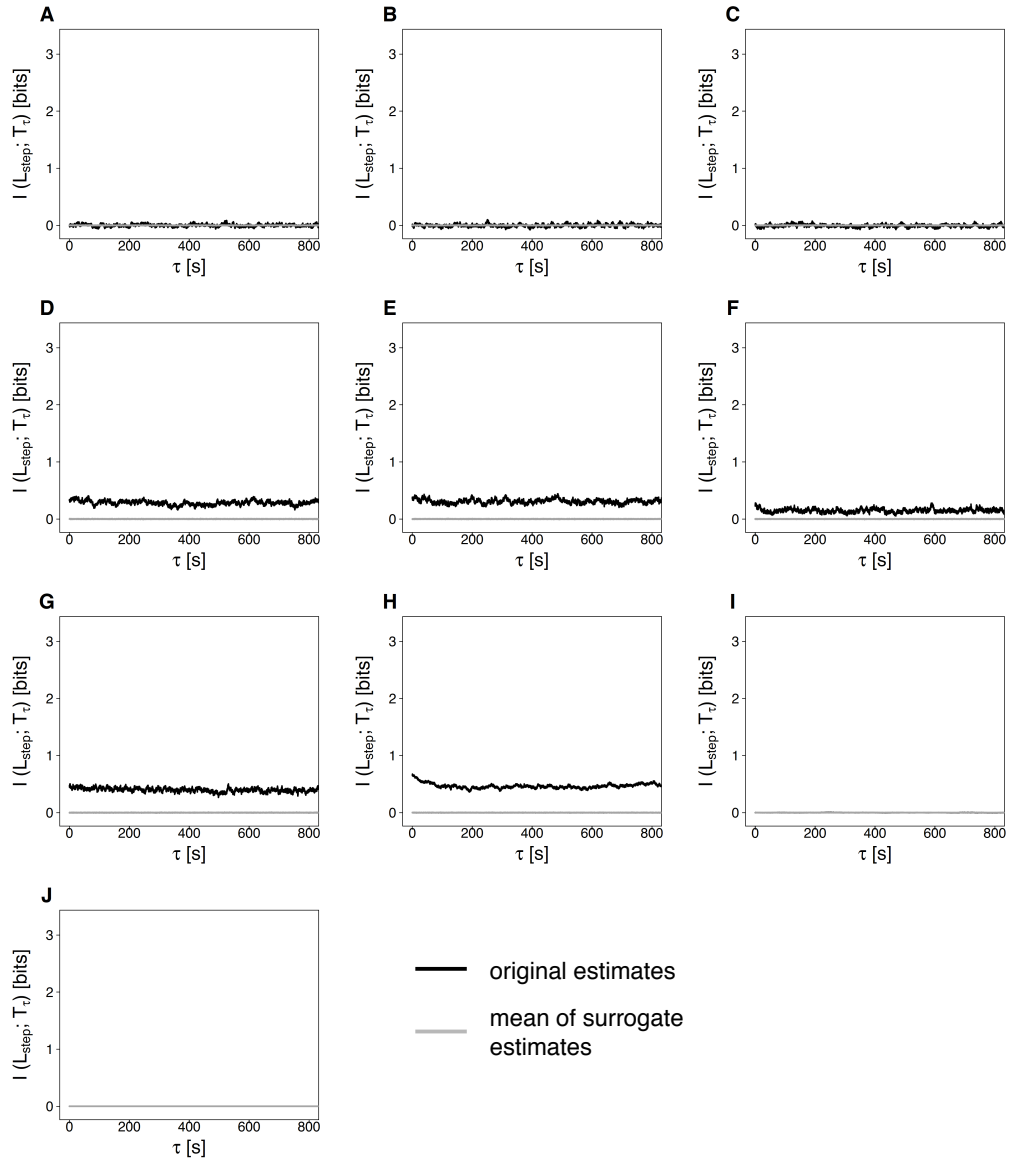


Fig. B.8. Mutual information estimates describing the loss of the methylation-based memory in *Escherichia coli* chemotaxis for a system size of $1.4 \cdot 10^{-18}$ L. Per attractant baseline level, I ran 1000 stochastic simulations. To this end, attractant levels were initialized from a step level and decreased to a baseline level at time point $\tau = 0$. In particular, attractant step levels were drawn out of a uniform distribution spanning from the selected baseline level to the baseline level plus 200 %. Thus, in the 1000 stochastic simulations, attractant levels were initially set to 1000 different step levels and the decreased to the same baseline level. Here, I present mutual information estimates between the baseline-specific batch of attractant step levels and the corresponding receptor methylation levels at a time point τ . Plots refer to the following attractant baseline levels: (A) 10^{-1} μ M, (B) 10^0 μ M, (C) 10^1 μ M, (D) 10^2 μ M, (E) 10^3 μ M, (F) 10^4 μ M, (G) 10^5 μ M, (H) 10^6 μ M, (I) 10^7 μ M, (J) 10^8 μ M,. By changing τ , I could visualize the process of memory loss. I employed surrogate estimations of mutual information to validate the original estimates. For surrogate estimates, I permuted the L_{step} variable to disrupt original dependencies to the receptor methylation level matrix. Per original estimate at a time point τ , I performed 100 surrogate estimates. Shown are the mean values of such τ -specific surrogate distributions in darkgrey. Applied system size: $1.4 \cdot 10^{-18}$ L.

B.3 Time scales for memory formation and memory loss in model versions differing in the maximal number of receptor methylations

I derived time scales for memory formation and memory loss from delayed estimates of mutual information measuring τ_{step} and τ_{drop} , as introduced in Section 5.5. In most cases, τ_{step} and τ_{drop} were particularly large for the largest attractant baseline levels at which memory could still be formed. In addition, the process of memory formation generally appeared to be slower than the process of memory loss (Figures B.9 and B.10).

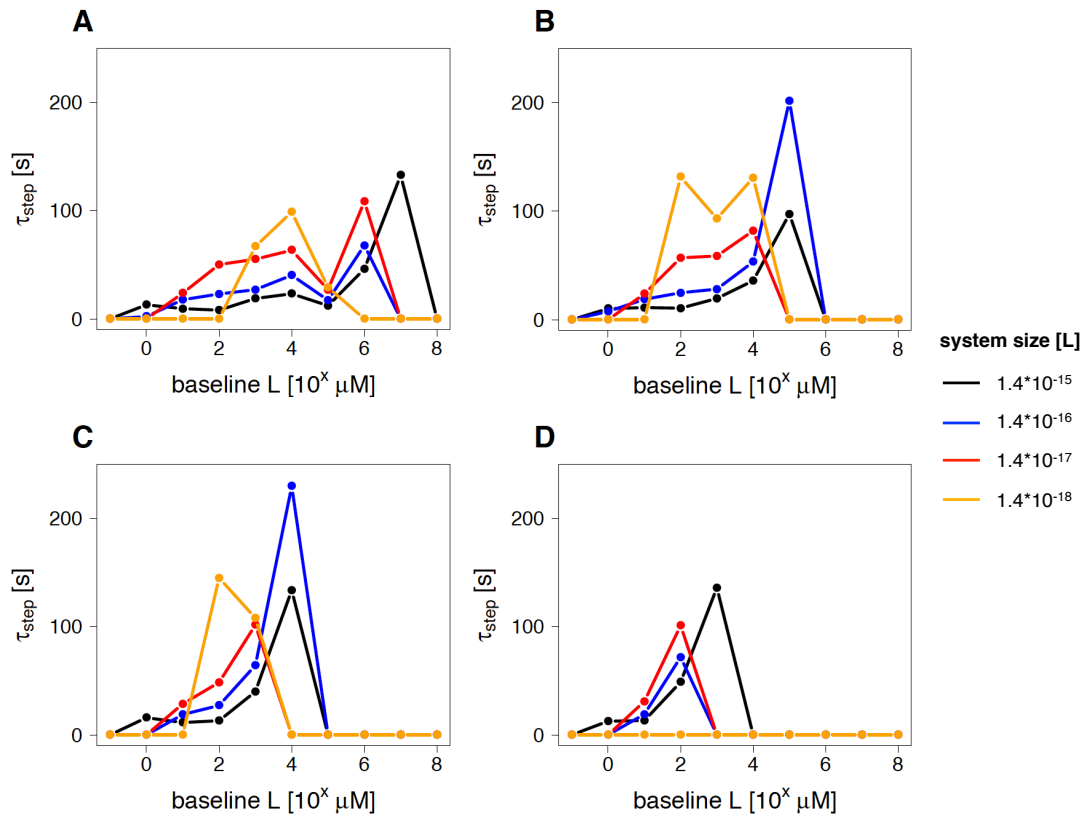


Fig. B.9. Time scales for memory formation in model versions differing in the maximal number of receptor methylations. For various versions of the chemotaxis model by Kollmann *et al.*, system sizes and attractant baseline levels, I quantified the dynamical process of memory formation by means of delayed estimates of mutual information, as previously shown in Figure 5.8. In case memory formation was present, I quantified τ_{step} , the time period starting in the moment the increase in the attractant level was applied until the moment half of the maximal mutual information between L_{step} and T_τ was reached. Model versions differed from each other with respect to the maximal number of receptor methylations: in (A) four, in (B) three, in (C) two and in (D) one methylation(s) allowed per receptor.

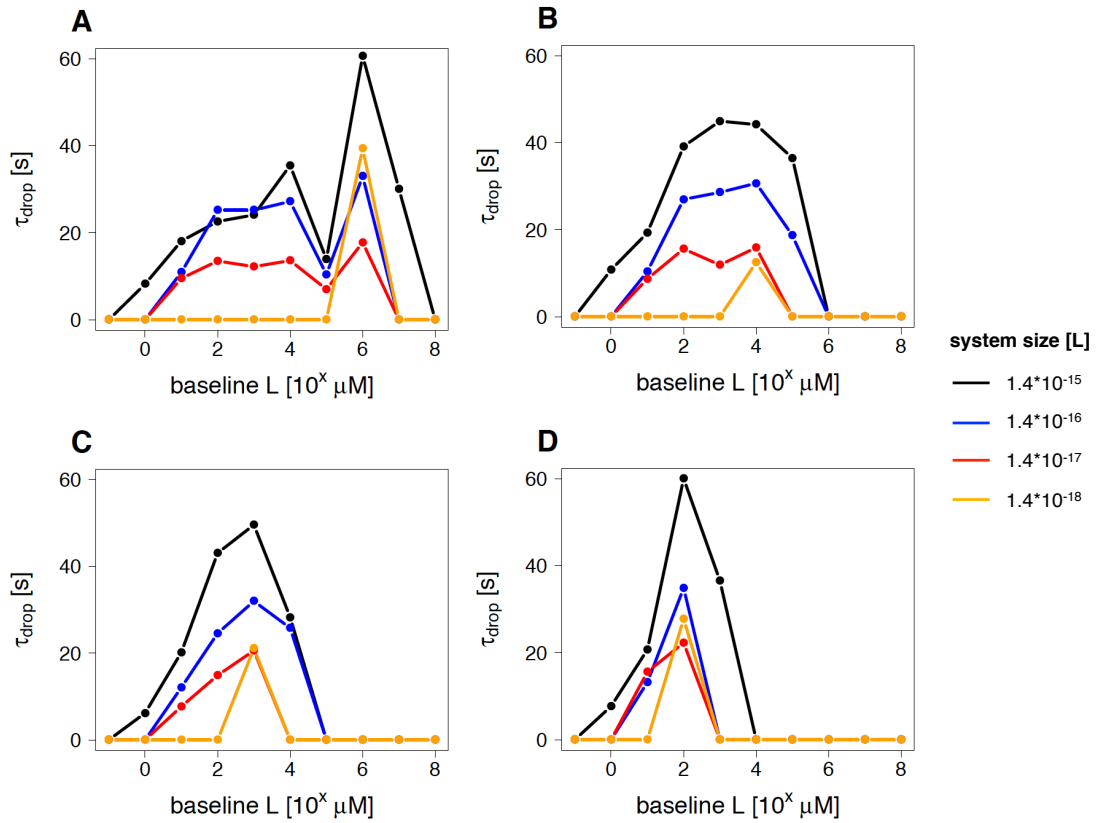


Fig. B.10. Time scales for memory loss in model versions differing in the maximal number of receptor methylations. For various versions of the chemotaxis model by Kollmann *et al.*, system sizes and attractant baseline levels, I quantified the dynamical process of memory loss by means of delayed estimates of mutual information, as previously shown in Figure 5.10. In case I could identify memory loss, I quantified τ_{drop} , the time period starting in the moment the decrease in the attractant level was applied until the moment half of the initial mutual information between L_{step} and T_τ was lost. Model versions differed from each other with respect to the maximal number of receptor methylations: in (A) four, in (B) three, in (C) two and in (D) one methylation(s) allowed per receptor.

Bibliography

- [1] Naama Barkai and Stan Leibler. “Robustness in simple biochemical networks”. In: *Nature* 387.6636 (1997), p. 913. DOI: 10.1038/43199.
- [2] Hiroaki Kitano. “Biological robustness”. In: *Nature Reviews Genetics* 5.11 (2004), p. 826.
- [3] Markus Kollmann, Linda Løvdok, Kilian Bartholomé, Jens Timmer, and Victor Sourjik. “Design principles of a bacterial signalling network”. In: *Nature* 438.7067 (2005), p. 504. DOI: 10.1038/nature04228.
- [4] Paolo Sassone-Corsi and Emiliana Borrelli. “Mutations in signal transduction pathways and inherited diseases”. In: *Current opinion in genetics & development* 2.3 (1992), pp. 455–458.
- [5] Richard Sever and Joan S Brugge. “Signal transduction in cancer”. In: *Cold Spring Harbor perspectives in medicine* 5.4 (2015), a006098. DOI: 10.1101/cshperspect.a006098.
- [6] Andrew J Maule. “Plasmodesmata: structure, function and biogenesis”. In: *Current opinion in plant biology* 11.6 (2008), pp. 680–686. DOI: 10.1016/j.pbi.2008.08.002.
- [7] Hans-Hermann Gerdes, Amin Rustom, and Xiang Wang. “Tunneling nanotubes, an emerging intercellular communication route in development”. In: *Mechanisms of development* 130.6-8 (2013), pp. 381–387. DOI: 10.1016/j.mod.2012.11.006.
- [8] Nalin M Kumar and Norton B Gilula. “The gap junction communication channel”. In: *Cell* 84.3 (1996), pp. 381–388. DOI: S0092-8674(00)81282-9[pil].
- [9] Hélène S Robert and Jiří Friml. “Auxin and other signals on the move in plants”. In: *Nature chemical biology* 5.5 (2009), p. 325. DOI: 10.1038/nchembio.170.
- [10] Roger Ekins. “Measurement of free hormones in blood”. In: *Endocrine Reviews* 11.1 (1990), pp. 5–46. DOI: 10.1210/edrv-11-1-5.
- [11] Melissa B Miller and Bonnie L Bassler. “Quorum sensing in bacteria”. In: *Annual Reviews in Microbiology* 55.1 (2001), pp. 165–199. DOI: 10.1146/annurev.micro.55.1.165.
- [12] IJ Uings and SN Farrow. “Cell receptors and cell signalling”. In: *Molecular Pathology* 53.6 (2000), p. 295. DOI: 10.1136/mp.53.6.295.
- [13] Gabor Forgacs, Soon Hyung Yook, Paul A Janmey, Hawoong Jeong, and Christopher G Burd. “Role of the cytoskeleton in signaling networks”. In: *Journal of cell science* 117.13 (2004), pp. 2769–2775. DOI: 10.1242/jcs.01122.
- [14] Colin Dingwall and Ronald A Laskey. “Nuclear targeting sequences - a consensus?” In: *Trends in biochemical sciences* 16 (1991), pp. 478–481.
- [15] UB Kaupp and KW Koch. “Role of cGMP and Ca²⁺ in vertebrate photoreceptor excitation and adaptation”. In: *Annual Review of Physiology* 54.1 (1992), pp. 153–176.
- [16] GM Cooper. “Pathways of intracellular signal transduction”. In: *The cell* (2004), pp. 558–571.

- [17] Claude E Shannon. “A Mathematical Theory of Communication”. In: *Bell Systems Technical Journal* 27 (1948), pp. 623–656. DOI: 10.1145/584091.584093.
- [18] Jeremy E Purvis and Galit Lahav. “Encoding and decoding cellular information through signaling dynamics”. In: *Cell* 152.5 (2013), pp. 945–956. DOI: 10.1016/j.cell.2013.02.005.
- [19] Yukiko Gotoh, Eisuke Nishida, Takashi Yamashita, Minako Hoshi, Minoru Kawakami, and Hikoichi Sakai. “Microtubule-associated-protein (MAP) kinase activated by nerve growth factor and epidermal growth factor in PC12 cells: Identity with the mitogen-activated MAP kinase of fibroblastic cells”. In: *European journal of biochemistry* 193.3 (1990), pp. 661–669.
- [20] TT Nguyen, JC Scimeca, C Filloux, P Peraldi, JL Carpentier, and E Van Obberghen. “Co-regulation of the mitogen-activated protein kinase, extracellular signal-regulated kinase 1, and the 90-kDa ribosomal S6 kinase in PC12 cells. Distinct effects of the neurotrophic factor, nerve growth factor, and the mitogenic factor, epidermal growth factor.” In: *Journal of Biological Chemistry* 268.13 (1993), pp. 9803–9810.
- [21] Sarah Traverse, Nestor Gomez, Hugh Paterson, Chris Marshall, and Philip Cohen. “Sustained activation of the mitogen-activated protein (MAP) kinase cascade may be required for differentiation of PC12 cells. Comparison of the effects of nerve growth factor and epidermal growth factor”. In: *Biochemical Journal* 288.2 (1992), pp. 351–355.
- [22] Galit Lahav, Nitzan Rosenfeld, Alex Sigal, Naama Geva-Zatorsky, Arnold J Levine, Michael B Elowitz, and Uri Alon. “Dynamics of the p53-Mdm2 feedback loop in individual cells”. In: *Nature genetics* 36.2 (2004), p. 147. DOI: 10.1038/ng1293.
- [23] Eric Batchelor, Alexander Loewer, Caroline Mock, and Galit Lahav. “Stimulus-dependent dynamics of p53 in single cells”. In: *Molecular systems biology* 7.1 (2011), p. 488. DOI: 10.1038/msb.2011.20.
- [24] Naama Geva-Zatorsky, Erez Dekel, Ariel A Cohen, Tamar Danon, Lydia Cohen, and Uri Alon. “Protein dynamics in drug combinations: a linear superposition of individual-drug responses”. In: *Cell* 140.5 (2010), pp. 643–651. DOI: 10.1016/j.cell.2010.02.011.
- [25] Sikander Pal Choudhary, Jing-Quan Yu, Kazuko Yamaguchi-Shinozaki, Kazuo Shinozaki, and Lam-Son Phan Tran. “Benefits of brassinosteroid crosstalk”. In: *Trends in plant science* 17.10 (2012), pp. 594–605. DOI: 10.1016/j.tplants.2012.05.012.
- [26] Grégory Vert and Joanne Chory. “Crosstalk in cellular signaling: background noise or the real thing?” In: *Developmental cell* 21.6 (2011), pp. 985–991. DOI: 10.1016/j.devcel.2011.11.006.
- [27] CJ Marshall. “Specificity of receptor tyrosine kinase signaling: transient versus sustained extracellular signal-regulated kinase activation”. In: *Cell* 80.2 (1995), pp. 179–185. DOI: 10.1016/0092-8674(95)90401-8.
- [28] Jeremy E Purvis, Kyle W Karhohs, Caroline Mock, Eric Batchelor, Alexander Loewer, and Galit Lahav. “p53 dynamics control cell fate”. In: *Science* 336.6087 (2012), pp. 1440–1444. DOI: 10.1126/science.1218351.
- [29] Leon O Murphy, Sallie Smith, Rey-Huei Chen, Diane C Fingar, and John Blenis. “Molecular interpretation of ERK signal duration by immediate early gene products”. In: *Nature cell biology* 4.8 (2002), p. 556. DOI: 10.1038/ncb822.
- [30] Leon O Murphy, Jeffrey P MacKeigan, and John Blenis. “A network of immediate early gene products propagates subtle differences in mitogen-activated protein kinase signal amplitude and duration”. In: *Molecular and cellular biology* 24.1 (2004), pp. 144–153. DOI: 10.1128/MCB.24.1.144.
- [31] Ido Amit, Ami Citri, Tal Shay, Yiling Lu, Menachem Katz, Fan Zhang, Gabi Tarcic, Doris Siwak, John Lahad, Jasmine Jacob-Hirsch, et al. “A module of negative feedback regulators defines growth factor signaling”. In: *Nature genetics* 39.4 (2007), p. 503. DOI: 10.1038/ng1987.

- [32] Marie Csete and John Doyle. “Bow ties, metabolism and disease”. In: *TRENDS in Biotechnology* 22.9 (2004), pp. 446–450. DOI: 10.1016/j.tibtech.2004.07.007.
- [33] Ernesto Carafoli, Luigia Santella, Donata Branca, and Marisa Brini. “Generation, control, and processing of cellular calcium signals”. In: *Critical reviews in biochemistry and molecular biology* 36.2 (2001), pp. 107–260. DOI: 10.1080/20014091074183.
- [34] Michael J Berridge, Peter Lipp, and Martin D Bootman. “The versatility and universality of calcium signalling”. In: *Nature reviews Molecular cell biology* 1.1 (2000), pp. 11–21. DOI: 10.1038/35036035.
- [35] Michael J Berridge, Martin D Bootman, and HL Roderick. “Calcium signaling: Dynamics, homeostasis, and remodeling”. In: *Nature* 4 (2003), pp. 517–529. DOI: 10.1038/nrm1155.
- [36] Peter HGM Willems, Jürgen Pahle, Xenia L Stalpers, Douaa Mugahid, Alexander Nikolaew, Werner JH Koopman, and Ursula Kummer. “PKC-mediated inhibitory feedback of the cholecystokinin 1 receptor controls the shape of oscillatory Ca^{2+} signals”. In: *The FEBS journal* 282.11 (2015), pp. 2187–2201. DOI: 10.1111/febs.13267.
- [37] J Kevin Foskett, Carl White, King-Ho Cheung, and Don-On Daniel Mak. “Inositol trisphosphate receptor Ca^{2+} release channels”. In: *Physiological reviews* 87.2 (2007), pp. 593–658. DOI: 10.1152/physrev.00035.2006.
- [38] Veerle Vanderheyden, Benoit Devogelaere, Ludwig Missiaen, Humbert De Smedt, Geert Bultynck, and Jan B Parys. “Regulation of inositol 1,4,5-trisphosphate-induced Ca^{2+} release by reversible phosphorylation and dephosphorylation”. In: *Biochimica et Biophysica Acta (BBA)-Molecular Cell Research* 1793.6 (2009), pp. 959–970. DOI: 10.1016/j.bbamcr.2008.12.003.
- [39] Johanna T Lanner, Dimitra K Georgiou, Aditya D Joshi, and Susan L Hamilton. “Ryanodine receptors: structure, expression, molecular details, and function in calcium release”. In: *Cold Spring Harbor perspectives in biology* 2.11 (2010), a003996. DOI: 10.1101/cshperspect.a003996.
- [40] Muthu Periasamy and Anuradha Kalyanasundaram. “SERCA pump isoforms: their role in calcium transport and disease”. In: *Muscle & nerve* 35.4 (2007), pp. 430–442. DOI: 10.1002/mus.20745.
- [41] Alexei Verkhratsky. “Physiology and pathophysiology of the calcium store in the endoplasmic reticulum of neurons”. In: *Physiological reviews* 85.1 (2005), pp. 201–279. DOI: 10.1152/physrev.00004.2004.
- [42] Gregory R Monteith, Natalia Prevarskaya, and Sarah J Roberts-Thomson. “The calcium–cancer signalling nexus”. In: *Nature Reviews Cancer* 17.6 (2017), p. 367. DOI: 10.1038/nrc.2017.18.
- [43] Michael J Berridge, Martin D Bootman, and Peter Lipp. “Calcium - a life and death signal”. In: *Nature* 395.6703 (1998), p. 645. DOI: 10.1038/27094.
- [44] Michael J Berridge. “The AM and FM of calcium signalling”. In: *Nature* 386 (1997), pp. 759–760. DOI: 10.1038/386759a0.
- [45] PE Rapp and Michael J Berridge. “The control of transepithelial potential oscillations in the salivary gland of *Calliphora erythrocephala*”. In: *Journal of Experimental Biology* 93.1 (1981), pp. 119–132.
- [46] Niall M Woods, KS Roy Cuthbertson, and Peter H Cobbold. “Repetitive transient rises in cytoplasmic free calcium in hormone-stimulated hepatocytes”. In: *Nature* 319.6054 (1986), pp. 600–602. DOI: 10.1038/319600a0.
- [47] N Schweizer, U Kummer, H Hercht, and T Braunbeck. “Amplitude-encoded calcium oscillations in fish cells”. In: *Biophysical chemistry* 159.2-3 (2011), pp. 294–302. DOI: 10.1016/j.bpc.2011.08.002.

- [48] Luis Aguilera, Frank Bergmann, Giovanni Dalmaso, Tobias Elsaesser, Ruth Grosseholz, Pascal Holzheu, Priyata Kalra, Ursula Kummer, Sven Sahle, and Nadine Veith. “Robustness of frequency vs. amplitude coding of calcium oscillations during changing temperatures”. In: *Biophysical chemistry* 245 (2019), pp. 17–24. DOI: 10.1016/j.bpc.2018.11.003.
- [49] Gethyn J Allen, Sarah P Chu, Karin Schumacher, Chad T Shimazaki, Dionne Vafeados, Andrea Kemper, Scott D Hawke, Gary Tallman, Roger Y Tsien, Jeffrey F Harper, et al. “Alteration of stimulus-specific guard cell calcium oscillations and stomatal closing in *Arabidopsis det3* mutant”. In: *Science* 289.5488 (2000), pp. 2338–2342. DOI: 10.1126/science.289.5488.2338.
- [50] C Jane Dixon, Niall M Woods, KS Roy Cuthbertson, and Peter H Cobbold. “Evidence for two Ca^{2+} -mobilizing purinoceptors on rat hepatocytes”. In: *Biochemical Journal* 269.2 (1990), pp. 499–502. DOI: 10.1042/bj2690499.
- [51] Tobias Meyer and Lubert Stryer. “Molecular model for receptor-stimulated calcium spiking”. In: *Proceedings of the National Academy of Sciences* 85.14 (1988), pp. 5051–5055.
- [52] KSR Cuthbertson and TR Chay. “Modelling receptor-controlled intracellular calcium oscillators”. In: *Cell calcium* 12.2-3 (1991), pp. 97–109.
- [53] Ursula Kummer, Lars F Olsen, C Jane Dixon, Anne K Green, Erich Bornberg-Bauer, and Gerold Baier. “Switching from simple to complex oscillations in calcium signaling”. In: *Biophysical journal* 79.3 (2000), pp. 1188–1195. DOI: 10.1016/S0006-3495(00)76373-9.
- [54] Antonio Politi, Lawrence D Gaspers, Andrew P Thomas, and Thomas Höfer. “Models of IP_3 and Ca^{2+} oscillations: frequency encoding and identification of underlying feedbacks”. In: *Biophysical Journal* 90.9 (2006), pp. 3120–3133. DOI: 10.1529/biophysj.105.072249.
- [55] Roland Somogyi and JW Stucki. “Hormone-induced calcium oscillations in liver cells can be explained by a simple one pool model.” In: *Journal of biological chemistry* 266.17 (1991), pp. 11068–11077.
- [56] Albert Goldbeter, Geneviève Dupont, and Michael J Berridge. “Minimal model for signal-induced Ca^{2+} oscillations and for their frequency encoding through protein phosphorylation.” In: *Proceedings of the National Academy of Sciences* 87.4 (1990), pp. 1461–1465. DOI: 10.1073/pnas.87.4.1461.
- [57] Michel Laurent and Michel Claret. “Signal-induced Ca^{2+} oscillations through the regulation of the inositol 1,4,5-trisphosphate-gated Ca^{2+} channel: an allosteric model”. In: *Journal of theoretical biology* 186.3 (1997), pp. 307–326.
- [58] Vladimir Grubelnik, Ann Zahle Larsen, Ursula Kummer, Lars Folke Olsen, and Marko Marhl. “Mitochondria regulate the amplitude of simple and complex calcium oscillations”. In: *Biophysical chemistry* 94.1-2 (2001), pp. 59–74. DOI: 10.1016/S0301-4622(01)00211-3.
- [59] J Sneyd, J Keizer, and MJ Sanderson. “Mechanisms of calcium oscillations and waves: a quantitative analysis.” In: *The FASEB Journal* 9.14 (1995), pp. 1463–1472. DOI: 10.1096/fasebj.9.14.7589988.
- [60] Stefan Schuster, Marko Marhl, and Thomas Höfer. “Modelling of simple and complex calcium oscillations: From single-cell responses to intercellular signalling”. In: *European Journal of Biochemistry* 269.5 (2002), pp. 1333–1355. DOI: 10.1046/j.0014-2956.2001.02720.x.
- [61] Martin Falcke. “Reading the patterns in living cells - the physics of Ca^{2+} signaling”. In: *Advances in physics* 53.3 (2004), pp. 255–440. DOI: 10.1080/00018730410001703159.
- [62] Erik Smedler and Per Uhlén. “Frequency decoding of calcium oscillations”. In: *Biochimica Et Biophysica Acta (BBA) - General Subjects* 1840.3 (2014), pp. 964–969. DOI: 10.1016/j.bbagen.2013.11.015.
- [63] Ricardo E Dolmetsch, Keli Xu, and Richard S Lewis. “Calcium oscillations increase the efficiency and specificity of gene expression”. In: *Nature* 392.6679 (1998), p. 933. DOI: 10.1038/31960.

- [64] Wen Li, Juan Llopis, Michael Whitney, Gregor Zlokarnik, and Roger Y Tsien. “Cell-permeant caged InsP3 ester shows that Ca^{2+} spike frequency can optimize gene expression”. In: *Nature* 392.6679 (1998), pp. 936–941. DOI: 10.1038/31965.
- [65] Paul De Koninck and Howard Schulman. “Sensitivity of CaM kinase II to the frequency of Ca^{2+} oscillations”. In: *Science* 279.5348 (1998), pp. 227–230. DOI: 10.1126/science.279.5348.227.
- [66] Feleke Eshete and R Douglas Fields. “Spike frequency decoding and autonomous activation of Ca^{2+} -calmodulin-dependent protein kinase II in dorsal root ganglion neurons”. In: *Journal of Neuroscience* 21.17 (2001), pp. 6694–6705. DOI: 10.1523/jneurosci.21-17-06694.2001.
- [67] Phyllis I Hanson, Tobias Meyer, Lubert Stryer, and Howard Schulman. “Dual role of calmodulin in autophosphorylation of multifunctional CaM kinase may underlie decoding of calcium signals”. In: *Neuron* 12.5 (1994), pp. 943–956. DOI: 10.1016/0896-6273(94)90306-9.
- [68] K Ulrich Bayer, Paul De Koninck, and Howard Schulman. “Alternative splicing modulates the frequency-dependent response of CaMKII to Ca^{2+} oscillations”. In: *The EMBO journal* 21.14 (2002), pp. 3590–3597. DOI: 10.1093/emboj/cdf360.
- [69] Geneviève Dupont, Gérald Houart, and Paul De Koninck. “Sensitivity of CaM kinase II to the frequency of Ca^{2+} oscillations: a simple model”. In: *Cell calcium* 34.6 (2003), pp. 485–497. DOI: 10.1016/S0143-4160(03)00152-0.
- [70] Elena Oancea and Tobias Meyer. “Protein kinase C as a molecular machine for decoding calcium and diacylglycerol signals”. In: *Cell* 95.3 (1998), pp. 307–318. DOI: 10.1016/S0092-8674(00)81763-8.
- [71] P Tompa, R Tóth-Boconádi, and P Friedrich. “Frequency decoding of fast calcium oscillations by calpain”. In: *Cell calcium* 29.3 (2001), pp. 161–170. DOI: 10.1054/ceca.2000.0179.
- [72] Sabine Kupzig, Simon A Walker, and Peter J Cullen. “The frequencies of calcium oscillations are optimized for efficient calcium-mediated activation of Ras and the ERK/MAPK cascade”. In: *Proceedings of the National Academy of Sciences of the United States of America* 102.21 (2005), pp. 7577–7582. DOI: 10.1073/pnas.040961102.
- [73] Gethyn J Allen, Sarah P Chu, Carrie L Harrington, Karin Schumacher, Thomas Hoffmann, Yat Y Tang, Erwin Grill, and Julian I Schroeder. “A defined range of guard cell calcium oscillation parameters encodes stomatal movements”. In: *Nature* 411.6841 (2001), p. 1053. DOI: 10.1038/35082575.
- [74] Ricardo E Dolmetsch, Richard S Lewis, Christopher C Goodnow, and James I Healy. “Differential activation of transcription factors induced by Ca^{2+} response amplitude and duration”. In: *Nature* 386.6627 (1997), p. 855. DOI: 10.1038/386855a0.
- [75] Lu Li, Melanie I Stefan, and Nicolas Le Novère. “Calcium input frequency, duration and amplitude differentially modulate the relative activation of calcineurin and CaMKII”. In: *PloS one* 7.9 (2012), e43810. DOI: 10.1371/journal.pone.0043810.
- [76] Geneviève Dupont and Albert Goldbeter. “Protein phosphorylation driven by intracellular calcium oscillations: a kinetic analysis”. In: *Biophysical chemistry* 42.3 (1992), pp. 257–270. DOI: 10.1016/0301-4622(92)80018-Z.
- [77] K Prank, L Läer, A Von Zur Muehlen, G Brabant, and C Schöfl. “Decoding of intracellular calcium spike trains”. In: *EPL (Europhysics Letters)* 42.2 (1998), p. 143. DOI: 10.1209/epl/i1998-00220-2.
- [78] Ann Zahle Larsen and Ursula Kummer. “Information processing in calcium signal transduction”. In: *Understanding Calcium Dynamics*. Springer, 2003, pp. 153–178.
- [79] Ann Zahle Larsen, Lars Folke Olsen, and Ursula Kummer. “On the encoding and decoding of calcium signals in hepatocytes”. In: *Biophysical chemistry* 107.1 (2004), pp. 83–99. DOI: 10.1016/j.bpc.2003.08.010.

- [80] Anvar Rozi and Ya Jia. "A theoretical study of effects of cytosolic Ca^{2+} oscillations on activation of glycogen phosphorylase". In: *Biophysical chemistry* 106.3 (2003), pp. 193–202. DOI: 10.1016/S0301-4622(03)00192-3.
- [81] Stefan Schuster, Beate Knoke, and Marko Marhl. "Differential regulation of proteins by bursting calcium oscillations - a theoretical study". In: *BioSystems* 81.1 (2005), pp. 49–63. DOI: 10.1016/j.biosystems.2005.02.004.
- [82] Beate Knoke, Marko Marhl, and Stefan Schuster. "Selective Regulation of Protein Activity by Complex Ca^{2+} Oscillations: A Theoretical Study". In: *Mathematical Modeling of Biological Systems, Volume I*. Springer, 2007, pp. 11–22. DOI: 10.1007/978-0-8176-4558-8_2.
- [83] Marko Marhl, Matjaž Perc, and Stefan Schuster. "A minimal model for decoding of time-limited Ca^{2+} oscillations". In: *Biophysical chemistry* 120.3 (2006), pp. 161–167. DOI: 10.1016/j.bpc.2005.11.005.
- [84] Victoria L Nixon, Mark Levasseur, Alex McDougall, and Keith T Jones. " Ca^{2+} oscillations promote APC/C-dependent cyclin B1 degradation during metaphase arrest and completion of meiosis in fertilizing mouse eggs". In: *Current Biology* 12.9 (2002), pp. 746–750. DOI: 10.1016/S0960-9822(02)00811-4.
- [85] Joseph J Falke, Steven K Drake, Andrea L Hazard, and Olve B Peersen. "Molecular tuning of ion binding to calcium signaling proteins". In: *Quarterly reviews of biophysics* 27.3 (1994), pp. 219–290. DOI: 10.1017/S0033583500003012.
- [86] Carlos Salazar, Antonio Politi, and Thomas Höfer. "Decoding of calcium oscillations by phosphorylation cycles". In: *Proceedings of Fourth International Workshop on Bioinformatics and Systems Biology*. Kyoto. 2004, pp. 50–51. DOI: 10.1529/biophysj.107.113084.
- [87] Carlos Salazar, Antonio Zaccaria Politi, and Thomas Höfer. "Decoding of calcium oscillations by phosphorylation cycles: analytic results". In: *Biophysical journal* 94.4 (2008), pp. 1203–1215. DOI: 10.1529/biophysj.107.113084.
- [88] Th W Engelmann. "Neue Methode zur Untersuchung der Sauerstoffausscheidung pflanzlicher und thierischer Organismen". In: *Pflügers Archiv European Journal of Physiology* 25.1 (1881), pp. 285–292. DOI: 10.1007/BF01661982.
- [89] Th W Engelmann. "Zur Biologie der Schizomyceten". In: *Pflügers Archiv European Journal of Physiology* 26.1 (1881), pp. 537–545. DOI: 10.1007/BF01628169.
- [90] Wilhelm Friedrich Philipp Pfeffer. "Locomotorische Richtungsbewegungen durch chemische Reize". 1884.
- [91] Julius Adler. "Chemotaxis in bacteria". In: *Annual review of biochemistry* 44.1 (1975), pp. 341–356.
- [92] Roland Thar and Michael Kühl. "Bacteria are not too small for spatial sensing of chemical gradients: an experimental evidence". In: *Proceedings of the National Academy of Sciences* 100.10 (2003), pp. 5748–5753. DOI: 10.1073/pnas.1030795100.
- [93] Robert M Macnab and Daniel E Koshland. "The gradient-sensing mechanism in bacterial chemotaxis". In: *Proceedings of the National Academy of Sciences* 69.9 (1972), pp. 2509–2512. DOI: 10.1073/pnas.69.9.2509.
- [94] Nora Tsang, Robert Macnab, and Daniel E Koshland. "Common mechanism for repellents and attractants in bacterial chemotaxis". In: *Science* 181.4094 (1973), pp. 60–63. DOI: 10.1126/science.181.4094.60.
- [95] Steven J Kleene, Myron L Toews, and Julius Adler. "Isolation of glutamic acid methyl ester from an *Escherichia coli* membrane protein involved in chemotaxis." In: *Journal of Biological Chemistry* 252.10 (1977), pp. 3214–3218.

- [96] Katherine A Borkovich, Lisa A Alex, and Melvin I Simon. "Attenuation of sensory receptor signaling by covalent modification". In: *Proceedings of the National Academy of Sciences* 89.15 (1992), pp. 6756–6760. DOI: 10.1073/pnas.89.15.6756.
- [97] Philippe Cluzel, Michael Surette, and Stanislas Leibler. "An ultrasensitive bacterial motor revealed by monitoring signaling proteins in single cells". In: *Science* 287.5458 (2000), pp. 1652–1655. DOI: 10.1126/science.287.5458.1652.
- [98] Nicholas C Darnton, Linda Turner, Svetlana Rojevsky, and Howard C Berg. "On torque and tumbling in swimming *Escherichia coli*". In: *Journal of bacteriology* 189.5 (2007), pp. 1756–1764. DOI: 10.1128/JB.01501-06.
- [99] George H Wadhams and Judith P Armitage. "Making sense of it all: bacterial chemotaxis". In: *Nature reviews Molecular cell biology* 5.12 (2004), p. 1024. DOI: 10.1038/nrm1524.
- [100] Anat Bren, Martin Welch, Yuval Blat, and Michael Eisenbach. "Signal termination in bacterial chemotaxis: CheZ mediates dephosphorylation of free rather than switch-bound CheY". In: *Proceedings of the National Academy of Sciences* 93.19 (1996), pp. 10090–10093.
- [101] Karen Lipkow, Steven S Andrews, and Dennis Bray. "Simulated diffusion of phosphorylated CheY through the cytoplasm of *Escherichia coli*". In: *Journal of bacteriology* 187.1 (2005), pp. 45–53. DOI: 10.1128/JB.187.1.45-53.2005.
- [102] Martin Welch, Kenji Oosawa, S-I Aizawa, and Michael Eisenbach. "Phosphorylation-dependent binding of a signal molecule to the flagellar switch of bacteria". In: *Proceedings of the National Academy of Sciences* 90.19 (1993), pp. 8787–8791. DOI: 10.1073/pnas.90.19.8787.
- [103] Paul Van Der Werf and Daniel E Koshland. "Identification of a gamma-glutamyl methyl ester in bacterial membrane protein involved in chemotaxis." In: *Journal of Biological Chemistry* 252.8 (1977), pp. 2793–2795.
- [104] Nikita Vladimirov and Victor Sourjik. "Chemotaxis: how bacteria use memory". In: *Biological chemistry* 390.11 (2009), pp. 1097–1104. DOI: 10.1515/BC.2009.130.
- [105] Dana Aswad and DE Koshland. "Role of methionine in bacterial chemotaxis". In: *Journal of bacteriology* 118.2 (1974), pp. 640–645.
- [106] Martin S Springer, Edward N Kort, Steven H Larsen, George W Ordal, Robert W Reader, and Julius Adler. "Role of methionine in bacterial chemotaxis: requirement for tumbling and involvement in information processing". In: *Proceedings of the National Academy of Sciences* 72.11 (1975), pp. 4640–4644. DOI: 10.1073/pnas.72.11.4640.
- [107] Michael F Goy, Martin S Springer, and Julius Adler. "Failure of sensory adaptation in bacterial mutants that are defective in a protein methylation reaction". In: *Cell* 15.4 (1978), pp. 1231–1240. DOI: 10.1016/0092-8674(78)90049-1.
- [108] Hanbin Mao, Paul S Cremer, and Michael D Manson. "A sensitive, versatile microfluidic assay for bacterial chemotaxis". In: *Proceedings of the National Academy of Sciences* 100.9 (2003), pp. 5449–5454. DOI: 10.1073/pnas.0931258100.
- [109] Victor Sourjik and Howard C Berg. "Receptor sensitivity in bacterial chemotaxis". In: *Proceedings of the National Academy of Sciences* 99.1 (2002), pp. 123–127. DOI: 10.1073/pnas.011589998.
- [110] Dennis Bray. "Bacterial chemotaxis and the question of gain". In: *Proceedings of the National Academy of Sciences* 99.1 (2002), pp. 7–9. DOI: 10.1073/pnas.022641699.
- [111] Victor Sourjik and Ned S Wingreen. "Responding to chemical gradients: bacterial chemotaxis". In: *Current opinion in cell biology* 24.2 (2012), pp. 262–268. DOI: 10.1016/j.ceb.2011.11.008.
- [112] Robert Mesibov, George W Ordal, and Julius Adler. "The range of attractant concentrations for bacterial chemotaxis and the threshold and size of response over this range: Weber law and related phenomena". In: *The Journal of general physiology* 62.2 (1973), pp. 203–223. DOI: 10.1085/jgp.62.2.203.

- [113] Uri Alon, Michael G Surette, Naama Barkai, and Stanislas Leibler. “Robustness in bacterial chemotaxis”. In: *Nature* 397.6715 (1999), p. 168. DOI: 10.1038/16483.
- [114] Linda Løvdok, Kajetan Bentele, Nikita Vladimirov, Anette Müller, Ferencz S Pop, Dirk Lebiedz, Markus Kollmann, and Victor Sourjik. “Role of translational coupling in robustness of bacterial chemotaxis pathway”. In: *PLoS biology* 7.8 (2009), e1000171.
- [115] Marcus J Tindall, Philip K Maini, Steven L Porter, and Judith P Armitage. “Overview of mathematical approaches used to model bacterial chemotaxis II: bacterial populations”. In: *Bulletin of mathematical biology* 70.6 (2008), p. 1570.
- [116] Evelyn F Keller and Lee A Segel. “Model for chemotaxis”. In: *Journal of theoretical biology* 30.2 (1971), pp. 225–234. DOI: 10.1016/0022-5193(71)90050-6.
- [117] Evelyn F Keller and Lee A Segel. “Traveling bands of chemotactic bacteria: a theoretical analysis”. In: *Journal of theoretical biology* 30.2 (1971), pp. 235–248. DOI: 10.1016/0022-5193(71)90051-8.
- [118] A Goldbeter and Daniel E Koshland Jr. “Simple molecular model for sensing and adaptation based on receptor modification with application to bacterial chemotaxis”. In: *Journal of molecular biology* 161.3 (1982), pp. 395–416. DOI: 10.1016/0022-2836(82)90246-7.
- [119] Steven M Block, Jeffrey E Segall, and Howard C Berg. “Adaptation kinetics in bacterial chemotaxis”. In: *Journal of bacteriology* 154.1 (1983), pp. 312–323.
- [120] Sho Asakura and Hajime Honda. “Two-state model for bacterial chemoreceptor proteins: The role of multiple methylation”. In: *Journal of molecular biology* 176.3 (1984), pp. 349–367. DOI: 10.1016/0022-2836(84)90494-7.
- [121] Lee A Segel, Albert Goldbeter, Peter N Devreotes, and Barry E Knox. “A mechanism for exact sensory adaptation based on receptor modification”. In: *Journal of theoretical biology* 120.2 (1986), pp. 151–179. DOI: 10.1016/S0022-5193(86)80171-0.
- [122] David C Hauri and John Ross. “A model of excitation and adaptation in bacterial chemotaxis”. In: *Biophysical journal* 68.2 (1995), pp. 708–722. DOI: 10.1016/S0006-3495(95)80232-8.
- [123] Peter A Spiro, John S Parkinson, and Hans G Othmer. “A model of excitation and adaptation in bacterial chemotaxis”. In: *Proceedings of the National Academy of Sciences* 94.14 (1997), pp. 7263–7268.
- [124] Matthew D Levin, Carl J Morton-Firth, Walid N Abouhamad, Robert B Bourret, and Dennis Bray. “Origins of individual swimming behavior in bacteria”. In: *Biophysical journal* 74.1 (1998), pp. 175–181. DOI: 10.1016/S0006-3495(98)77777-X.
- [125] Carl Jason Morton-Firth and Dennis Bray. “Predicting temporal fluctuations in an intracellular signalling pathway”. In: *Journal of Theoretical Biology* 192.1 (1998), pp. 117–128. DOI: 10.1006/jtbi.1997.0651.
- [126] D Bray and RB Bourret. “Computer analysis of the binding reactions leading to a transmembrane receptor-linked multiprotein complex involved in bacterial chemotaxis.” In: *Molecular biology of the cell* 6.10 (1995), pp. 1367–1380. DOI: 10.1091/mbc.6.10.1367.
- [127] Carl Jason Morton-Firth, Thomas Simon Shimizu, and Dennis Bray. “A free-energy-based stochastic simulation of the Tar receptor complex”. In: *Journal of molecular biology* 286.4 (1999), pp. 1059–1074. DOI: 10.1006/jmbi.1999.2535.
- [128] Christopher V Rao, John R Kirby, and Adam P Arkin. “Design and diversity in bacterial chemotaxis: a comparative study in *Escherichia coli* and *Bacillus subtilis*”. In: *PLoS biology* 2.2 (2004), e49. DOI: 10.1371/journal.pbio.0020049.
- [129] Nikita Vladimirov, Linda Løvdok, Dirk Lebiedz, and Victor Sourjik. “Dependence of bacterial chemotaxis on gradient shape and adaptation rate”. In: *PLoS computational biology* 4.12 (2008), e1000242. DOI: 10.1371/journal.pcbi.1000242.

- [130] Diana Clausznitzer, Olga Oleksiuk, Linda Løvdok, Victor Sourjik, and Robert G Endres. “Chemotactic response and adaptation dynamics in *Escherichia coli*”. In: *PLoS computational biology* 6.5 (2010). DOI: 10.1371/journal.pcbi.1000784.
- [131] Marcus J Tindall, SL Porter, PK Maini, G Gaglia, and Judith P Armitage. “Overview of mathematical approaches used to model bacterial chemotaxis I: the single cell”. In: *Bulletin of mathematical biology* 70.6 (2008), pp. 1525–1569. DOI: 10.1007/s11538-008-9321-6.
- [132] Howard C Berg and PM Tedesco. “Transient response to chemotactic stimuli in *Escherichia coli*”. In: *Proceedings of the National Academy of Sciences* 72.8 (1975), pp. 3235–3239. DOI: 10.1073/pnas.72.8.3235.
- [133] John L Spudich and Daniel E Koshland. “Quantitation of the sensory response in bacterial chemotaxis”. In: *Proceedings of the National Academy of Sciences* 72.2 (1975), pp. 710–713. DOI: 10.1073/pnas.72.2.710.
- [134] Michael F Goy, Martin S Springer, and Julius Adler. “Sensory transduction in *Escherichia coli*: role of a protein methylation reaction in sensory adaptation”. In: *Proceedings of the National Academy of Sciences* 74.11 (1977), pp. 4964–4968. DOI: 10.1073/pnas.74.11.4964.
- [135] Wayne R Springer and Daniel E Koshland. “Identification of a protein methyltransferase as the *cheR* gene product in the bacterial sensing system”. In: *Proceedings of the National Academy of Sciences* 74.2 (1977), pp. 533–537. DOI: 10.1073/pnas.74.2.533.
- [136] Jeffry B Stock and Daniel E Koshland. “A protein methylesterase involved in bacterial sensing”. In: *Proceedings of the National Academy of Sciences* 75.8 (1978), pp. 3659–3663. DOI: 10.1073/pnas.75.8.3659.
- [137] Daniel E Koshland Jr. “Bacterial chemotaxis in relation to neurobiology”. In: *Annual Review of Neuroscience* 3.1 (1980), pp. 43–75. DOI: 10.1146/annurev.ne.03.030180.000355.
- [138] Shail K Sharma, Werner A Klee, and Marshall Nirenberg. “Dual regulation of adenylate cyclase accounts for narcotic dependence and tolerance”. In: *Proceedings of the National Academy of Sciences* 72.8 (1975), pp. 3092–3096. DOI: 10.1073/pnas.72.8.3092.
- [139] Johanna McEntyre and David Lipman. “PubMed: bridging the information gap”. In: *Canadian Medical Association Journal* 164.9 (2001), pp. 1317–1319. DOI: 10.1016/S1471-4906(01)02042-7.
- [140] Roman Jakobson. “Linguistics and communication theory”. In: *Proceedings of symposia in applied mathematics*. Vol. 12. 1961, pp. 245–52.
- [141] Julian Warner. “Analogies between linguistics and information theory”. In: *Journal of the American Society for Information Science and Technology* 58.3 (2007), pp. 309–321. DOI: 10.1002/asi.20490.
- [142] Fred Attneave. “Applications of information theory to psychology: A summary of basic concepts, methods, and results.” In: (1959).
- [143] Wendell R Garner. “Uncertainty and structure as psychological concepts.” In: (1962).
- [144] John Maynard Smith. “The concept of information in biology”. In: *Philosophy of science* 67.2 (2000), pp. 177–194. DOI: 10.1017/CB09780511778759.007.
- [145] Christoph Adami. “Information theory in molecular biology”. In: *Physics of Life Reviews* 1.1 (2004), pp. 3–22. DOI: 10.1016/j.plrev.2004.01.002.
- [146] Thomas M Cover and Joy A Thomas. “Elements of information theory”. John Wiley & Sons, 2012. DOI: 10.1002/047174882X.
- [147] Raymond Cheong, Alex Rhee, Chiao Chun Joanne Wang, Ilya Nemenman, and Andre Levchenko. “Information transduction capacity of noisy biochemical signaling networks”. In: *science* 334.6054 (2011), pp. 354–358. DOI: 10.1126/science.1204553.

- [148] Alex Rhee, Raymond Cheong, and Andre Levchenko. “The application of information theory to biochemical signaling systems”. In: *Physical biology* 9.4 (2012), p. 045011. DOI: 10.1088/1478-3975/9/4/045011.
- [149] Tadashi Nakano and Jian-Qin Liu. “Design and analysis of molecular relay channels: An information theoretic approach”. In: *IEEE Transactions on NanoBioscience* 9.3 (2010), pp. 213–221.
- [150] Sahand Hormoz. “Cross talk and interference enhance information capacity of a signaling pathway”. In: *Biophysical journal* 104.5 (2013), pp. 1170–1180. DOI: 10.1016/j.bpj.2013.01.033.
- [151] Amiran Keshelava, Gonzalo P Solis, Micha Hersch, Alexey Koval, Mikhail Kryuchkov, Sven Bergmann, and Vladimir L Katanaev. “High capacity in G protein-coupled receptor signaling”. In: *Nature communications* 9.1 (2018), p. 876. DOI: 10.1038/s41467-018-02868-y.
- [152] Arne Schoch and Jürgen Pahle. “Requirements for band-pass activation of Ca^{2+} -sensitive proteins such as NFAT”. In: *Biophysical chemistry* 245 (2019), pp. 41–52. DOI: 10.1016/j.bpc.2018.10.005.
- [153] R Core Team. “R: A language and environment for statistical computing”. In: *R Foundation for Statistical Computing. Vienna, Austria* (2017).
- [154] Karlene ER Soetaert, Thomas Petzoldt, and R Woodrow Setzer. “Solving differential equations in R: package *deSolve*”. In: *Journal of Statistical Software* 33 (2010).
- [155] AC Hindmarsh and LR Petzold. “LSODAR, Ordinary Differential Equation Solver for Stiff or Non-Stiff System with root-finding”. In: (2005).
- [156] Stefan Hoops, Sven Sahle, Ralph Gauges, Christine Lee, Jürgen Pahle, Natalia Simus, Mudita Singhal, Liang Xu, Pedro Mendes, and Ursula Kummer. “COPASI - a complex pathway simulator”. In: *Bioinformatics* 22.24 (2006), pp. 3067–3074. DOI: 10.1093/bioinformatics/btl1485.
- [157] Daniel T Gillespie. “A general method for numerically simulating the stochastic time evolution of coupled chemical reactions”. In: *Journal of computational physics* 22.4 (1976), pp. 403–434. DOI: 10.1016/0021-9991(76)90041-3.
- [158] Daniel T Gillespie. “Markov processes: an introduction for physical scientists”. Elsevier, 1991.
- [159] John A Nelder and Roger Mead. “A simplex method for function minimization”. In: *The computer journal* 7.4 (1965), pp. 308–313. DOI: 10.1093/comjnl/7.4.308.
- [160] Alexander Kraskov, Harald Stögbauer, and Peter Grassberger. “Estimating mutual information”. In: *Physical review E* 69.6 (2004), p. 066138. DOI: 10.1103/PhysRevE.69.066138.
- [161] Gauthier Doquire, Michel Verleysen, et al. “A Comparison of Multivariate Mutual Information Estimators for Feature Selection.” In: *ICPRAM (1)*. Citeseer. 2012, pp. 176–185.
- [162] Ralf Steuer, Jürgen Kurths, Carsten O Daub, Janko Weise, and Joachim Selbig. “The mutual information: detecting and evaluating dependencies between variables”. In: *Bioinformatics* 18.suppl_2 (2002), S231–S240.
- [163] Robert Marschinski and Holger Kantz. “Analysing the information flow between financial time series”. In: *The European Physical Journal B-Condensed Matter and Complex Systems* 30.2 (2002), pp. 275–281. DOI: 10.1140/epjb/e2002-00379-2.
- [164] Richard Blahut. “Computation of channel capacity and rate-distortion functions”. In: *IEEE transactions on Information Theory* 18.4 (1972), pp. 460–473. DOI: 10.1109/TIT.1972.1054855.
- [165] Suguru Arimoto. “An algorithm for computing the capacity of arbitrary discrete memoryless channels”. In: *IEEE Transactions on Information Theory* 18.1 (1972), pp. 14–20. DOI: 10.1109/TIT.1972.1054753.

- [166] Hadley Wickham. “ggplot2: elegant graphics for data analysis”. Springer, 2016. DOI: 10.1111/j.1541-0420.2011.01616.x.
- [167] Jian-Qin Liu and Tadashi Nakano. “An information theoretic model of molecular communication based on cellular signaling”. In: *Bio-Inspired Models of Network, Information and Computing Systems, 2007. Bionetics 2007. 2nd*. IEEE. 2007, pp. 316–321. DOI: 10.1109/BIMNICS.2007.4610136.
- [168] Archibald Vivian Hill. “The possible effects of the aggregation of the molecules of haemoglobin on its dissociation curves”. In: *j. physiol.* 40 (1910), pp. 4–7. DOI: 10.1113/jphysiol.1910.sp001386.
- [169] JF Maune, CB Klee, and K Beckingham. “Ca²⁺ binding and conformational change in two series of point mutations to the individual Ca²⁺-binding sites of calmodulin.” In: *Journal of Biological Chemistry* 267.8 (1992), pp. 5286–5295.
- [170] Luke H Chao, Patricia Pellicena, Sebastian Deindl, Lauren A Barclay, Howard Schulman, and John Kuriyan. “Intersubunit capture of regulatory segments is a component of cooperative CaMKII activation”. In: *Nature Structural and Molecular Biology* 17.3 (2010), p. 264. DOI: 10.1038/nsmb.1751.
- [171] Nicholas J Carruthers and Paul M Stemmer. “Methionine oxidation in the calmodulin-binding domain of calcineurin disrupts calmodulin binding and calcineurin activation”. In: *Biochemistry* 47.10 (2008), pp. 3085–3095. DOI: 10.1021/bi702044x.
- [172] Susy C Kohout, Senena Corbalán-García, Alejandro Torrecillas, Juan C Gómez-Fernández, and Joseph J Falke. “C2 domains of protein kinase C isoforms α , β , and γ : Activation parameters and calcium stoichiometries of the membrane-bound state”. In: *Biochemistry* 41.38 (2002), pp. 11411–11424. DOI: 10.1021/bi026041k.
- [173] Jürgen Pahle, Anne K Green, C Jane Dixon, and Ursula Kummer. “Information transfer in signaling pathways: a study using coupled simulated and experimental data”. In: *BMC bioinformatics* 9.1 (2008), p. 139. DOI: 10.1186/1471-2105-9-139.
- [174] Taichiro Tomida, Kenzo Hirose, Azusa Takizawa, Futoshi Shibasaki, and Masamitsu Iino. “NFAT functions as a working memory of Ca²⁺ signals in decoding Ca²⁺ oscillation”. In: *The EMBO journal* 22.15 (2003), pp. 3825–3832. DOI: 10.1093/emboj/cdg381.
- [175] Naoya Onohara, Motohiro Nishida, Ryuji Inoue, Hiroyuki Kobayashi, Hideki Sumimoto, Yoji Sato, Yasuo Mori, Taku Nagao, and Hitoshi Kurose. “TRPC3 and TRPC6 are essential for angiotensin II-induced cardiac hypertrophy”. In: *The EMBO journal* 25.22 (2006), pp. 5305–5316. DOI: 10.1038/sj.emboj.7601417.
- [176] Per Uhlén, Peter M Burch, Christina Ivins Zito, Manuel Estrada, Barbara E Ehrlich, and Anton M Bennett. “Gain-of-function/Noonan syndrome SHP-2/Ptpn11 mutants enhance calcium oscillations and impair NFAT signaling”. In: *Proceedings of the National Academy of Sciences of the United States of America* 103.7 (2006), pp. 2160–2165. DOI: 10.1073/pnas.0510876103.
- [177] Patrick G Hogan, Lin Chen, Julie Nardone, and Anjana Rao. “Transcriptional regulation by calcium, calcineurin, and NFAT”. In: *Genes & development* 17.18 (2003), pp. 2205–2232. DOI: 10.1101/gad.1102703.
- [178] Scott M MacDonnell, Jutta Weisser-Thomas, Hajime Kubo, Marie Hanscome, Qinghang Liu, Naser Jaleel, Remus Berretta, Xiongwen Chen, Joan H Brown, Abdel-Karim Sabri, et al. “CaMKII negatively regulates calcineurin-NFAT signaling in cardiac myocytes”. In: *Circulation research* 105.4 (2009), pp. 316–325. DOI: 10.1161/CIRCRESAHA.109.194035.
- [179] Yoshiaki Hashimoto, Marita M King, and Thomas R Soderling. “Regulatory interactions of calmodulin-binding proteins: phosphorylation of calcineurin by autophosphorylated Ca²⁺/calmodulin-dependent protein kinase II”. In: *Proceedings of the National Academy of Sciences* 85.18 (1988), pp. 7001–7005. DOI: 10.1073/pnas.85.18.7001.

- [180] Neil A Clipstone and Gerald R Crabtree. "Identification of calcineurin as a key signalling enzyme in T-lymphocyte activation". In: *Nature* 357.6380 (1992), p. 695. DOI: 10.1038/357695a0.
- [181] Chan R Beals, Colleen M Sheridan, Christoph W Turck, Phyllis Gardner, and Gerald R Crabtree. "Nuclear export of NF-ATc enhanced by glycogen synthase kinase-3". In: *Science* 275.5308 (1997), pp. 1930–1933. DOI: 10.1126/science.275.5308.1930.
- [182] Cynthia M Porter, Michael A Havens, and Neil A Clipstone. "Identification of amino acid residues and protein kinases involved in the regulation of NFATc subcellular localization". In: *Journal of Biological Chemistry* 275.5 (2000), pp. 3543–3551. DOI: 10.1074/JBC.275.5.3543.
- [183] Wayne G Fisher, Pei Yang, Ram K Medikonduri, and M Saleet Jafri. "NFAT and NFκB activation in T lymphocytes: a model of differential activation of gene expression". In: *Annals of biomedical engineering* 34.11 (2006), pp. 1712–1728. DOI: 10.1007/s10439-006-9179-4.
- [184] Arren Bar-Even, Elad Noor, Yonatan Savir, Wolfram Liebermeister, Dan Davidi, Dan S Tawfik, and Ron Milo. "The moderately efficient enzyme: evolutionary and physicochemical trends shaping enzyme parameters". In: *Biochemistry* 50.21 (2011), pp. 4402–4410. DOI: 10.1021/bi2002289.
- [185] Jason D Runyan, Anthony N Moore, and Pramod K Dash. "A role for prefrontal calcium-sensitive protein phosphatase and kinase activities in working memory". In: *Learning & memory* 12.2 (2005), pp. 103–110. DOI: 10.1101/lm.89405.
- [186] Zhexiong Wen, Carmine Guirland, Guo Ming, and James Q Zheng. "A CaMKII/calcineurin switch controls the direction of Ca²⁺-dependent growth cone guidance". In: *Neuron* 43.6 (2004), pp. 835–846. DOI: 10.1016/j.neuron.2004.08.037.
- [187] Brian T Nasipak, Teresita Padilla-Benavides, Karin M Green, John D Leszyk, Wenjie Mao, Silvana Konda, Saïd Sif, Scott A Shaffer, Yasuyuki Ohkawa, and Anthony N Imbalzano. "Opposing calcium-dependent signalling pathways control skeletal muscle differentiation by regulating a chromatin remodelling enzyme". In: *Nature communications* 6 (2015). DOI: 10.1038/ncomms8441.
- [188] Frank Rusnak and Pamela Mertz. "Calcineurin: form and function". In: *Physiological reviews* 80.4 (2000), pp. 1483–1521. DOI: 10.1152/physrev.2000.80.4.1483.
- [189] Clinton H Hansen, Robert G Endres, and Ned S Wingreen. "Chemotaxis in *Escherichia coli*: a molecular model for robust precise adaptation". In: *PLoS computational biology* 4.1 (2008), e1. DOI: 10.1371/journal.pcbi.0040001.
- [190] Daniel E Koshland. "Chemotaxis as a model for sensory systems". In: *FEBS letters* 40.S1 (1974), S2–S2.
- [191] Daniel E Koshland Jr. "Biochemistry of sensing and adaptation in a simple bacterial system". In: *Annual review of biochemistry* 50.1 (1981), pp. 765–782. DOI: 10.1146/annurev.bi.50.070181.004001.
- [192] Filipe Tostevin and Pieter Rein Ten Wolde. "Mutual information between input and output trajectories of biochemical networks". In: *Physical review letters* 102.21 (2009), p. 218101. DOI: 10.1103/PhysRevLett.102.218101.
- [193] Danny Fuller, Wen Chen, Micha Adler, Alex Groisman, Herbert Levine, Wouter-Jan Rappel, and William F Loomis. "External and internal constraints on eukaryotic chemotaxis". In: *Proceedings of the National Academy of Sciences* 107.21 (2010), pp. 9656–9659.
- [194] Anthony L DeFranco and DE Koshland. "Multiple methylation in processing of sensory signals during bacterial chemotaxis". In: *Proceedings of the National Academy of Sciences* 77.5 (1980), pp. 2429–2433. DOI: 10.1073/pnas.77.5.2429.
- [195] Peter Engström and Gerald L Hazelbauer. "Multiple methylation of methyl-accepting chemotaxis proteins during adaptation of *E. coli* to chemical stimuli". In: *Cell* 20.1 (1980), pp. 165–171. DOI: 10.1016/0092-8674(80)90244-5.

- [196] Anna Krembel, Remy Colin, and Victor Sourjik. "Importance of multiple methylation sites in *Escherichia coli* chemotaxis". In: *PloS one* 10.12 (2015), e0145582. DOI: 10.1371/journal.pone.0145582.
- [197] Yuhai Tu, Thomas S Shimizu, and Howard C Berg. "Modeling the chemotactic response of *Escherichia coli* to time-varying stimuli". In: *Proceedings of the National Academy of Sciences* 105.39 (2008), pp. 14855–14860. DOI: 10.1073/pnas.0807569105.
- [198] Robert G Endres and Ned S Wingreen. "Precise adaptation in bacterial chemotaxis through "assistance neighborhoods"". In: *Proceedings of the National Academy of Sciences* 103.35 (2006), pp. 13040–13044. DOI: 10.1073/pnas.0603101103.
- [199] Mingshan Li and Gerald L Hazelbauer. "Cellular stoichiometry of the components of the chemotaxis signaling complex". In: *Journal of bacteriology* 186.12 (2004), pp. 3687–3694. DOI: 10.1128/JB.186.12.3687-3694.2004.
- [200] Linda Turner, William S Ryu, and Howard C Berg. "Real-time imaging of fluorescent flagellar filaments". In: *Journal of bacteriology* 182.10 (2000), pp. 2793–2801. DOI: 10.1128/JB.182.10.2793-2801.2000.
- [201] Mayukh K Sarkar, Koushik Paul, and David Blair. "Chemotaxis signaling protein CheY binds to the rotor protein FliN to control the direction of flagellar rotation in *Escherichia coli*". In: *Proceedings of the National Academy of Sciences* 107.20 (2010), pp. 9370–9375. DOI: 10.1073/pnas.1000935107.
- [202] Howard C Berg, Douglas A Brown, et al. "Chemotaxis in *Escherichia coli* analysed by three-dimensional tracking". In: *Nature* 239.5374 (1972), pp. 500–504. DOI: 10.1038/239500a0.
- [203] Sonja Elke Schulmeister. "Rezeptormethylierung und Stabilität von Chemotaxisclustern in *Escherichia coli*". PhD thesis. 2010.
- [204] Taejin L Min, Patrick J Mears, Ido Golding, and Yann R Chemla. "Chemotactic adaptation kinetics of individual *Escherichia coli* cells". In: *Proceedings of the National Academy of Sciences* 109.25 (2012), pp. 9869–9874.
- [205] Masao Fukushima, Kenichi Kakinuma, and Ryuji Kawaguchi. "Phylogenetic analysis of *Salmonella*, *Shigella*, and *Escherichia coli* strains on the basis of the *gyrB* gene sequence". In: *Journal of clinical microbiology* 40.8 (2002), pp. 2779–2785. DOI: 10.1128/JCM.40.8.2779-2785.2002.
- [206] MR Kehry and FW Dahlquist. "The methyl-accepting chemotaxis proteins of *Escherichia coli*. Identification of the multiple methylation sites on methyl-accepting chemotaxis protein I." In: *Journal of Biological Chemistry* 257.17 (1982), pp. 10378–10386.
- [207] Thomas C Terwilliger and DE Koshland. "Sites of methyl esterification and deamination on the aspartate receptor involved in chemotaxis." In: *Journal of Biological Chemistry* 259.12 (1984), pp. 7719–7725.
- [208] Margaret S Rice and FW Dahlquist. "Sites of deamidation and methylation in Tsr, a bacterial chemotaxis sensory transducer." In: *Journal of Biological Chemistry* 266.15 (1991), pp. 9746–9753.
- [209] Dawn M Nowlin, John Bollinger, and GL Hazelbauer. "Sites of covalent modification in Trg, a sensory transducer of *Escherichia coli*." In: *Journal of Biological Chemistry* 262.13 (1987), pp. 6039–6045.
- [210] Jeffrey E Segall, Steven M Block, and Howard C Berg. "Temporal comparisons in bacterial chemotaxis". In: *Proceedings of the National Academy of Sciences* 83.23 (1986), pp. 8987–8991. DOI: 10.1073/pnas.83.23.8987.
- [211] Catherine Kim, Marilyn Jackson, Renate Lux, and Shahid Khan. "Determinants of chemotactic signal amplification in *Escherichia coli*". In: *Journal of molecular biology* 307.1 (2001), pp. 119–135. DOI: 10.1006/jmbi.2000.4389.

- [212] Ursula Kummer, Borut Krajnc, Jürgen Pahle, Anne K Green, C Jane Dixon, and Marko Marhl. "Transition from stochastic to deterministic behavior in calcium oscillations". In: *Biophysical journal* 89.3 (2005), pp. 1603–1611. DOI: 10.1529/biophysj.104.057216.
- [213] James P Keener. "Stochastic calcium oscillations". In: *Mathematical Medicine and Biology* 23.1 (2006), pp. 1–25. DOI: 10.1093/imammb/dql002.
- [214] Joseph J Falke. "Cooperativity between bacterial chemotaxis receptors". In: *Proceedings of the National Academy of Sciences* 99.10 (2002), pp. 6530–6532. DOI: 10.1073/pnas.112214199.
- [215] Victor Sourjik and Howard C Berg. "Functional interactions between receptors in bacterial chemotaxis". In: *Nature* 428.6981 (2004), p. 437. DOI: 10.1038/nature02406.
- [216] Katharina F Sonnen and Alexander Aulehla. "Dynamic signal encoding - From cells to organisms". In: *Seminars in Cell & Developmental Biology*. Vol. 34. Elsevier. 2014, pp. 91–98. DOI: 10.1016/j.semcdb.2014.06.019.

